Infrared supercontinuum generation and aging challenges in sulfur-based chalcogenide glasses suspended core highly non linear optical fibers

Oussama Mouawad

To cite this version:

Oussama Mouawad. Infrared supercontinuum generation and aging challenges in sulfur-based chalcogenide glasses suspended core highly non linear optical fibers. Chemical Physics [physics.chem-ph]. Université de Bourgogne, 2014. English. NNT : 2014DIJOS072 . tel-01409555

HAL Id: tel-01409555
https://theses.hal.science/tel-01409555
Submitted on 6 Dec 2016

UNIVERSITE DE BOURGOGNE

Laboratoire Interdisciplinaire Carnot de Bourgogne (ICB)
Département OMR Equipe SLCO
UMR 6303 CNRS–UNIVERSITE DE BOURGOGNE - DIJON - FRANCE

THÈSE

Pour obtenir le grade de

Docteur de l'Université de Bourgogne

Discipline : **Chimie-Physique (Sciences des Matériaux)**

Par

Oussama MOUAWAD

le 5 December 2014

Génération de Supercontinuum Infrarouge et Enjeux de Vieillissement au Sein de Fibres Optiques à Cœur Suspendu Hautement Non Linéaires en Verre de Chalcogénures à Base de Sulfures

Directeur de thèse : **Pr. Frédéric SMEKTALA**

Devant le jury composé de :

CARDINAL Thierry	Directeur de Recherche, ICMCB, Université de Bordeaux	Rapporteur
OHISHI Yasutake	Professeur, Toyota Technological Institute (Japon)	Rapporteur
MESSADDEQ Younès	Professeur, C.O.P.L. Université Laval (Canada)	Rapporteur
SYLVESTRE Thibaut	Chargé de Recherche, FEMTO, Université de Franche-Comté	Examinateur
VIGREUX Caroline	Maître de Conférences, I.C.G., Université de Montpellier 2	Examinateur
SMEKTALA Frédéric	Professeur, ICB, Université de Bourgogne	Directeur

UNIVERSITE DE BOURGOGNE

Laboratoire Interdisciplinaire Carnot de Bourgogne (ICB)
Département OMR Equipe SLCO
UMR 6303 CNRS–UNIVERSITE DE BOURGOGNE - DIJON - FRANCE

A dissertation

In Partial Fulfillment of the requirements for the Degree of

DOCTOR OF PHILOSOPHY

Chemistry-Physics (Materials science)

Submitted by

Oussama MOUAWAD

The 5th December 2014

Infrared Supercontinuum Generation and Aging Challenges in Sulfur-Based Chalcogenide Glasses Suspended Core Highly Non Linear Optical Fibers

---

Thesis supervisor: **Pr. Frédéric SMEKTALA**

Committee members :

CARDINAL Thierry	Directeur de Recherche, ICMCB, Université de Bordeaux
OHISHI Yasutake	Professor, Toyota Technological Institute (Japan)
MESSADDEQ Younès	Professor, C.O.P.L. Laval University, Canada
SYLVESTRE Thibaut	Chargé de Recherche, FEMTO, Université de Franche-Comté
VIGREUX Caroline	Associate Professor, I.C.G., Université de Montpellier 2
SMEKTALA Frédéric	Professor, ICB, Université de Bourgogne

ACKNOWLEDGEMENTS

It is with immense gratitude that I acknowledge in this short foreword the support of all the people who have contributed to the preparation and completion of this research work.

I wish to thank, first and foremost, my supervisor Pr. Frederic SMEKTALA. He continually and convincingly conveyed a spirit of courage and adventure in regard to research. Without his guidance and persistent help, completion of this work would not have been possible. I hope to be remembered as one of his proud students.

I would like to express the deepest appreciation and share the credit of my work with my advisors Dr Frederic DESEVEDAVY, Dr Jean-Charles JULES and Dr Gregory GADRET for their incredible support and guidance in the helpful group meetings.

It gives me great pleasure in acknowledging the support and confidence of Pr. Guy MILLOT and Pr. Frederic SMEKTALA for the opportunity to join their group SLCO (Solitons, Lasers and Optical Communications)

I gratefully acknowledge The Centre Nationale de Recherche Scientifique (CNRS) and the Conseil Régional de Bourgogne (CRB) for their financial support to the project.

I would like to thank and share the credit of my work with Dr Bertrand KIBLER and Dr Julien FATOME.

I would like to thank my committee members, Pr. Yasutake OHISHI, Pr. Younes MESSADEQ, Dr. Thierry CARDINAL, Dr. Thibaut SYLVESTRE, and Dr. Caroline VIGREUX.

Throughout my work I had the opportunity and pleasure to collaborate with Toyota Technological Institute (TTI)-Nagoya, Japan and with whose contribution NonLinear Experiments.

I would like to thank Pr. Eric LESNIEWSKA and Pauline VITRY who contributed to carry out the AFM measurements. I would like to thank Dr. Olivier HEINTZ for his contribution the XPS measurements.

I would like to thank all my friends and acquaintances who have come and gone throughout my academic career and throughout life. Many thanks to all my colleagues for the privilege of working with you.

Finally, I wish to express my love and gratitude to my parents for the endless support and encouragement throughout this whole educational adventure. I would like to give you my sincerest thanks because without your sacrifices and help I would not be what I am.

PUBLICATIONS AND CONFERENCES

➢ Publications

1. Savelii, **O. Mouawad**, J. Fatome, B. Kibler, F. Désévédavy, G. Gadret, J-C Jules, P-Y Bony, H. Kawashima, W. Gao, T. Kohoutek, T. Suzuki, Y. Ohishi, and F. Smektala, "**Mid-infrared 2000-nm bandwidth supercontinuum generation in suspended-core microstructured Sulfide and Tellurite optical fibers,**" Opt. Express **20**, 27083-27093 (2012).
2. **O. Mouawad**, J. Picot-Clémente, F. Amrani, C. Strutynski, J. Fatome, B. Kibler, F. Désévédavy, G. Gadret, J. C. Jules, D. Deng, Y. Ohishi, and F. Smektala, "**Multioctave midinfrared supercontinuum generation in suspended-core chalcogenide fibers**," Optics Letters **39**, 2684-2687.
3. **O. Mouawad,** F. Amrani, B. Kibler, J. Picot-Clémente, C. Strutynski, J. Fatome, F. Désévédavy, G. Gadret, J. C. Jules, O. Heintz, E. Lesniewska, and F. Smektala, **"Impact of optical and structural aging in As_2S_3 microstructured optical fibers on mid-infrared supercontinuum generation,"** Optics Express **22**, 23912-23919 (2014).
4. **O. Mouawad,** C. Strutynski, J. Picot-Clémente, F. Désévédavy, G. Gadret, J. C. Jules, and F. Smektala, **"Optical aging behaviour naturally induced on As_2S_3 microstructured optical fibres**," Optical Materials Express **4**, 2190-2203 (2014).
5. **O. Mouawad**,P. Vitry, C. Strutynski, J. Picot-Clémente, F. Désévédavy, G. Gadret, J-C Jules, E. Lesniewskaand F. Smektala, **“Further Demonstration of Atmospheric Optical Aging and Surface Degradation in As_2S_3 Optical Fibers”**. Submitted to Optical Materials Journal.

➢ Conferences in international congresses

1. **O. Mouawad**, F. Désévédavy, Savelii, J. C. Jules, G. Gadret, M. Duhant, G. Canat, Y. Ohishi, H. Kawashima, L. Brilland, J Troles and F. Smektala, **As_2S_3 Microstructured Optical Fibers Pumped Near 2 µm For Infrared Broadband Sources**., *18th Symposium on Non-Oxide and New Optical Glasses (ISNOG)*Saint Malo, France, 1-5 Juillet 2012.
2. **O. Mouawad**, F. Désévédavy, J. Picot-Clemente, J. C. Jules, G. Gadret, B. Kibler, J. Fatome, W. Gao, H. Kawashima, Y. Ohishi, and F. Smektala, **2000nm spanning**

supercontinuum in suspended-core As_2S_3 microstructured optical fibers, *23th Symposium on International Congress on Glass (ICG)Prague, République Tchèque, 1-5 Juillet 2013*.

3. **<u>O. Mouawad</u>**, F. Désévédavy, J. Picot-Clemente, J. C. Jules, G. Gadret, B. Kibler, J. Fatome, W. Gao, H. Kawashima, Y. Ohishi, and F. Smektala, **2000nm spanning supercontinuum in suspended-core As_2S_3 microstructured optical fibers**, *23th Symposium on International Congress on Glass (ICG)Prague, République Tchèque, 21-24 Septembre 2014*.

- **Conferences in national congresses**

1. **<u>O. Mouawad</u>**, F. Désévédavy, I. Savelii, J. C. Jules, G. Gadret, B. Kibler, J. Fatome, W. Gao, H. Kawashima, Y. Ohishi, and F. Smektala, **2000nm spanning supercontinuum in suspended-core As_2S_3 microstructured optical fibers**. *Journée de la photonique*, Besançon, France - 13 Novembre 2012.
2. **<u>O. Mouawad</u>**, F. Désévédavy, I. Savelii, J. C. Jules, G. Gadret, B. Kibler, J. Fatome, W. Gao, H. Kawashima, Y. Ohishi, and F. Smektala, **2000nm spanning supercontinuum in suspended-core As_2S_3 microstructured optical fibers**. *XIVème Journées de l'école doctorale Carnot-Pasteur (XIVème JED)*, Dijon, France, 30 – 31 mai 2013

- **Grant for a collaboration program**

1. **<u>Projet MIWaTSU</u>** : Mid-Infrared Widely Tunable coherent fibered SoUrces Sources fibrées cohérentes largement accordables dans le moyen infrarouge.
   1.1. Bourse de programme PRC CNRS-JSPS Franco-Japonais, *Bourse de stage au Japon,* Nagoya, Japon, Novembre 2014.
   1.2. Labex ACTION Programme ANR-11-LABX-0001-01
2. **<u>Programme ANR CONFIAN</u>** : CONtinuum à Fibres Infrarouges hAutement Non linéaires.
3. **<u>Programme Hubert Curien</u>** : PHC Sakura CNRS (France) - JSPS (Japon)-Ultra octave coherent light source development.
4. **<u>Programme PHOTCOM</u>** : Programme PARI du Conseil Régional de Bourgogne (CRB): Photonique avancée pour les télécommunications et sources lasers de nouvelle génération.

TABLE OF CONTENTS

LIST OF FIGURES

LIST OF TABLES

LIST OF APPENDIX

ABBREVIATIONS

AFM	Atomic Force Microscopy
LFM	Lateral Force Microsciopy
XPS	X-ray Photoelectron Spectroscopy
SIF	Step Index Fiber
MOF	Microstructured Optical Fiber
ZDW	Zero Dispersive Wavelength
GVD	Group Velocity Dispersion
OKE	Optical Kerr Effect
RS	Raman Scattering
BS	Brillouin Scatering
FWM	Four Wave Mixing
XPM	Cross Wave Modulation
SPM	Self Phase Modulation
SC	SuperContinuum
SCG	Supercontinuum Generation
OPO	Optical Parametric Oscillator
OSA	Optical Spectrum Analyser
FTIR	Fourrier Transform Infrared Spectroscopy
Vis	Visible
IR	Infrared
MidIR	MidInfrared
TIR	Total Internal Reflection
ChG	Chalcogenide Glasses
NLO	NonLinear Optics
NL	NonLinear
HMO	Heavy Metal Oxide

GENERAL INTRODUCTION

The use of glass-based technologies in different fields such as telecommunication, photonics, spectroscopy, medical and other sectors is unavoidable in our daily modern life. Improving the technical and economic performance of these technologies is required. Thus, the glass has been subjected to continuous investigations in fundamental materials science allowing innovation in glass properties and fabrication processes. A variety of glass systems and geometries have been developed.

Among the various glass systems, chalcogenide glasses stand out as the only family of optical glasses that are transparent across the atmospheric transmission windows according to the glass composition [1]. In addition, these glasses may also be stably drawn into extended optical fibres [1, 2]. Moreover, chalcogenides exhibit higher optical nonlinearities than most promising glasses in the mid-infrared region [3]. These exceptional features predict promising outcome in the sector of linear and nonlinear optics, among the others, supercontinuum generation. However, chalcogenides suffers from high material dispersion and low damage threshold. Thus, the requirements and specifications of chalcogenide fibres for spectral broadening demand more versatility to manipulate light that challenge the capabilities of traditional step-index optical fibres.

After the first report on Microstructured Optical Fibers (MOFs) in 1973 by Kaiser and al. [4], the fibre optics field has knew an exceptional leap following the development of photonic crystal fibers (PCF) from 1996 [5]. These structures exhibit unique optical properties and a high level of versatility, including the possibility of tuning the dispersion over a wide wavelength range and enhancing the nonlinear coefficient by strong light confinement. The advent of the PCF technologies allowed to engineer the dispersive properties of the chalcogenide-based optical fibers. After a first attempt in 2002 [6], the first guiding chalcogenide PCF was reported in 2006 [7], and have since been used in demonstrating supercontinuum generation. Following the fruitful experimental demonstration of near IR supercontinuum generation in As_2S_3 PCF [8, 9], the idea came up to explore further the potentials of these glass fibers, in view to generate a spectral broadening spreading from 1.0 to 6.0 µm.

The remainder of this dissertation is organized as follows:

- Part I is the theoretical background review. It comprises two chapters. Chapter 1 gives an overview of optical processes involved in supercontinuum generation, taking place as an optical pulse crossing an optical fibre. We focus on the linear and nonlinear phenomena allowing to understand results presented in later chapters. Chapter 2 is an introduction to the basics optical properties of glass materials, discussing especially the optical properties of different soft glass families as regards their application to MIR supercontinuum generation.
- Part II gathers results of the nonlinear optics experiments performed during this work. These results are presented on the basis of published articles. This part comprises three published articles. The first article report on 2000 nm spectral broadening on As_2S_3 suspended-core microstructured fiber (MOF), and presume an optical aging of this fiber. The second article report on enhancement of spectral broadening on carefully preserved fiber specimen. The third article presents a theoretical investigation studying the interdependence between the spectral broadening potentials of the As_2S_3 MOF and his optical aging. This presumed aging is experimentally confirmed by means of different techniques.
- Part III gathers results of the material's aging experiments performed during this work, which investigated in details the aging phenomena previously reported in the third article of Part II. These results are presented on the basis of one published article and one submitted article. The first provides an extensive study of the natural optical aging of the As_2S_3 MOF. The second article studies the surface aging of As_2S_3 fibers, and confirms the oxidation and hydrolysis of the glass structure under the atmospheric conditions.
- Part IV focuses on the selection of new arsenic- and antimony-free germanium-based glass systems, with the goal to use them as substituent to arsenic containing glasses in optical fiber technologies. The synthesis procedure is optimized and successful fiber drawing attempts are reported.
- A summary of the results obtained in this thesis is presented in the end.

References

1. J.-L. Adam, and X. Zhang, *Chalcogenide Glasses: Preparation, Properties and Applications* (Woodhead Publishing, 2014).
2. G. E. Snopatin, V. S. Shiryaev, V. G. Plotnichenko, E. M. Dianov, and M. F. Churbanov, "High-purity chalcogenide glasses for fiber optics," Inorganic Materials **45**, 1439-1460 (2009).
3. J. H. V. Price, T. M. Monro, H. Ebendorff-Heidepriem, F. Poletti, P. Horak, V. Finazzi, J. Y. Y. Leong, P. Petropoulos, J. C. Flanagan, G. Brambilla, F. Xian, and D. J. Richardson, "Mid-IR supercontinuum generation from nonsilica microstructured optical fibers," IEEE Journal of selected topics in quantum electronics **13**, 738-749 (2007).
4. P. Kaiser, E. A. J. Marcatili, and S. Miller, "A new optical fiber," The Bell system Technological Journal **52**, 265-269 (1973).
5. J. C. Knight, T. A. Birks, P. S. J. Russell, and D. M. Atkin, "All-silica single-mode optical fiber with photonic crystal cladding," Optics Letters **21**, 1547-1549 (1996).
6. T. M. Monro, Y. D. West, D. W. Hewak, N. G. R. Broderick, and D. J. Richardson, "Chalcogenide holey fibres," Electronics Letters **36**, 1998-2000 (2000).
7. L. Brilland, F. Smektala, G. Renversez, T. Chartier, J. Troles, T. Nguyen, N. Traynor, and A. Monteville, "Fabrication of complex structures of Holey Fibers in Chalcogenide glass," Optics Express **14**, 1280-1285 (2006).
8. M. El-Amraoui, J. Fatome, J. C. Jules, B. Kibler, G. Gadret, C. Fortier, F. Smektala, I. Skripatchev, C. F. Polacchini, Y. Messaddeq, J. Troles, L. Brilland, M. Szpulak, and G. Renversez, "Strong infrared spectral broadening in low-loss As-S chalcogenide suspended core microstructured optical fibers," Optics Express **18**, 4547-4556 (2010).
9. M. El-Amraoui, G. Gadret, J. C. Jules, J. Fatome, C. Fortier, F. Désévédavy, I. Skripatchev, Y. Messaddeq, J. Troles, L. Brilland, W. Gao, T. Suzuki, Y. Ohishi, and F. Smektala, "Microstructured chalcogenide optical fibers from As_2S_3 glass: towards new IR broadband sources," Optics Express **18**, 26655-26665 (2010).

Part 1: Optical Nonlinearities, Vitreous Materials: a General Overview

Chapter 1 : Linear and Nonlinear Optical Properties of Fibers

I. Introduction

The study of light transmission is very old, already in 1841, J-D Colladon showed that light was guided into the filaments of a fountain in Geneva (Figure 1). The following year, in 1842, Jacques Babinet noted the same thing in the water streams and glass sticks. In 1880, William Wheeler employed glass tubes to illuminate a place with a light source placed elsewhere: light could be guided by the glass. In 1888, Roth and Reuss used glass tubes in medicine for illuminating cavities and viscera of the body [1].

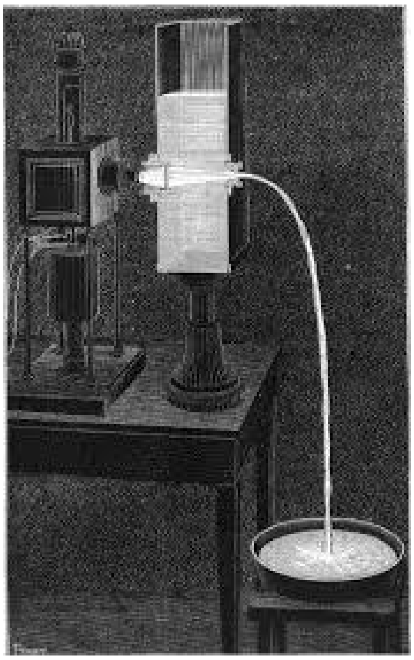

Figure 1: The luminous fountain of Colladon.

In 1927, Baird and Hansell had the idea to work on fiber optics in the sense we understand it today. The first successful application of optical fiber appeared only in 1950 with the fibroscope, created by Van Heel. Thanks to this device, we could observe with much more efficiency the inside of the human body and welds inside the aircraft engines. Unfortunately, the optical quality of the silica glasses did not allow the use of this device over long lengths of fiber. By the late 1960s born the idea of making pure silica optical fibers to transmit light over long distances, while having the lowest possible attenuation.

In 1966, C. Kao and al. demonstrate the possible use of silica fibers in optical data transmission [2]. In 1970, three inventors in Corning glass company succeeded to reduce the loss level down to 20 dB/km at ~1550 nm [3]. Their optical fiber was capable of carrying 65,000 times more information than a copper cable [4]. In 1979, NTT demonstrate losses of about 0.2 dB/km measured at the wavelength of 1.55 µm [5]. Such progress allowed a long distance (around a hundred km) transmission of information without using repeaters.

In parallel to efforts devoted to enhance the optical quality of silica glass fibers, other alternatives were explored for the same purpose. In 1973, P. Kaiser proposed a new geometry assumed to improve the light guiding efficiency of the fiber [6]. This work has given rise to a new type of optical fibers: microstructured optical fibers (MOFs).

In 1996, Group of Optoelectronics at the University of Bath described the manufacture of microstructured optical fiber obtained by implantation of a periodic array of air holes around a silica core [7]. This particular architecture induces unusual propagation properties unreachable using conventional fibers. This work signaled the beginning of the development of fiber geometries using glasses of different compositions.

After this history summary, we will discuss optical fibers in more details since they are the object of our work. We will describe the specific mechanisms of light guidance in optical fiber, the limitations due especially to optical loss, as well as the nonlinear optical effects involved during the propagation of light pulses along the fiber.

II. Light transmission in conventional optical fibers

II.1 Total internal reflection (TIR).

The guidance of the light beam through the optical fiber takes place because of total internal reflection. The mathematical expression that governs this phenomenon has appeared in the early XVII century. The modern laws explaining the TIR has been developed by Snell (1621) and Descartes (1637). Consequently, laws that rule this phenomenon are known as "Snell-Descartes Laws".

Snell and Descartes introduced firstly the "refractive index" as the ability of each medium to "slow down and deflect" the light. The refractive index "n" of a substance is equal to the ratio velocity of light in a vacuum to its phase velocity in that substance. It is given as follow:

$$\boldsymbol{n = c/\mathrm{v}} \tag{1}$$

Where $\boldsymbol{c}$ ($\approx 3 \times 10^8$ m/s) is the velocity of light in vacuum and ―v” represents the velocity of light in the considered medium.

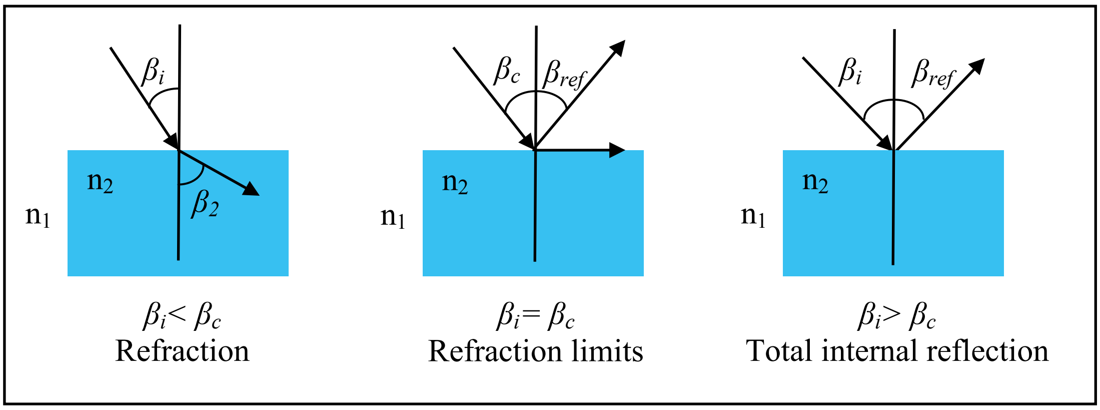

Figure 2: Behavior of incident ray as it passes from high index medium to lower index medium ($n_1>n_2$) as a function of the incident angle. β_i, β_c and β_i represent the incident, the critical and the reflected angles.

When a light ray passes from one medium to another having a different refractive index, its velocity and direction of propagation change. The beam propagating in the same medium symmetrically (with respect to the normal at the incidence point) to the incident ray is called ―reflected ray" (Figure 2-right). The reflection angle equals the angle of incidence. The transmitted beam is called "refracted ray" (Figure 2-left). According to Snell's law, if a ray is incident at the lower index medium interface, the transmitted ray is bent away from the normal, and the angle of refraction is greater than the angle incidence (Figure 2-left). These laws are described by the following equation:

$$\boldsymbol{n_1 sin\beta_i = n_2 sin\beta_2} \tag{2}$$

Herein, n_1 and n_2 represent the refractive index of the first and second medium respectively, whereas the angles that make the incident and the refracted rays with the normal are represented by β_i and β_2, respectively.

Since the angle of refraction grows faster than the angle of incidence, refracted ray may be transmitted perpendicularly to the normal (Figure 2-middle). The angle of incidence, for which the angle of refraction with the surface normal is 90°, is known as the critical angle and is often denoted by β_c. It is expressed by:

$$\boldsymbol{\beta_c = sin^{-1}\left\{\frac{n_2}{n_1}\right\}} \tag{3}$$

When the angle of incidence exceeds the characteristic critical angle β_c, the ray is not refracted anymore but reflected symmetrically at the same angle with respect to the normal. This phenomenon is called "total internal reflection (TIR)". In this case, the wave theory of light implies that a portion of the energy of the incident wave is transmitted into the second medium as a so-called "evanescent" wave. Its energy density exponentially decreases through the normal at the interface, and eventually vanishes at a distance of the same order of magnitude of the incident wavelength. A schematic representation of the evanescence phenomenon is provided in the figure below.

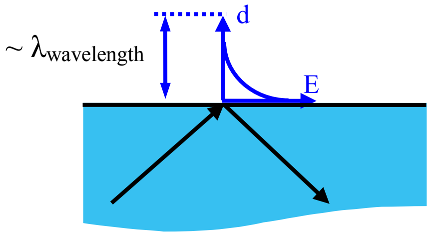

Figure 3: Schematic illustration of evanescent wave

Previous knowledge of the refractive index of two mediums and of the angle of incidence allows to predict the behavior of the light beam (Figure 2). Thus, in the cases where the incident angle is lower than or equal to the critical angle, the reflection phenomenon is observed (Figure 2-middle & left). At normal incidence, the reflection coefficient (R) is given by equation (4), where n_1 and n_2 are the refractive indices of the two media:

$$\boldsymbol{R = \left[\frac{n_2 - n_1}{n_2 + n_1}\right]^2} \tag{4}$$

The transmission coefficient (T) is given by T=1-R for non-absorbent medium. The decrease of the transmitted energy due to reflection is called "Fresnel losses". When light propagates in the atmosphere before entering a high refractive index material, the loss of intensity is substantial, due to the large refractive indices difference. Chalcogenide glasses are known as high index materials, and hence the light experiences high reflection losses when entering and exiting chalcogenide plates or fibers. These light intensity losses are estimated around 17% per interface for As_2S_3 glasses [8].

II.2 Classical structure of glass fiber

A glass fiber consists of a cylindrical central core embedded within a surrounding clad by a material of slightly lower refractive index. The light guidance is allowed by ensuring the light confinement within the fiber core. Several glass systems suffering from mechanical weakness, corresponding glass fibers are reinforced with an external polymeric cladding giving them greater resistance to physical constraints at which they are exposed during real operation conditions.

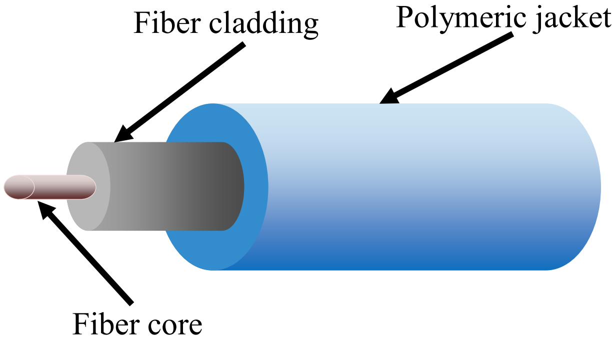

Figure 4: Schematic representation of glass fiber.

II.3 Light transmission in optical fiber by total internal reflection.

All incident rays launched into the entrance facet of the fiber will not be guided in the core. There is a threshold (limit) incidence angle beyond which guidance of signal in the core is not insured (i_m in Figure **5**), hence defining the "acceptance cone" (Figure 5). Striking the fiber entrance with incidence angle smaller than the threshold, the ray will be guided in the fiber in a direction parallel to the axis of the fiber. A ray whose incidence is within the acceptance cone will be guided following the principle of total internal reflection at the core-cladding interface. A schematic illustration of these phenomena is gathered in Figure 5.

The sine of the limit angle (i_m) of the incident, often called "numerical aperture", is a characteristic parameter of optical fibers. It is given by the following equation:

$$\boldsymbol{NA = \sin i_m = \left(n_c^2 - n_{cd}^2\right)^{1/2}} \qquad (5)$$

where, NA, i_m, n_{cd} and n_c represent the numerical aperture, the limit incidence angle, the clad refractive index and the core refractive index, respectively.

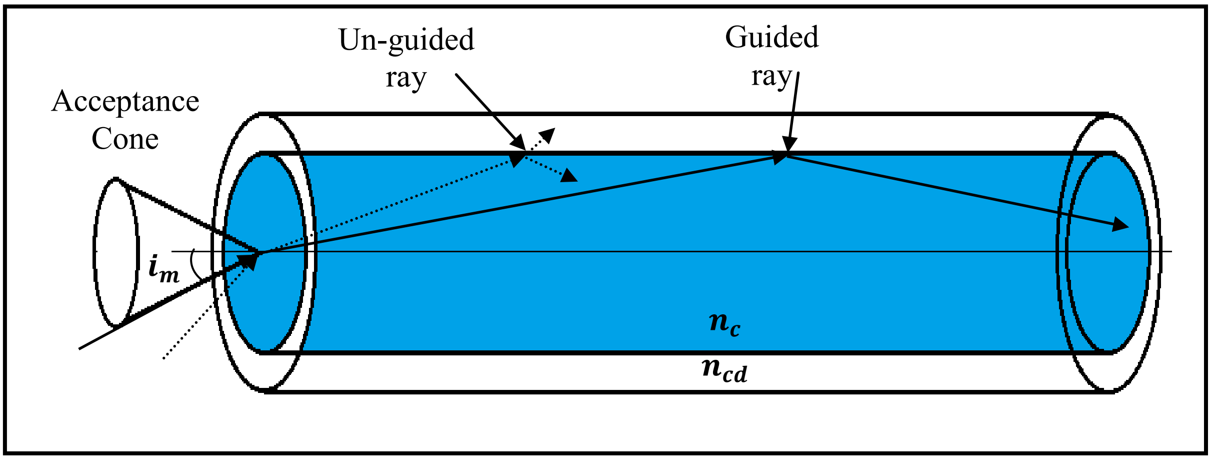

Figure 5: Schematic representation of light guidance inside a conventional step-index glass fiber.

II.4 Modes propagation inside an optical fiber

Geometrical optics presume that everything happens as if only a discrete number of incidence angles within the acceptance cone give rise to light propagation inside the fiber. These different values of incident angles are associated with different "propagation modes". Rigorously speaking, the concept of "modes" results from solving the light propagation equation in the optical fiber through the involvement of the electromagnetic field boundary conditions (continuity at the core-cladding interface) and the symmetry of the medium (fiber geometry).

An estimation of how many modes can propagate along the fiber is furnished by the key fiber parameter "V", often referred to as the "normalized frequency". For a step-index fiber, the "V" parameter is given as follows:

$$\boldsymbol{V = \frac{2\pi a}{\lambda}\sqrt{n_c^2 - n_{cd}^2} = \frac{2\pi a}{\lambda} \times NA} \qquad (6)$$

Where a is the core radius, λ the light wavelength, n_{cd} and n_c representing the refractive index of the clad and the core, respectively.

If the normalized frequency is below 2.405 for a given wavelength, the fiber is single mode at this wavelength. In order to characterize a single mode fiber, we introduce the concept of cutoff wavelength as the wavelength below which the optical fiber is no longer single-mode. In multimode fiber, the approximate number of distinguishable modes that can propagate in the fiber is given by:

$$\boldsymbol{M} = \boldsymbol{V}^2/\mathbf{2} \tag{7}$$

Where M represents the number of modes.

II.5 Conventional glass optical fibers

Conventional fibers are mainly classified, on the one hand by the index profile of the fiber, and on the other hand by the mode propagation ability. As was previously suggested, there are therefore single and multimode fibers. A schematic presentation of the various categories of conventional fibers is provided in Figure 6.

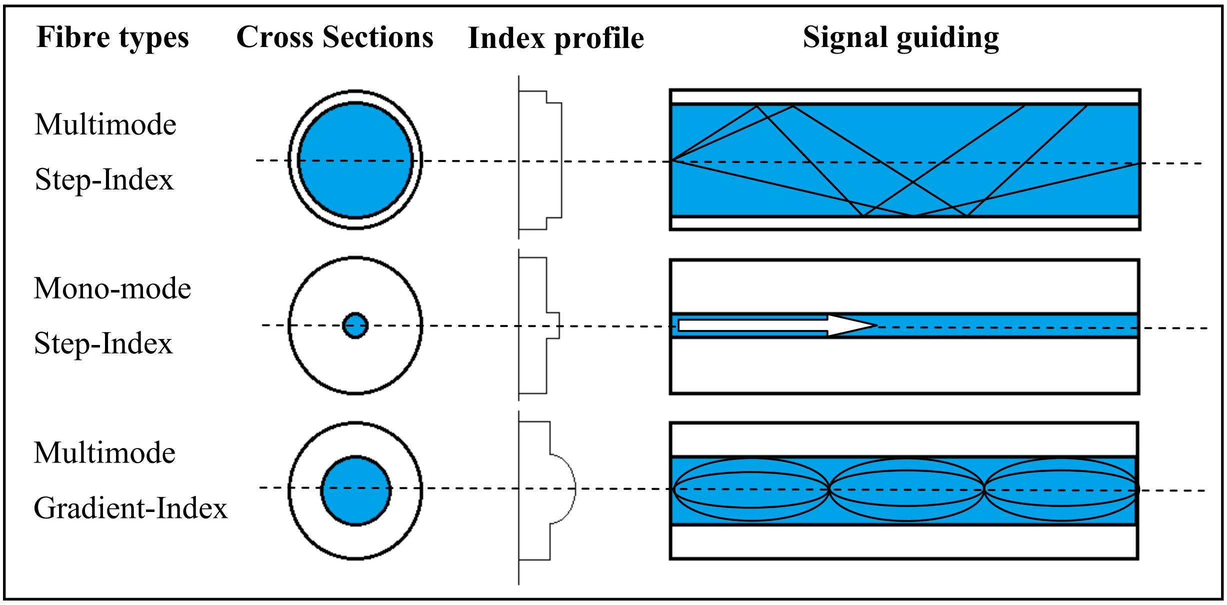

Figure 6: Overview of fundamental fiber types

Multimode silica fibers were the first to appear on the market. They exist in the form of step-index or gradient-index fibers.

Fiber owing large numerical aperture exhibits an important light-gathering capacity. This allows to increase the amount of light coupled into the fiber. However, any given light source delivers signal which is never truly monochromatic but composed of various spectral frequencies. Thus, rays take different times to propagate through a given length of the fiber (Figure 6-top). In other words, pulses propagate in several modes inside a multimode fiber and undergo temporal broadening (intermodal dispersion) upon propagation.

Graded index fibers were conceived in order to reduce impact of the intermodal dispersion caused by the differences in the group velocities of the modes within a multimode fiber, while maintaining a high numerical aperture. These fibers exhibit a parabolic-index profile, with a maximum in the center and a minimum at the core-cladding bounding (Figure 6-bottom). The transmitted modes are guided following a sinusoidal path, from the center to the cladding. Consequently, the velocity of modes is reduced in the center and increased with the radial distance. Modes undergoing a longer distance propagate at average higher velocity. The excess in distances are balanced by opposite excess in mode velocities, and the intermodal dispersion is significantly reduced.

A step-index fiber which exhibits a small core diameter (a few microns) and a low refractive index contrast (less than 0.5%), is denoted as single mode fiber (Figure 6-middle). Such fiber supports only one mode that propagates through the fiber. This mode is also referred to as the "fundamental mode". Unlike the multimode fiber, the intermodal dispersion within a single mode fiber is significantly neglected, which explains the pioneering role of such fibers in the transmission of light pulses over large distances.

II.6 Dispersion of guided signal

The signal dispersion also known as "intramodal dispersion" includes two components, the dispersion of the glass material and that of the waveguide.

The light pulse is never truly monochromatic but composed of various spectral frequencies. Since the refractive index of the fiber material is wavelength dependent, the travel velocities for different signal components will not be the same, leading to a temporal broadening of the pulse.

The refractive index as a function of wavelength is given by Sellmeier equation [9, 10]:

$$\boldsymbol{n^2(\omega) = 1 + \sum_{j=1}^{m} \frac{B_j\lambda^2}{\lambda^2-\lambda_j^2}} \tag{8}$$

Where λ is the vacuum wavelength, λ_j is the j_{th} absorption resonance wavelength and B_j is the strength of the j_{th} resonance. ω represents the signal frequency expressed as $\omega = (2\pi/\lambda)c$.

The Sellmeier parameters are usually obtained from experimental data. The summation is extended over all material absorption resonances that contribute to the frequency range of interest. Since the propagation velocity of a monochromatic wave in a medium of refractive index $n\ (\omega)$ is given by $c/n(\omega)$ (c is the light velocity in vacuum), when a multi-component pulse propagates through an optical fiber, the velocities at which the different spectral components are traveling along the fiber vary. This results in significantly different transmission delays or arrival times for the various spectral components of the signal, leading eventually to pulse temporal broadening. In general, we use the propagation constant $\beta(\omega)$ which is expended in Taylor series about the central frequency ω_0 of the pulse spectrum, in order to assess the dispersion effects of the fiber [9, 10].

$$\boldsymbol{\beta(\omega) = n_{eff}(\omega)\frac{\omega}{c} = \beta_0 + \beta_1(\omega-\omega_0) + \frac{1}{2}\beta_2(\omega-\omega_0)^2 + \frac{1}{6}\beta_3(\omega-\omega_0)^3} \tag{9}$$

β_2 parameter represents the dependence of the energy propagation velocity versus the frequency of the guided wave. It is called "second order dispersion parameter" and is expressed in ps²/nm. β_2 is also called "coefficient of group velocity dispersion" (GVD). The dispersion parameter D, related to β_2 by the following relation, is commonly used in place of β_2 [11]:

$$\boldsymbol{\beta_2 = -\frac{1}{v_g^2}\frac{\partial v_g}{\partial \omega}} \tag{10}$$

$$\boldsymbol{D = -\frac{2\pi c}{\lambda^2}\beta_2}$$

By definition, the GVD represents the $\delta\lambda$ (I, nm) spectral width pulse time duration broadening (in ps) by fiber length unit (in km). Therefore, GVD is expressed in "*ps.nm*$^{-1}$*.km*$^{-1}$".

The dispersion of a fiber is defined as the sum of the material dispersion (D_{material}) and waveguide dispersion ($D_{\text{waveguide}}$), which originates from the chromatic dispersion of the effective index. It is defined as follow:

$$\boldsymbol{D_{total} = D_{material} + D_{waveguide}} \tag{11}$$

The influence of the waveguide dispersion is lower and depends on the light confinement due to opto-geometric properties of the fiber. Generally, both phenomena exhibit an opposite evolution as a function of wavelength (Figure 7). Their opposite contribution can be balanced, so the disparities in material dispersion can be compensated by opposite disparities in waveguide dispersion. As a consequence, the total dispersion at certain wavelengths can be set to zero. This characteristic wavelength is often called "zero dispersion wavelength" (ZDW).

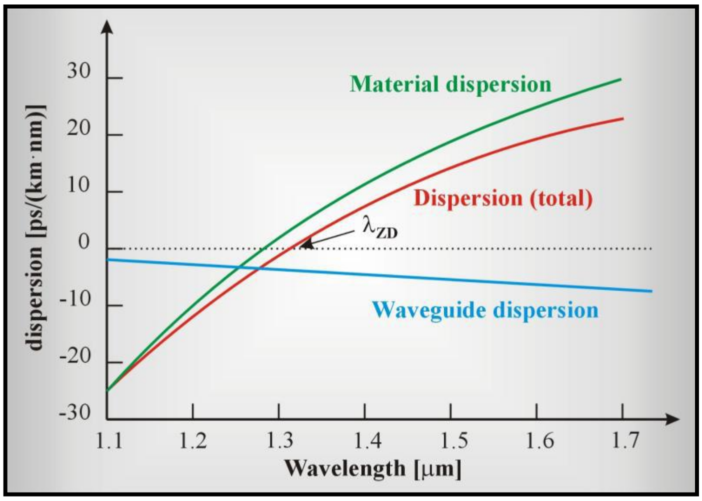

Figure 7: Material and waveguide contributions for dispersion-shifted step-index fiber.

One can also conceive a suitable ZDW by manipulating the core diameter and/or the refractive index contrast between the core and the cladding.

The pulse dispersion behaviors and the signal guidance regime within the fiber change depending on the sign of the GVD parameter. Figure 8 shows the properties of the pulse broadening by GVD. The spectral region located below the ZDW is called ‗normal‘ or ‗negative‘ dispersion regime (D<0; β_2>0; Figure 8-bottom). The long-wavelength components (red-edge) under the pulse envelop propagates faster than the short-wavelength components (blue-edge) of the same pulse. For wavelengths longer than the ZDW, the opposite effect occurs. This region is called ‗anomalous‘ or ‗positive‘ dispersion regime (D>0; β_2<0; Figure 8-top). The anomalous-dispersion regime is of major interest because in this regime, optical fibers support solitons.

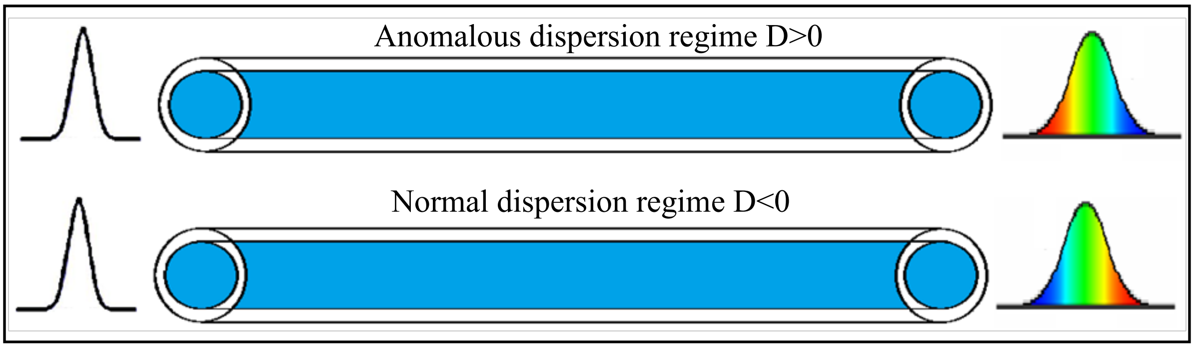

Figure 8: Illustration of pulse time broadening by group-velocity dispersion

II.7 Microstructured optical fibers (MOFs)

Microstructured optical fibers consist in guiding hollow or solid core surrounded by periodic array of air holes running along their length [7, 12]. Light transmission within solid-core MOF is governed by total internal reflection (TIR). Careful managing of the MOF opto-geometrical parameters (air hole diameter (*d*) and inter-hole spacing also called pitch (Λ); Figure 9), allows to control the guidance properties.

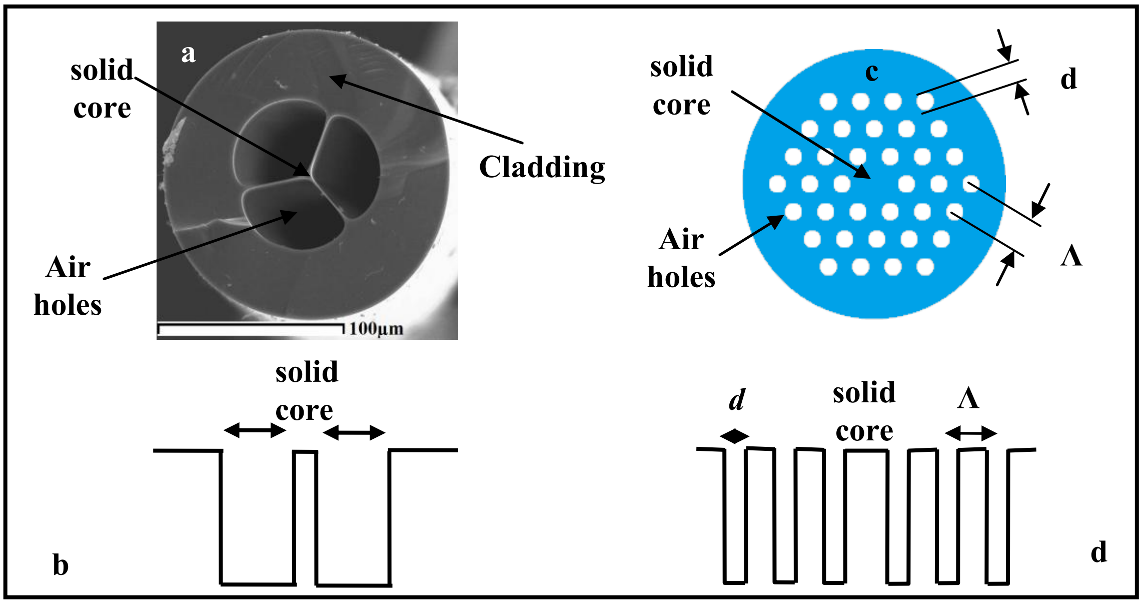

Figure 9: (a) Transverse cross sections of three holes suspended-core MOF and (b) schematic representation of corresponding refractive index profile. (c) Transverse cross sections of classical MOF with 3 rings of air holes around a solid central core, and (d) schematic representation of corresponding refractive index profile.

II.8 Light transmission and dispersion properties of MOFs.

II.8.1 Light transmission in MOFs

The solid-core MOFs have many similarities with the standard step-index fibers. The periodic arrangement of air holes forms a cladding of effective index (n_{geff}) lower than the index of the base material that makes up the core. In practice, n_{geff} corresponds to the effective refractive index of the higher order mode allowable to propagate in the core. The light guiding is governed by total internal reflection. However, the confinement of light in a solid-core microstructured fiber is much stronger than that in a step-index fiber.

To ensure the light guiding in the MOF's core, the propagation constant β has to fulfill the condition (12), for which only an evanescent wave can exist in the cladding. The range defined in 12 determines the maneuverability range of β while maintaining an efficient guidance in the core. If the value of β is below the maximum propagation constant allowable in the cladding, the light will leak in the cladding.

$$\boldsymbol{kn_{cl} < \beta < kn_{c}} \tag{12}$$

where kn_{cl} define the maximum propagation constant allowable in the clad for efficient core guiding, kn_c define the maximum propagation constant allowable in the core for efficient core guiding, n_g and n_c represent the refractive index of cladding and core, respectively.

II.8.2 Single mode MOF

The guiding properties of the MOF depend on their opto-geometrical parameters. For example, for a high core index fiber, appropriate ratio of hole area to total cladding area (d/Λ) allow to achieve single-mode propagation throughout the transparency range of the fiber. For step-index fiber, the single-mode propagation corresponds to a normalized frequency (V) less than 2.405. In order to calculate the normalized frequency (V) for MOFs, we use the same equation (13) as that applied for the step-index fiber, wherein the refractive index of the cladding is replaced by the effective index of the microstructured cladding.

Thereby, for a ratio of hole diameter to inter-hole spacing (*d/*Λ) below 0.4, the fibers may be single mode regardless of the wavelength. It is therefore possible to achieve a broadband single mode fiber while maintaining large core dimension [13]. For MOFs, the normalized frequency is expressed as follow:

$$\boldsymbol{V_{eff}} = \frac{2\pi a}{\lambda}\sqrt{\boldsymbol{n_c^2 - n_{eff}^2}} \tag{13}$$

where, V_{eff} is the normalized frequency, a is the core radius, λ is the propagating light wavelength, n_c represents the refractive index of the material that makes up the core and n_{eff} is the effective index of the microstructure cladding.

II.8.3 Group velocity dispersion of MOFs

Solid core MOFs allow greater freedom of choice of the geometrical parameters for setting of the dispersion properties of the fiber. Considering a solid core MOF surrounded by holes of low diameters, the influence of their size will be limited and the dispersion of the fiber is close to the dispersion of the material. Whereas, for the same pattern, when the hole diameter begins to increase, the shape of the fiber's dispersion curve significantly changes (Figure 10-a). Similar behavior appeared when the pitch (Λ) increases while the hole diameter is maintained constant (Figure 10-b).

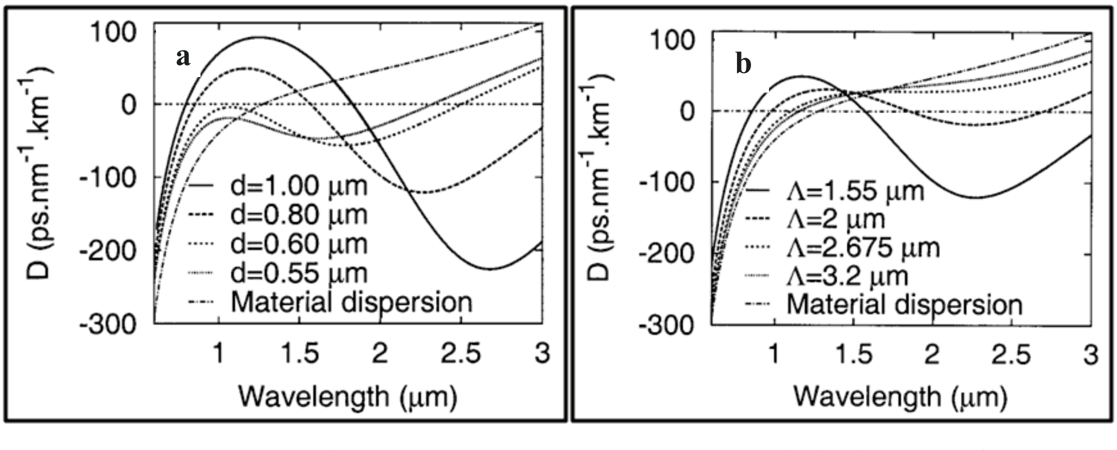

Figure 10: Dispersion for a three-ring MOF as a function of (a) hole diameter d (Λ=1.55µm), and (b) Pitch (d=0.8µm) [14].

III. Signal attenuation and losses in optical fibers

During its propagation throughout the fiber, a light pulse is continuously undergoing degradation: on one hand, its amplitude decreases (attenuation) and on the other hand the pulse "broadens in time" (dispersion). Many phenomena are involved in the attenuation of the pulse. One generally distinguishes those originating from the material (absorption, diffusion) of those revealing a "leakage" of energy from the fiber (propagation). Figure 11 shows the attenuation spectrum on As_2S_3 glass as printed from [15].

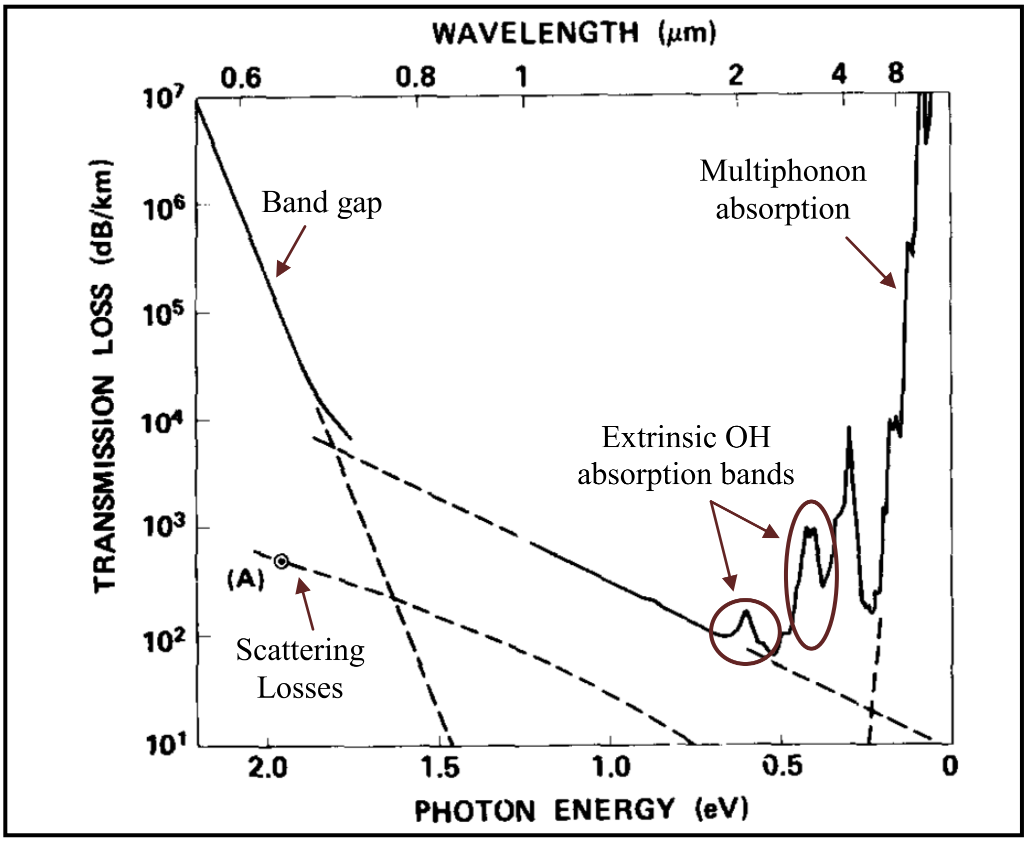

Figure 11: Schematic diagram of the transmission-loss mechanism in low-OH-content As_2S_3 optical fibers as printed from [15]. This spectrum shows a typical Urbach tail, multiphonon absorption, scattering losses as well as extrinsic absorptions. Extrinsic absorption bands appear as inclusions interrupting the transmission window.

III.1 Material absorptions

There are two types of material's absorption: intrinsic and extrinsic absorptions. The intrinsic one is caused by interaction of the guided light with major constituents of the glass: in the short wavelengths range, the radiation energy is sufficient to excite the outer electrons of the atoms constituting the glass and curtail the transmission spectrum. By analogy with crystalline semiconductors, corresponding cut-off wavelength is called "gap". In the long wavelengths range, the radiation energy corresponds to vibrational energy of the constituent chemical bonds of the glass (multiphonon absorption), and beyond the glass becomes opaque. These two absorption bands limit the transparency window of the glass and determine the minimum possible losses within this window.

Extrinsic absorption originates from the interaction of the guided light with impurities present in the glass. These impurities may be transition metallic ions (such as Fe^{2+}, Cu^{2+}, Cr^{3+}, V^{4+}) [16], which absorb in the wavelength range lying between 600 nm and 1600 nm. In silica fiber, a concentration of 1 ppm of these metallic impurities results in attenuation losses ranging between 1 and 3 dB/km. Rigorous purification of raw materials allows to significantly reduce the concentration of these impurities to 1 ppb threshold. Hydroxyl ions (OH) present in glass are also considered as extrinsic impurities. Corresponding absorption bands appear within the wavelength range extended from 600 nm to 6300 nm. These impurities are difficult to remove. Currently, with new manufacturing technologies, it is possible to obtain silica fibers with concentrations of OH ions below 1 ppm [17].

III.2 Optical scattering

The scattering losses are due to the interaction of guided light with the material constituting base of the guiding structure. There are two types of scattering: linear scattering (elastic), for which the scattered photons maintain the same frequencies as the incident photons, and the nonlinear scattering (inelastic), for which the scattered photons change their frequencies compared to incident photons. There are two sub-types of linear scattering, Rayleigh and Mie scattering.

III.2.1 Rayleigh scattering

The electric field of an electromagnetic wave incident onto an atom distorts the electron cloud of this atom, leading to the creation of an induced electrical dipole. This induced dipole emits isotropic radiations at the same wavelength of the incidence ray. This interaction process is known as the Rayleigh scattering.

The scattering intensity is inversely proportional to the fourth power of the wavelength: $I \sim {}^{1}/_{\lambda^4}$. Thus, the attenuation due to Rayleigh scattering increases towards shorter wavelengths [18].

III.2.2 Mie scattering

Mie scattering is caused by the interaction of the guided light with particles of size of the same order of magnitude as the incident wavelength. This scattering originates from the presence of refractive index fluctuations in the core and the cladding (glass inhomogeneities, impurities, defects...). The scattered intensity is inversely proportional to the square of the wavelength: $I \sim 1/_{\lambda^2}$. Reduction or even elimination of this diffusion process is possible by improving the glass quality. Nowadays, silica fibers with low Mie scattering levels are available in the market [19].

III.3 Bending losses

Bending can increase the attenuation of optical fiber by two mechanisms: macrobending and microbending. Propagating modes within the fiber might be accompanied with an electric field distribution with maxima inside the fiber and evanescent fields that extend outside the fiber core into the surrounding cladding.

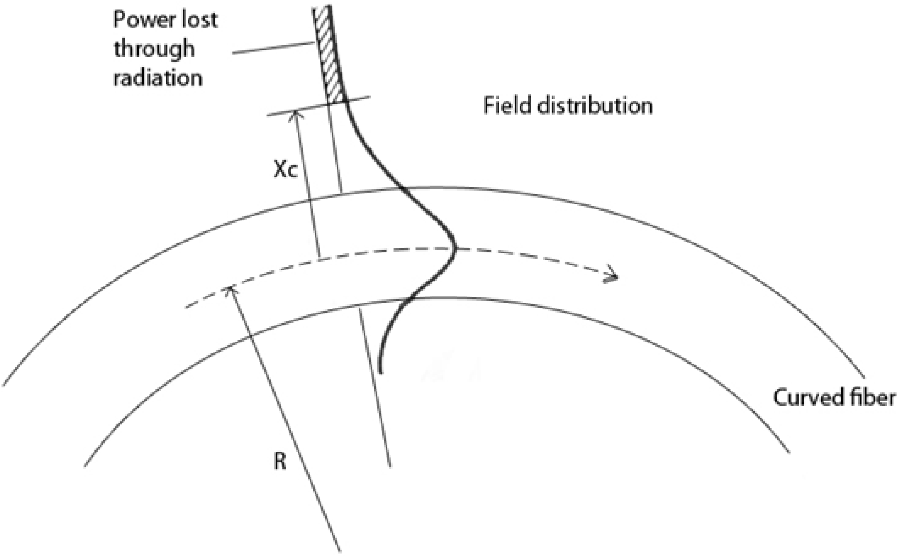

Figure 12: Sketch of the fundamental mode filed in a curved optical fiber.

III.3.1 Macrobending losses

Macrobending losses of an optical fiber are associated with bending or wrapping the fiber. Electromagnetic field can leak out of the fiber when it is bent. As the bend becomes more acute, leakage becomes more severe [20]. Bending losses are related to the curvature radius. The critical radius of curvature R_c is the threshold radius at which bending loss sharply increases from negligible values to intolerably high values. This is delineated as follows [21]:

$$\boldsymbol{R_c} = \frac{\boldsymbol{3n\lambda}}{\boldsymbol{4\pi(NA)^3}} \tag{14}$$

Where R_c is the critical radius of bending, n is the refractive index of the clad, NA is the numerical aperture of the fiber and λ is the wavelength.

III.3.2 Microbending losses

Microbending losses of an optical fiber lead to attenuations associated to random axial distortions of the core-clad interface generated from mechanical tensile forces during drawing when the fiber is pressed against surface that is not perfectly smooth [20]. These losses may be avoided by careful fiber drawing, avoiding excessive mechanical forces, and controlling the temperature variations of the fiber.

III.4 Optical pumping and coupling losses

The term pumping losses refers to an optical fiber not being able to propagate all the incoming light rays from an optical source. This phenomenon occurs during the process of coupling light into the fiber.

There are also initial face (Fresnel) losses due to reflections at the entrance aperture. The Fresnel losses are greater if the fiber-source coupling is performed in free space. Coupling losses are associated with the coupling of the output of one fiber with the input of another fiber or other components. Significant losses may arise in fiber connectors and splices of the cores of the joined fibers having unequal diameters or misaligned centers, or if their axes are tilted. There are other connection losses such as offsets or tilts or air gaps between fibers, and poor surface finishes. Some of these are illustrated in Figure 13.

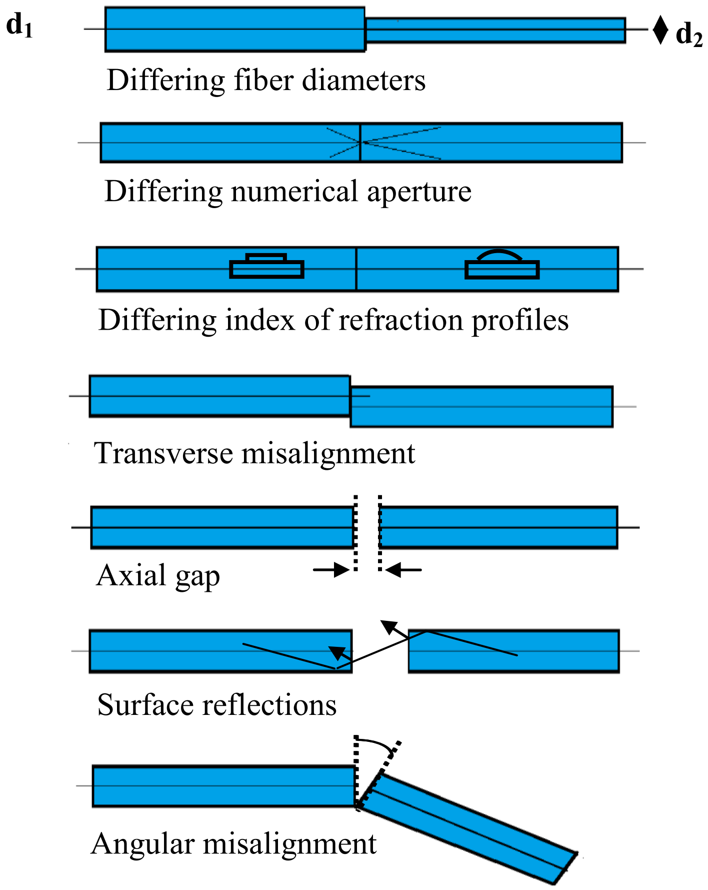

Figure 13: Various configurations for multimode fibers with cleaved terminations.

III.5 Loss measurements by cut-back technique

Any process that results in a reduction in the light intensity during propagation through a material contributes to the observed optical attenuation. According to Beer-Lambert law, optical power exhibits an exponential decrease with distance as it propagates within the fiber:

$$\boldsymbol{P = P_0 e^{-\alpha_{total} z}} \tag{15}$$

$$\boldsymbol{T}(\%) = {}^{\boldsymbol{P}}\!/_{\boldsymbol{P_0}} \tag{16}$$

where P_0 is the power at distance z=0, P the power at distance z, α_{total} the total attenuation coefficient and T the transmission.

As clearly seen in equation 15, a rigorous measurement of the input and output powers is required in order to calculate the total attenuation coefficient. Such measurement is not trivial. The cut-back technique as illustrated in Figure 14 allows overcoming this limitation by comparing the output power P_1, measured for a fiber length L_1, to the output power P_2 measured for a shorter length L_2, while maintaining a constant input power. Then, applying the subtraction of equation 15 for two different lengths, α_{total} is expressed as follow:

$$\boldsymbol{\alpha_{total} = \frac{1}{L_1 - L_2} \ln\left(\frac{P_2}{P_1}\right)} \tag{17}$$

where α_{total} is the total attenuation coefficient in m^{-1} for the segment $L_1 - L_2$.

In an optical fiber transmission context, the total attenuation coefficient is usually defined in units of dB/m, and often expressed in logarithm of base-10 form as follows:

$$\boldsymbol{\alpha_{total} = \alpha_{m^{-1}} \times \frac{10}{\ln 10}} \qquad \textit{(dB/m)} \tag{18}$$

$$\boldsymbol{\alpha_{total} = \frac{10}{L_1 - L_2} \log\left(\frac{P_2}{P_1}\right)} \qquad \textit{(dB/m)}$$

α_{total} *(dB/m)* is often referred as the "fiber loss". The factor $\ln(10)$ accounts for a conversion of the base of the logarithm since the attenuation coefficient ($\alpha_{m^{-1}}$) is defined on the basis of neperien logarithm while the fiber losses (α_{total}) are defined on the basis of decimal logarithm.

Losses in "dB/m" units are additive (cumulative). It is worthy to note that α_{total} is an extrinsic measure which integrates multiple contributions described above to an overall loss value.

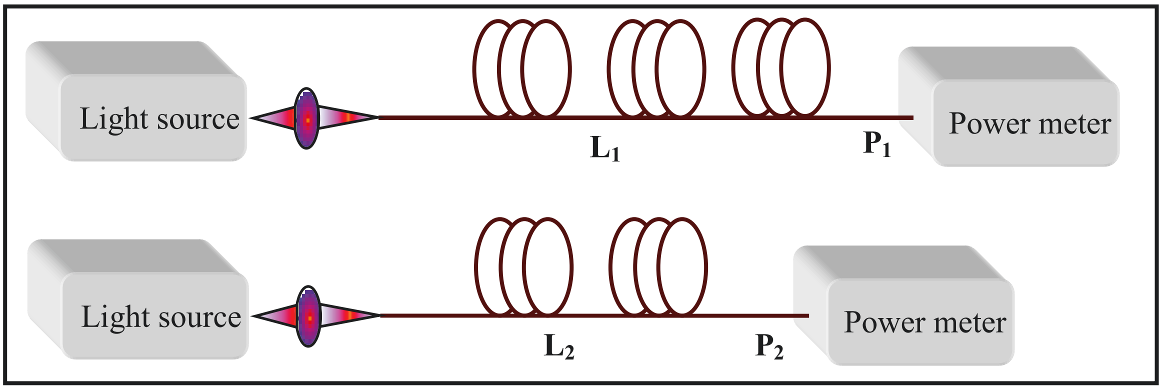

Figure 14: Schematic representation of cut-back technique used to measure the losses in optical fibers

IV. Nonlinear optics

In the frame of this work, we are interested in the effect of spectral broadening of a high peak power pulse as it propagates into a fiber made of a highly optically nonlinear material, wherein the confinement of guided modes is important. This spectral broadening, called "supercontinuum" (SC) originates from a number of nonlinear optical effects. An important parameter to obtain a supercontinuum is the peak power of the pump pulses.

From a historical perspective, nonlinear optics experiments was not possible until the 1960s with the advent of laser technology [22], and particularly pulsed lasers. The first significant spectral enlargements were observed for the first time in 1963 [23]. Generation of a wide spectrum covering the whole visible, in a bulk material (a borosilicate glass BK7) was performed by Alfano and Shapiro in 1970 [24] using picosecond pulses (5 mJ energy at 532 nm). In 1976, and for the first time, Lin and Stolen have reported on spectral broadening in fiber (silica fiber) [25]. The spectrum spread over 200 THz toward wavelengths greater than those of the pump [25]. The most remarkable results have been obtained with the development of the microstructured optical fibers (MOFs) in the 1990s. These fibers are known for their ability to effectively confine the light. The freedom degrees provided by these fibers through their geometry allow to adjust their dispersive properties to the pump wavelength. At the same time, the high nonlinearity of MOFs enables the use of lower peak power pulses. In 2000, JK Ranka and al [26] coupled 100 fs pulses at 770 nm in a 75 cm microstructured optical fiber whose zero dispersion was located around 770 nm. The coupled signal enabled a spectral broadening extending from 400 to 1500 nm.

SC generation has found applications in spectroscopy, metrology, medicine and military fields [27-30].

The efficiency of the spectral broadening observed at the output of a MOF depends on several parameters (fiber length, injected peak power and wavelength of the pump pulse), but the phenomena originate from the nonlinear optical properties of the material. We will therefore in the following, after a brief reminder of the linear and nonlinear polarizations generated in a material subjected to an electromagnetic field, describe the resulting nonlinear optical phenomena involved in the supercontinuum generation.

IV.1 Interaction light-matter and polarization behavior in isotropic medium

When a dielectric medium is submitted to an external electric field, it becomes polarized. When the applied electric field is weak, the induced polarization is proportional to that field. Whereas, when the applied electric field reaches values of the same order of magnitude as the intra-atomic electric fields, the induced polarization is no longer proportional to that field: at this stage, we enter the domain of nonlinear optics.

From a microscopic point of view, each atom or molecule of a dielectric medium is surrounded by an electron cloud susceptible to deformation under the effect of an electric field, thereby creating an electric dipole (electronic polarizability). This dipole, for a small deformation, is proportional to the field, but this is no longer the case when the deformation becomes more acute.

The vectorial summation of microscopic dipoles generates macroscopic polarization. This polarization can be written in its most general form as follows:

$$\boldsymbol{P} = \boldsymbol{\varepsilon_0}\{\boldsymbol{\chi^1 E} + \boldsymbol{\chi^2 E.E} + \boldsymbol{\chi^3 E.E.E} + \cdots\} \tag{19}$$

where $\boldsymbol{E}$ is the amplitude of the electric field, ε_0 is the electrical permittivity of free space, χ^i represents the i^{th} order of dielectric susceptibility, which are characteristic of the material.

This polarization consists of a linear component (21) and a nonlinear contribution (22), expressed as follow:

$$\boldsymbol{P} = \boldsymbol{P_L} + \boldsymbol{P_{NL}} \tag{20}$$

$$\boldsymbol{P_L} = \boldsymbol{\varepsilon_0 \chi^1 E} \tag{21}$$

$$\boldsymbol{P_{NL}} = \boldsymbol{\varepsilon_0}\{\boldsymbol{\chi^2 E.E} + \boldsymbol{\chi^3 E.E.E} + \cdots\} \tag{22}$$

The linear component (21) describes the conventional linear optics (Snell laws, Rayleigh ...), for which the resulting (irradiated) wave maintains the same frequency as that of the incident wave.

Nonlinear effects can be classified according to different orders.

For amorphous (glasses) or crystalline materials having a center of symmetry (center of inversion), the nonlinear susceptibility of the second order χ^2 vanishes. This is of course valid for all the even (pair) orders of polarization effects.

Nonlinear phenomena of the third order have lower amplitude than those of the second order. However, in practice, they are very important because they are the first non-linear effects encountered in the glass.

According to the involved mechanism, the nonlinear polarization effects induced by the third order susceptibility can be divided into:

- elastic effects without any exchange of energy between the incident radiation and the crossed medium (Kerr effect),
- inelastic effects or nonlinear scattering, which involve an energy exchange between the incident radiation and the material (Raman and Brillouin scattering).

IV.2 Optical Kerr effect (OKE)

The optical Kerr effect (OKE) can be described as the modification of the refractive index of a material under the effect of an electric field. Materials whose are prone to this phenomenon are known as "Kerr media". In particular, when a Kerr medium is exposed to the electric field of a light wave of intensity I, its refractive index can be written as follows:

$$\boldsymbol{n} = \boldsymbol{n_0} + \boldsymbol{n_2}\,\mathbf{I} \tag{23}$$

where n is the refractive index, n_0 is the linear refractive index, n_2 is the nonlinear refractive index and I is the intensity of the light beam.

As claimed in equation (23), the refractive index consists of a linear component related to first-order dielectric susceptibility, and a nonlinear component related to the third order dielectric susceptibility. When the intensity of the applied electric field is high, the nonlinear contribution to the refractive index must be taken into account.

For silica glasses, the nonlinear refractive index is measured around 3,2 x 10^{-20} m^2/W at 1.06 µm [10]. As_2S_3 glass exhibits a nonlinear refractive index around 594 x 10^{-20} m^2/W at 1.55 µm [29].

The Kerr effect leads to various nonlinear effects, like self-phase modulation (SPM) and cross-phase modulation (XPM) phenomena.

IV.2.1 Self-phase modulation (SPM)

Upon interaction between an electric field and a nonlinear Kerr medium, a modification occurs in the refractive index due to the Kerr effect. This momentary and local change induces in turn a phase modulation of the electric field. This effect leads to the decrease of the instantaneous frequency of the leading edge of the pulse, and to the increase of the frequency of its trailing edge (Figure 15). Self-phase modulation introduces therefore a broadening of the pulse's spectrum, but the corresponding temporal envelope remains unchanged. The combination of dispersion and self-phase modulation allows to generate low dispersion pulses often called "temporal solitons". These solitons are usually used in telecommunication technology to carry data over long distances.

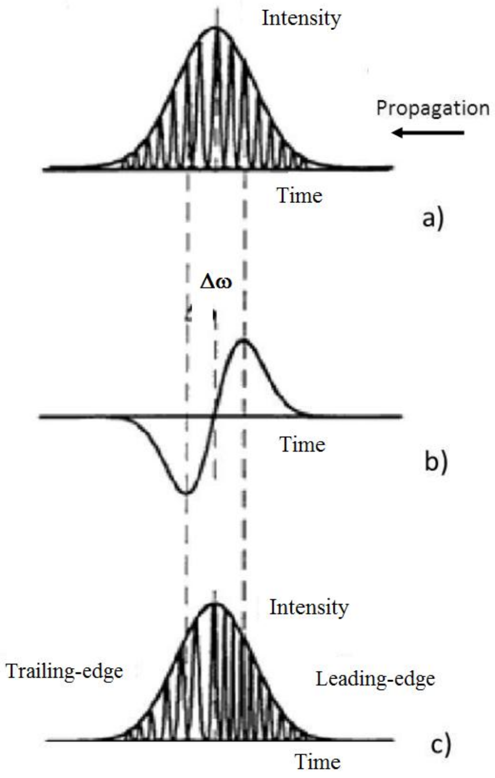

Figure 15: Illustration of the mechanism of self phase modulation (SPM). (a) Gaussian profile of the input pulse, (b) frequency chirp Δω for Gaussian pulses and (c) profile of the frequency modulated pulse.

IV.2.2 Solitons

In general, a soliton is defined as a pulse which propagates without changes in its temporal shape, ignoring the classical laws of dispersion of energy. This pulse is sufficiently intense to induce a nonlinear effect that will counteract the normal dispersion effects [31, 32]. In optics, one distinguishes two types of solitons:

- temporal solitons resulting from dispersion effects and Kerr nonlinearity
- spatial solitons resulting from the diffraction effects and Kerr nonlinearity

IV.2.3 Cross-phase modulation (XPM)

Another consequence of the Kerr effect is observed in the case where multiple pulses propagate in the fiber. The refractive index induced by one of these pulses is modified by the Kerr effect generated by others copropagating pulses. This phenomenon is known as cross phase modulation (XPM).

IV.2.4 Four wave mixing (FWM)

This phenomenon corresponds to the interaction of three co-propagating electromagnetic waves, which generate or amplify a fourth one. Their frequencies are related by the following expression:

$$\boldsymbol{\omega_4 = \omega_1 \pm \omega_2 \pm \omega_3} \tag{24}$$

Theoretically, different combinations of frequencies are possible. However, in general, it is difficult to have FWM of high efficiency in optical fibers owing to the difficulties in satisfying the phase-matching condition for such processes.

IV.3 Inelastic nonlinear effects

Inelastic nonlinear effects involve energy exchange between the electromagnetic field and the dielectric medium. We distinguish two effects: Raman and Brillouin scattering [33]. At low pulse power, their contribution is negligible but can become important at high power. The first experimental observation of Raman and Brillouin scattering in optical fibers has been reported in 1970 [34-37].

IV.3.1 Raman scattering (RS)

This effect consists of an exchange of energy between the incident photon and the atom (or molecule) via the creation or annihilation of an *optical* phonon. As the result of such interaction is obtained, in addition to a phonon, a photon with upshifted frequency (lower energy) from the incident photon, called "Stokes shift". (Figure 16-middle). If the interaction of an incident photon with a phonon leads to the emission of a photon having energy higher than that of the incident photon, it is called –anti-Stokes shift” (Figure 16-left). In both cases, the scattered photon does not have the same wavelength as the incident one.

If such interaction does not involve any energy exchange between the incident photon and the molecules or atoms, the scattering is elastic and the wavelength of the scattered photon is not shifted, one finds the Rayleigh scattering already described (Figure 16-right).

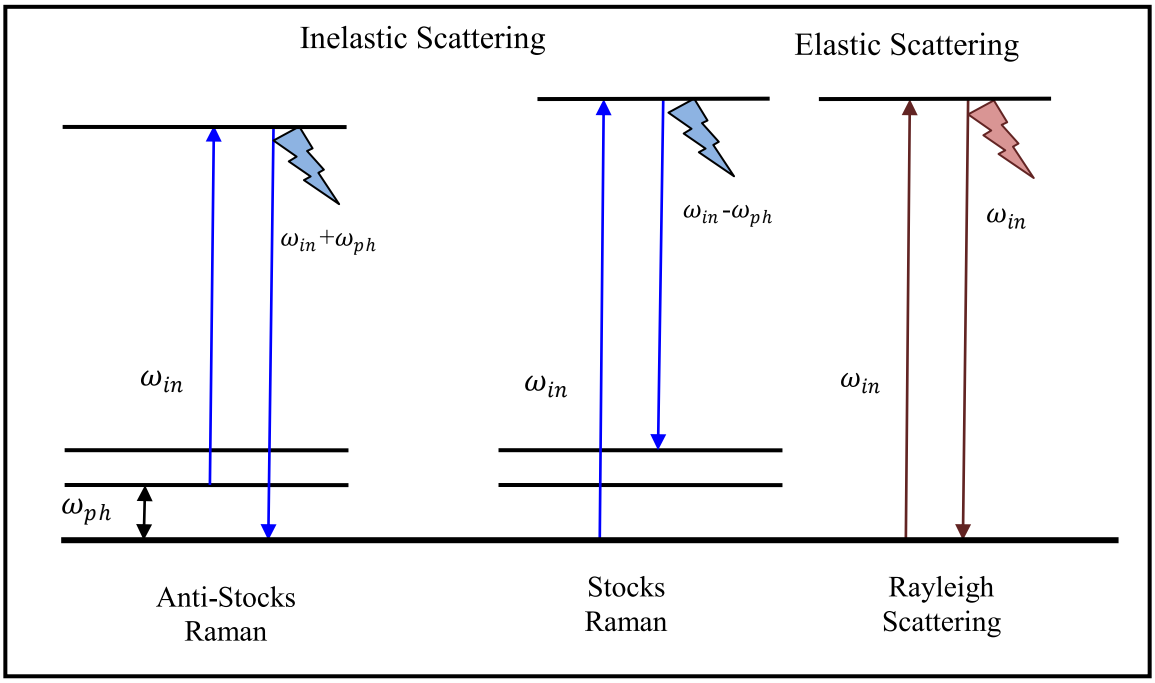

Figure 16: Illustration of the Raman scattering

IV.3.2 Brillouin scattering (BS)

The light scattering caused by interaction with *acoustic* phonons of a medium is called Brillouin scattering. The energy of molecular vibrations delivers acoustic phonons capable of interacting with light to generate photons and acoustic phonons, through a process similar to that involved in the Raman scattering process.

The generated acoustic wave modulates the refractive index of the medium by creating a local network of Bragg grating type, which then reflects a portion of incident light in the form of Stokes photons. Brillouin scattering is therefore produced in the opposite direction to the incident light propagation direction.

The BS frequency shifts are observed in the range of 1 to 200 GHz, compared to Raman shifts (over 300 GHz). Brillouin bandwidth is narrower than that of the Raman bands.

Brillouin scattering may be observed spontaneously even at low pump power. However, the development of stimulated Brillouin scattering (SBR), wherein the involved acoustic phonons are generated by the optical photon itself, requires significant power.

IV.4 Supercontinuum generation

The set of non-linear effects discussed above contributes to generate a spectral broadening of the light pulses propagating in a Kerr medium. This is known as supercontinuum. The magnitude of this broadening strongly depends on the time-regime of the input pulse launched from the pump source. Thus, so-called "ultra-short" femtosecond pulses promote self-phase modulation and the creation of solitons, while nanosecond pulses regimes foster the Raman and Brillouin effects.

In optical fibers, Raman scattering and self-phase modulation are responsible for spectral broadening towards longer wavelengths [38], whereas cross phase modulation intervenes in the spectral broadening towards the shorter wavelengths. Spectral components generated by four wave mixing (FWM) can also contribute to the spectral broadening.

In addition to Kerr nonlinearity introduced by the material, other parameters can influence the efficiency of nonlinear effects involved in supercontinuum generation, particularly the fiber length used for this purpose (cumulative effect). However, the optical losses in this case must be taken into account.

V. Conclusion

This chapter provides a theoretical background of the main optical topics required to understand some of the results presented in this dissertation.

An introduction of the pulse transmission along the fiber, with the emphasis of the guidance mechanisms and the general definitions are given. In addition, a brief preliminary description of various conventional, as well as microstructured fibers geometries is provided.

The general background of the dispersive and the nonlinear effects in optical fiber is described in this chapter. Finally, a few of the most relevant nonlinear effects and concepts are reviewed for reference in following chapters.

VI. References

1. B. R. (Burgami.com).
2. K. C. Kao, and G. A. Hockham, "Dielectric-fibre surface waveguides for optical frequencies," Proceedings of the Institution of Electrical Engineers **113**, 1151 – 1158 (1966).
3. D. Keck, and P. Schultz, "Method of producing optical waveguide fibers," US Patent 3711262 (1970).
4. R. Maurer, D. Beck, and P. Schultz, "Fused silica optical waveguide," US Patent 3711262 (1970).
5. T. Miya, Y. Terunma, T. Hosaka, and T. Miyashita, "Ultimate low-loss single-mode fiber at 1.55 µm," Electronic Letters **15**, 106-108 (1979).
6. P. Kaiser, E. A. J. Marcatili, and S. Miller, "A new optical fiber," The Bell System Technological Journal **52**, 265-269 (1973).
7. J. C. Knight, T. A. Birks, P. S. J. Russell, and D. M. Atkin, "All-silica single-mode optical fiber with photonic crystal cladding," Optics Letters **21**, 1547-1549 (1996).
8. J. S. Sanghera, I. D. Aggrawal, L. B. Shaw, C. M. Florea, P. Pureza, V. Q. Nguyen, and F. Kung, "Nonlinear properties of chalcogenide glass fibers," Journal of Optoelectronics and Advanced Materials **8**, 2148-2155 (2006).
9. M. Bass, E. Van Stryland, D. Williams, and W. Wolfe, *Handbook of optics, Volume II, Part 5, Chp. 38&39* (McGraw-Hill, 1996).
10. G. P. Agrawal, *Nonlinear fiber optics* (Academic press, 2007).
11. D. Mogilevtsev, T. A. Birks, and P. S. J. Russell, "Group-velocity dispersion in photonic crystal fibers," Optics Letters **23**, 1662-1664 (1998).
12. A. Y. Chamorovskiy, and S. A. Nikitov, "Nonlinear optical devices based on suspended-core microstructured optical fibers," Journal of Communications Technology and Electronics **58**, 879-890 (2013).
13. J. C. Knight, T. A. Birks, P. S. J. Russell, and J. P. de Sandro, "Properties of photonic crystal fiber and the effective index model," Journal of the Optical Society of America A **15**, 748-752 (1998).
14. B. Kuhlmey, G. Renversez, and D. Maystre, "Chromatic dispersion and losses of microstructured optical fibers," Applied Optics **42**, 634-639 (2003).

15. T. Kanamori, Y. Terunuma, S. Takahashi, and T. Miyashita, "Transmission loss characteristics of $As_{40}S_{60}$ and $As_{38}Ge_5Se_{57}$ glass unclad fibers," Journal of Non-Crystalline Solids **69**, 231-242 (1985).
16. M. F. Churbanov, G. E. Snopatin, V. S. Shiryaev, V. G. Plotnichenko, and E. M. Dianov, "Recent advances in preparation of high-purity glasses based on arsenic chalcogenides for fiber optics," Journal of Non-Crystalline Solids **357**, 2352-2357 (2011).
17. G. A. Thomas, B. I. Shraiman, P. F. Glodis, and M. J. Stephen, "Towards the clarity limit in optical fibre," Nature **404**, 262-264 (2000).
18. M. Born, and E. Wolf, *Principles of optics* (Cambridge University Press, 1999).
19. S. J. Russell, "Holey new fibers," *Optical Fiber Communication Conference,*OSA Technical Digest Series (Optical Society of America, 2001) Papier TuL1, Anheim California, USA (2001).
20. Laferrière, J. a. Lietaert, G. a. Taws, and S. R and Wolszczok, *Reference guide to fiber optic testing* (JDS Uniphase Corporation, 2007).
21. A. Zendehnam, M. Mirzaei, A. Farashiani, and L. Horabadi Farahani, "Investigation of bending loss in a single-mode optical fibre," Pramana **74**, 591-603 (2010).
22. G. Vitrant, "Effets non linéaires en optique guidée," Collection de la Société Française d'Optique **6**, (6) 157-184 (1998).
23. B. P. Stoicheff, "Characteristics of stimulated Raman radiation generated by coherent light," Physics Letters **7**, 186-188 (1963).
24. R. R. Alfano, and S. L. Shapiro, "Emission in the region 4000 to 7000 Å via four-photon coupling in glass," Physical Review Letters **24**, 584-587 (1970).
25. C. Lin, and R. H. Stolen, "New nanosecond continuum for excited-state spectroscopy," Applied Physics Letters **28**, 216-218 (1976).
26. J. K. Ranka, R. S. Windeler, and A. J. Stentz, "Visible continuum generation in air-silica microstructure optical fibers with anomalous dispersion at 800 nm," Optics Letters **25**, 25-27 (2000).
27. R. Holzwarth, T. Udem, T. W. Hansch, J. C. Knight, W. J. Wadsworth, and P. S. J. Russell, "Optical frequency synthesizer for precision spectroscopy," Physical Review Letters **85**, 2264-2267 (2000).
28. I. Hartl, X. D. Li, C. Chudoba, R. K. Ghanta, T. H. Ko, J. G. Fujimoto, J. K. Ranka, and R. S. Windeler, "Ultrahigh-resolution optical coherence tomography using continuum generation in an air-silica microstructure optical fiber," Optics Letters **26**, 608-610 (2001).

29. J. H. V. Price, T. M. Monro, H. Ebendorff-Heidepriem, F. Poletti, P. Horak, V. Finazzi, J. Y. Y. Leong, P. Petropoulos, J. C. Flanagan, G. Brambilla, F. Xian, and D. J. Richardson, "Mid-IR supercontinuum generation from nonsilica microstructured optical fibers," IEEE Journal of Selected Topics in Quantum Electronics **13**, 738-749 (2007).
30. V. L. Kalashnikov, E. Sorokin, and I. T. Sorokina, "Raman effects in the infrared supercontinuum generation in soft-glass PCFs," Applied Physics B **87**, 37-44 (2007).
31. V. E. Zakharov, and S. Wabnitz, *Optical Solitons: Theoretical Challenges and Industrial Perspectives* (Springer Berlin Heidelberg, 1998).
32. Y. V. Kartashov, V. A. Vysloukh, and L. Torner, "Soliton shape and mobility control in optical lattices," Progress in Optics **52**, 63-148 (2009).
33. R. W. Boyd, "*Nonlinear optics"* (Academic Press, 1992).
34. R. H. Stolen, E. P. Ippen, and A. R. Tynes, "Raman oscillation in glass optical waveguide" Appiled Physics Letters **21**, 62-64 (1971).
35. E. P. Ippen, and R. H. Stolen, "Stimulated Brillouin scattering in optical fibers " Appiled Physics Letters **21**, 539-540 (1972).
36. D. Cotter, "Observation of stimulated Brillouin scattering in low-loss silica fibre at 1.3 µm," Electronics Letters **18**, 495-496 (1982).
37. R. W. Tkach, A. R. Chraplyvy, and R. M. Derosier, "Spontaneous Brillouin scattering for single-mode optical fiber characterization," Electronics Letters **22**, 62-64 (1986).
38. J. M. Dudley, and J. R. Taylor, *Supercontinuum Generation in Optical Fibers* (Cambridge University, 2010).

Chapter 2 : Glass materials for infrared supercontinuum generation: state of the art.

I. What is a glass?

I.1 Definition of glass system.

The American Society of Testing Materials (ASTM) defines the glass as: an inorganic product of fusion which has cooled to a rigid condition without crystallizing (absence of X-ray diffraction pattern) [1, 2]. Another definition of glass system is proposed by Zarzycki, who defines the glass as a non crystallized solid which exhibits the phenomenon of glass transition [3].

I.2 Thermodynamic properties of glass system.

The dynamics and thermodynamics of solidified material depend on temporal and thermal regime of cooling process [4]. It allows to explain physical properties of solidified materials. In general, during cooling of molten solution, at critical temperature, solidification and brutal reduction of molar volume occur, Figure 17. This is due to the growth of crystals. It is the melting temperature (T_m). It is characteristic of crystalline phase. It is adopted as first order-phase transition. Resulting liquid material that manages to get below T_m without crystallization are so called supercooled liquid [4]. Its viscosity undergoes gradual increase on temperature reduction. They become harder with further lowering of temperature. Gradual decrease of molar volume is registered. Maintaining cooling rates avoiding crystal‘s nucleation and growth, leads to form glassy materials. Such state is achieved at the second-order transition phase localized at the glass transition temperature (T_g), see Figure 17. Temperature at which mobility inside glass materials is almost blocked; it takes long time compared to the time scale of the experimental observation. Viscosity of cooled materials attains an order of magnitude of 10^{13} Poises, the same as that for solid materials. Glass molar volume is relative to expansion coefficient. It continues to decrease as temperature is lowered but maintain values higher to that of crystalline state. In both cases, atomic vibrations which are very similar dominate thermal expansion coefficient [4].

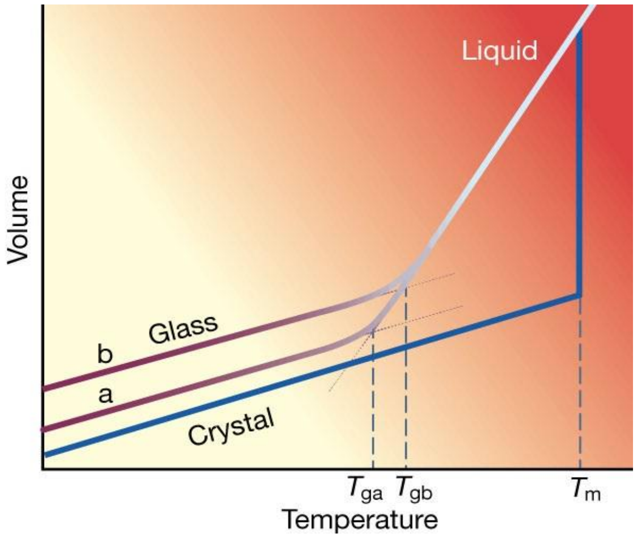

Figure 17: Isobaric relationship between volume and temperature in the liquid, glassy, and crystalline states. T_m is the melting temperature, and T_g is the glass transition temperature. T_g depends upon the cooling rate, T_{ga} and T_{gb} are the glass transition temperatures corresponding to slow (a) and fast (b) cooling rates [5] .

Figure 17 shows that glass formation is kinetically dependant process.

I.3 Structure of glass materials

All solids that do not have long range periodicity in their atoms arrangement can be termed as amorphous or ―structureless". They are best defined when compared to a crystalline solid which has a distinctive regular spatial arrangement of atoms throughout the whole material. In fact they are often simply referred to as non-crystalline materials. Although their structure appears random over the long range, an amorphous substance still has a high degree of short range spatial order in its atomic structure. This is because individual atoms in an amorphous solid must still fulfill their requirement for valence bonding. However, unlike their crystalline counterpart, there are some small deviations in the bonding angles between adjacent atoms and this leads to a disruption of the periodicity in the material. An example of crystalline and amorphous material is given in Figure 18 showing the difference between the atomic arrangements. Zachariasen proposed this model of a relatively open structure of glass (Figure 18.b) as compared to the crystalline structure (Figure 18.a) of the same material, in this case silicon oxide [6].

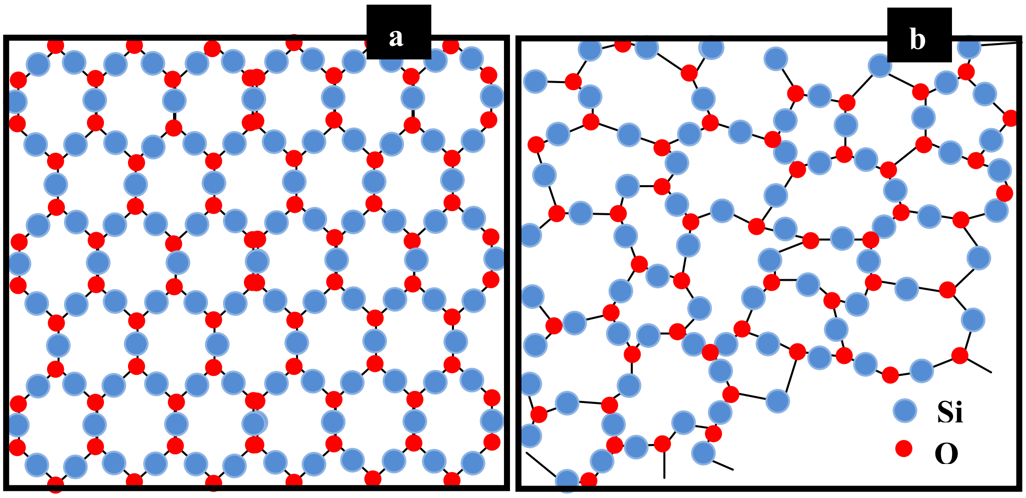

Figure 18: Schematic arrangement in crystal and amorphous solid.

II. Optical properties of soft-glass materials.

Soft-glasses (low T_g), can be classified in three main families: heavy oxides as tellurite, fluoride and chalcogenide glasses. In the following section, the fundamental characteristics of these glass families will be reviewed from the viewpoint of use as infrared transparent and highly nonlinear glass fibers. Nonlinear optics (NLO) requires intense incident light beam and a strong interaction with material. Planar waveguides and fiber geometry are of major interest. They allow to reduce waveguide‘s core dimension down to the submicron scales. This permits a tight mode confinement increasing the light power density. Fibers provide long light path, lengthens its interaction with the glass, these scale factors provide apparent enhancements of nonlinear (NL) effects in glasses [7-9].

The first successful SC generation in optical fiber was reported in 1976 [8, 10]. In particular, the spectral broadening was registered in standard silica-based optical fiber with zero group velocity dispersion (GVD) wavelength around 1.3 µm. Consequently, it was obvious that the following researches will focus on the silica fiber. Thus, supercontinuum generation (SCG) in silica based fibers was extensively studied in the following years. It yielded to commercialize a silica-based fiber supercontinuum source, delivering energy in a wide output spectrum that covers the entire 450-2400 nm region [11]. However, extending further the SC infrared edge is a challenging task due to the multiphonon absorption edge of silica glass network, which limits the transmission window in the infrared region [12, 13].

Thus, beyond a wavelength of 2.4 µm (Figure 19-b), it is necessary to consider the use of non-silica glasses also known as soft-glasses. SCG research with soft glass fibers has benefitted from the understanding of the mechanisms leading to the formation of the continuum obtained from prior work with silica fibres [7, 9].

Soft-glasses are low phonon energy materials, having their phonon absorptions in the long wavelength region. In addition, they are known as soft-glass materials due to their low melting temperature and fragile nature comparing to silica glass. The main advantage of soft glasses over silica glass is that the first glass category has a wider IR transmission window, and therefore allows further spanning of the SC IR edge. But the losses for the soft glasses fibers are higher, and for some, the material's dispersion is located far in the MIR.

II.1 Transmission window and loss characteristics

II.1.1 Multiphonon absorption

Figure 19 compares the transmission spectra and the position of infrared wavelength edge, routinely registered for different families of glasses according to their composition.

Family of heavy metal oxide (HMO) glasses exhibit lower phonon energies than silica. HMO glasses include among others tellurite and germanate compounds based on the glass-network formers tellurium and germanium dioxide (TeO_2 and GeO_2). Certain compositions of these glasses can transmit light beyond 5 µm up to 7 µm [14].

The cut-off edge of fluoride glass family is more extended in the IR compared to silica. Heavy metal fluoride glasses are transparent in the infrared (IR) region up to 5-6.5 µm [14-16] depending on the thickness of the sample and the glass composition. By analogy with harmonic oscillator law, phonon resonance frequency is synonymous with weak bond strength [17] and large atomic masses. The IR cut-off is shifted by the nature of the lighter cation and its concentration. As a general rule, the position of IR edge is shifted toward longer wavelengths according to the sequence: $AlF_3 < ZrF_4 < HfF_4 < ScF_3 < GaF_3 < InF_3$ [18]. The most popular fluoride glass for fabrication into fibers is the fluorozirconate glass of which the most common are ZBLAN (ZrF_4-BaF_2-LaF_3-AlF_3-NaF). ZBLAN fibers exhibit a transmission window from 0.3 µm to 4.5 µm (Figure 19). This transparency window is IR shifted on indium fluoride glasses. Indium fluoride glass fibers have a transmission window extended from 0.3 to 5.5 µm. It is 1.5 µm much larger than ZBLAN fiber's window, without any absorption peaks [19].

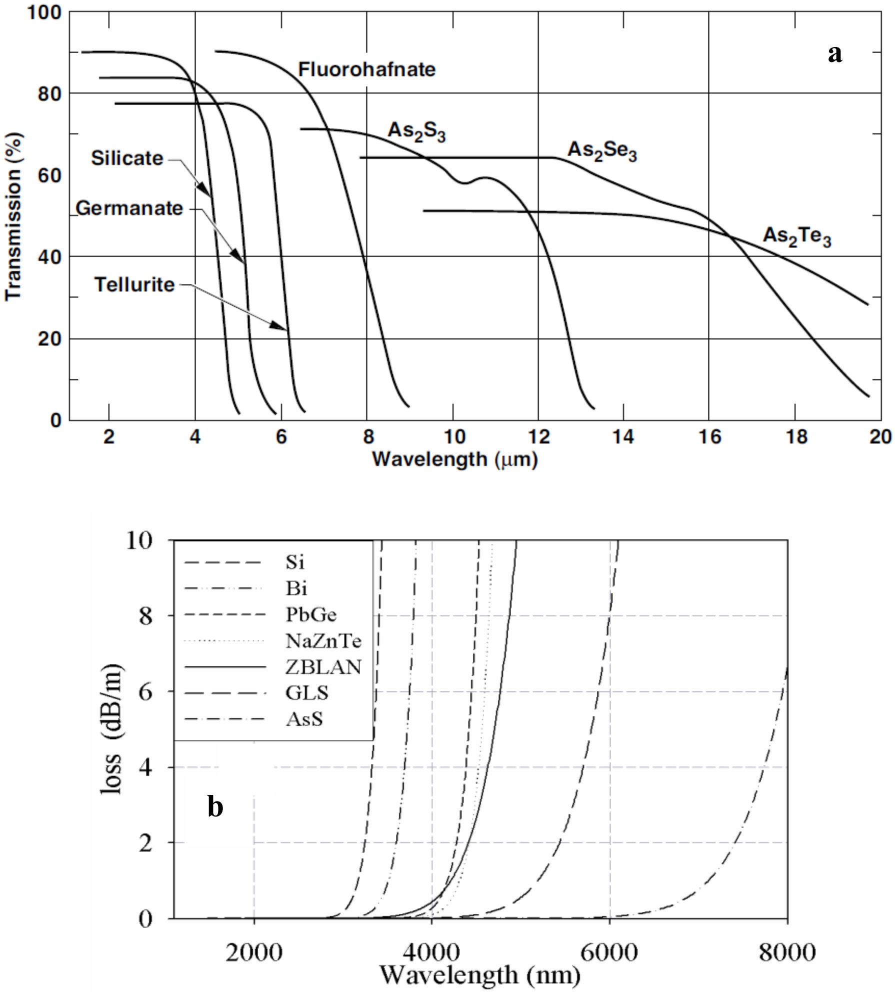

Figure 19: Transmission window of various families of glasses (a) and zoom on the multiphonon absorption edge of the corresponding glass fibers (b) as printed from [25].

Chalcogenide glasses are known for their broad mid-IR transparency window resulting from an extremely low phonon energy and lack of deleterious molecular resonances interrupting the continuity of the IR transmission. For this glass family, the transmission multiphonon edge lies in the mid-IR due to large atomic masses and relatively weak bond strengths. From the periodic table of the elements, we have $M_S < M_{Se} < M_{Te}$. Thus, as a general rule, the position of IR edge is shifted toward longer wavelengths according to the sequence: S < Se < Te. In general and as shown in Figure 19-a, the mid-IR transparency edge on bulk specimen is 12 µm for sulfide based glasses, 15 µm for selenide glasses and 20 µm for telluride glasses [20]. However, this characteristic wavelength decreases on fiber samples to reach 7 µm, 10 µm, and 12 µm, respectively (Figure 19-b) [21, 22]. Chalcogenide glasses suffer from small band-gap edge resulting in a poor transparency in the visible region [22]. Sulfides usually are transparent in the high wavelength range of the visible region where selenides or tellurides are completely opaque [14, 22-24].

II.1.2 Extrinsic transmission losses.

The presence of impurities is responsible for optical absorptions bands at characteristic frequencies in the transmission window edge. This interrupts the continuity of the transmission and reduces the width of the fiber‘s bandwidth. One of the primary absorbing species common to all families of glass fibers are hydroxyl groups (H_2O or -OH) [14, 15, 26-31]. The fundamental resonances for hydroxyl species, associated with bending and stretching modes of vibrations, occur mainly around 2.8 µm [26, 29, 31-33]. Other absorption bands arise at different wavelengths, depending on the considered glass system, as well as, according to the combination of different vibration modes of a variety of hydroxyl groups tightly as weakly linked to the glass network [15, 26, 28, 30, 31].

In photonic applications such as supercontinuum generation (SCG), low OH content has become relevant for fibers whose optical performance is related to OH overtones absorption bands [29, 34-38]. These absorbing moieties severely reduce the efficiency of the various nonlinear optical effects, responsible of the spectral broadening, and consequently prevent the extension of the SC spectrum further in the IR region [29, 34, 37, 39]. This has serious implications for the development of low-loss fiber optic [29, 37, 38, 40].

The use of reactive chemicals and batch drying method can substantially reduce the amount of impurities incorporated into the glass [29, 41-43]. Such techniques allow to remove the moistures traces present on the grain surface and / or interface in the starting products used to fabricate different glasses such as tellurite, fluoride and chalcogenide. Others allow to trap the hydroxyl components present within the glass melt. This technique was successfully used on tellurite glasses in our laboratory. Fruitful work of fluoridation of the melt batch allowed to reduce by one order of magnitude the optical losses on single index fiber [29].

Several researches were conducted to develop low loss fluoride glass fibers. This technological achievement, has resulted in impressive low transmission loss values [44-47]. ZBLAN (ZrF_4-BaF_2-LaF_3-AlF_3-NaF) glass system are the most known to fabricate fluoride fibers. Early in the 1990th, the minimum optical loss in ZBLAN fiber was lowered to 0.45 10^{-3} dB/m around 2.35 µm [44]. Nowadays, commercial ZBLAN fibers are available in the market with typical background loss of 10–100. 10^{-3} dB/m due to the extrinsic scattering and absorption that are relatively difficult to control in the fabrication process [45]. Nishida and al. [46] have reported low loss PbF_2-InF_3 based fluoride glass fibers with a minimum attenuation of 0.043 dB/m at 3.33 µm [46]. One year later, they succeeded to reduce this value to 0.025 dB/m on InF_3-GaF_3 glass fibers [48]. Recently, a multimode fluoride-based fibers with an optical loss of 0.85 dB/m at 1.3 µm was achieved using a fluorination process during the glass melting [47, 49-51].

In light of efforts to produce low loss chalcogenide glasses, binary glass system such as As-S, As-Se, Ge-S and Ge-Se compounds were investigated [52-60]. These efforts have coincided with extensive studies in order to reach high-quality optical fibers in view of special features of chalcogenide fibers. Snopatin and al. [52, 53] have optimized the synthesis process of As_2S_3 glasses and managed to beat the record of minimum optical losses in optical fibers produced from As_2S_3 glass. The minimum optical losses registered on optical fiber produced from this glass were 12.10^{-3} dB/m at 3.0 µm and 14.10^{-3} dB/m at 4.8 µm [52, 53]. This loss threshold slightly increases in single-mode As–S glass fibers, but remains below 0.1 dB/m in the 2.2-2.3 µm range [53]. Here, glass fibers with a core diameter from 3 to 20 µm and a clad diameter of 125 µm were prepared by the double-crucible method. In optical fibers from $As_{38}S_{25}Se_{37}$ (core) and $As_{38}S_{27}Se_{35}$ (clad) produced by the double-crucible method with core/clad diameters of 300/400 and 200/400 µm and numerical aperture of 0.28, the lowest optical loss was found to be 0.06 dB/m at 4.8 µm and 0.2−0.3 dB/m between 4 and 6 µm [54].

Te-As-Se glass compounds were extensively developed. Consequently, low loss single-index and multimode core–clad Te-As-Se based fiber are reported in the literature. An unclad fiber from $As_{40}Se_{30}Te_{30}$ glass with optical losses of 3.5 dB/m at 10.6 µm was reported in [59]. The minimal optical loss was enhanced to reach 0.07 dB/m at 7.3µm for $As_{40}Se_{35}Te_{25}$ glass fiber and decreases to 0.04 dB/m at 6.7 µm for $As_{30}Se_{50}Te_{20}$ based fiber [60]. Recently, new record of minimum loss level of 0.33 dB/m at 7.5 µm was reported on $As_{39}Se_{42.4}Te_{18.6}$/ $As_{39}Se_{42.7}Te_{18.3}$ core–clad single-mode optical fibers [55]. These fibers were drawn with core diameter of 20 µm embedded within clad of 450 µm external diameter [56]. A single-index fiber based on $Ge_{30}As_{10}Se_{30}Te_{30}$ glass has been reported with optical losses of 0.11 and 1.88 dB/m at, 6.6 and 10.6 µm, respectively [56]. These are the minimal optical losses ever registered for $Ge_{30}As_{10}Se_{30}Te_{30}$ glass fiber [57]. Using double crucible technique, Shiryaev and al. [57] have succeeded to improve the fiber quality, and to manufacture high purity GeAsSeTe based step index fiber. The fiber exhibited 210 µm core diameter that consisted of $Ge_2As_{38}Se_{40}Te_{20}$ and 330 µm clad diameter which consisted of $Ge_2As_{36}Se_{44}Te_{18}$ glass. This Multimode fiber exhibited a minimum optical losses of 0.15-0.20 dB/m in the wavelength range of 6-7 µm and losses less than 1.0 dB/m in the 3.5-9.5 µm range [57].

Table 1: Lowest loss levels achieved on silica, fluoride, tellurite and chalcogenides glass fibers.

Glass		Minimum optical losses on fibers	
		α_{min} (10^{-3}.dB/m)	λ (µm)
Silica	[61]SiO_2	0.2	1.5
Tellurite	[62]TZN	< 2.0	2.2
Fluoride	[29] ZBLAN	0.45	2.3
	[48] InF_3-FaF_3/ZBLAN	200	1.2
Chalcogenide	[63] As_2S_3	12	3.0
	[53]$As_{38}S_{25}Se_{37}$	60	4.8
	[60] $As_{40}Se_{35}Te_{25}$	70	7.3
	[56]$Ge_{30}As_{10}Se_{30}Te_{30}$	110	6.6

In addition to extrinsic absorption species, local defects induce scattering losses and contribute to increase the transmission losses. These scattering centers (bubble, metallic impurities….) come from starting products, synthesis and drawing process. These imperfections can be divided into volume and surface defects. These scattering sites depend on the melting and quenching conditions during glass fabrication. Volume defects such as bubbles, un-dissolved particles and crystals are imperfections within the glass matrices that are principally formed during glass melting. Surface defects grow with surface contaminations, micro-cracks and surface crystallization originate from the reaction of the glass surface with moisture from the atmosphere of fiber fabrication or storage [52].

Records of purity reported on different glass families are gathered in Table 1.

II.2 Linear and Nonlinear refractive index

The linear refractive index "n" is a macroscopic material parameter characterizing the phase propagation velocity of the light depending on microscopic dielectric polarization p(ω) of the medium by the optical E-field. Hence, it is related to the chemical composition of the material and depends on individual ions present in the glass, their packing along with their polarizability. Furthermore, the refractive index generally increases with increasing size of ions [25], as by introducing a heavy-metal components within the glass medium.

Below we briefly report several studies to provide a complete picture of evolution of both linear and nonlinear optical properties of different soft glass families.

In tellurite glasses the nonlinearity is presumably due to large non-linear electronic polarization of TeO_2 entities [64]. Tellurite based glass TZN (TeO_2-ZnO_2-Na_2O), exhibit significant improvement of nonlinearity by introducing Nb_2O_5 components. Whereas, opposite behavior appears when Nb_2O_5 is replaced by BaO. The increased nonlinearity with Nb_2O_5 doping is likely associated with the higher oxygen-to-cation ratio effectively increasing the polarizability of the glass [64] although the exact mechanism is not clear [65]. While Nb_2O_5 appears to function as a intermediate network former [66], resulting in a more stable glass matrix, BaO should enter the glass network as a network modifier, which are known to decrease the nonlinear properties of TeO_2 based glasses [67]. Similar results are also reported in [68], where the presence of GeO_2 decreases the value of the nonlinear refractive index [69].

Refractive index in heavy metal fluoride glasses is changed by systematic substitution of cations elements in standard glass fluorozirconate glasses including ZBLA (ZrF_4 BaF_2 LaF_3 AlF_3) and ZBLAN (ZrF_4 BaF_2 LaF_3 AlF_3 NaF) [18]. This process allowed to modify the polarizibility within the glass network. However, substantial change of refractive index has not been reported by composition manipulation. Here, the maneuver merge is limited by a set of requirements, in particular the minimum stability of the vitreous phases against devitrification.

In chalcogenide glasses, depending on the chemical composition, the nonlinear refractive index n_2 has been measured to be between 100 to 1000 times larger than for silica glass [70]. In sulfur- and selenide-based chalcogenide glasses, both S and Se exhibit two electronic lone pairs [24]. It has been confirmed that Se-based chalcogenide glasses possess higher nonlinearity than S-based chalcogenide glasses which may be attributed to the excess of selenium-selenium or selenium-sulfur covalent bonds [24]. One can note also that in case of selenium, electronic lone pairs are higher in energy than that of sulfur. On the other hand, the minor substitution of selenium having two electronic lone pairs by germanium exempt of electronic lone pairs, sharply decreases the non-linear refractive index. Furthermore, it seems that addition of tellurium does not enhance significantly the nonlinear refraction index, but exalts more the nonlinear absorption [71]. Table 2 presents evolution of nonlinear optical properties of various chalcogenide glasses according to corresponding chemical composition.

Table 2: Nonlinear optical constants for different glass compositions, of highly linear chalcogenide glasses. n_2 : non linear refractive index. Parameters were measured at 1.064 µm wavelength.

Composition	**n_2 (10^{-18} $m^2.W^{-1}$)**
[23, 71]**$As_{40}S_{60}$**	2.5-5.2
[23, 72]**$As_{40}Se_{60}$**	12.6
[23]**$Ge_{20}Se_{80}$**	13
[72]**$Ge_{10}As_{10}Se_{80}$**	16.5
[23]**$Ge_{20}As_{40}Se_{40}$**	8.5
[72]**$Ge_{10}As_{10}Se_{70}Te_{10}$**	19
[72]**$Ge_{10}As_{10}Se_{60}Te_{20}$**	20
[23]**$Ge_{20}Se_{80}$**	13

Figure 20 displays the merges of nonlinear refractive index, and its relation to linear index with the glass classification. It is clearly seen that the glass nonlinearity follows the polarizability of anions, and as a general rule, both linear and nonlinear refractive index increase according to the sequence: $F^- < O^{2-} < S^{2-} < Se^{2-}$ respectively.

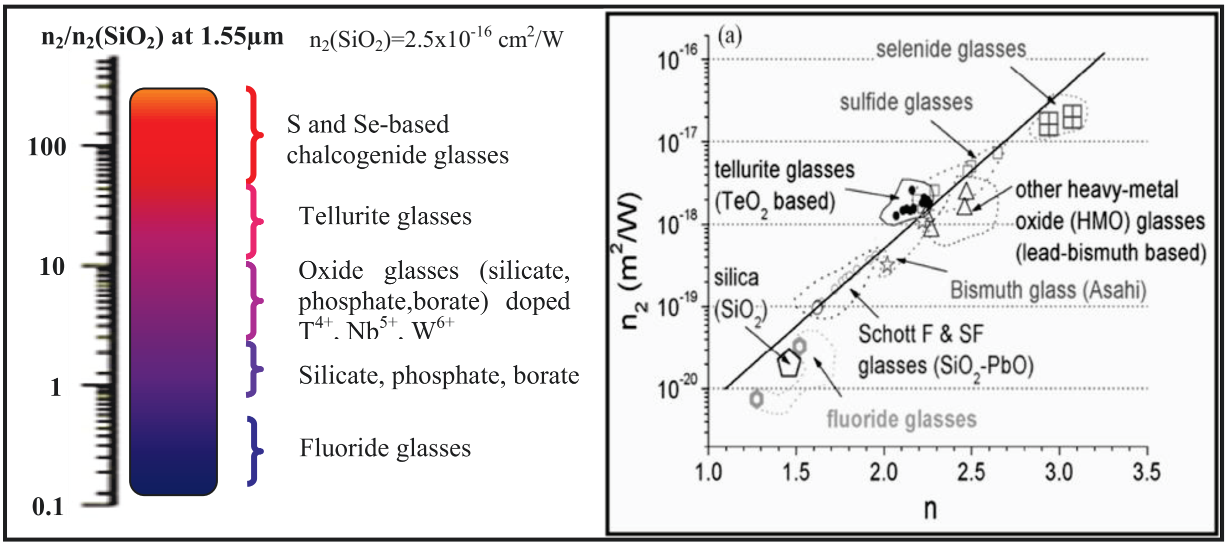

Figure 20: Summary of the trends in nonlinear refractive index "n_2" measured at 1.5 μm (a) and its relation to the linear refractive index "n" for different families of glasses (b) as reprinted from [25, 73].

II.3 Dispersion

In general, there is a direct relationship between dispersion and refractive index in optical glasses. In other word, the glass with a relatively high refractive index has a relatively high dispersion. Linear, non linear refractive index and material's zero dispersive wavelengths are summarized in Table 3.

Table 3: Summarize of various key properties of soft glasses and silica for comparison [8].

Glass type	Code	Main components	n_0	n_2 (10^{-20} m^2/w)	ZDW (μm)
Silica	Si	SiO_2	1.45	2.7	1.26
Lead silicate	SF57	$PbO-SiO_2$	1.81	41	2.0
Bismuth oxide	Bi	Bi_2O_3	2.02	32	2.29
Germanate	PbGe	$PbO-GeO_2$	1.8	22	1.78
Tellurite	ZnTe	$ZnO-TeO_2$	2.03	51	2.24
Fluoride	ZBLAN	ZrF_4-BaF_4	1.5	3.3	1.62
Chalcogenide	AsS	As_2S_3	2.44	597	4.81
	GLS	$Ga_2S_3-La_2S_3$	2.41	2.16	--
	AsSe	As_2Se_3	2.81	1100-2400	~6

Microstructured optical fibers (MOFs) technology allowed to overcome limitations of the material's dispersion [25, 74], especially for those owing ZDW far in the IR such as chalcogenide glasses. MOF geometry successfully permitted to modify the guidance properties within the glass fibers and to tailor the fiber chromatic dispersion [74-77] and are well suited as the basis of a supercontinuum source. These effects are achievable by carefully engineered patterns of well defined parameters of the MOF.

III. Supercontinuum generation records in soft-glasses

Despite numerous successful [78, 79] spectral broadening reported on bulk specimens by self focusing (filamentation) technique, we believe that such strategy is disadvantageous at many levels. First, self-focusing requires the use of high pulse intensities, usually close to the damage threshold of the operated glass system [80, 81]. In addition, output SC suffers from reduced brightness and coherence, caused by the multiple filament that can occur within the illuminated bulk when power above the self focusing threshold is applied [82]. These constraints are overcome on fiber geometry. In a first approach, a fiber provides a long path length requiring relatively low power to enable the spectral broadening. In addition, special structure of fiber, known as MOF allows to engineer its ZDW and improve the light confinement highly suitable for the sequence of events in supercontinuum generation [82]. Thus, in this section, we exclusively review experiments on mid-infrared supercontinuum generation on dispersion engineered fluoride, tellurite and chalcogenide glass fibers.

Quin and al. [83] succeeded to registered a 6000 nm supercontinuum spectrum in a fluoride fiber by 2009. The fibre used in this experiment was a ZrF_4–BaF_2–LaF_3–AlF_3–NaF (ZBLAN) step-index fiber. The fiber has a core diameter of 9 µm, a numerical aperture (NA) of 0.2. A short 2 cm length of fibre was used in this experiment to overcome the substantial propagation losses that occur at longer wavelengths. The specimen was seeded in the normal dispersion regime at 1450 nm using femtosecond laser. When the fiber is seeded with peak power of 50 MW, it enables a broadening extended from ~0.35 nm in the UV up to 6.28 µm (Figure 21).

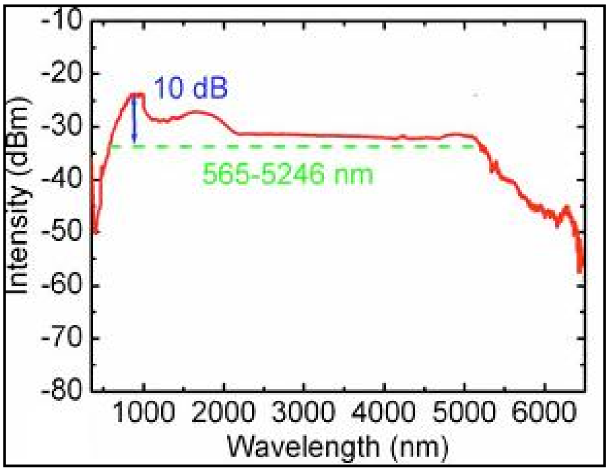

Figure 21: Record continuum registered in centimeter scale step-index ZBLAN fiber [83].

SC Spanning record extended over 4000 nm was successfully registered on tellurite fiber and reported by Domachuk and al. in 2008 [84]. The fiber was fabricated using an extrusion process from a bulk tellurite glass billet with stoichiometry $75TeO_2$-12ZnO-5PbO-$3PbF_2$-$5Nb_2O_5$. The fiber was designed to tailor the fiber ZDW down to 1380 nm in order to allow anomalous dispersion pumping. Microstructure consists of six thin struts of 120 nm thickness, supporting a suspended core of 2.5 µm of diameter. Short fiber (8 mm) length was used in order to decrease the substantial material's loss of the MOF at long wavelengths. When pumped with a 1550 nm femtosecond source, a SC extending from 0.79 to 4.87 µm is measured (Figure 22).

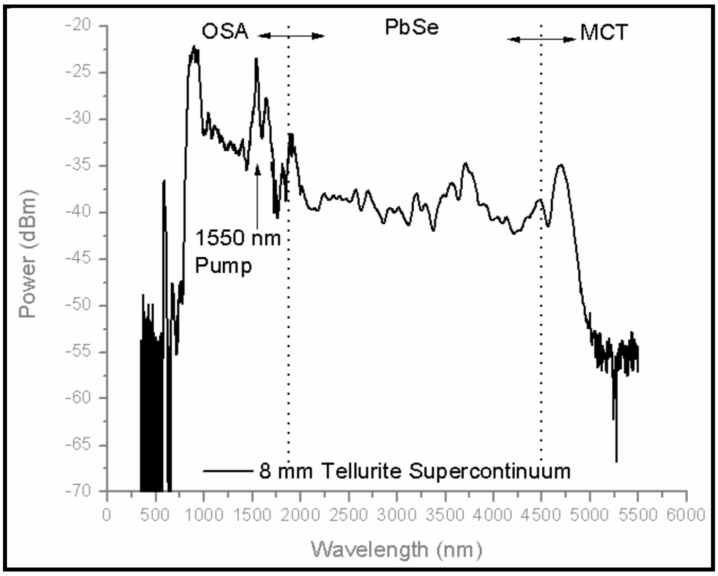

Figure 22: Record continuum registered in sub-centimeter suspended core tellurite fiber [84]

Shaw and al. [85] reported a SC spectrum spreading over ~2.9 µm from a As_2S_3 step index nonlinear optical fiber. The 2 m long fiber used in this experiment exhibits a 10 µm core diameter and is pumped in the normal dispersion regime at 2.45 µm by means of fibered femtosecond laser source. Following light coupling in the fiber, the spectral broadening extends from 1.9 to 4.8 µm (Figure 23). The relatively high loss level can be mitigated using short fiber length and / or by ensuring anomalous dispersion pumping increasing the non linear effects efficiency. Both scenarios can not be reached on step index fiber which imposes a transition to MOF allowing chromatic dispersion engineering in order to pump in the anomalous dispersion regime. In addition, MOF ensure high confinement of coupled signal, enhancing thus the non linear optical effects efficiency and reducing significantly the fiber length required to ensure the spectral broadening.

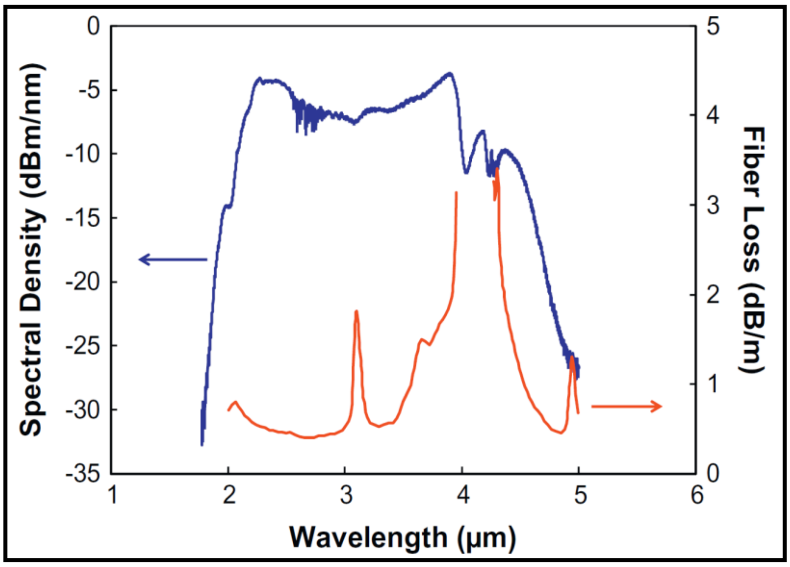

Figure 23: SC spectrum covering from 1.9 µm to 4.8 µm from a single mode step-index As_2S_3 fiber pumped at 2.45 µm and the measured fiber loss. [85].

Spectral enlargement records reported on both tellurite and fluoride glasses outstandingly overcome the corresponding multiphonon absorption edge located below 4.5 µm (Figure 19-b). In order to bypass this detrimental material absorption, the later achievements required the use of short length samples and high peak power pump lasers. In addition, SC spectra suffer from low flatness and low dynamic power.

Despite the spectral spanning registered on chalcogenide-based fibers has not exceeded those reported for tellurite and fluoride-based fibers, chalcogenides remain significantly advantageous when seeking to cover the midinfrared and infrared region.

IV. Conclusion

Chalcogenide glasses are characterized by a wide IR transmission and high nonlinearity comparing to fluoride and tellurite glasses. These features make these glasses promising candidate for SCG covering both atmospheric transmission windows, extended between 3-5 and 8-12 µm, respectively. Sulfide based chalcogenide glasses are the most transparent in the near visible range, it is around 500 nm for As_2S_3 [14]. Compared to the previous glass materials, chalcogenide nonlinearity is very high. As_2S_3 ZDW (4.8 µm) is one of the lowest among chalcogenide glasses, furthermore microstructured profile allows to lower the ZDW of the fibres [25, 80, 86-88]. Moreover, in suspended core case, sulfide glasses low ZDW leads to core diameter bigger than selenide glasses which is an advantage for light coupling.

In addition, latest improvement of glass fabrication technology allowed to fabricate chalcogenide fibers with optical losses close to their corresponding theoretical threshold. Besides that, microstructured optical fiber technology has enabled engineering of the fiber chromatic dispersion allowing thus to pump the fiber with commercially available laser sources. The combination of these features predicts promising results for supercontinuum generation.

For the following works about supercontinuum generation in fiber, among chalcogenide glasses we selected a sulfide one: As_2S_3.

V. References

1. A. K. Varshneya, and J. C. Mauro, "Comment on misconceived ASTM definition of –Glass” by A. C. Wright," Glass Technology **51**, 28-30 (2010).
2. M. D.-Y. SEUNG, "Approche structurale et étude de la conduction ionique de verres a base de thioarsenite de lithium et de verres a formateur mixte, thioborate et thioarsenite de lithium," PhD in *Université Sciences et Technologies - Bordeaux I* (Université de Bordeaux I, France, 1995).
3. J. Zarzycki, *Les verres et l'état vitreux* (Masson, 1982).
4. M. D. Ediger, C. A. Angell, and S. R. Nagel, "Supercooled liquids and glasses," The Journal of Physical Chemistry **100**, 13200-13212 (1996).
5. P. G. Debenedetti, and F. H. Stillinger, "Supercooled liquids and the glass transition," Nature **410**, 259-267 (2001).
6. H. Rawson, *Glasses and their applications* (Institute of Metals, London, 1991).
7. G. P. Agrawal, *Nonlinear fiber optics* (Academic press, 2007).
8. J. M. Dudley, G. Genty, and S. Coen, "Supercontinuum generation in photonic crystal fiber," Reviews of Modern Physics **78**, 1135-1184 (2006).
9. J. M. Dudley, and J. R. Taylor, *Supercontinuum Generation in Optical Fibers* (Cambridge University, 2010).
10. C. Lin, and R. H. Stolen, "New nanosecond continuum for excited-state spectroscopy," Applied Physics Letters **28**, 216-218 (1976).
11. http://www.nktphotonics.com/.
12. J. Fatome, B. Kibler, M. El-Amraoui, J. C. Jules, G. Gadret, F. Desevedavy, and F. Smektala, "Mid-infrared extension of supercontinuum in chalcogenide suspended core fibre through soliton gas pumping," Electronics Letters **47**, 398-400 (2011).
13. X. Chenan, M. Kumar, C. Ming-Yuan, O. P. Kulkarni, M. N. Islam, A. Galvanauskas, F. L. Terry, M. J. Freeman, D. A. Nolan, and W. A. Wood, "Supercontinuum generation in silica fibers by amplified nanosecond laser diode pulses," IEEE Journal of Selected Topics in Quantum Electronics **13**, 789-797 (2007).
14. D. Lezal, "Chalcogenide glasses - survey and progress," Journal of Optoelectronics and Advanced Materials **5**, 23-34 (2003).
15. F. Huang, Y. Ma, W. Li, X. Liu, L. Hu, and D. Chen, "2.7 µm emission of high thermally and chemically durable glasses based on AlF_3," Scientific Reports **4**, 1-6 (2014).

16. X. Zhu, and N. Peyghambarian, "High-power ZBLAN glass fiber lasers: review and prospect," Advances in OptoElectronics **2010**, 1-23 (2010).
17. J. Lucas, "Infrared glasses," Current Opinion in Solid State and Materials Science **4**, 181-187 (1999).
18. M. Poulain, A. Soufiane, Y. Messaddeq, and M. A. Aegerter, "Fluoride glasses: synthesis and properties " Brazilian Journal of Physics **22**, 205-217 (1992).
19. F. g. fibers, "Fluoride glass fibers," in *Photonics Society Summer Topical Meeting Series, 2011 IEEE* (IEEE, Montreal, QC, M Saad).
20. J. A. Savage, and S. Nielsen, "Chalcogenide glasses transmitting in the infrared between 1 and 20 µm a state of the art review," Infrared Physics **5**, 195-204 (1965).
21. V. Kokorina, *Glasses for infrared optics* (The CRC Press, 1996).
22. J.-L. Adam, and X. Zhang, *Chalcogenide Glasses: Preparation, Properties and Applications* (Woodhead Publishing, 2014).
23. C. Quémard, F. Smektala, V. Couderc, A. Barthélémy, and J. Lucas, "Chalcogenide glasses with high non linear optical properties for telecommunications," Journal of Physics and Chemistry of Solids **62**, 1435-1440 (2001).
24. T. Cardinal, K. A. Richardson, H. Shim, A. Schulte, R. Beatty, K. Le Foulgoc, C. Meneghini, J. F. Viens, and A. Villeneuve, "Non-linear optical properties of chalcogenide glasses in the system As-S-Se," Journal of Non-Crystalline Solids **256-257**, 353-360 (1999).
25. J. H. V. Price, T. M. Monro, H. Ebendorff-Heidepriem, F. Poletti, P. Horak, V. Finazzi, J. Y. Y. Leong, P. Petropoulos, J. C. Flanagan, G. Brambilla, F. Xian, and D. J. Richardson, "Mid-IR supercontinuum generation from nonsilica microstructured optical fibers," IEEE Journal of Selected Topics in Quantum Electronics **13**, 738-749 (2007).
26. E. Stolper, "Water in silicate glasses: an infrared spectroscopic study," Contributions to Mineralogy and Petrology **81**, 1-17 (1982).
27. B. Richards, A. Jha, Y. Tsang, D. Binks, J. Lousteau, F. Fusari, A. Lagatsky, C. Brown, and W. Sibbett, "Tellurite glass lasers operating close to 2 µm," Laser Physics. Letters **7**, 177-193 (2010).
28. P. Toupin, L. Brilland, D. Mechin, J. Adam, and J. Troles, "Optical aging of chalcogenide microstructured optical fibers," Journal of Lightwave Technology, **32**, 2428-2432 (2014).
29. I. Savelii, F. Desevedavy, J.-C. Jules, G. Gadret, J. Fatome, B. Kibler, H. Kawashima, Y. Ohishi, and F. Smektala, "Management of OH absorption in tellurite optical fibers and related supercontinuum generation," Optical Materials **35**, 1595-1599 (2013).

30. M. Saito, "Optical loss increase in an As-S glass infrared fiber due to water diffusion," Applied Optics **26**, 202-203 (1987).

31. V. G. Plotnichenko, V. O. Sokolov, and E. M. Dianov, "Hydroxyl groups in high-purity silica glass," Journal of Non-Crystalline Solids **261**, 186-194 (2000).

32. A. M. Efimov, and V. G. Pogareva, "Water-related IR absorption spectra for some phosphate and silicate glasses," Journal of Non-Crystalline Solids **275**, 189-198 (2000).

33. A. M. Efimov, and V. G. Pogareva, "IR absorption spectra of vitreous silica and silicate glasses: The nature of bands in the 1300 to 5000 cm^{-1} region," Chemical Geology **229**, 198-217 (2006).

34. I. Savelii, O. Mouawad, J. Fatome, B. Kibler, F. Désévédavy, G. Gadret, J. C. Jules, P. Y. Bony, H. Kawashima, W. Gao, T. Kohoutek, T. Suzuki, Y. Ohishi, and F. Smektala, "Mid-infrared 2000-nm bandwidth supercontinuum generation in suspended-core microstructured Sulfide and Tellurite optical fibers," Optics Express **20**, 27083-27093 (2012).

35. A. Kudlinski, G. Bouwmans, O. Vanvincq, Y. Quiquempois, A. Le Rouge, L. Bigot, G. Mélin, and A. Mussot, "White-light cw-pumped supercontinuum generation in highly GeO_2-doped-core photonic crystal fibers," Optics Letters **34**, 3631-3633 (2009).

36. J. C. Travers, R. E. Kennedy, S. V. Popov, J. R. Taylor, H. Sabert, and B. Mangan, "Extended continuous-wave supercontinuum generation in a low-water-loss holey fiber," Optics Letters **30**, 1938-1940 (2005).

37. O. Mouawad, J. Picot-Clémente, F. Amrani, C. Strutynski, J. Fatome, B. Kibler, F. Désévédavy, G. Gadret, J. C. Jules, D. Deng, Y. Ohishi, and F. Smektala, "Multioctave midinfrared supercontinuum generation in suspended-core chalcogenide fibers," Optics Letters **39**, 2684-2687 (2014).

38. I. Gris-Sanchez, and J. C. Knight, "Time-dependent degradation of photonic crystal fiber attenuation around OH absorption wavelengths," Journal of Lightwave Technology **30**, 3597-3602 (2012).

39. S. A. Dekker, A. C. Judge, R. Pant, I. Gris-Sánchez, J. C. Knight, C. M. de Sterke, and B. J. Eggleton, "Highly-efficient, octave spanning soliton self-frequency shift using a specialized photonic crystal fiber with low OH loss," Optics Express **19**, 17766-17773 (2011).

40. I. Gris-Sánchez, B. J. Mangan, and J. C. Knight, "Reducing spectral attenuation in small-core photonic crystal fibers," Optical Materials Express **1**, 179-184 (2011).

41. V. Q. Nguyen, J. S. Sanghera, P. Pureza, F. H. Kung, and I. D. Aggarwal, "Fabrication of arsenic selenide optical fiber with low hydrogen impurities," Journal of the American Ceramic Society **85**, 2849-2851 (2002).

42. V. Q. Nguyen, J. S. Sanghera, B. Cole, P. Pureza, F. H. Kung, and I. D. Aggarwal, "Fabrication of arsenic sulfide optical fiber with low hydrogen impurities," Journal of the American Ceramic Society **85**, 2056-2058 (2002).

43. P. Joshia, B. Richardsa, and A. Jhaa, "Reduction of OH^{-} ions in tellurite glasses using chlorine and oxygen gases," Journal of Materials Research **28**, 3226-3233 (2013).

44. D. Szebesta, S. T. Davey, J. R. Williams, and M. W. Moore, "OH absorption in the low loss window of ZBLAN (P) glass fibre," Journal of Non-Crystalline Solids **161**, 18-22 (1993).

45. J. A. Harrington, *Infrared fibers and their applications* (SPIE press Bellingham, 2004).

46. Y. Nishida, T. Kanamori, T. Sakamoto, Y. Ohishi, and S. Sudo, "Development of PbF_2-GaF_3-InF_3-ZnF_2-YF_3-LaF_3 glass for use as a 1.3 µm Pr^{3+}-doped fiber amplifier host," Journal of Non-Crystalline Solids **221**, 238-244 (1997).

47. M. Saad, "Fluoride glass fiber: state of the art," Proceeding SPIE **7316**, 73160N-73160N-73116 (2009).

48. T. Kanamori, Y. Nishida, Y. Ohishi, T. Sakamoto, and S. Sudo, "Fluoride glass fiber," in *Google Patents-US Patent 5,774,620* (1998).

49. S. Mitachi, Y. Terunuma, Y. Ohishi, and S. Takahashi, "Reduction of impurities in fluoride glass fibers," Journal of Lightwave Technology **2**, 587-592 (1984).

50. A. M. Mailhota, A. Elyamania, and R. E. Rimana, "Reactive atmosphere synthesis of sol-gel heavy metal fluoride glasses," Journal of Materials Research **7**, 1534-1540 (1992).

51. J. Bei, T. M. Monro, A. Hemming, and H. Ebendorff-Heidepriem, "Reduction of scattering loss in fluoroindate glass fibers," Optical Materials Express **3**, 1285-1301 (2013).

52. G. E. Snopatin, V. S. Shiryaev, V. G. Plotnichenko, E. M. Dianov, and M. F. Churbanov, "High-purity chalcogenide glasses for fiber optics," Inorganic Materials **45**, 1439-1460 (2009).

53. G. E. Snopatin, M. F. Churbanov, A. A. Pushkin, V. V. Gerasimenko, E. M. Dianov, and V. G. Plotnichenko, "High purity arsenic-sulfide glasses and fibers with minimum attenuation of 12 dB/km," Optoelectronics and Advanced Materials **3**, 669-671 (2009).

54. E. M. Dianov, V. G. Plotnichenko, Y. N. Pyrkov, I. V. Smol'nikov, S. A. Koleskin, G. G. Devyatykh, M. F. Churbanov, G. E. Snopatin, I. V. Skripachev, and R. M. Shaposhnikov, "Single-mode As-S glass fibers," Inorganic Materials **39**, 627-630 (2003).

55. M. F. Churbanov, V. S. Shiryaev, I. V. Skripachev, G. E. Snopatin, V. G. Pimenov, S. V. Smetanin, R. M. Shaposhnikov, I. E. Fadin, Y. N. Pyrkov, and V. G. Plotnichenko, "High-purity $As_2S_{1.5}Se_{1.5}$ glass optical fibers," Inorganic Materials **38**, 193-197 (2002).

56. V. S. Shiryaev, C. Boussard-Plédel, P. Houizot, T. Jouan, J. L. Adam, and J. Lucas, "Single-mode infrared fibers based on TeAsSe glass system," Materials Science and Engineering: B **127**, 138-143 (2006).
57. J. S. Sanghera, V. Q. Nguyen, P. C. Pureza, F. H. Kung, R. Miklos, and I. D. Aggarwal, "Fabrication of low-loss IR-transmitting $Ge_{30}As_{10}Se_{30}Te_{30}$ glass fibers," Journal of Lightwave Technology **12**, 737-741 (1994).
58. V. S. Shiryaev, M. F. Churbanov, E. M. Dianov, V. G. Plotnichenko, J.-L. Adam, and J. Lucas, "Recent propgress in preparation of chalcogenide As-Se-Te glasses with low impurity content," Journal of Optoelectronics and Advanced Materials **7**, 1773 - 1779 (2005).
59. G. G. Devyatykh, E. M. Dianov, V. G. Plotnichenko, A. A. Pushkin, Y. N. Pyrkov, I. V. Skripachev, G. E. Snopatin, M. F. Churbanov, and V. S. Shiryaev, "Low-loss infrared arsenic-chalcogenide glass optical fibers," SPIE Proceedings on Advances in Fiber Optics **4083**, 229 (2000).
60. V. S. Shiryaev, J. L. Adam, X. H. Zhang, C. Boussard-Plédel, J. Lucas, and M. F. Churbanov, "Infrared fibers based on Te-As-Se glass system with low optical losses," Journal of Non-Crystalline Solids **336**, 113-119 (2004).
61. M. F. Churbanov, G. E. Snopatin, V. S. Shiryaev, V. G. Plotnichenko, and E. M. Dianov, "Recent advances in preparation of high-purity glasses based on arsenic chalcogenides for fiber optics," Journal of Non-Crystalline Solids **357**, 2352-2357 (2011).
62. G. A. Thomas, B. I. Shraiman, P. F. Glodis, and M. J. Stephen, "Towards the clarity limit in optical fibre," Nature **404**, 262-264 (2000).
63. K. Itoh, H. Yanagita, H. Tawarayama, K. Yamanaka, E. Ishikawa, K. Okada, H. Aoki, Y. Matsumoto, A. Shirakawa, Y. Matsuoka, and H. Toratani, "Pr^{3+} doped InF3/GaF3 based fluoride glass fibers and Ga-Na-S glass fibers for light amplification around 1.3 μm," Journal of Non-Crystalline Solids **256-257**, 1-5 (1999).
64. H. Nasu, O. Matsushita, K. Kamiya, H. Kobayashi, and K. i. Kubodera, "Third harmonic generation from Li_2O-TiO_2-TeO_2 glasses," Journal of Non-Crystalline Solids **124**, 275-277 (1990).
65. I. Fanderlik, *Optical Properties of Glass, Glass Science and Technology* (Elsevier, Amsterdam, 1983).
66. S.-H. Kim, and T. Yoko, "Nonlinear optical properties of TeO_2-based glasses: MOx-TeO_2 (M = Sc, Ti, V, Nb, Mo, Ta, and W) binary glasses," Journal of the American Ceramic Society **78**, 1061-1065 (1995).

67. U. Hoppe, E. Yousef, C. Russel, J. Neuefeind, and A. C. Hannon, "Structure of zinc and niobium tellurite glasses by neutron and x-ray diffraction," Journal of Physics : Condensed Matter **16**, 1645–1663 (2004).
68. F. E. P. d. Santos, F. C. Fávero, A. S. L. Gomes, J. Xing, Q. Chen, M. Fokine, and I. C. S. Carvalho, "Evaluation of the third-order nonlinear optical properties of tellurite glasses by thermally managed eclipse Z-scan," Journal of Applied Physics **105**, 024512: 1-4 (2009).
69. R. F. Souza, M. A. R. C. Alencara, J. M. Hickmann, R. Kobayashi, and L. R. P. Kassab, "Femtosecond nonlinear optical properties of tellurite glasses," Journal of Applied Physics **89**, 171917: 1-3 (2006).
70. S.-H. Kim, "Nonlinear optical properties of TeO_2-based glasses: Li(Na and $K)_2O–TeO_2$ binary glasses," Journal of Materials Research **14**, 1074-1083 (1999).
71. F. Smektala, C. Quemard, L. Leneindre, J. Lucas, A. Barthélémy, and C. De Angelis, "Chalcogenide glasses with large non-linear refractive indices," Journal of Non-Crystalline Solids **239**, 139-142 (1998).
72. S. Cherukulappurath, M. Guignard, C. Marchand, F. Smektala, and G. Boudebs, "Linear and nonlinear optical characterization of tellurium based chalcogenide glasses," Optics Communications **242**, 313-319 (2004).
73. L. Petit, "Amplification optique dans des verres borophosphate de niobium et tellurite dopés aux ions de terres rares présentant un indice optique non linéaire élevé," PhD in *Université Sciences et Technologies - Bordeaux I* (Univertité de Bordeaux I, France, 2002).
74. M. H. Frosz, P. Falk, and O. Bang, "The role of the second zero-dispersion wavelength in generation of supercontinua and bright-bright soliton-pairs across the zero-dispersion wavelength: erratum," Optics Express **15**, 5262-5263 (2007).
75. M. H. Frosz, O. Bang, and A. Bjarklev, "Soliton collision and Raman gain regimes in continuous-wave pumped supercontinuum generation," Optics Express **14**, 9391-9407 (2006).
76. A. Apolonski, B. Povazay, A. Unterhuber, W. Drexler, W. J. Wadsworth, J. C. Knight, and P. S. J. Russell, "Spectral shaping of supercontinuum in a cobweb photonic-crystal fiber with sub-20-fs pulses," Journal of the Optical Society of America B **19**, 2165-2170 (2002).
77. G. Genty, M. Lehtonen, H. Ludvigsen, and M. Kaivola, "Enhanced bandwidth of supercontinuum generated in microstructured fibers," Optics Express **12**, 3471-3480 (2004).

78. M. Liao, W. Gao, T. Cheng, Z. Duan, X. Xue, H. Kawashima, T. Suzuki, and Y. Ohishi, "Ultrabroad supercontinuum generation through filamentation in tellurite glass," Laser Physics Letters **10**, 036002 (2013).

79. M. Liao, W. Gao, T. Cheng, X. Xue, Z. Duan, D. Deng, H. Kawashima, T. Suzuki, and Y. Ohishi, "Five-Octave-Spanning Supercontinuum Generation in Fluoride Glass," Applied Physics Express **6**, 032503 (2013).

80. D. D. Hudson, S. A. Dekker, E. C. Mägi, A. C. Judge, S. D. Jackson, E. Li, J. S. Sanghera, L. B. Shaw, I. D. Aggarwal, and B. J. Eggleton, "Octave spanning supercontinuum in an As_2S_3 taper using ultralow pump pulse energy," Optics Letters **36**, 1122-1124 (2011).

81. M. Szpulak, and S. Février, "Chalcogenide As_2S_3 suspended core fiber for Mid-IR wavelength conversion based on degenerate four-wave mixing," IEEE Photonics Technology Letters **21**, 884-886 (2009).

82. Y. Yu, X. Gai, T. Wang, P. Ma, R. Wang, Z. Yang, D.-Y. Choi, S. Madden, and B. Luther-Davies, "Mid-infrared supercontinuum generation in chalcogenides," Optical Materials Express **3**, 1075-1086 (2013).

83. G. Qin, X. Yan, C. Kito, M. Liao, C. Chaudhari, T. Suzuki, and Y. Ohishi, "Ultrabroadband supercontinuum generation from ultraviolet to 6.28μm in a fluoride fiber," Applied Physics Letters **95**, 161103 (2009).

84. P. Domachuk, N. A. Wolchover, M. Cronin-Golomb, A. Wang, A. K. George, C. M. B. Cordeiro, J. C. Knight, and F. G. Omenetto, "Over 4000 nm bandwidth of mid-IR supercontinuum generation in sub-centimeter segments of highly nonlinear tellurite PCFs," Optics Express **16**, 7161-7168 (2008).

85. R. R. Gattass, L. Brandon Shaw, V. Q. Nguyen, P. C. Pureza, I. D. Aggarwal, and J. S. Sanghera, "All-fiber chalcogenide-based mid-infrared supercontinuum source," Optical Fiber Technology **18**, 345-348 (2012).

86. M. R. Lamont, B. Luther-Davies, D.-Y. Choi, S. Madden, and B. J. Eggleton, "Supercontinuum generation in dispersion engineered highly nonlinear (γ = 10/W/m) As_2S_3 chalcogenide planar waveguide," Optics Express **16**, 14938-14944 (2008).

87. M. El-Amraoui, J. Fatome, J. C. Jules, B. Kibler, G. Gadret, C. Fortier, F. Smektala, I. Skripatchev, C. F. Polacchini, Y. Messaddeq, J. Troles, L. Brilland, M. Szpulak, and G. Renversez, "Strong infrared spectral broadening in low-loss As-S chalcogenide suspended core microstructured optical fibers," Optics Express **18**, 4547-4556 (2010).

88. M. El-Amraoui, G. Gadret, J. C. Jules, J. Fatome, C. Fortier, F. Désévédavy, I. Skripatchev, Y. Messaddeq, J. Troles, L. Brilland, W. Gao, T. Suzuki, Y. Ohishi, and F.

Smektala, "Microstructured chalcogenide optical fibers from As_2S_3 glass: towards new IR broadband sources," Optics Express **18**, 26655-26665 (2010).

Part 2 :Mid-Infrared Supercontinuum Generation In As_2S_3 Microstructured Optical Fibers

I. Introduction

Supercontinuum generation (SCG) describes a process, in which, the spectrum of a narrow bandwidth incident pulse undergoes a substantial spectral broadening through the interplay of various nonlinear processes, as it propagates throughout a nonlinear medium. Supercontinuum (SC) generation was first reported in the early 1970s in bulk by Alfano and Shapiro [1]. Six years later, Lin and Stolen [2] reported on the first continuum in glass fiber. Ever since, broadband SC generation in optical fibers is of particular interest because of the optical fibers' unique advantages in their pump interactions with the nonlinearities of the fiber materials. Over the past decade, the introduction of special fibers, and in particular photonic crystal fibers have enabled major strides in obtaining a broad continuum, leading to development of compact and efficient broadband sources [3-7]. SC generation in MOFs has found potential applications in such diverse fields as spectroscopy, metrology, telecommunication or biology [8, 9].

Continuum generation has been demonstrated in silica photonic crystal fiber in the visible and near infrared. Broadband sources based on silica photonic crystal fibers operating from visible to near-infrared range have been already commercialized. However, further extension of the SC infrared edge is a challenging task due to the multiphonon absorption of the silica glass network, which limits the transmission window in the infrared. Consequently, supercontinuum spectra have only been able to span to about 2.2 µm [10, 11].

A high power mid-IR SC source operating in the atmospheric transmission windows that lie between 3-5 µm and 8-12 µm, has numerous applications in the field of IR such as biology, sensing, spectroscopy, and other fields. Thus, the recent trend is to provide alternative materials so as to spread further the SC in the mid-infrared (MIR) region. However, to generate SC spectrum in the MIR region, optical fibers of low optical losses in the corresponding wavelength range and suitable nonlinearity are required. For instance, there have been several demonstrations of mid-IR supercontinuum generation using chalcogenide, fluoride, and tellurite-based optical fibers [11-24]. However, the intrinsic multiphonon absorption edge in fluoride and tellurite glasses remains the main limitation of further spanning of the continuum MIR edge [25]. Partial overcoming of the limitations due to multiphonon absorption edge has been demonstrated in tellurite [12-15] and fluoride fibres [26] using short lengths of fibre and high pump power.

Chalcogenide glasses (ChGs) stand out as the only family of vitreous materials that are widely transparent across the infrared on both, bulk and fiber forms [27]. Moreover, ChGs exhibit relatively high linear refractive index (n_0) giving rises to highest nonlinear refractive index (n_2) of glass systems. According to glass composition, it might be 1000 times higher than silica [10, 11].

Although ChG fibers were first demonstrated decades ago, and have since found uses in a wide range of linear and nonlinear infrared applications [28-30], the first guiding ChG PCFs were reported in 2006 [31]. This delay was in large part due to several limitations, in particular their high normal group velocity dispersion (GVD) [11], since their material's zero dispersion wavelength (ZDW) is located far in the MIR, above 5µm [11]. In some applications such as supercontinuum generation, the GVD sign and magnitude play a crucial role, and hence must be precisely controlled [7]. In order to overcome these limitations in ChGs and allow broad spectrum spanning, novel approaches and fiber designs are proposed. Among the various proposed strategies, microstructured fibers [32-34] have shown promising potentials and results. One of the attractive features of microstructured fibers is their greater tolerance in tailoring various fiber properties. The main advantage of microstructured fibers is that they enable GVD engineering in order to compensate the material-GVD [16, 35]. Adopting adequate microstructured pattern allows to adapt the ZDW to suitable pump wavelength and to reduce the effective mode area, enhancing consequently the nonlinear interaction for efficient SCG [11, 16, 36]. In addition, because suspended-core microstructured fiber can be made from a single material, it is possible to eliminate the problems potentially caused by the core-cladding interface of two different glasses.

As_2S_3-based chalcogenide glass fibers are highly suitable for the purpose aimed from this work. Although other chalcogenide-based system can be used as long as it is highly nonlinear and meets other prerequisites, it has been determined that As_2S_3-system is the composition of choice for purposes herein. As_2S_3 glass has linear refractive index n_0 of 2.44 at 1.55 µm, nonlinear refractive index n_2 100 times higher than silica, around 594×10^{-20} m^2/W [11], material ZDW around 5 µm, and the fibre MIR transmission edge is located at 7.4 µm [11].

However, in order to achieve efficient supercontinuum generation, a number of conditions must be met, as among the others: sufficiently high power density within the waveguide, and low optical losses, typically less than 1 dB/m. To harness the intrinsic As_2S_3 glass and respond the need for efficient SC generation, low loss microstructured glasses fibers are elaborated. Adequate microstructure pattern are adopted to manage the modal dispersion of the fiber device. The MOFs are conceived to shift their corresponding ZDW to the 2.0-2.5 µm range, which correspond to the maximum emission range of the pump source, systematically used for non-linear experiment in this work. This source consists in an optical parametric oscillator (OPO) pumped by a Ti:Sapphire laser, and tunable from 1.7 to 2.55 µm, available with our colleagues from TTI, in Japan.

In this part, we present some of the nonlinear optics experiments we have conducted during this PhD period. More specifically, each following article of this part is dedicated to address one particular challenge or present one major improvement we have achieved in developing the mid-IR SC light source in As_2S_3 MOFs.

In Article 1, we describe a mid-IR supercontinuum generation in low loss As_2S_3 suspended-core microstructured optical fibers as well as in tellurite fibers. Sulfide ones are to be considered in the framework of this work. The continuum spreads over 2000 nm, from 1.2 µm up to 3.2 µm. The fiber specimen was pumped close to the zero-dispersion wavelength in the femtosecond regime by means of an optical parametric oscillator pumped by a Ti: Sapphire laser. In addition, we report comprehensive numerical simulations to assign the nonlinear effects responsible for the above spectral spanning, as to define the limitations of further MIR expansion of the spectrum long wavelength edge. We presumed aging phenomenon that prevent to fit the experimental results with theoretical ones.

In Article 2, we demonstrate an enhanced and flat 3500 nm SC spanning in As_2S_3 MOF subjected to protection procedures from the presumed aging phenomenon previously described in Article 1. A preventive storage strategy is used to control the surrounding atmosphere at which the chalcogenide MOFs are exposed prior to nonlinear optics (NLO) experiments. The MOF is pumped in the anomalous dispersion regime close to its zero-dispersion, using the same pump source and quite similar seed energy (~1nJ/pulse) as in Article 1. As_2S_3 fibers with comparable geometric design and optical loss level as described in

Article 1 are used in the experiments. The SC spectrum extends into the mid-IR from ~0.6 µm to beyond 4.0 µm, which is consistent with the extrinsic SH absorption band located at 4.0 µm.

In Article 3, we report a detailed theoretical study of fiber aging impact on the spectrum broadening, especially the position of MidIR SC edge. The later study relies on numerical simulations based on the generalized nonlinear Schrödinger equation. It is confirmed by the obtained good agreement with the experimental results reported in article 1. A general overview on the extinction of the transmission spectrum, the evolution of surface roughness, and the change in chemical composition of microstructured fiber due to aging processes are also briefed in this paper.

II. Glass Synthesis, Preform fabrication and Fiber drawing

As preamble to the articles, the experimental part concerning As_2S_3 glass preparation and optical fibers drawing used for this study is presented.

II.1 Synthesis of bulk.

The As_2S_3 glasses were prepared by the conventional melt-quenching technique inside a vacuum-sealed silica ampoule in order to maintain the composition's stoichiometric since the sulfur exhibit high volatility at the synthesis temperature. In addition, as for all the chalcogenide glasses, syntheses are performed under secondary vacuum in order to avoid the pollution by the water and oxygen naturally present in atmosphere.

The experimental system designed in this context is described in Figure 24. It comprises a turbo molecular pumping group providing a high vacuum around 10^{-6} mbar, liquid nitrogen trap and silica glassware. Prior to each experiment, the inner surface of the glassware is cleaned by sequential washing by hydrofluoric acid and de-ionized water, before being connected to the vacuum system to be well dried at room temperature. The objective of this treatment is to eliminate loosely held SiO_2 particles on the inner tube surface which may cause scattering losses, causing a high attenuation of the transmission in the short wavelength range. The glassware is made from high-purity Silica, (Ilmasil), with OH content below 5 ppm. The nitrogen trap allows to protect the pump by trapping any volatile species coming from the starting products.

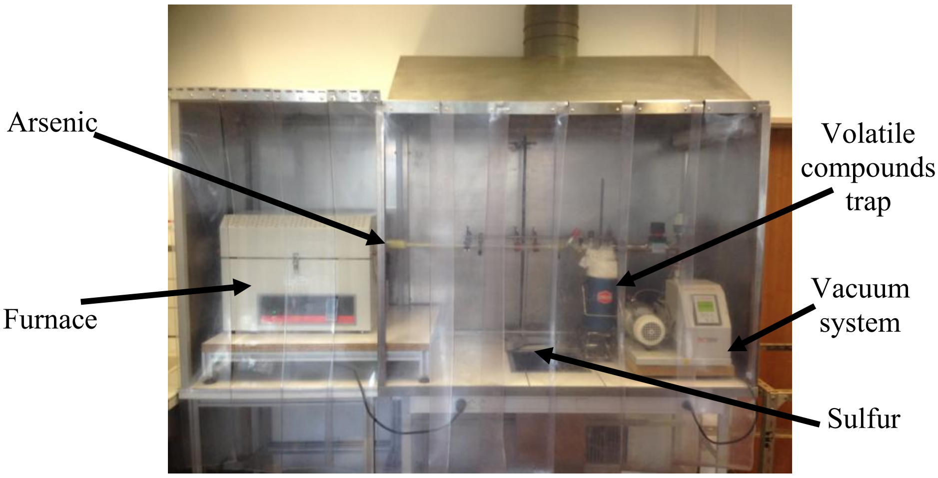

Figure 24: Glass synthesis set-up

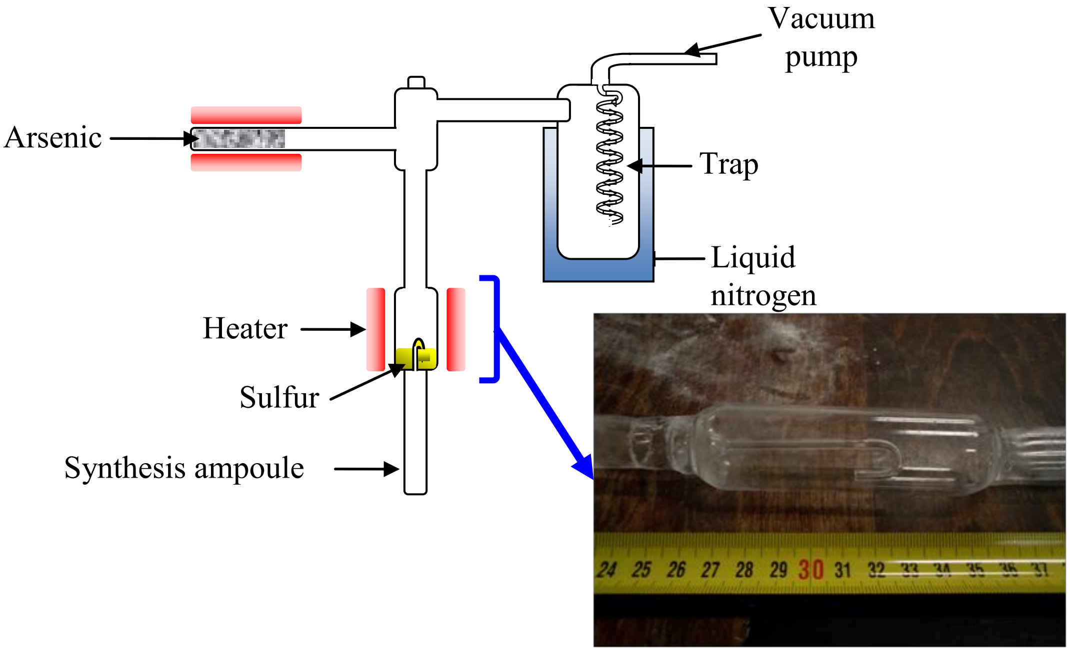

Figure 25: Schematic illustration of the synthesis set-up. Inset a photo of the capillary container.

The sulfur is introduced into the container comprising a small capillary (Figure 25 and Figure 26) while arsenic is placed in the second ampoule (Figure 24 and Figure 25). High purity elemental arsenic and sulfur (5N) reagents used in these experiments were of analytical grade purity. The quoted purity levels are based on the metallic content only. In this figure, content of oxygen, hydrogen, carbon and surface deposits are not taken into account. Since the purpose of this job is to fabricate a high purity glasses, the starting products are purified by thermal treatment from their respective impurities under a dynamic vacuum (10^{-6} mbar).

After that the necessary vacuum (10^{-6} mbar) is established, the charges are separately purified by thermal treatment. The purification of arsenic consists in heating ampoule with charge at 290°C for several hours in order to remove volatile inclusions such as moisture, oxides and gases adsorbed by charge materials. Heating temperature correspond to the arsenic oxide sublimation point (T_{sub}=290°C) [37], thereby removing As_2O_3 and As_2O_5 from the surface. On the other hand, purification of sulfur consists in heating in a dynamic vacuum to its melting point (T_f =120°C). The evaporated sulfur condenses on the walls of the silica glassware locally cooled using a cooler (Figure 26-1), while the most volatile impurities such as water are removed by the pumping system. Once all of the sulfur is condensed in the upper part of the glassware, they are melted down to be collected in their original container (Figure 26-2). This corresponds to a cycle of distillation of sulfur. We can then continue to perform multiple distillations in order to remove every time the persistent residual impurities. Figure 26 presents the sequence followed in this job.

At the end of this step, the arsenic is transferred into the ampoule containing the sulfur, the set-up is then sealed at the point #1 (Figure 26-2), and fed into a furnace for mixture purification under statistic vacuum (Figure 27). Distillation was performed by heating the upper portion of the tube to 480°C and the lower portion was kept at room temperature. At these temperatures, the As and S were volatilized in the upper portion and condensed in the lower portion over a period between 16 and 24 h. This allows us to isolate carbon and non-volatile impurities in the upper portion of the tube. Corresponding temperature profile is shown on Figure 28.

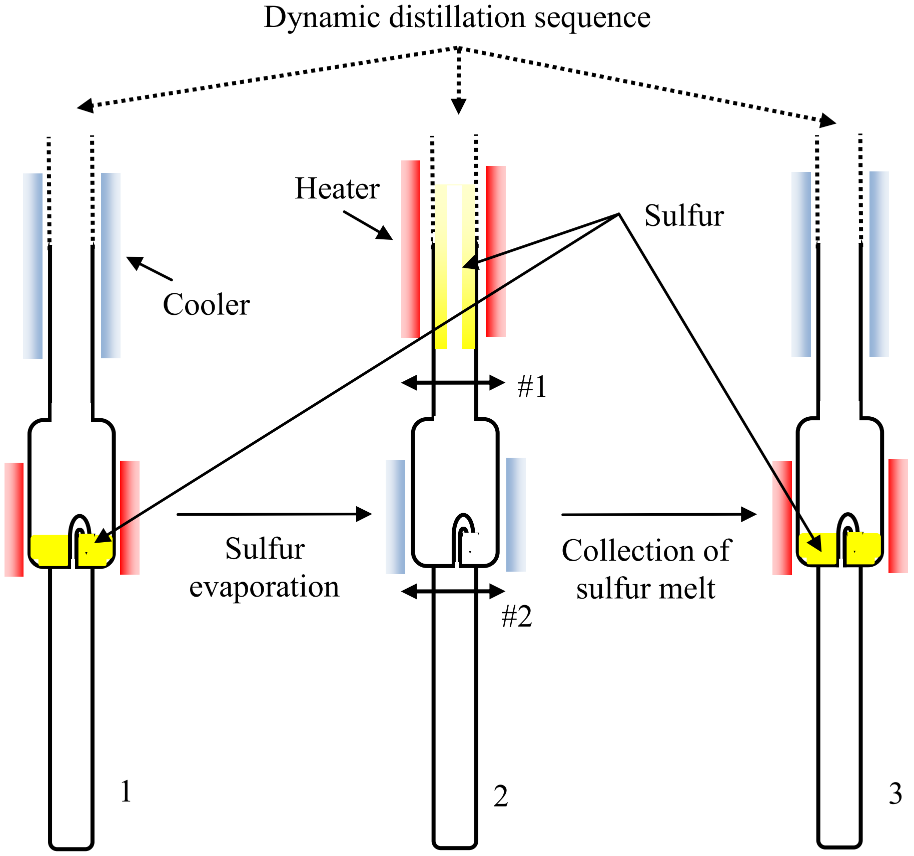

Figure 26: Sulfur multi-distillation process.

The distillate is collected in the mixing synthesis ampoule (Figure 27). Again, the set-up is sealed at the point #2 (Figure 26-2).

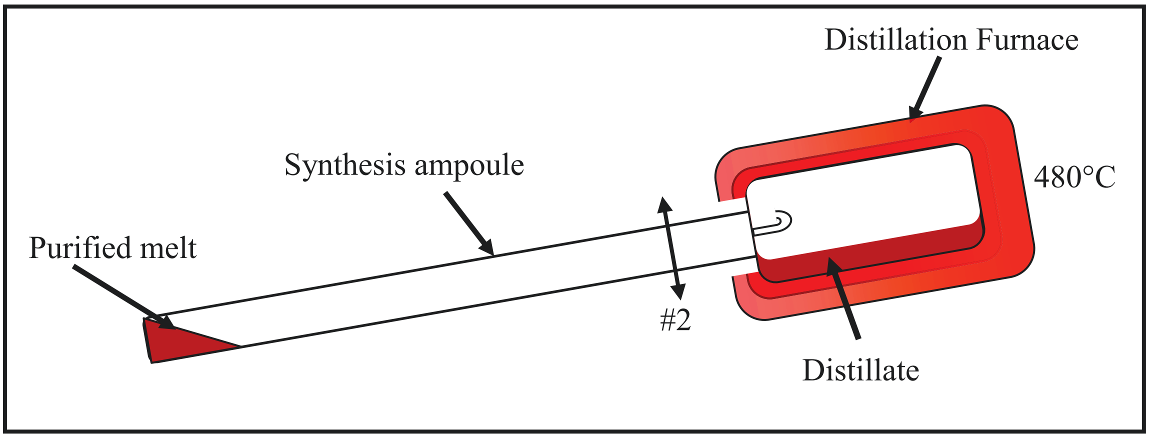

Figure 27: Schematic of the inclined furnace synthesis ampoule system

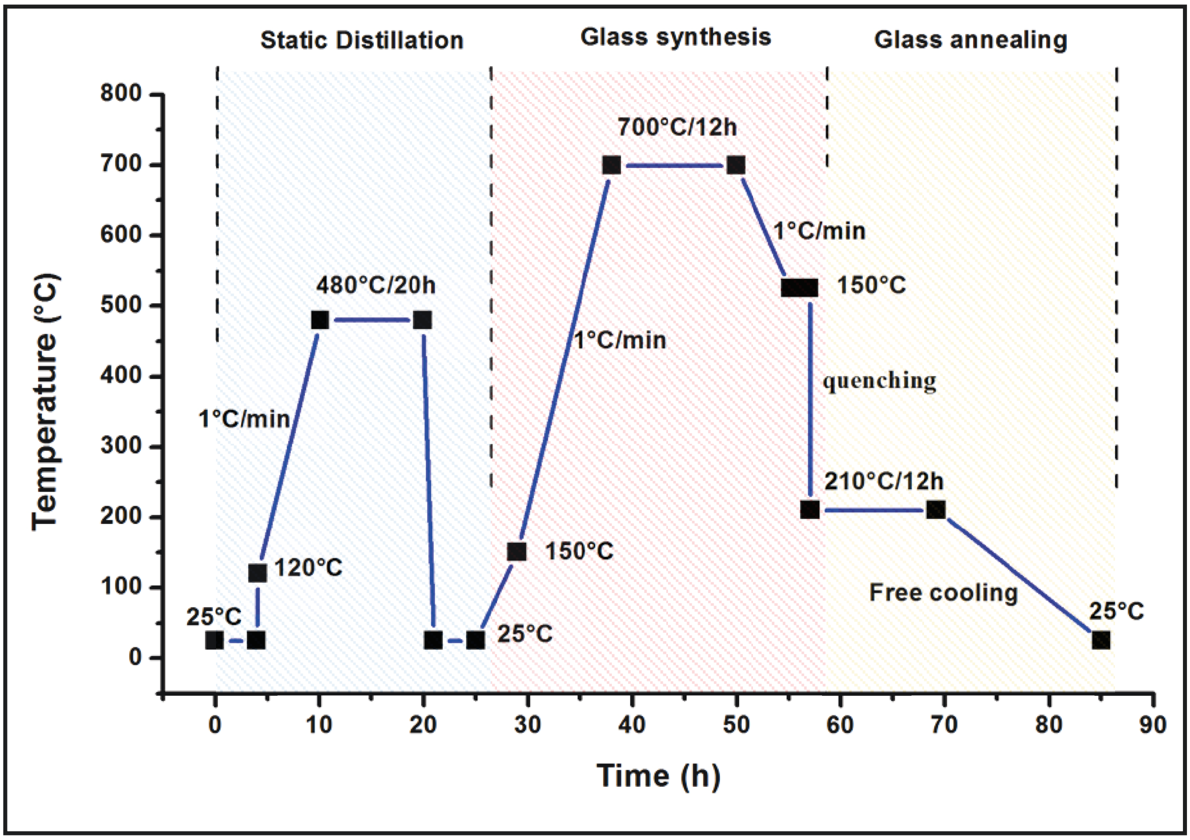

Figure 28: Temperature-time schedule applied during sulfur static distillation, glass synthesis and batch annealing processes.

The synthesis process is carried out in special rotating electric furnace. The melt is held at 700°C for several hours, until glass-forming comes to the end. Glass homogenizing is carried out by rotating the furnace about the minor axis. After the last mixing, the furnace is placed vertically, cooled down, and maintained at 525°C for several minutes, it leads to increase glass viscosity and reduce the steam above the melt. At this point, the melt is quenched in water at room temperature to solidify the liquid in the vitreous state. The time-temperature schedule adopted during the synthesis process is presented on Figure 28.

Mechanical stress in the amorphous medium makes it mechanically fragile. Thus, thermal treatment at adequate point around (210°C) glass transition temperature is necessary for stress relieving. Corresponding time-temperature regime is shown in Figure 28.

II.2 Preform elaboration.

The stack and draw technique is the most commonly used to fabricate most of the microstructured optical fibers. It is based on stacking of fiber capillaries and it is systematically used to fabricate silica-based microstructured fibers. However, the use of materials of lower glass transition temperature (Tg) such as heavy metal oxides and polymers enables the use of other techniques such as extrusion and drilling.

In the frame of our work, the mechanical drilling technique was used for the preparation of glass preforms with a variety of geometrical patterns in view of MOFs drawing. This technique was previously developed on chalcogenide glasses in our laboratory [16]. It consists to drill holes in the chalcogenide glass rod. The position of the holes as well as the thickness of bridges between two neighboring holes are precisely controlled. This technique has allowed to prepare versatile patterned preforms [16]. Preform design adopted in this work consist in three holes placed in a triangular arrangement around a solid core. For all these preforms, the outer diameter is 16 mm, the diameter of holes is equal to 0.8 mm and their length to about 30 mm. The cross-section images of the elaborated glass preform is presented in Figure 29.

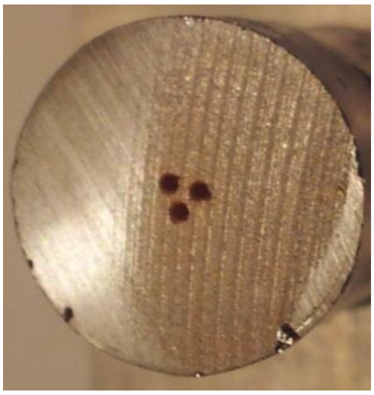

Figure 29: Cross section profile of preform design adopted in this work.

II.3 Fiber drawing.

The drawing of glass fibers is governed by the force of gravity or by a mechanical tension applied on a glass rod vertically suspended, and sufficiently softened to be able to drawing. Hence the need for a heat source to enable the melting and deformation of glass. Figure 30-right represents the various elements from which a drawing tower is composed. The translation system allows a continuous and controlled vertical penetration of the glass preform inside the heating zone. The furnace provides a localized and symmetric heating zone, optimal for drawing process. The inert gas is used to continuously purge the interior of the furnace. It forms a protective curtain avoiding the diffusion of the unsuitable oxidizing atmosphere inside the heating zone. The pressurized inert gas allows to avoid the collapse of the microstructure and to control the holes dimension upon drawing. The diameter and tension measurement devices allow to monitor the fiber diameter and the drawing force.

Prior the heating, the furnace is purged for several hours by a flow of nitrogen (or helium), in order to remove traces of moisture present in the chamber and on the preform's surface. This flow is maintained throughout the fiber drawing process.

A heating rate of 10 ° C / min maintained until the softening temperature of the glass (T>Tg), causes the formation of a droplet of glass at the lower end of the glass rod. Under the effect of gravity, the droplet fall downward, shrink in diameter into a fine-diameter filament and gives a glass fiber, subsequently fixed on the winding drum. A schematic illustration of this process is displayed in Figure 30-left.

The parameters of drawing process (core and fiber diameter, drum speed and perform speed) were determined before the experimental step by means of the dimensions of the preform and the desired fiber. During drawing, the mass conservation principle is respected. The consumed preform's volume is equal to the volume of the drawn fiber.

The diameter of the fiber is controlled by two parameters:

- The speed of penetration of the preform inside the heating zone: by increasing the speed of penetration, we increase the amount of material inside the furnace, and thus the diameter of the fiber and vice versa.
- The winding speed of the drum: by increasing the speed of rotation of the drum, we decrease the diameter of the fiber and vice versa.

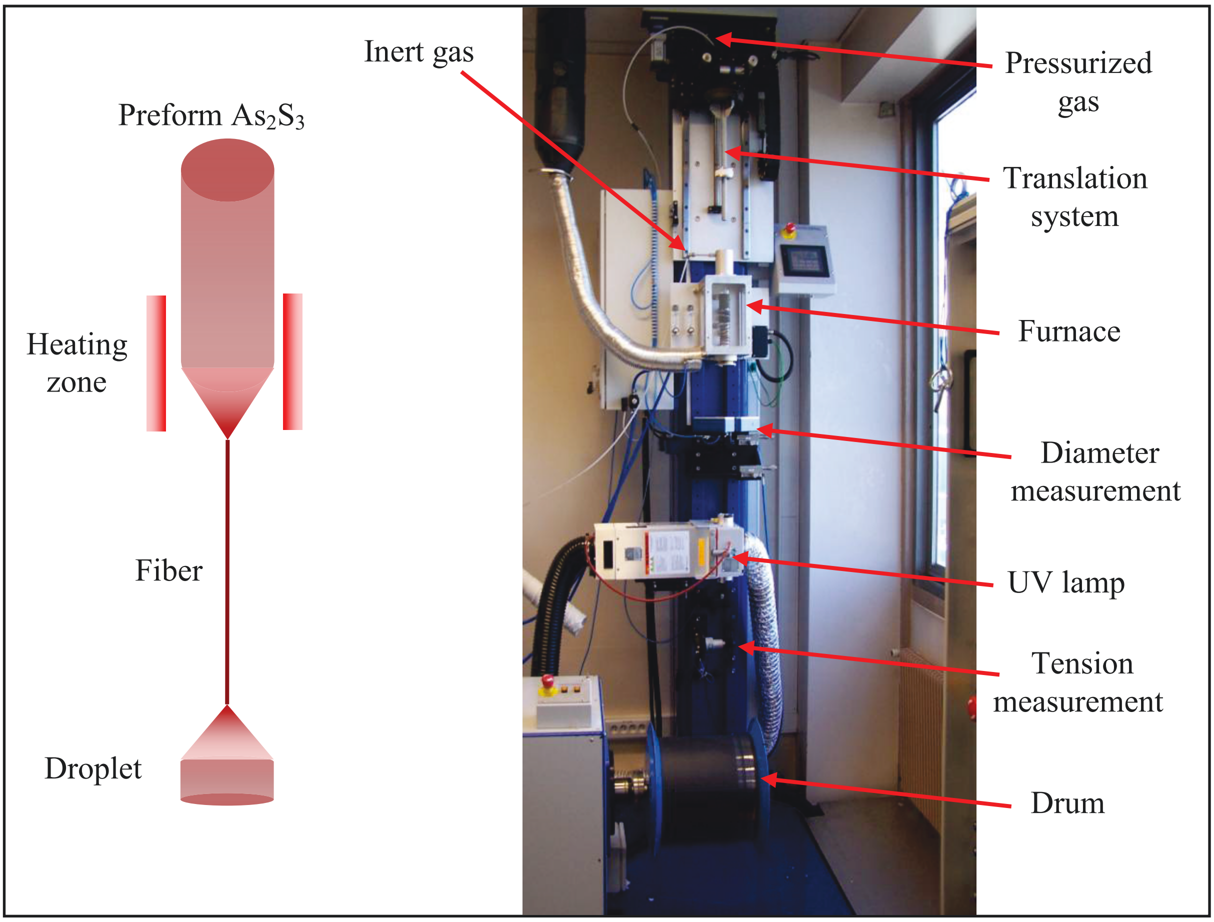

Figure 30: Glass rod geometrical evolution during drawing process (left) and drawing tower (right).

Following drawing process of the preform's design adopted in this work, resulting microstructured fiber consists in a triangular lattice of air holes which extend along the fiber. They surround a small central core with triangle geometry attached to robust jacket by three thin struts. Figure 31 shows the general cross section profile of the MOFs drawn from the preforms obtained using the mechanical drilling technique (Figure 29).

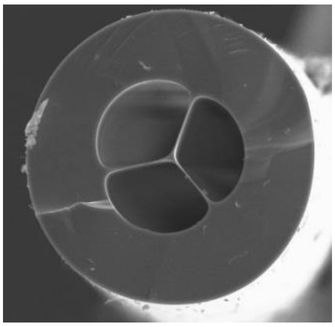

Figure 31: Geometric profile of the chalcogenide As_2S_3 suspended-core fiber captured by means of a scanning electron microscope drawn from the preform depicted in Figure 29.

III. References

1. R. R. Alfano, and S. L. Shapiro, "Emission in the region 4000 to 7000 Å via four-photon coupling in glass," Physical Review Letters **24**, 584-587 (1970).
2. C. Lin, and R. H. Stolen, "New nanosecond continuum for excited-state spectroscopy," Applied Physics Letters **28**, 216-218 (1976).
3. A. L. Gaeta, "Nonlinear propagation and continuum generation in microstructured optical fibers," Optics Letters **27**, 924-926 (2002).
4. M.-L. V. Tse, P. Horak, F. Poletti, N. G. Broderick, J. H. Price, J. R. Hayes, and D. J. Richardson, "Supercontinuum generation at 1.06 µm in holey fibers with dispersion flattened profiles," Optics Express **14**, 4445-4451 (2006).
5. B. Eggleton, C. Kerbage, P. Westbrook, R. Windeler, and A. Hale, "Microstructured optical fiber devices," Optics Express **9**, 698-713 (2001).
6. G. Genty, S. Coen, and J. M. Dudley, "Fiber supercontinuum sources (Invited)," Journal of the Optical Society of America B **24**, 1771-1785 (2007).
7. J. M. Dudley, and J. R. Taylor, *Supercontinuum Generation in Optical Fibers* (Cambridge University, 2010).
8. D. M. Brown, K. Shi, Z. Liu, and C. R. Philbrick, "Long-path supercontinuum absorption spectroscopy for measurement of atmospheric constituents," Optics Express **16**, 8457-8471 (2008).
9. L. Zhang, Q. Lin, Y. Yue, Y. Yan, R. G. Beausoleil, and A. E. Willner, "Silicon waveguide with four zero-dispersion wavelengths and its application in on-chip octave-spanning supercontinuum generation," Optics Express **20**, 1685-1690 (2012).
10. R. E. Slusher, G. Lenz, J. Hodelin, J. Sanghera, L. B. Shaw, and I. D. Aggarwal, "Large Raman gain and nonlinear phase shifts in high-purity As_2Se_3 chalcogenide fibers," Journal of the Optical Society of America B **21**, 1146-1155 (2004).
11. J. H. V. Price, T. M. Monro, H. Ebendorff-Heidepriem, F. Poletti, P. Horak, V. Finazzi, J. Y. Y. Leong, P. Petropoulos, J. C. Flanagan, G. Brambilla, F. Xian, and D. J. Richardson, "Mid-IR supercontinuum generation from nonsilica microstructured optical fibers," IEEE Journal of Selected Topics in Quantum Electronics **13**, 738-749 (2007).
12. V. V. R. K. Kumar, A. George, J. Knight, and P. Russell, "Tellurite photonic crystal fiber," Optics Express **11**, 2641-2645 (2003).
13. P. Domachuk, N. A. Wolchover, M. Cronin-Golomb, A. Wang, A. K. George, C. M. B. Cordeiro, J. C. Knight, and F. G. Omenetto, "Over 4000 nm bandwidth of mid-IR supercontinuum generation in sub-centimeter segments of highly nonlinear tellurite PCFs," Optics Express **16**, 7161-7168 (2008).

14. M. Liao, C. Chaudhari, G. Qin, X. Yan, T. Suzuki, and Y. Ohishi, "Tellurite microstructure fibers with small hexagonal core for supercontinuum generation," Optics Express **17**, 12174-12182 (2009).

15. I. Savelii, J. C. Jules, G. Gadret, B. Kibler, J. Fatome, M. El-Amraoui, N. Manikandan, X. Zheng, F. Désévédavy, J. M. Dudley, J. Troles, L. Brilland, G. Renversez, and F. Smektala, "Suspended core tellurite glass optical fibers for infrared supercontinuum generation," Optical Materials **33**, 1661-1666 (2011).

16. M. El-Amraoui, G. Gadret, J. C. Jules, J. Fatome, C. Fortier, F. Désévédavy, I. Skripatchev, Y. Messaddeq, J. Troles, L. Brilland, W. Gao, T. Suzuki, Y. Ohishi, and F. Smektala, "Microstructured chalcogenide optical fibers from As_2S_3 glass: towards new IR broadband sources," Optics Express **18**, 26655-26665 (2010).

17. N. Granzow, S. P. Stark, M. A. Schmidt, A. S. Tverjanovich, L. Wondraczek, and P. S. J. Russell, "Supercontinuum generation in chalcogenide-silica step-index fibers," Optics Express **19**, 21003-21010 (2011).

18. D. D. Hudson, S. A. Dekker, E. C. Mägi, A. C. Judge, S. D. Jackson, E. Li, J. S. Sanghera, L. B. Shaw, I. D. Aggarwal, and B. J. Eggleton, "Octave spanning supercontinuum in an As_2S_3 taper using ultralow pump pulse energy," Optics Letters **36**, 1122---1124 (2011).

19. M. R. Lamont, B. Luther-Davies, D.-Y. Choi, S. Madden, and B. J. Eggleton, "Supercontinuum generation in dispersion engineered highly nonlinear (γ = 10/W/m) As_2S_3 chalcogenide planar waveguide," Optics Express **16**, 14938-14944 (2008).

20. R. Buczynski, H. T. Bookey, D. Pysz, R. Stepien, I. Kujawa, J. E. McCarthy, A. J. Waddie, A.K. Kar, and M.R. Taghizadeh, "Supercontinuum generation up to 2.5µm in photonic crystal fiber made of lead-bismuth-galate glass," Laser Physics. Letters. **7**, 666-672 (2010).

21. G. Qin, X. Yan, C. Kito, M. Liao, C. Chaudhari, T. Suzuki, and Y. Ohishi, "Supercontinuum generation spanning over three octaves from UV to 3.85 µm in a fluoride fiber," Optics Letters **34**, 2015-2017 (2009).

22. F. G. Omenetto, N. A. Wolchover, M. R. Wehner, M. Ross, A. Efimov, A. J. Taylor, V. V. R. K. Kumar, A. K. George, J. C. Knight, N. Y. Joly, and P. S. J. Russell, "Spectrally smooth supercontinuum from 350 nm to 3 µm in sub-centimeter lengths of soft-glass photonic crystal fibers," Optics Express **14**, 4928-4934 (2006).

23. C. Xia, M. Kumar, O. P. Kulkarni, M. N. Islam, J. F. L. Terry, M. J. Freeman, M. Poulain, and G. Mazé, "Mid-infrared supercontinuum generation to 4.5 µm in ZBLAN fluoride fibers by nanosecond diode pumping," Optics Letters **31**, 2553-2555 (2006).

24. C. Agger, C. Petersen, S. Dupont, H. Steffensen, J. K. Lyngsø, C. L. Thomsen, J. Thøgersen, S. R. Keiding, and O. Bang, "Supercontinuum generation in ZBLAN fibers-detailed comparison between measurement and simulation," Journal of the Optical Society of America B **29**, 635-645 (2012).
25. R. R. Gattass, L. Brandon Shaw, V. Q. Nguyen, P. C. Pureza, I. D. Aggarwal, and J. S. Sanghera, "All-fiber chalcogenide-based mid-infrared supercontinuum source," Optical Fiber Technology **18**, 345-348 (2012).
26. G. Qin, X. Yan, C. Kito, M. Liao, C. Chaudhari, T. Suzuki, and Y. Ohishi, "Ultrabroadband supercontinuum generation from ultraviolet to 6.28μm in a fluoride fiber," Applied Physics Letters **95**, 161103 (2009).
27. J. A. Savage, and S. Nielsen, "Chalcogenide glasses transmitting in the infrared between 1 and 20 µm a state of the art review," Infrared Physics **5**, 195-204 (1965).
28. J. S. Sanghera, L. B. Shaw, and I. D. Aggarwal, "Applications of chalcogenide glass optical fibers," Comptes Rendus Chimie **5**, 873-883 (2002).
29. V. Ta'eed, N. J. Baker, L. Fu, K. Finsterbusch, M. R. E. Lamont, D. J. Moss, H. C. Nguyen, B. J. Eggleton, D.-Y. Choi, S. Madden, and B. Luther-Davies, "Ultrafast all-optical chalcogenide glass photonic circuits," Optics Express **15**, 9205-9221 (2007).
30. T. M. Monro, S. Warren-Smith, E. P. Schartner, A. François, S. Heng, H. Ebendorff-Heidepriem, and S. Afshar V, "Sensing with suspended-core optical fibers," Optical Fiber Technology **16**, 343-356 (2010).
31. L. Brilland, F. Smektala, G. Renversez, T. Chartier, J. Troles, T. Nguyen, N. Traynor, and A. Monteville, "Fabrication of complex structures of Holey Fibers in Chalcogenide glass," Optics Express **14**, 1280-1285 (2006).
32. D. Mogilevtsev, T. A. Birks, and P. S. J. Russell, "Group-velocity dispersion in photonic crystal fibers," Optics Letters **23**, 1662-1664 (1998).
33. K. Saitoh, M. Koshiba, T. Hasegawa, and E. Sasaoka, "Chromatic dispersion control in photonic crystal fibers: application to ultra-flattened dispersion," Optics Express **11**, 843-852 (2003).
34. W. J. Wadsworth, A. Ortigosa-Blanch, J. C. Knight, T. A. Birks, T. P. M. Man, and P. S. J. Russell, "Supercontinuum generation in photonic crystal fibers and optical fiber tapers: a novel light source," Journal of the Optical Society of America B **19**, 2148-2155 (2002).
35. M. Liao, X. Yan, G. Qin, C. Chaudhari, and O. T. S. Yasutake, "Controlling the chromatic dispersion of soft glass highly nonlinear fiber through complex microstructure," Journal of Non-Crystalline Solids **356**, 2613-2617 (2010).

36. C. Chaudhari, T. Suzuki, and Y. Ohishi, "Design of zero chromatic dispersion chalcogenide As_2S_3 glass nanofibers," Journal of Lightwave Technology **27**, 2095-2099 (2009).

37. J. Douady, B. Boulanger, E. Fuchs, F. Smektala, and J. Troles, "Symmetry and phase-matching properties of third-harmonic generation under the photoelastic effect in Ge-As-Se chalcogenide glasses," Journal of the Optical Society of America B **22**, 1486-1492 (2005).

IV. Article 1

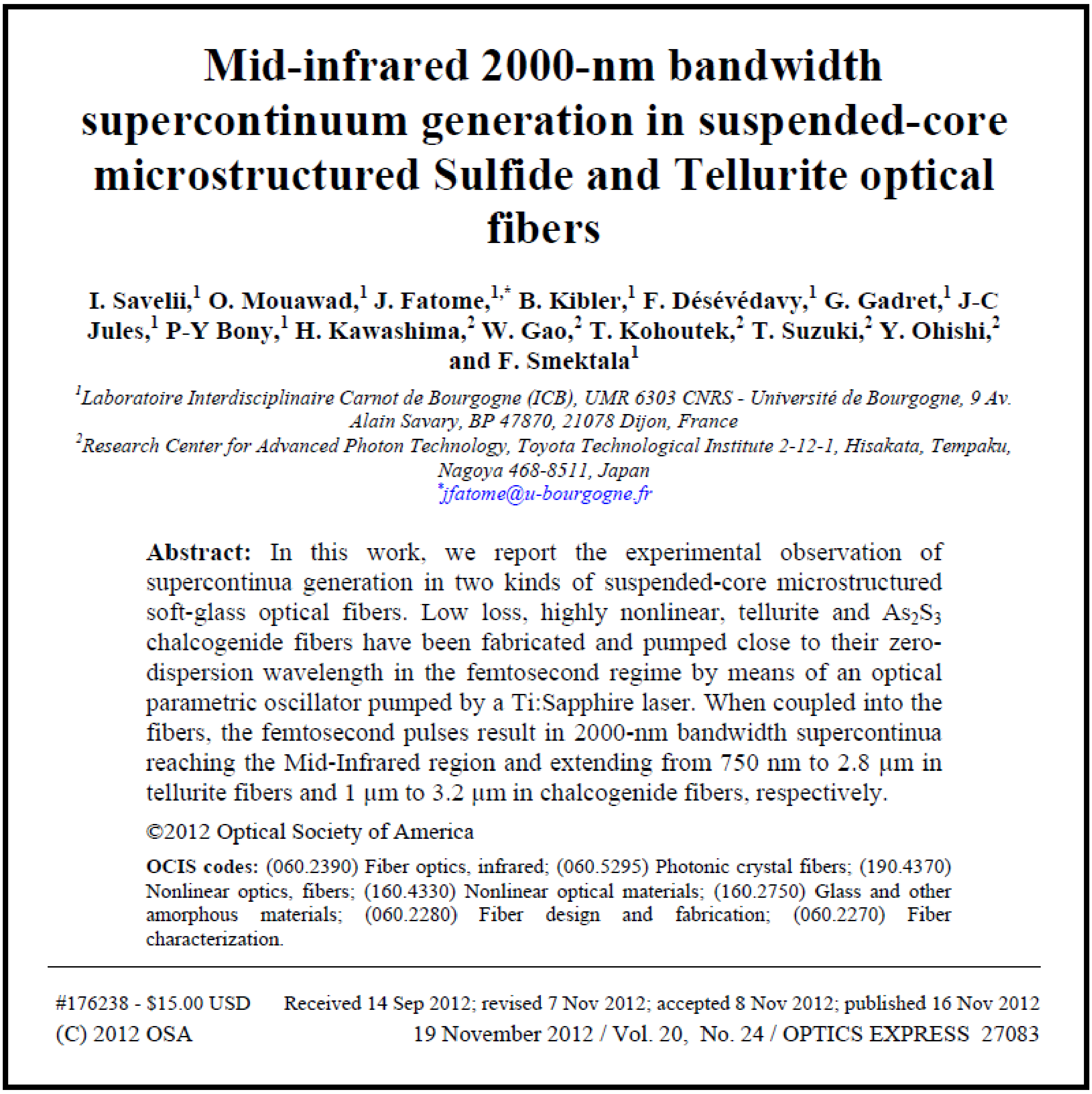

Mid-infrared 2000-nm bandwidth supercontinuum generation in suspended-core microstructured Sulfide and Tellurite optical fibers

I. Savelii,[1] O. Mouawad,[1] J. Fatome,[1,*] B. Kibler,[1] F. Désévédavy,[1] G. Gadret,[1] J-C Jules,[1] P-Y Bony,[1] H. Kawashima,[2] W. Gao,[2] T. Kohoutek,[2] T. Suzuki,[2] Y. Ohishi,[2] and F. Smektala[1]

[1]Laboratoire Interdisciplinaire Carnot de Bourgogne (ICB), UMR 6303 CNRS - Université de Bourgogne, 9 Av. Alain Savary, BP 47870, 21078 Dijon, France
[2]Research Center for Advanced Photon Technology, Toyota Technological Institute 2-12-1, Hisakata, Tempaku, Nagoya 468-8511, Japan
[*]jfatome@u-bourgogne.fr

Abstract: In this work, we report the experimental observation of supercontinua generation in two kinds of suspended-core microstructured soft-glass optical fibers. Low loss, highly nonlinear, tellurite and As$_2$S$_3$ chalcogenide fibers have been fabricated and pumped close to their zero-dispersion wavelength in the femtosecond regime by means of an optical parametric oscillator pumped by a Ti:Sapphire laser. When coupled into the fibers, the femtosecond pulses result in 2000-nm bandwidth supercontinua reaching the Mid-Infrared region and extending from 750 nm to 2.8 µm in tellurite fibers and 1 µm to 3.2 µm in chalcogenide fibers, respectively.

OCIS codes: (060.2390) Fiber optics, infrared; (060.5295) Photonic crystal fibers; (190.4370) Nonlinear optics, fibers; (160.4330) Nonlinear optical materials; (160.2750) Glass and other amorphous materials; (060.2280) Fiber design and fabrication; (060.2270) Fiber characterization.

#176238 - $15.00 USD Received 14 Sep 2012; revised 7 Nov 2012; accepted 8 Nov 2012; published 16 Nov 2012
(C) 2012 OSA 19 November 2012 / Vol. 20, No. 24 / OPTICS EXPRESS 27083

Mid-infrared 2000-nm bandwidth supercontinuum generation in suspended-core microstructured Sulfide and Tellurite optical fibers

I. Savelli[1], **O. Mouawad[1]**, J. Fatome[1,*], B. Kibler[1], F. Désévédavy[1], G. Gadret[1], J-C Jules[1], P-Y Bony[1], H. Kawashima[2], W. Gao[2], T. Kohoutek[2], T. Suzuki[2], Y. Ohishi[2], and F. Smektala[1]

[1]Laboratoire Interdisciplinaire Carnot de Bourgogne (ICB), UMR 6303 CNRS - Université de Bourgogne, 9 Av. Alain Savary, BP47870, 21078 Dijon, France

[2]Research Center for Advanced Photon Technology, Toyota Technological Institute 2-12-1, Hisakata, Tempaku, Nagoya 468-8511, Japan

Corresponding author: jfatome@u-bourgogne.fr

Abstract

In this work, we report the experimental observation of supercontinua generation in two kinds of suspended-core microstructured soft-glass optical fibers. Low loss, highly nonlinear, tellurite and As_2S_3 chalcogenide fibers have been fabricated and pumped close to their zero-dispersion wavelength in the femtosecond regime by means of an optical parametric oscillator pumped by a Ti:Sapphire laser. When coupled into the fibers, the femtosecond pulses result in 2000-nm bandwidth supercontinua reaching the Mid-Infrared region and extending from 750 nm to 2.8 µm in tellurite fibers and 1 µm to 3.2 µm in chalcogenide fibers, respectively.

OCIS codes: (060.2390) Fiber optics, infrared; (060.5295) Photonic crystal fibers; (190.4370) Nonlinear optics, fibers; (160.4330) Nonlinear optical materials; (160.2750) Glass and other amorphous materials; (060.2280) Fiber design and fabrication; (060.2270) Fiber characterization.

1. Introduction

Because of combined properties of high coherence, large bandwidth, brightness and potential compactness, supercontinuum generation has been a topic of high interest in nonlinear optics.

Indeed, broadband light sources have found many applications in the field of spectroscopy, metrology, telecommunication or biology. To this aim, numerous efforts have been first dedicated to investigate supercontinuum generation in fused silica fibers with record brightness and spectral expansion ranging from ultraviolet (UV) to mid-infrared (MIR) [1-8]. However, since intrinsic transmission window of fused silica makes supercontinuum expansion a challenging task above 2.2 µm [9, 10], the recent trend is thus to provide alternative materials so as to spread further in the MIR region [11-26]. In this context, larger transmission windows and stronger nonlinear materials have been proposed as an alternative to the conventional fused silica such as tellurite [11-14], chalcogenide [15-20], heavy oxides [21, 22] or fluoride glasses [23-26]. Tellurite and chalcogenide glasses have serious advantages because of their wide transmittance window, chemical durability and high nonlinearity. Depending on their composition, infrared transparency can exceed 10 µm while the Kerr nonlinearity can be 500 times stronger than fused silica [27]. These different features make them serious candidates for broad mid-infrared supercontinuum generation. For example, supercontinuum as broad as 4000-nm bandwidth has been generated in a sub-cm long Tellurite microstructured fiber by Domachuk *et al.* in Ref. [12] thanks to a femtosecond pulse pumping at telecommunication wavelength. Regarding chalcogenide fibers, pumping in the anomalous dispersive regime is a much challenging task since the chromatic dispersion contribution of the material generally induces a zero dispersion wavelength far in the infrared region (typically around 5 µm) and thus far from commercially available femtosecond pulse sources. Consequently, a careful design of the waveguide structure has to be performed so as to shift down the zero dispersion wavelength (ZDW) and thus allowing an anomalous dispersion pumping. To this aim, several strategies have been considered such as waveguide fabrication, tapering, nanowire and microstructured optical fibers, which give rise to efficient spectral broadening and supercontinuum generation [19, 20, 27-30]. In this work, we report the experimental fabrication and characterization of two kinds of soft-glasses, low loss, suspended-core microstructured optical fibers. More precisely, both tellurite and As_2S_3 chalcogenide suspended-core fibers with nearly 3-µm core diameter have been designed and pumped in their anomalous dispersion regime by means of an optical parametric oscillator delivering 200-fs pulses between 1700 and 2500 nm. When coupled into the fibers, the nJ-level femtosecond pulses result in 2000-nm bandwidth supercontinuum spreading in the mid-infrared region until 2.8 µm in Tellurite fiber and 3.2 µm in chalcogenide fiber.

2. Tellurite fiber design

The fiber preform is first elaborated from a tellurite $80TeO_2$-10ZnO-$10Na_2O$ glass (mol. %) synthesized by the fusion method under oxidizing atmosphere. High-purity, commercial raw materials are used for the glass fabrication without any additional purification: tellurium (IV) oxide (Alfa Aesar, 99.9995%), zinc oxide (Alfa Aesar, 99.999%) and sodium carbonate (Alfa Aesar, 99.997%). The oxide mixture is melted in a platinum crucible at a temperature of 800-850°C between 1h and 2h. The resulting melt is then poured in a brass mould preheated at 270°C. The annealing of the glass sample is finally completed around its transition temperature (Tg = 285°C) during several hours before being slowly cooled down to room temperature. The resulting glass rod is thus characterized by a typical length of 4.5 cm and a round diameter of 16 mm. The preform elaboration is achieved by means of a mechanical drilling process, which ensures better loss performances than the traditional time-consuming, numerous handy manipulations stack-and-draw technique [16, 31]. The resulting preform consists in a triangular solid core surrounded by three holes of typically 0.8-mm diameter and 30-mm length. In a final stage, the preform is then drawn to fiber under a helium atmosphere. Indeed, from glass classical DSC measurements at a heating rate of 10°C/min between room temperature and 400°C, no exothermic crystallization peak is registered. Thus, the temperature difference between Tg and crystallization temperature is higher than 115°C, making indeed the glass suitable for fiber drawing which is performed around 360°C.

The transmittance of the bulk was first measured using a FTIR Fourier Transform InfraRed spectrometer (Perkin–Elmer Spectrum One) on a 4-mm thick rod sample for two casting processes, more precisely under room atmosphere conditions and under dry atmosphere in a glove box. Figure 32 shows typical transmittance spectra recorded in the range of 1300-6700 nm.

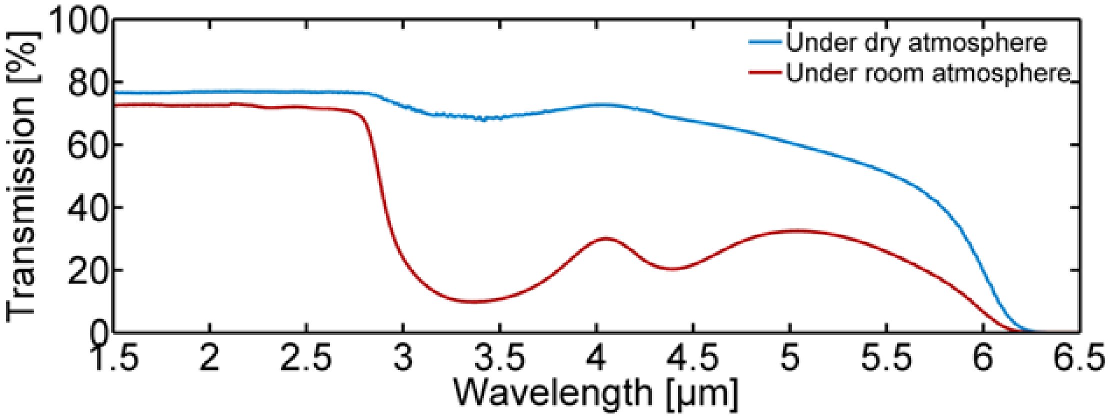

Figure 32: Transmittance of the tellurite bulk as a function of wavelength measured on a 4-mm thick sample. Glass casted under room atmosphere (red solid line), glass casted under dry atmosphere in a glove box (blue solid line).

The crucial point here is the residual OH absorption which induces excess of losses. Indeed, the tellurite glasses, as all oxide glasses, are known to suffer from a strong water absorption in the infrared range that decreases the glass transmission [31-33]. In the case of the glass elaborated under air atmosphere (red line in Figure 32), we can clearly observe two main OH bands: strongly bonded OH (strong OH) and weakly bonded OH (weak OH) combined with free OH. This OH pollution is mainly due to reaction between the atmospheric moisture and the glass batch during glass synthesis. The central positions of these bands depend on the degree of OH hydrogen bonding (H-bonding) present in the glass [34]. The strongly bonded OH absorb around 4350 nm, while the combination of weakly H-bonded OH and free OH in the glass provides a huge 1-µm bandwidth absorption band located around 3350 nm, which results in a poor 15% transmission at 3.3 µm and thus preventing any practical application beyond 3 µm. In order to overcome this issue, we have completed the glass fabrication process under a dry atmosphere inside a glove box. Resulting transmission spectrum is then depicted in Figure 32 thanks to the blue solid line. We can notice a high flatness of the transmittance level around 76% until 2.8 µm as well as a significant reduction of the OH absorption band around 3.3 µm, for which transmittance is greatly improved from 15% to 70%.

More precisely, the concentration of OH-groups can be estimated by means of the following equation [35]:

$$N_{OH} = \frac{N_A}{\varepsilon \cdot L} \cdot \ln(\frac{1}{T}) \tag{25}$$

where N_A is the Avogadro constant, L the sample thickness (cm), T the transmittance, and ε the molar absorption of the free OH groups in the glass. In the calculations we use the molar absorption of the OH groups in silicate glasses (49.1×10^3 cm^2/mol) [36]. Then the amount of OH-groups can be presented in parts per million (ppm) [37]. After calculations, we found that the glass fabrication under dry atmosphere allows us to reduce the OH-ions concentration by a factor 36: 510 ppm under air atmosphere vs 14 ppm in the glove box. In this latter case the origin of the remaining OH-groups is attributed to the initial pollution of the raw materials.

After drawing process, we obtained the fiber profile illustrated in Figure 33 (a) captured by means of a scanning electron microscope (SEM). The resulting tellurite fiber is characterized by a 120-µm outside diameter with a typical suspended-core shape consisting in a triangular 3.4-µm solid core surrounded by three petal-like holes with 1 µm thickness bridges. Because of the critical small size of the microstructured fiber core, a measurement of fiber spectral losses could only be successfully performed on a large core quasi mono-index profile fiber, which is drawn just before the microstructured fiber itself, in the early stage of the drawing process, when the holes of the microstructure are not yet under pressure. It is thus possible to correctly inject the light coming from a Fourier Transformed InfraRed (FTIR) spectrometer in this large core fiber. The cut-back technique is implemented for that purpose. Typically, cut back measurements are performed on 5 meters of fiber, with around 20% accuracy, attributed to variations of the fibre cross section when cutting the fiber. Note additionally that fiber losses were also measured punctually at 1.55 µm for the small-core microstructured fiber itself, at a level of 1.5 dB/m, thus corroborating previous results on quasi mono-index one. Spectral fiber losses are nearly flat up to 2.5 µm but increase rapidly beyond 2.7 µm. This flatness was also confirmed experimentally by the resulting supercontinuum spectrum obtained in section 5. It is also important to notice here that, even if we achieved a strong reduction of the residual OH absorption in the bulk glass, the cumulative effect of these linear losses in the fiber remain dramatic for practical application above 2.8 µm. This point underlines the fact that an order of magnitude improvement is still required regarding the OH-groups concentration, so as to achieve a concentration below 1 ppm.

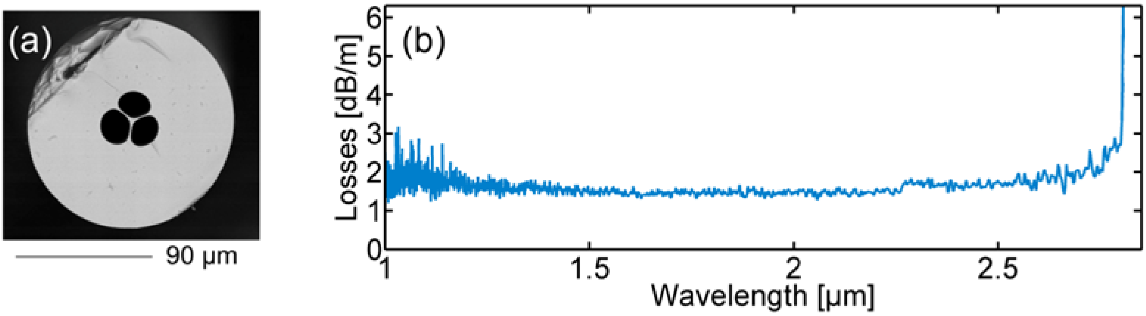

Figure 33: (a) Profile of the tellurite fiber captured by means of a scanning electron microscope. (b) Fiber losses as a function of wavelength measured on a quasi mono-index fiber.

Group velocity dispersion of the tellurite fiber has been also measured thanks to the well-known low coherence interferometric method, which has been proved to be convenient to characterize short segments of optical fibers [27]. Experimental results are compared to numerical simulations of modal properties based on the fiber geometry derived from the SEM analysis (see Figure 34). The good agreement confirms that our fiber exhibits a zero-dispersion wavelength (ZDW) close to 1660 nm while the bulk glass is characterized by a ZDW close to 2.2 µm. The suspended core profile has then successfully allowed us to manage with the chromatic dispersion and to shift the ZDW to shorter values more suitable for SC generation.

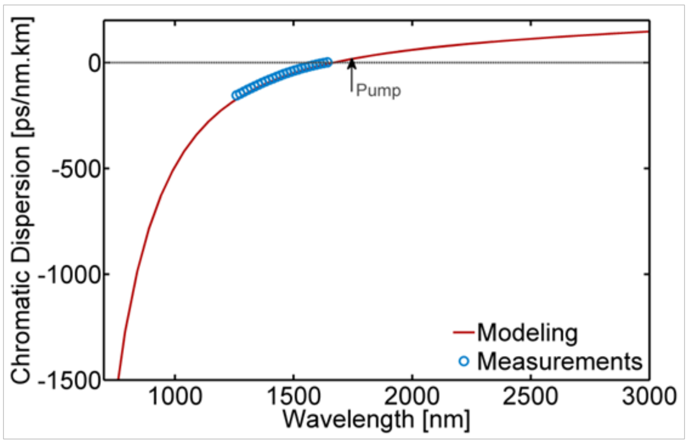

Figure 34: Chromatic dispersion curve of the suspended-core tellurite fiber. Circle: experimental data, solid-line: numerical modeling.

3. As_2S_3 chalcogenide fiber design

For sulfide fibers, first of all, the As_2S_3 glass is prepared from elemental high-purity 5N starting products: arsenic and sulphur. However, initial sulphur is generally polluted by water and carbon, while the metallic arsenic surface is often polluted by As oxide [38]. Thus, the starting products have to be purified from their respective impurities by thermal treatment under a dynamic vacuum (10^{-6} mbar). Sulphur and arsenic are thus dried by heating for a few hours at respectively 120°C and 290°C [39]. Arsenic is then mixed with sulphur and the batch is sealed under vacuum in a silica setup. A static distillation is performed which allows the separation of carbon while the mixture is collected in a silica ampoule. Finally, the silica ampoule is sealed under vacuum, placed in a rocking furnace and heated up to 700°C at a slow heating rate (1 – 2°C min^{-1}). The heating treatment allows the fusion and the reaction of the starting products. Obtained liquid batch is refined at high temperature for 10 to 12 hours. The melt is then quenched at room temperature. Resulting solid glass rod is then annealed at its glass transition temperature Tg ($Tg \approx 200$ °C) for 12 hours and slowly cooled down to room temperature. A thick glass rod (7-cm long, 16-mm in diameter) is finally obtained at the end of this stage. As in the previous case of tellurite glass, DSC measurements at a heating rate of 10°C/min between room temperature and 400 °C do not exhibit any exothermic crystallization peak so that the glass can be drawn into fiber at a temperature around 270°C, at which no re-crystallization phenomenon takes place.

The technique used to elaborate the chalcogenide microstructured optical fiber was the same as the previous tellurite one. The elaboration of the preform was based on a mechanical machining of the rod. Our process presents the originality to be performed entirely mechanically with the help of mechanical tools only and without the need of any ultrasonic assistance. This mechanical drilling process has been largely used in order to prepare a variety of geometric profiles and to control the positions and diameters of the holes, inner surfaces and core surfaces by optimization of the drilling conditions [16, 39, 40]. We designed a preform with three holes of typically 0.8 mm diameter and 30 mm length placed in a triangular arrangement around a solid core. Such a preform was then drawn into fiber in our laboratory under optimized conditions, leading to a 3.2-µm suspended-core fiber with 0.6 µm thickness bridges, which transversal section can be observed in Figure 35(a). More precisely, the drawing process has been performed in an inert and dry atmosphere, at a temperature of 270°C and at a drawing speed of 5 meters/min.

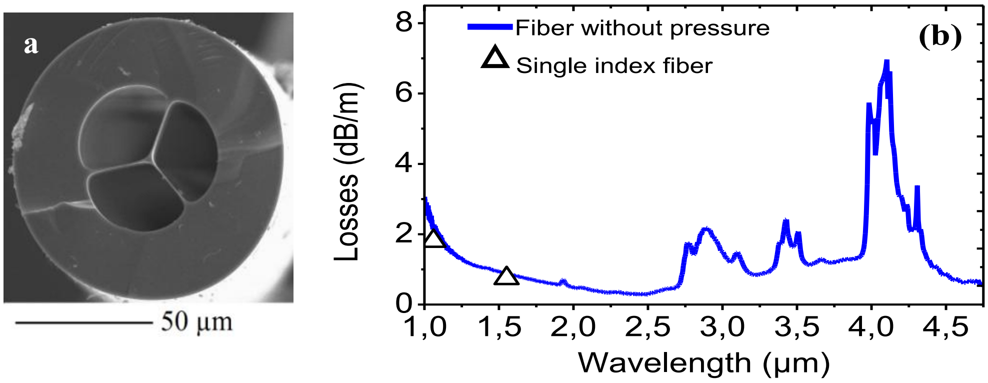

Figure 35: (a) Profile of the chalcogenide As_2S_3 suspended-core fiber captured by means of a scanning electron microscope (b) Fiber losses of the quasi mono-index chalcogenide fiber as a function of wavelength (solid-line) and losses of the suspended core fiber measured at fixed wavelengths 1.06 and 1.55 µm (Triangles).

As in the previous study on tellurite fibers, linear losses were first characterized on the pre-drawing mono-index chalcogenide fiber sample by means of the FTIR spectrometer. Experimental data are depicted in Figure 35 (b) in the range of 1 to 4.5 µm (blue solid-line). Experimental measurements show relatively flat spectral losses in the range from 1.5 to 2.5 µm with a minimum below 1 dB/m around the pump wavelength at 2.3 µm.

The attenuation curve obtained for this glass (Figure 35 (b)) shows that the material losses contribution is quite similar to our previous results in [16] and [39]. We can also see narrow and large extrinsic absorption bands, centered at characteristic wavelengths which corresponds to residual OH and SH pollution of the glass. SH concentration (≈2.5 ppm) can be estimated from the spectrum referring to [41] for which extinction coefficient associated to the SH vibration at 4 µm is 2.5 dB/m/ppm. Finally, note that results of Figure 35(b) are well confirmed by loss measurements in the suspended-core fiber at fixed wavelengths (1.06 and 1.55 µm, see Triangles in Figure 35 (b)), using a corresponding fixed wavelength laser source and the cut-back technique.

As in the previous study on tellurite fibers described above, group velocity dispersion of the chalcogenide suspended-core fiber has been also characterized using the same interferometric set-up [27]. Experimental results are depicted in Figure 36 and compared to numerical analysis of the modal properties. We clearly reveal a zero-dispersion wavelength close to 2330 nm, which has to be compared to the ZDW of the bulky sulfide glass located around 5 µm.

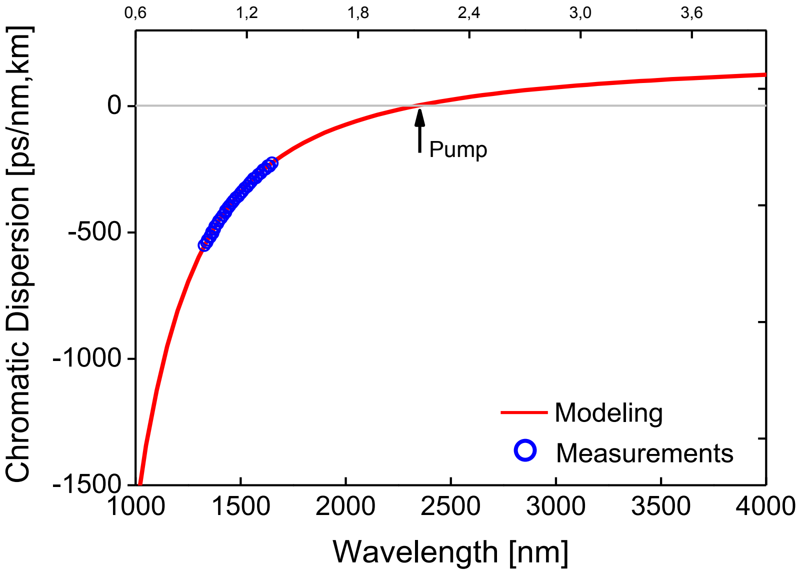

Figure 36: Chromatic dispersion curve of the suspended-core chalcogenide fiber. Circle: experimental data, solid-line: numerical modeling.

4. Experimental set-up

The experimental set-up depicted in Figure 37 consists in an optical parametric oscillator (OPO) pumped by a Ti:Sapphire laser. The OPO delivers 200-fs pulses at a repetition rate of 80 MHz with an average power close to 450 mW. The idler output, tunable from 1.7 to 2.6 µm was used to pump both tellurite and chalcogenide fibers under test in the anomalous dispersion regime and close to their ZDW in order to efficiently generate supercontinua [6]. Fibers are cleaved by means of a scalpel blade and quality of the interfaces is carefully checked under microscope before mounting the sample onto a 3-axis holder. Pulses are then focused into the fiber under test by means of a 20X microscope objective. At the output of the fiber, resulting supercontinuum is collected by a fluoride ZBLAN fiber and spectrally characterized by means of either two Yokogawa optical spectrum analyzers covering 350 to 1200 nm and 1200 to 2400 nm respectively or a FTIR spectrometer in the range of 2400 to 4000 nm.

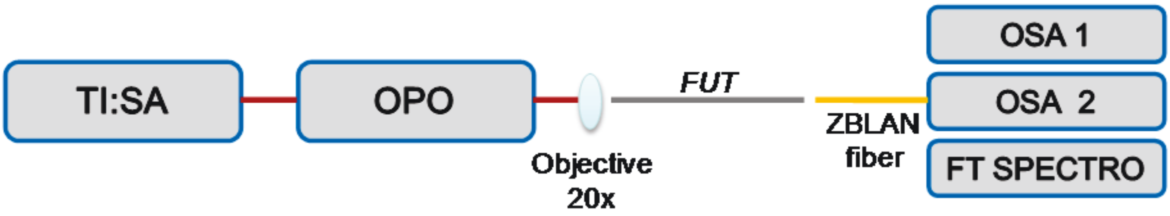

Figure 37: Experimental set-up used to generate supercontinua in tellurite and chalcogenide suspended-core fibers. FUT: Fiber under test.

5. Experimental results and discussions

5.1. Tellurite fiber supercontinuum

Figure 38 (a) shows the experimental results achieved by pumping a 40-cm long sample of our tellurite fiber. The pump wavelength is fixed to 1745 nm and resulting spectra have been recorded as a function of injected input power. The nonlinear index of the material is given by $n_2 \sim 3.8 \times 10^{-19}$ m^2/W at 1550 nm [42], which implies a nonlinear Kerr coefficient $\gamma = 175$ W^{-1}.km^{-1} (the numerical effective mode area is 7.8 µm^2). We clearly observe the well-known physical picture of supercontinuum generation, mainly driven by self-phase modulation, soliton fission and Raman based soliton self-frequency shift [6], which allow extending the resulting spectrum towards the mid-infrared up to 2.8 µm for an input pump power of 112 mW. This input pulse power corresponds to a soliton number close to N=25 and a pulse energy of 1.5 nJ. The resulting 112-mW supercontinuum is characterized by a 2000-nm bandwidth, corresponding to almost 2 octaves and is remarkably flat (a 1900-nm span contained in a -20 dB range). Here, the corresponding output power is ~90% of the input power. Note also that the depicted data above 2.8 µm in the 112-mW spectrum of Figure 38 (a) corresponds to the noise floor level of the FTIR spectrometer. The lower edge of the supercontinuum is mainly enlarged through phase-matched dispersive wave generation. Indeed, during propagation the frequency-shifted solitons can trap short-wavelength radiations and shift them to yet shorter wavelengths. The shortest wavelength generated in the supercontinuum is then determined by the maximum soliton shift towards the infrared. This interaction is characterized by a group-index matching between both spectral components and it can be determined by analyzing the shape of the group index curve of the tested fiber [7]. In Figure 39 we plot the experimental supercontinuum edges for different output powers together with the group index curve obtained numerically for the fundamental mode. We clearly join the points on either edge by straight lines, thus confirming both the concept of group-index matching as well as chromatic dispersion modeling and measurements on the whole span of wavelengths. Moreover, this physical process allowed us to efficiently optimize the experimental supercontinuum generation in the tellurite fiber without any need to continuously monitor the resulting spectrum on the whole wavelength range but just by focusing on the shortest wavelength spreading.

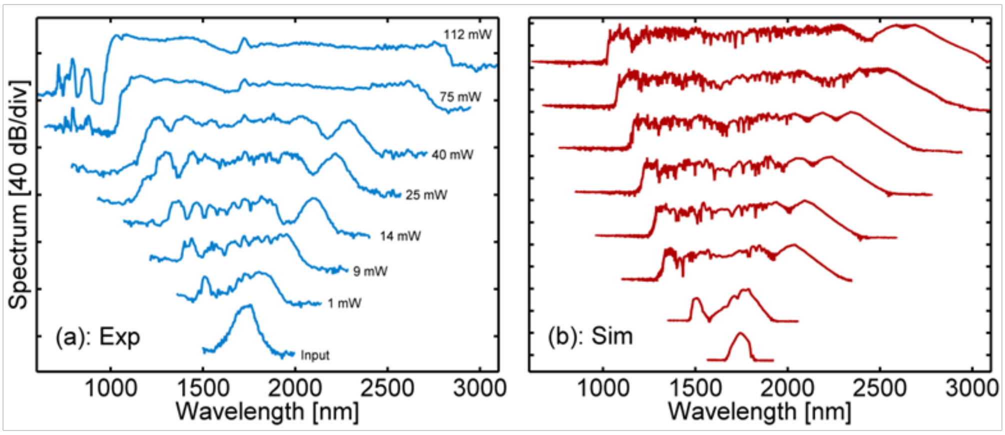

Figure 38: (a) Experimental recording of supercontinua generation in a 40-cm long suspended-core Tellurite fiber as a function of pump power. (b) Corresponding numerical simulations.

Figure 38 (b) presents the numerical simulation corresponding to these experimental data and obtained through the split-step Fourier-based solving of the generalized nonlinear Schrödinger equation [6] taking into account the full dispersion curve from Figure 34, measured fiber losses as well as self-steepening and analytical model of the Raman gain spectrum [42-44]. The numerical results fit quite well the dynamics observed in the experiments and confirm that the spectral broadening is not mainly limited by the intrinsic linear losses for the optimized power and fiber length used here. However we cannot extend the supercontinuum bandwidth in the mid-Infrared region with a longer fiber due to the residual OH absorption which, even if it has been greatly reduced in the fabrication process under dry atmosphere, still prevents some application beyond 3 µm.

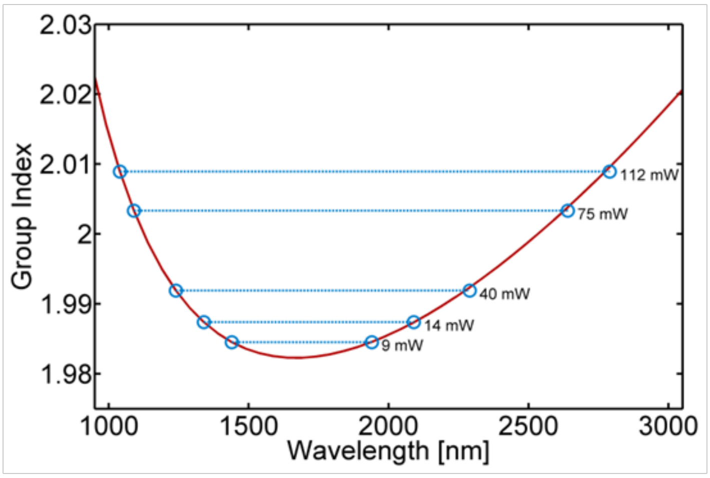

Figure 39: Modeled group index curve as a function of wavelength for the suspended-core tellurite fiber (red solid line) as well as experimental short and long wavelength edges of resulting supercontinua as a function of average power (circles).

5.2. Sulfide fiber supercontinuum

Figure 40 (a) illustrates the experimental results obtained from a 45-mm-long segment of our suspended-core chalcogenide fiber. Figure 40 (a) shows the resulting supercontinuum for a pump wavelength of 2300 nm and an injected power of 70 mW (4.6 kW peak power). Here, the output power is ~70% of the input power. The nonlinear index of the material is $n_2 \sim 2.8\text{x}10^{-18}$ m^2/W at 1550 nm [45], which gives a nonlinear Kerr coefficient $\gamma = 1175$ W^{-1}/km^{-1} (the effective mode area is 6.5 μm^2). The injected pulse corresponds to a high soliton number N=84 and a pulse energy of 0.9 nJ. The chalcogenide fiber is here clearly pumped close to the zero-dispersion wavelength, in the anomalous dispersion regime, and is characterized by a strong and rapid self-phase modulation process followed by soliton fission in the earlier centimeters of fiber. In this case the fission occurs randomly due to the significant role of modulation instability when N >> 20 [6]. Subsequent propagation is then associated with a degradation of the coherence. The resulting supercontinuum extends from 1200 nm to 3200 nm in the -20 dB range (excluding the absorption peak at 2.9 µm). Note however that large residual OH absorption bands are clearly visible around 2.9 µm, which implies to work with only short fiber lengths. This point underlines the fact that OH and SH absorption bands characterized on the pre-drawing mono-index fiber and depicted in Figure 35 (b) are undervalued by this measurement method and that the drawing process as well as resulting

OH induced absorption time deterioration of the microstructure dramatically increased these extrinsic absorption losses. Nevertheless, the resulting spectrum also indicates that supercontinuum extension is performed in the early millimeters of the fiber, allowing the solitons to shift out the spectrum above the absorption band.

Figure 40 (b) represents the numerical simulations corresponding to these experimental results. Thanks to a careful modeling of transmission losses and Raman gain [46] and using the full dispersion curve from Figure 36, we have obtained a good agreement which confirms our experimental observations. However, in order to better fit the experimental data, particularly the SH and OH absorption bands, extra losses have to be taken into account around 2.9 µm and 4 µm, which confirms the under-evaluation of these absorption bands measured in Figure 35 (b) and an ageing of our non coated fibers under room atmosphere. This point is actually under study. Nevertheless, numerical simulations depicted in Figure 40 (c) and neglecting extra losses of absorption peaks reveal that the dynamic of supercontinuum generation could be extended until 5.5 µm, thus confirming the dramatic limitation imposed by OH- and SH-groups induced extra losses.

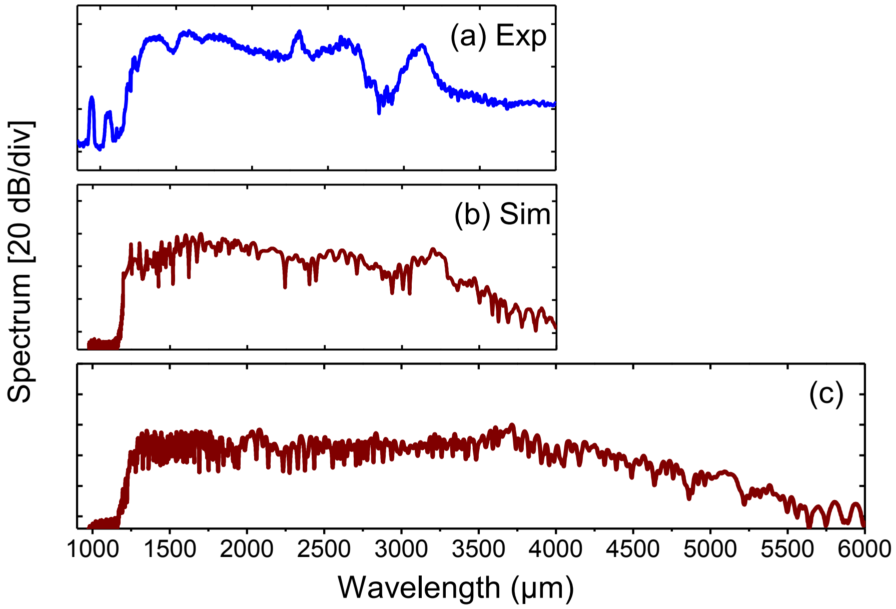

Figure 40: (a) Experimental recording of supercontinuum generation in a 45-mm long sample of suspended-core chalcogenide fiber for a pump power of 70 mW (b) Corresponding numerical simulations (c) Corresponding numerical simulations without OH group absorption peaks.

6. Conclusion

In summary, we report here the experimental generation of supercontinuum in two kinds of suspended-core microstructured soft-glass optical fibers, namely tellurite and sulfide fibers. Thanks to an optical parametric oscillator pumped by a Ti:Sapphire laser and delivering 200-fs pulses between 1700 and 2500 nm, we achieved efficient pumping of both fibers above their respective zero-dispersion wavelength in the anomalous dispersion regime. When coupled into the fibers, the femtosecond pulses result in 2000-nm bandwidth supercontinua reaching the mid-infrared region and extending from 750 nm to 2.8 µm in tellurite fibers and 1 µm to 3.2 µm in sulfide fibers for input pulse energy of ~1 nJ, respectively.

Acknowledgements

We acknowledge the financial support from the French Agence Nationale de la Recherche project ANR CONFIAN, Hubert Curien Sakura Egide program, the CNRS and the Conseil Régional de Bourgogne, Photcom PARI program.

7. References

1. T. A. Birks, W. J. Wadsworth, and P. S. J. Russell, "Supercontinuum generation in tapered fibers," Optics Letters **25**, 1415-1417 (2000).
2. J. K. Ranka, R. S. Windeler, and A. J. Stentz, "Visible continuum generation in air-silica microstructure optical fibers with anomalous dispersion at 800 nm," Optics Letters **25**, 25-27 (2000).
3. A. L. Gaeta, "Nonlinear propagation and continuum generation in microstructured optical fibers," Optics Letters **27**, 924-926 (2002).
4. P. S. J. Russell, "Photonic crystal fibers," Science **299**, 358-362 (2003).
5. J. C. Knight, "Photonic crystal fibres," Nature **424**, 847-857, (2003).
6. J. M. Dudley, G. Genty, and S. Coen, "Supercontinuum generation in photonic crystal fiber," Reviews of Modern Physics **78**, 1135-1184 (2006).
7. J. M. Stone, and J. C. Knight, "From zero dispersion to group index matching: How tapering fibers offers the best of both worlds for visible supercontinuum generation," Optical Fiber Technology **18**, 315-321 (2012).
8. T. Sylvestre, A. R. Ragueh, M. W. Lee, B. Stiller, G. Fanjoux, B. Barviau, A. Mussot, and A. Kudlinski, "Black-light continuum generation in a silica-core photonic crystal fiber," Optics Letters **37**, 130-132 (2012).
9. C. Xia, M. Kumar, M.-Y. Cheng, O. P. Kulkarni, M. N. Islam, A. Galvanauskas, F. L. Terry, M. J. Freeman, D. A. Nolan, and W. A. Wood, "Supercontinuum generation in silica fibers by amplified nanosecond laser diode pulses," IEEE Journal of Selected Topics in Quantum Electronics **13**, 789-797 (2007).
10. J. Fatome, B. Kibler, M. El-Amraoui, J. C. Jules, G. Gadret, F. Desevedavy, and F. Smektala, "Mid-infrared extension of supercontinuum in chalcogenide suspended core fibre through soliton gas pumping," Electronics Letters **47**, 398-400 (2011).
11. V. V. R. K. Kumar, A. George, J. Knight, and P. Russell, "Tellurite photonic crystal fiber," Optics Express **11**, 2641-2645 (2003).
12. P. Domachuk, N. A. Wolchover, M. Cronin-Golomb, A. Wang, A. K. George, C. M. B. Cordeiro, J. C. Knight, and F. G. Omenetto, "Over 4000 nm bandwidth of mid-IR supercontinuum generation in sub-centimeter segments of highly nonlinear tellurite PCFs," Optics Express **16**, 7161-7168 (2008).
13. M. Liao, C. Chaudhari, G. Qin, X. Yan, T. Suzuki, and Y. Ohishi, "Tellurite microstructure fibers with small hexagonal core for supercontinuum generation," Optics Express **17**, 12174-12182 (2009).

14. I. Savelii, J. C. Jules, G. Gadret, B. Kibler, J. Fatome, M. El-Amraoui, N. Manikandan, X. Zheng, F. Désévédavy, J. M. Dudley, J. Troles, L. Brilland, G. Renversez, and F. Smektala, "Suspended core tellurite glass optical fibers for infrared supercontinuum generation," Optical Materials **33**, 1661-1666 (2011).

15. M. Liao, C. Chaudhari, G. Qin, X. Yan, C. Kito, T. Suzuki, Y. Ohishi, M. Matsumoto, and T. Misumi, "Fabrication and characterization of a chalcogenide-tellurite composite microstructure fiber with high nonlinearity," Optics Express **17**, 21608-21614 (2009).

16. M. El-Amraoui, G. Gadret, J. C. Jules, J. Fatome, C. Fortier, F. Désévédavy, I. Skripatchev, Y. Messaddeq, J. Troles, L. Brilland, W. Gao, T. Suzuki, Y. Ohishi, and F. Smektala, "Microstructured chalcogenide optical fibers from As_2S_3 glass: towards new IR broadband sources," Optics Express **18**, 26655-26665 (2010).

17. J. Hu, C. R. Menyuk, L. B. Shaw, J. S. Sanghera, and I. D. Aggarwal, "Computational study of 3-5 μm source created by using supercontinuum generation in As_2S_3 chalcogenide fibers with a pump at 2 μm," Optics Letters **35**, 2907-2909 (2010).

18. N. Granzow, S. P. Stark, M. A. Schmidt, A. S. Tverjanovich, L. Wondraczek, and P. S. J. Russell, "Supercontinuum generation in chalcogenide-silica step-index fibers," Optics Express **19**, 21003-21010 (2011).

19. D. D. Hudson, S. A. Dekker, E. C. Mägi, A. C. Judge, S. D. Jackson, E. Li, J. S. Sanghera, L. B. Shaw, I. D. Aggarwal, and B. J. Eggleton, "Octave spanning supercontinuum in an As_2S_3 taper using ultralow pump pulse energy," Optics Letters **36**, 1122-1124 (2011).

20. M. R. Lamont, B. Luther-Davies, D.-Y. Choi, S. Madden, and B. J. Eggleton, "Supercontinuum generation in dispersion engineered highly nonlinear (γ = 10/W/m) As_2S_3 chalcogenide planar waveguide," Optics Express **16**, 14938-14944 (2008).

21. J. H. V. Price, T. M. Monro, H. Ebendorff-Heidepriem, F. Poletti, P. Horak, V. Finazzi, J. Y. Y. Leong, P. Petropoulos, J. C. Flanagan, G. Brambilla, F. Xian, and D. J. Richardson, "Mid-IR supercontinuum generation from nonsilica microstructured optical fibers," IEEE Journal of Selected Topics in Quantum Electronics **13**, 738-749 (2007).

22. R. Buczynski, H. T. Bookey, D. Pysz, R. Stepien, I. Kujawa, J. E. McCarthy, A. J. Waddie, A.K. Kar, and M.R. Taghizadeh, "Supercontinuum generation up to 2.5μm in photonic crystal fiber made of lead-bismuth-galate glass," Laser Physics Letters **7**, 666-672 (2010).

23. G. Qin, X. Yan, C. Kito, M. Liao, C. Chaudhari, T. Suzuki, and Y. Ohishi, "Supercontinuum generation spanning over three octaves from UV to 3.85 μm in a fluoride fiber," Optics Letters **34**, 2015-2017 (2009).

24. F. G. Omenetto, N. A. Wolchover, M. R. Wehner, M. Ross, A. Efimov, A. J. Taylor, V. V. R. K. Kumar, A. K. George, J. C. Knight, N. Y. Joly, and P. S. J. Russell, "Spectrally smooth supercontinuum from 350 nm to 3 µm in sub-centimeter lengths of soft-glass photonic crystal fibers," Optics Express **14**, 4928-4934 (2006).

25. C. Xia, M. Kumar, O. P. Kulkarni, M. N. Islam, J. F. L. Terry, M. J. Freeman, M. Poulain, and G. Mazé, "Mid-infrared supercontinuum generation to 4.5 µm in ZBLAN fluoride fibers by nanosecond diode pumping," Optics Letters **31**, 2553-2555 (2006).

26. C. Agger, C. Petersen, S. Dupont, H. Steffensen, J. K. Lyngsø, C. L. Thomsen, J. Thøgersen, S. R. Keiding, and O. Bang, "Supercontinuum generation in ZBLAN fibers-detailed comparison between measurement and simulation," Journal of the Optical Society of America B **29**, 635-645 (2012).

27. J. Fatome, C. Fortier, T. N. Nguyen, T. Chartier, F. Smektala, K. Messaad, B. Kibler, S. Pitois, G. Gadret, C. Finot, J. Troles, F. Desevedavy, P. Houizot, G. Renversez, L. Brilland, and N. Traynor, "Linear and nonlinear characterizations of chalcogenide photonic crystal fibers," Journal of Lightwave Technology **27**, 1707-1715 (2009).

28. J. Troles, L. Brilland, F. Smektala, P. Houizot, F. Désévédavy, Q. Coulombier, N. Traynor, T. Chartier, T. N. Nguyen, J. L. Adam, and G. Renversez, "Chalcogenide microstructured fibers for infrared systems, elaboration modelization, and characterization," Fiber and Integrated Optics **28**, 11-26 (2009).

29. C. Chaudhari, T. Suzuki, and Y. Ohishi, "Design of zero chromatic dispersion chalcogenide As_2S_3 glass nanofibers," Journal of Lightwave Technology **27**, 2095-2099 (2009).

30. G. Tao, S. Shabahang, E.-H. Banaei, J. J. Kaufman, and A. F. Abouraddy, "Multimaterial preform coextrusion for robust chalcogenide optical fibers and tapers," Optics Letters **37**, 2751-2753 (2012).

31. L. Brilland, J. Troles, P. Houizot, F. Désévédavy, Q. Coulombier, G. Renversez, T. Chartier, T. N. Nguyen, J.-L. Adam, and N. Traynor, "Interfaces impact on the transmission of chalcogenides photonic crystal fibres," Journal of the Ceramic Society of Japan **116**, 1024-1027 (2008).

32. A. M. Efimov, and V. G. Pogareva, "Water-related IR absorption spectra for some phosphate and silicate glasses," Journal of Non-Crystalline Solids **275**, 189-198 (2000).

33. M. Churbanov, A. N. Moiseev, A. V. Chilyasov, V. V. Dorofeev, I. A. Kraev, M. M. Lipatova, T. V. Kotereva, E. M. Dianov, V. G. Plotnichenko, and E. B. kryukova, "Production of high-purity TeO_2-ZnO and TeO_2-WO_3 glasses with reduced content of OH groups," Journal of Optoelectronics and Advanced Materials **9**, 3229-3234 (2007).

34. X. Feng, S. Tanabe, and T. Hanada, "Hydroxyl groups in erbium-doped germane-tellurite glasses," Journal of Non-Crystalline Solids **281**, 48-54 (2001).

35. J. Massera, A. Haldeman, J. Jackson, C. Rivero-Baleine, L. Petit, and K. Richardson, "Processing of tellurite-based glass with low OH content," Journal of the American Ceramic Society **94**, 130-136 (2011).

36. L. Nemec, and J. Gotz, "Infrared absorption of OH− in E glass," Journal of the American Ceramic Society **53**, 526-526 (1970).

37. K. Chida, F. Hanawa, and M. Nakahara, "Fabrication of OH-free multimode fiber by vapor phase axial deposition," IEEE Journal of Selected Topics in Quantum Electronics **18**, 1883-1889 (1982).

38. J. Douady, B. Boulanger, E. Fuchs, F. Smektala, and J. Troles, "Symmetry and phase-matching properties of third-harmonic generation under the photoelastic effect in Ge-As-Se chalcogenide glasses," Journal of the Optical Society of America B **22**, 1486-1492 (2005).

39. M. El-Amraoui, J. Fatome, J. C. Jules, B. Kibler, G. Gadret, C. Fortier, F. Smektala, I. Skripatchev, C. F. Polacchini, Y. Messaddeq, J. Troles, L. Brilland, M. Szpulak, and G. Renversez, "Strong infrared spectral broadening in low-loss As-S chalcogenide suspended core microstructured optical fibers," Optics Express **18**, 4547-4556 (2010).

40. X. Feng, A. K. Mairaj, D. W. Hewak, and T. M. Monro, "Nonsilica glasses for holey fibers," Journal of Lightwave Technology **23**, 2046 (2005).

41. V. G. Borisevich, V. G. Plotnichenko, I. V. Scripachev, and M.F. Churbanov, "Extinction coefficient of SH groups in vitreous arsenic sulphide," Russian High Purity Substances Journal **4**, 759-762 (1990).

42. A. Lin, A. Zhang, E. J. Bushong, and J. Toulouse, "Solid-core tellurite glass fiber for infrared and nonlinear applications," Optics Express **17**, 16716-16721 (2009).

43. M. D. O'Donnell, K. Richardson, R. Stolen, C. Rivero, T. Cardinal, M. Couzi, D. Furniss, and A. B. Seddon, "Raman gain of selected tellurite glasses for IR fibre lasers calculated from spontaneous scattering spectra," Optical Materials **30**, 946-951 (2008).

44. X. Yan, G. Qin, M. Liao, T. Suzuki, and Y. Ohishi, "Transient Raman response and soliton self-frequency shift in tellurite microstructured fiber," Journal of Applied Physics **108**, 123110 (2010).

45. V. Ta'eed, N. J. Baker, L. Fu, K. Finsterbusch, M. R. E. Lamont, D. J. Moss, H. C. Nguyen, B. J. Eggleton, D.-Y. Choi, S. Madden, and B. Luther-Davies, "Ultrafast all-optical chalcogenide glass photonic circuits," Optics Express **15**, 9205-9221 (2007).

46. R. J. Kobliska, and S. A. Solin, "Temperature dependence of the Raman spectrum and the depolarization spectrum of armophous As_2S_3," Physical Review B **8**, 756-768 (1973).

V. Article 2

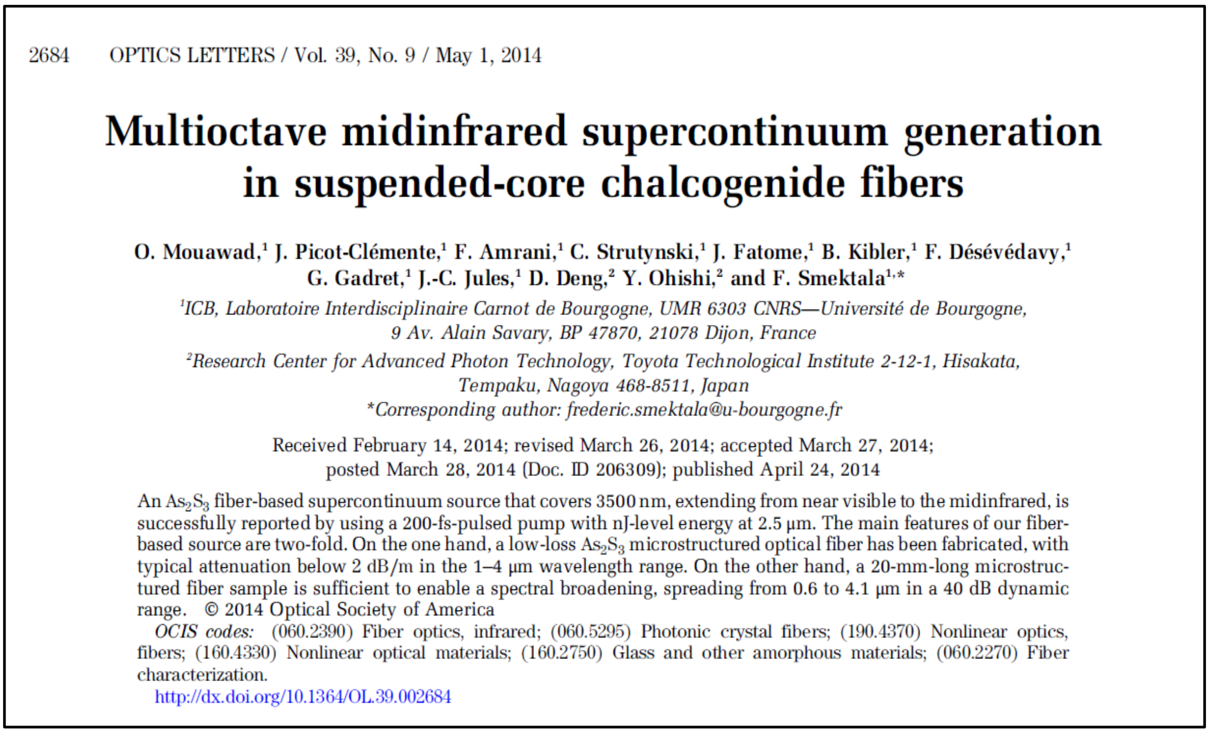

2684 OPTICS LETTERS / Vol. 39, No. 9 / May 1, 2014

Multioctave midinfrared supercontinuum generation in suspended-core chalcogenide fibers

O. Mouawad,[1] J. Picot-Clémente,[1] F. Amrani,[1] C. Strutynski,[1] J. Fatome,[1] B. Kibler,[1] F. Désévédavy,[1] G. Gadret,[1] J.-C. Jules,[1] D. Deng,[2] Y. Ohishi,[2] and F. Smektala[1,*]
[1]*ICB, Laboratoire Interdisciplinaire Carnot de Bourgogne, UMR 6303 CNRS—Université de Bourgogne, 9 Av. Alain Savary, BP 47870, 21078 Dijon, France*
[2]*Research Center for Advanced Photon Technology, Toyota Technological Institute 2-12-1, Hisakata, Tempaku, Nagoya 468-8511, Japan*
**Corresponding author: frederic.smektala@u-bourgogne.fr*

Received February 14, 2014; revised March 26, 2014; accepted March 27, 2014;
posted March 28, 2014 (Doc. ID 206309); published April 24, 2014

An As_2S_3 fiber-based supercontinuum source that covers 3500 nm, extending from near visible to the midinfrared, is successfully reported by using a 200-fs-pulsed pump with nJ-level energy at 2.5 μm. The main features of our fiber-based source are two-fold. On the one hand, a low-loss As_2S_3 microstructured optical fiber has been fabricated, with typical attenuation below 2 dB/m in the 1–4 μm wavelength range. On the other hand, a 20-mm-long microstructured fiber sample is sufficient to enable a spectral broadening, spreading from 0.6 to 4.1 μm in a 40 dB dynamic range.

OCIS codes: (060.2390) Fiber optics, infrared; (060.5295) Photonic crystal fibers; (190.4370) Nonlinear optics, fibers; (160.4330) Nonlinear optical materials; (160.2750) Glass and other amorphous materials; (060.2270) Fiber characterization.
http://dx.doi.org/10.1364/OL.39.002684

Multi-octave mid-infrared supercontinuum generation in suspended-core chalcogenide fibers

O. Mouawad[1], J. Picot-Clémente[1], F. Amrani[1], C. Strutynski[1], J. Fatome[1], B. Kibler[1], F. Désévédavy[1], G. Gadret[1], J-C Jules[1], D. Deng[2], Y. Ohishi[2] and F. Smektala[1,*]

[1]*Laboratoire Interdisciplinaire Carnot de Bourgogne (ICB), UMR 6303 CNRS - Université de Bourgogne, 9 Av. Alain Savary, BP47870, 21078 Dijon, France*
[2]*Research Center for Advanced Photon Technology, Toyota Technological Institute 2-12-1, Hisakata, Tempaku, Nagoya 468-8511, Japan*
Corresponding author: frederic.smektala@u-bourgogne.fr

Abstract

As_2S_3 fiber-based supercontinuum source that covers 3500 nm extending from near visible to the mid-infrared is successfully reported by using a 200-fs pulsed pump with nJ-level energy at 2.5 μm. The main features of our fiber-based source are twofold. On the one hand, a low-loss As_2S_3 microstructured optical fiber has been fabricated with typical attenuation below 2 dB/m in the 1-4 µm wavelength range. On the other hand, a 20-mm long microstructured fiber sample is sufficient to enable a spectral broadening spreading from 0.6 to 4.1 µm in a 40 dB dynamic range.

OCIS codes: (060.2390) Fiber optics, infrared; (060.5295) Photonic crystal fibers; (190.4370) Nonlinear optics, fibers; (160.4330) Nonlinear optical materials; (160.2750) Glass and other amorphous materials; (060.2280) Fiber design and fabrication.

1. Introduction

Expanding the wavelength range of supercontinua towards the mid-infrared region is of high technological interest in numerous applications such as spectroscopy, sensing, biology, metrology or defense. However, exceeding the fused silica transparency limits beyond 2 µm remains a challenging task [1]. To this aim, several strategies and alternative materials have been proposed so as to push back the edges of supercontinuum (SC) sources still further in the mid-infrared region. In particular, wider transmission windows and stronger nonlinear materials have been studied as an alternative to fused silica such as tellurite [2, 3], fluoride glasses [4, 5], heavy oxides [6] or chalcogenide glasses [7-15]. Given their remarkable optical and chemical properties, chalcogenide-based materials have been found to be promising candidates. Indeed, depending on their chemical composition, the infrared transparency can exceed 10 µm, whereas the Kerr nonlinearity can be three orders of magnitude higher than standard fused silica [7]. This combination of both properties makes them particularly attractive for broadband mid-infrared SC generation. However, chalcogenide glasses suffer from a large normal group velocity dispersion (GVD) in the infrared, which dramatically reduces the efficiency of SC expansion. Indeed, the zero dispersion wavelength (ZDW) is commonly located far in the mid-infrared and far from standard commercially available laser sources. For instance, the ZDW of sulfide glasses are usually located around 5 µm, which makes them challenging to pump in their anomalous dispersion regime. Therefore, a well-designed geometry is required to shift down the ZDW to lower wavelengths. To this aim, several scenarios have been considered such as waveguide design [8-10], tapering [11-13] and microstructured optical fibers [2, 14, 15], which give rise to record spectral expansions in the mid-infrared [2, 8-15]. In this paper, we report the generation of a 3500-nm bandwidth SC in a 2-cm long segment of low loss As_2S_3 suspended core microstructured optical fiber (MOF). Fiber geometry was carefully designed for an efficient pumping close to its ZDW in the anomalous dispersion regime by means of an optical parametric oscillator delivering 200-fs pulses at an operating wavelength of 2.5 µm. To the best of our knowledge, this is the largest SC bandwidth generated in chalcogenide fibers.

2. Glass and fiber elaboration

In order to fabricate the MOF, commercially available high purity elemental precursors (S and As of 5N purity) were first used to prepare a glass rod. Nevertheless, their subsequent distillation remains mandatory since the sulphur powder is generally polluted by water and carbon, while the surface of metallic arsenic by oxides. Thus, starting products were subjected to thermal treatment under vacuum inside a silica set-up to get rid of their respective impurities. Sulphur is thus dried by heating for a few hours at 120°C under dynamic vacuum. Simultaneously, the arsenic is heated few hours at the oxide sublimation temperature (290°C) [2]. At a later stage, the mixed batches are enclosed inside silica glassware prior to static distillation. By means of the static distillation process, the batch collected inside the silica synthesis ampoule is exempt of unsuitable carbon. Finally, the synthesis ampoule was sealed and placed inside a three zone melting rocking furnace. The ampoule was then heated up to the reaction temperature (700°C) and maintained at this stage for several hours (12 h). At such high temperature, the melt reagents interact to form the glass. Enforced by high volatility of sulfur, the ampoule was slowly heated to avoid its explosion. Finally, the silica ampoule containing the liquid batch was quenched in water. The obtained sulfide glass was subsequently annealed at the glass transition temperature (Tg= 210°C) for 12 hours. A mechanical drilling technique was adopted to elaborate the glass preforms. Thanks to this original technique, a variety of geometrical designs conceived to achieve well controlled parameters (core size, holes positions, inner surface) were prepared [2, 7]. Here, the preform geometry consists of three holes centered on a central solid core. The length of the fiber preform is 40 mm and the diameter of air holes is 1 mm. Following the drawing process, the fiber microstructure consists in a triangular lattice of air holes which extend along the fiber. They surround a small central core with triangle geometry attached to robust jacket by three thin struts. The corresponding cross-section image of the suspended core MOF is displayed in Figure 41.a.

The fiber has an outer diameter of 130 µm and a central solid core of 3.4 µm in diameter, held to the clad through three surrounding holes by means of three thin struts. Due to technical constraints, the spectral losses cannot be directly measured on this resulting small core MOF. However, an estimation of fiber optical losses by means of Fourier Transformed InfraRed (FTIR) spectrometer can be performed on a mono-index large core multimode fiber [2].

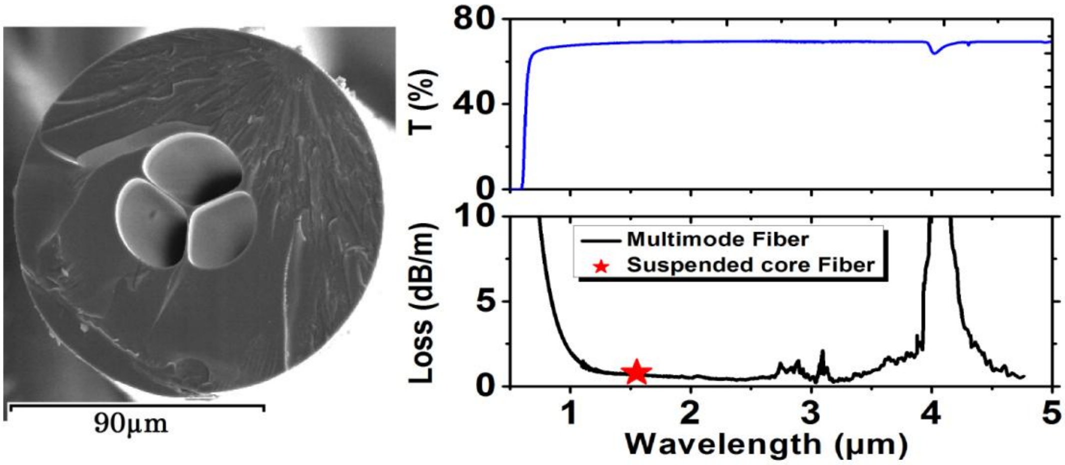

Figure 41: (a) Profile of the chalcogenide As_2S_3 suspended-core fiber captured by means of scanning electronic microscopy (b) Chalcogenide bulk transmission (c) Optical loss of the mono-index large core multimode fiber as a function of wavelength. Loss measured at 1.55 µm for the suspended core MOF (star).

Results are depicted in Figure 41 b-c in the range of 0.5 to 5 µm. In particular we compare optical losses obtained from the chalcogenide bulk and the mono-index fiber. Two typical extrinsic absorption bands slightly emerge from the background. The first band is large and centered at 2.77 and 2.89 µm. This phenomenon is due to fundamental vibration modes of OH bonds. A second narrow band attributed to vibration mode of SH bonds is centered at 3.1 µm. The SH concentration level is quite high, above detection limits of our detection set-up (integrating sphere connected to an InSb detector) which explains the noisy aspect of the depicted spectrum and the lack of the SH absorption peak around its fundamental vibration wavelength at 4.0 µm. Taking advantage of the cut-back technique, and using a continuous wave laser source, we confirmed previous loss measurements for the suspended-core fiber at 1.55 µm (star in Figure 41 c). However in our previous work [2], we have suspected a dynamic time variation of the attenuation, especially related with OH absorption, which could be at the origin of limitation of the extension of the supercontinuum further in the infrared region. Thus, in order to confirm the aforementioned hypothesis, as well as to avoid any unsuitable variation of the attenuation of the fiber sample, the microstructured fiber freshly drawn has been permanently preserved under suitable conditions. Chalcogenide fibers were stored under anhydrous Nitrogen atmosphere inside a sealed box. This procedure allows us to control the moisture content of atmosphere at which the glass fibers are exposed and therefore to prevent the suspected aging process of As_2S_3 fibers.

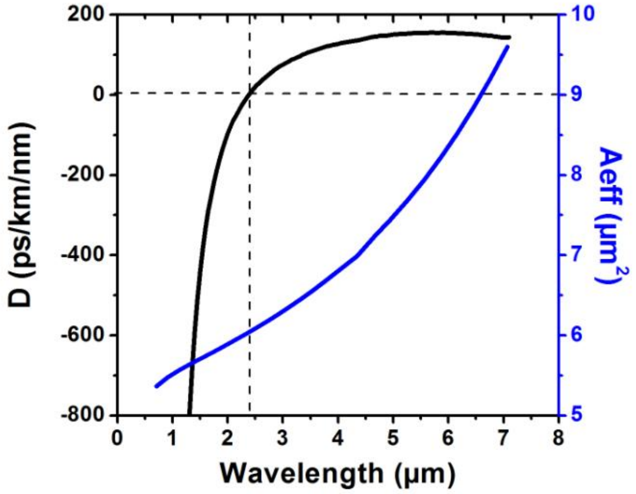

Figure 42: Numerical modeling of the fundamental mode of the suspended-core chalcogenide fiber. Chromatic dispersion curve (black line) and effective mode area (blue curve).

Figure 42 reports numerical simulations of modal properties based on the fiber geometry derived from the SEM analysis (see Figure 41.a).

Our suspended core fiber exhibits a zero-dispersion wavelength (ZDW) close to 2.4 µm. The core size mainly governs the fiber dispersion properties and it was chosen in such a way that the ZDW fits in the wavelength range of maximal power of the tunable mid-infrared laser source used below.

3. Experimental set-up

Figure 43 shows the experimental setup used for supercontinuum generation. It consists of an Optical Parametric Oscillator (OPO) pumped by a Ti-Sapphire laser. It generates tunable pulses extending from 1.7 up to 3.2 µm, with pulse width of 200 fs at a repetition rate of 80 MHz. The 2-cm long sample of chalcogenide fiber is fixed onto a 3 axis holder. Incident beam is focused into the fiber using a mid-infrared aspheric Zinc Selenide (ZnSe) focus lens with a numerical aperture (NA) of 0.25 at 3.75 µm. This set-up allows us to pump the fiber under study on a wide range of wavelengths around its ZDW, so as to ensure an efficient SC generation [16]. Output supercontinuum is collected through a 0.5 m long multimode fluoride (InF_3) fiber with high transmission over the 0.3 - 5.5 µm spectral range. It is then analyzed by means of two Optical Spectrum Analyzers (OSA) covering 350 to 1200 nm and 1200 to 2400 nm, respectively as well as by a FTIR spectrometer in the range of 2.4 to 5 µm.

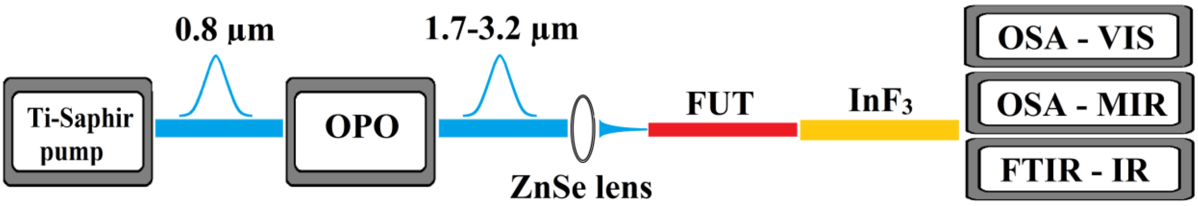

Figure 43: Experimental setup used for supercontinuum generation in the suspended-core chalcogenide fiber. FUT: fiber under-test.

4. Experimental results and discussions

A series of in-situ tests that evaluate the measured spectral broadening versus pump wavelength allowed us to select the suitable anomalous regime pump wavelength at 2.5 µm. From Figure 42 we evaluated the group-velocity dispersion β_2 to -0.06 $ps^2.m^{-1}$. The incoming average power was measured after the focusing lens, before being injected into the fiber. The maximum peak power available was 12 kW at an average power of 194 mW. Next we measured the coupling coefficient about 40% when using low input powers. Figure 44 shows the output spectra recorded for the tested fiber under 2.5-µm pump wavelength according to injected peak power increasing from 1.25 to 4.86 kW.

The nonlinear index of the material is $n_2 \sim 2.8\ 10^{-18}\ m^2.W^{-1}$ at 1550 nm, which corresponds, from the 6.1-μm^2 effective mode area depicted in Figure 42, to a nonlinear Kerr coefficient

$\gamma = 1.15\ W^{-1}.m^{-1}$. The nonlinear length ($L_{NL}$) decreases from 0.7 mm to 0.18 mm when the input peak power is increased from 1.25 kW to 4.86 kW respectively. Since the nonlinear length scale of this As_2S_3 MOF is estimated below the millimeter range according to the input pulse power, the large spectral broadening is expected to take place in the first millimeters of the MOF. For the highest peak power, the injected pulse corresponds to a high soliton number N = 36. The chalcogenide fiber is here clearly pumped in the anomalous dispersion regime, and is characterized by a strong and rapid self-phase modulation process followed by soliton fission. Subsequent propagation is then associated with soliton dynamics and dispersive wave generation. Note that in this case the fission occurs randomly due to the significant role of modulation instability when N>20 [16], thus leading to significant degradation of supercontinuum coherence properties. The broadest resulting spectrum extends from 600 nm to 4100 nm in the -40 dB range whereas the generated bandwidth at -20 dB covers from 700 nm to 3800 nm. Note that we outstandingly reached the glass transmission limit from the visible side. Besides, no damage was reported on the MOF sample even at maximum incoming power. Here, the corresponding output average power is ~ 90% of the input power.

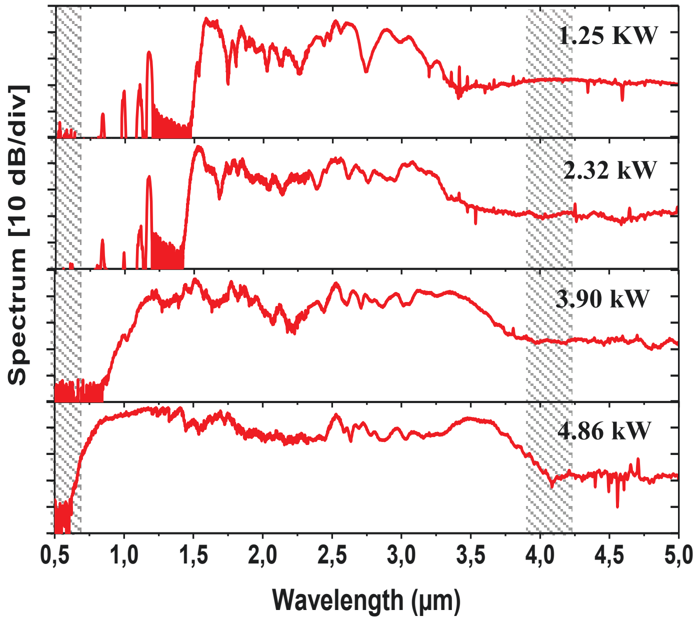

Figure 44: Experimental recording of supercontinuum generation in a 20-mm long sample of suspended-core chalcogenide fiber for pump peak power increasing from 1.25 to 4.86 kW. Main features of the As_2S_3 transmission window are also displayed by means of hashed areas, the glass band gap (hashed zone at 0.6 µm) and SH absorption band (hashed zone at 4.0 µm).

In our previous work [2], the output spectrum bandwidth was critically correlated to MOF attenuation, especially to OH and SH absorptions, whereas numerical simulations neglecting these dramatic absorption peaks revealed that dynamics of supercontinuum generation could be extended until 5.5 µm. Here, the control of aging combined with a gradual reduction of the length of the fiber sample under-test allows to overcome the issue of OH absorption, but not completely that related to SH absorption. Hence, only 2 cm of fiber was used for this experiment to extend the SC long wavelength edge further to the MIR region. The broad spectrum cuts off in the MIR side at around 4.1 µm. It is primarily due to fiber attenuation, especially SH absorption around 4.0 µm. The signature of OH absorption can be observed using longer fiber segments, it depends at the same time on its concentration, its vibration modes and the degree of OH hydrogen bonding present in the glass. The combination of different vibration modes (stretching and bending) of weekly H-bonded OH and free OH in the glass provide a 500 nm bandwidth absorption band located around 2.76 µm spreading from 2.5 to 2.99 µm. Here, solitons successfully overcome these crucial absorptions and subsequently allow a better expansion of the spectrum in the MIR compared to our previous studies [2] However, the impact of SH absorption at 4.0 µm appears for high input pulse power. Gradual increasing of the pump power allows shifting the spectrum long wavelength edge further in the MIR region. However, note that the high SH absorption prevents here the efficient expansion of the spectral broadening beyond 4.1 µm.

5. **Conclusion**

In conclusion, we report here an As_2S_3 fiber-based supercontinuum source that covers 3500 nm extending from near visible to the mid-infrared by using a 200-fs pulsed pump with about 1 nJ energy at 2.5 µm. In particular, the SC bandwidth extends from the glass bandgap limit at 0.6 µm to the mid-infrared region around 4.1 µm. To our knowledge, this is the largest SC bandwidth generated in chalcogenide fibers. The remaining limitation of SC bandwidth is mainly related to the presence of the SH absorption peak. Additionally, we find that deleterious temporal evolution of the OH species of As_2S_3 MOF has been limited by the dry atmosphere storage technique, confirming thus the proposed aging hypothesis. A detailed study is in progress in order to discern the aging process and their inherent deleterious phenomena.

Acknowledgements

We acknowledge the financial support from the JSPS-CNRS Bilateral French-Japanese Program, the Conseil Régional de Bourgogne through the Photcom PARI program, as well as the French DGA. This project has been performed in cooperation with the Labex ACTION program (contract ANR-11-LABX-0001-01).

6. References

1. J. Hu, J. Meyer, K. Richardson, and L. Shah, "Feature issue introduction: mid-IR photonic materials," Optical Materials Express **3**, 1571-1575 (2013).
2. I. Savelii, O. Mouawad, J. Fatome, B. Kibler, F. Désévédavy, G. Gadret, J. C. Jules, P. Y. Bony, H. Kawashima, W. Gao, T. Kohoutek, T. Suzuki, Y. Ohishi, and F. Smektala, "Mid-infrared 2000-nm bandwidth supercontinuum generation in suspended-core microstructured Sulfide and Tellurite optical fibers," Optics Express **20**, 27083-27093 (2012).
3. P. Domachuk, N. A. Wolchover, M. Cronin-Golomb, A. Wang, A. K. George, C. M. B. Cordeiro, J. C. Knight, and F. G. Omenetto, "Over 4000 nm bandwidth of mid-IR supercontinuum generation in sub-centimeter segments of highly nonlinear tellurite PCFs," Optics Express **16**, 7161-7168 (2008).
4. F. Théberge, J.-F. Daigle, D. Vincent, P. Mathieu, J. Fortin, B. E. Schmidt, N. Thiré, and F. Légaré, "Mid-infrared supercontinuum generation in fluoroindate fiber," Optics Letters **38**, 4683-4685 (2013).
5. G. Qin, X. Yan, C. Kito, M. Liao, C. Chaudhari, T. Suzuki, and Y. Ohishi, "Ultrabroadband supercontinuum generation from ultraviolet to 6.28 μm in a fluoride fiber," Applied Physics Letters **95**, 161103 (2009).
6. J. H. V. Price, T. M. Monro, H. Ebendorff-Heidepriem, F. Poletti, P. Horak, V. Finazzi, J. Y. Y. Leong, P. Petropoulos, J. C. Flanagan, G. Brambilla, F. Xian, and D. J. Richardson, "Mid-IR supercontinuum generation from nonsilica microstructured optical fibers," IEEE Journal of Selected Topics in Quantum Electronics **13**, 738-749 (2007).
7. J. Fatome, C. Fortier, T. N. Nguyen, T. Chartier, F. Smektala, K. Messaad, B. Kibler, S. Pitois, G. Gadret, C. Finot, J. Troles, F. Desevedavy, P. Houizot, G. Renversez, L. Brilland, and N. Traynor, "Linear and nonlinear characterizations of chalcogenide photonic crystal fibers," Journal of Lightwave Technology **27**, 1707-1715 (2009).
8. Y. Yu, X. Gai, T. Wang, P. Ma, R. Wang, Z. Yang, D.-Y. Choi, S. Madden, and B. Luther-Davies, "Mid-infrared supercontinuum generation in chalcogenides," Optical Materials Express **3**, 1075-1086 (2013).
9. M. R. Lamont, B. Luther-Davies, D.-Y. Choi, S. Madden, and B. J. Eggleton, "Supercontinuum generation in dispersion engineered highly nonlinear (γ = 10/W/m) As_2S_3 chalcogenide planar waveguide," Optics Express **16**, 14938-14944 (2008).
10. J. McCarthy, H. Bookey, S. Beecher, R. Lamb, I. Elder, and A. K. Kar, "Spectrally tailored mid-infrared super-continuum generation in a buried waveguide spanning 1750

nm to 5000 nm for atmospheric transmission," Applied Physics Letters **103**, 151103 (2013).

11. A. Al-kadry, C. Baker, M. El Amraoui, Y. Messaddeq, and M. Rochette, "Broadband supercontinuum generation in As_2Se_3 chalcogenide wires by avoiding the two-photon absorption effects," Optics Letters **38**, 1185-1187 (2013).
12. S. Shabahang, G. Tao, J. J. Kaufman, and A. F. Abouraddy, "Dispersion characterization of chalcogenide bulk glass, composite fibers, and robust nanotapers," Journal of the Optical Society of America B **30**, 2498-2506 (2013).
13. C. W. Rudy, A. Marandi, K. L. Vodopyanov, and R. L. Byer, "Octave-spanning supercontinuum generation in in situ tapered As_2S_3 fiber pumped by a thulium-doped fiber laser," Optics Letters **38**, 2865-2868 (2013).
14. J. Hu, C. R. Menyuk, L. B. Shaw, J. S. Sanghera, and I. D. Aggarwal, "Computational study of 3-5 μm source created by using supercontinuum generation in As_2S_3 chalcogenide fibers with a pump at 2 μm," Optics Letters **35**, 2907-2909 (2010).
15. W. Gao, M. El Amraoui, M. Liao, H. Kawashima, Z. Duan, D. Deng, T. Cheng, T. Suzuki, Y. Messaddeq, and Y. Ohishi, "Mid-infrared supercontinuum generation in a suspended-core As_2S_3 chalcogenide microstructured optical fiber," Optics Express **21**, 9573-9583 (2013).
16. J. M. Dudley, G. Genty, and S. Coen, "Supercontinuum generation in photonic crystal fiber," Reviews of Modern Physics **78**, 1135-1184 (2006).

VI. Article 3

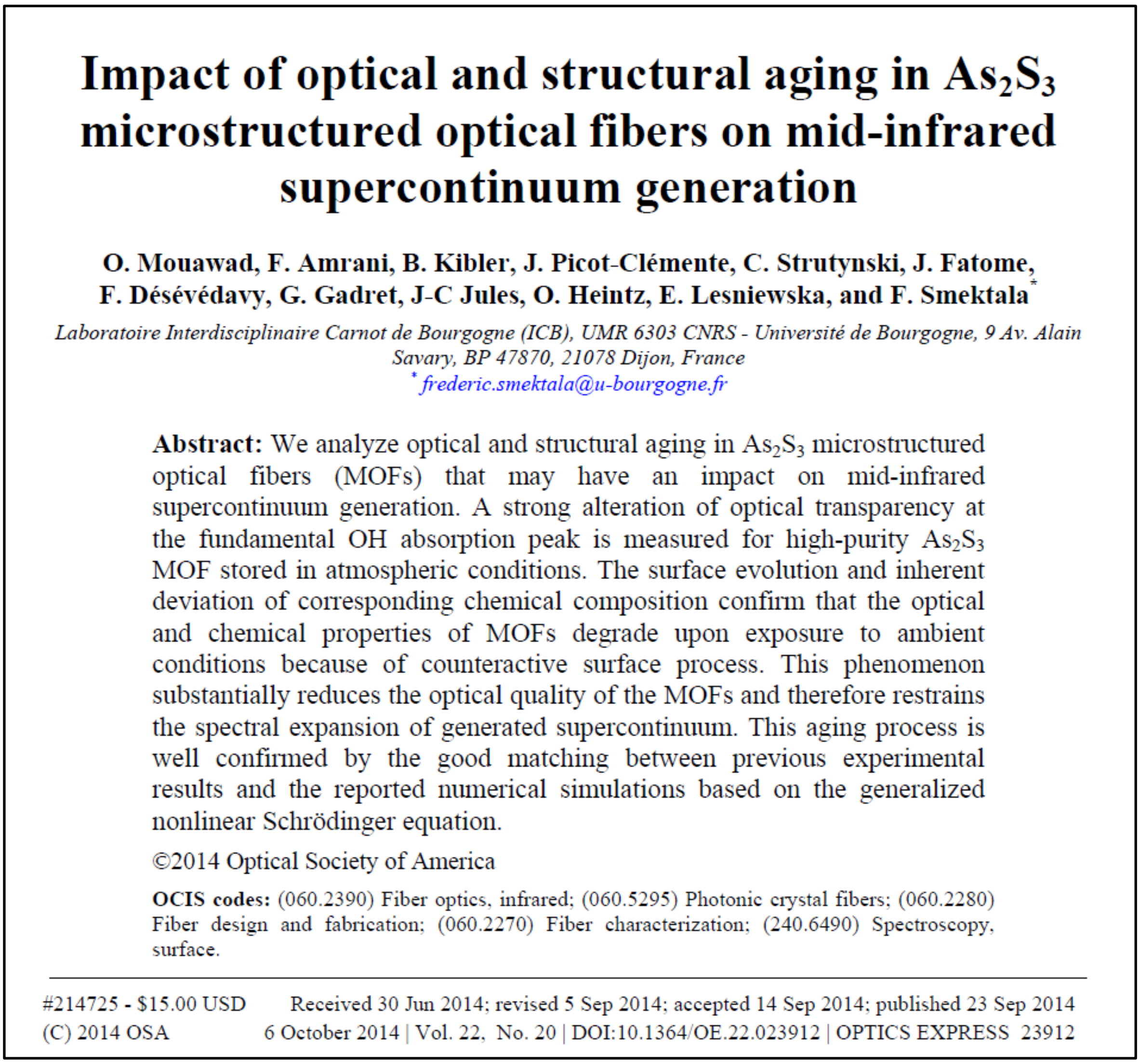

Impact of optical and structural aging in As_2S_3 microstructured optical fibers on mid-infrared supercontinuum generation

O. Mouawad, F. Amrani, B. Kibler, J. Picot-Clémente, C. Strutynski, J. Fatome, F. Désévédavy, G. Gadret, J-C Jules, O. Heintz, E. Lesniewska, and F. Smektala*

Laboratoire Interdisciplinaire Carnot de Bourgogne (ICB), UMR 6303 CNRS - Université de Bourgogne, 9 Av. Alain Savary, BP 47870, 21078 Dijon, France

* *frederic.smektala@u-bourgogne.fr*

Abstract: We analyze optical and structural aging in As_2S_3 microstructured optical fibers (MOFs) that may have an impact on mid-infrared supercontinuum generation. A strong alteration of optical transparency at the fundamental OH absorption peak is measured for high-purity As_2S_3 MOF stored in atmospheric conditions. The surface evolution and inherent deviation of corresponding chemical composition confirm that the optical and chemical properties of MOFs degrade upon exposure to ambient conditions because of counteractive surface process. This phenomenon substantially reduces the optical quality of the MOFs and therefore restrains the spectral expansion of generated supercontinuum. This aging process is well confirmed by the good matching between previous experimental results and the reported numerical simulations based on the generalized nonlinear Schrödinger equation.

OCIS codes: (060.2390) Fiber optics, infrared; (060.5295) Photonic crystal fibers; (060.2280) Fiber design and fabrication; (060.2270) Fiber characterization; (240.6490) Spectroscopy, surface.

#214725 - $15.00 USD Received 30 Jun 2014; revised 5 Sep 2014; accepted 14 Sep 2014; published 23 Sep 2014

(C) 2014 OSA 6 October 2014 | Vol. 22, No. 20 | DOI:10.1364/OE.22.023912 | OPTICS EXPRESS 23912

Impact of optical and structural aging in As_2S_3 microstructured optical fibers on mid-infrared supercontinuum generation

O. Mouawad, F. Amrani, B. Kibler, J. Picot-Clémente, C. Strutynski, J. Fatome,
F. Désévédavy, G. Gadret, J-C Jules, O. Heintz, E. Lesniewska, and F. Smektala*

Laboratoire Interdisciplinaire Carnot de Bourgogne (ICB), UMR 6303 CNRS - Université de Bourgogne, 9 Av. Alain Savary, BP47870, 21078Dijon, France
Corresponding author: frederic.smektala@u-bourgogne.fr

Abstract

We analyze optical and structural aging in As_2S_3microstructured optical fibers (MOFs) that may have an impact on mid-infrared supercontinuum generation. A strong alteration of optical transparency at the fundamental OH absorption peak is measured for high-purity As_2S_3 MOF stored in atmospheric conditions. The surface evolution and inherent deviation of corresponding chemical composition confirm that the optical and chemical properties of MOFs degrade upon exposure to ambient conditions because of counteractive surface process. This phenomenon substantially reduces the optical quality of the MOFs and therefore restrains the spectral expansion of generated supercontinuum. This aging process is well confirmed by the good matching between previous experimental results and the reported numerical simulations based on the generalized nonlinear Schrödinger equation.

OCIS codes: (060.2390) Fiber optics, infrared; (060.5295) Photonic crystal fibers; (060.2280) Fiber design and fabrication; (060.2270) Fiber characterization; (240.6490) Spectroscopy, surface.

1. Introduction

Among the wide range of functionalities currently realized by photonic devices, providing reliable and stable light source that covers a broad spectral bandwidth is of major importance. Such supercontinuum (SC) sources can be obtained through nonlinear propagation of a pump beam into an optical waveguide by exploiting various nonlinear wavelength conversion processes [1]. For efficient SC generation, one has to use a low loss and highly nonlinear medium pumped with high power density close to its zero dispersion regime. Many applications exist for broadband mid-infrared (MIR) sources operating in the chemical and biological fingerprint regions within the atmospheric transmission windows [2-5]. To this end, MIR SC sources based on chalcogenide fibers and waveguides appear as an attractive solution thanks to their wide transparency, high nonlinearity [6-8], and thanks to the latest achievements of synthesis of low loss As_2S_3 fibers [6, 9-13]. However, this glass composition suffers from weakness represented by an uncontrolled drift in performance over time. This is mainly due to physical and chemical aging processes [14]. Thus extending efficient MIR SC generation requires a detailed understanding and control of the evolution of optical and chemical properties for such a material [9, 15, 16].

We previously reported on experimental observation of MIR SC generation in low-loss As_2S_3 suspended-core MOFs [Article 1-9]. The spectral broadening was beyond 2000-nm bandwidth from 1 μm to 3.2 μm. Numerical simulations were performed in order to check the underlying nonlinear processes. When considering the fiber losses which were experimentally measured in a single-index fiber, numerical results predicted a theoretical broadening with the MIR edge until 5.5 μm, whereas that experimentally recorded was located around 3.2 μm. In order to better fit the experimental SC, in particular close to the SH and OH absorption bands, extra losses were taken into account around 2.9 μm and 4 μm. This confirmed the under-evaluation of extrinsic absorption bands experimentally measured, or an aging process of our fibers under room atmosphere. Optical degradation is a natural consequence of the aging process [9, 15, 16]. However, the origin, mechanism and kinetics of chemical as well as optical aging of As_2S_3 MOFs remain unclear. The objective of this study is to show unequivocally the aging process of an As_2S_3 based suspended-core MOF in atmospheric conditions and its impact on SC generation. We perform numerical simulations that confirm the dynamic evolution of spectral broadening and its relation to extrinsic losses related to aging process evolving over storage at ambient atmospheric conditions. We identify the chemical and the inherent optical aging behaviors of the sulfide MOF by using a Fourier Transform InfraRed (FTIR) spectrometer. We present a first attempt to follow and prove the evolution occurring on the As_2S_3 glass surface upon naturally induced aging process in atmospheric conditions by means of Atomic Force Microscopy (AFM). The inherent chemical composition deviation on the surface is also studied thanks to X-ray Photoelectron Spectroscopy (XPS). Such an analysis confirms that the aging process substantially reduces the optical quality of the MOF, thus limiting SC generation further in the MIR.

2. Preparation of glass and fiber samples.

Glass used in this work was fabricated by the traditional melt quenching method. The detailed fabrication process of glass and fibers was described earlier [Article 1-9]. The obtained glass rod is 80 mm long with a diameter of 16 mm. It was cut evenly to two samples using a diamond saw. The first one was designated to draw MOFs with well defined parameters responding to experimental need. The corresponding MOF cross-section is shown in Figure 45. The second one was dedicated to preparation of specimens for AFM and XPS experiments.

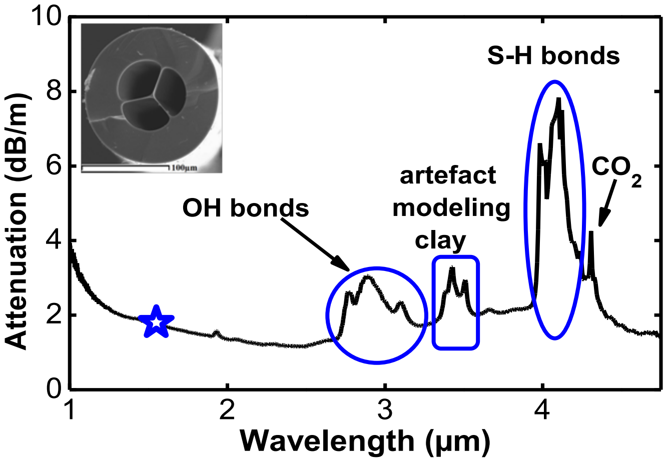

Figure 45: Attenuation spectrum of freshly drawn single index fiber (black solid line) and attenuation of the MOF measured at 1.55µm (blue star). Note that the absorption peak around 3.4µm is not related to the transmission of our fiber (i.e. artefact of our experimental setup [Article 1-9]). Inset: Cross-section image of our As_2S_3-suspended-small-core MOF captured by means of a scanning electron microscope

Figure 45 gives the attenuation spectrum of our low-loss As_2S_3 single-index fiber shortly after being drawn [Article 1-9]. Losses of optical fiber were estimated in free space by means of a FTIR spectrometer and using cut-back technique. Measurements were carried out on 5-m-long fiber segment with 20% of accuracy primarily caused by the quality of fiber cleaves.

Similar spectral loss measurements could not be successfully performed on suspended core fiber because of the small core diameter. However, cut-back measurements for the small-core MOF were performed using a continuous laser source emitting at 1.55µm, again readily after drawing, confirming thus the previous results registered on single-index fiber. Note that fundamental OH and SH absorption peaks emerge around 2.9 and 4.0µm respectively. According to the extinction coefficient $\varepsilon = 5$ dB/m/ppm (wt.) [17, 18], the OH absolute content is about 0.5ppm (wt.). SH concentration ($\approx$3.2 ppm) can be estimated from the spectrum referring to [19] for which extinction coefficient associated to the SH vibration at 4 µm is 2.5 dB/m/ppm. The peak arising at 4.26 µm is due to CO_2 absorption. This absorption does not evolve over time unlike those of OH and SH groups. Consequently, the CO_2 absorption was neglected in this study. Absorption peaks around 3.4 µm are unequivocally assigned to C-H bonds present in the modeling clay systematically used to fix the fiber during cut-back measurements. They are not always eliminated through cut back data treatment because of the possible irreproducibility in the way we fix the fibers. Note that clay is not used during SC generation experiments. The MOF design is such that it allows to tailor its zero-dispersion wavelength (ZDW) as close as possible to the range of maximum emission capability of the pump source near 2.3 µm while keeping a very high nonlinear coefficient as well as an efficient coupling of light into the core. We computed the fundamental mode properties of suspended core MOF based on the cross-section profile (see Figure 35 and [9]for more details). The combined material and waveguide modal dispersions result in a ZDW wavelength located close to 2.3 µm for the 3.2 µm core size. The corresponding effective mode area is about 6.5 µm^2 at the ZDW. Combined with high nonlinear refractive index ~2.8x10^{-18} m^2/W at 1.55 µm, the resulting nonlinear Kerr coefficient γ is 1175 W^{-1}.km^{-1} [9].

3. SC generation and impact of absorption bands

Figure 46 (a) shows the experimental SC spectrum obtained with a 12-days aged 45-mm-long MOF segment pumped by 200-fs pulses at 2.3 µm with 4.6 kW injected power (see Figure 37 and [9] for more details about the setup). The spectral broadening extends from 1.2 to 3.2 µm in the - 20dB range with a dip around 2.9 µm, where the different combinations of strongly and weakly bonded OH groups manifest themselves (Figure 45). Eventual influence of atmospheric absorptions in this wavelength range have been checked by registering the atmospheric spectrum in the conditions of our measurements. The absorptions of atmospheric water remains in the noise of the experimental measurements and are not detectable in the configuration of our set up. Here we provide a detailed analysis based on numerical simulations and chemical analysis to elucidate the strong limitations imposed in the nonlinear dynamics of this SC generation. Numerical results are obtained through the split-step Fourier-based solving of the generalized nonlinear Schrödinger equation [1] taking into account the full dispersion curve from (Figure 36) [9], measured fiber losses as well as self-steepening and analytical model of the Raman gain spectrum [9]. We recall that our pumping condition induces a strong and rapid self-phase modulation process followed by random soliton fission in the earlier centimeters of fiber [1, 9]. The generated SC is then associated to significant fluctuations from pulse to pulse and high degradation of the coherence degree. As a result, averaging over 50 simulations with different input noise imposed on the pulse pump was carried out to obtain spectral smoothing, similarly to our optical spectrum analyzer. Taking only into account the loss level experimentally measured for the single-index fiber (see Figure 45 and Figure 46 (b2)), the simulated SC spectrum does not match with the experimental one, as shown in Figure 46 (b1). Indeed considering measured losses on fibers freshly drawn implies a theoretical spectral broadening up to 5.5 µm, Figure 46 (b1). In order to reach a good agreement, extra losses at 2.9 and 4.0 µm have to be taken into account as previously suggested in (Article 1 [9]). This underlines that a time evolution of deleterious extrinsic absorption bands occurs over time upon exposure to atmosphere. This aging is mainly related to the chalcogenide glass sensitivity to ambient moisture [14-16].

To reveal the impact of OH and SH absorption bands on SC generation, we simulated extra losses at 2.9 and 4 µm by considering a simple Gaussian envelope for each absorption band while keeping background losses at the same level. We increased step by step absorption peaks of the two bands as shown in Figure 46 (c2)-2(e2) until retrieving a good agreement between the simulated SC and the experimental one. The amount of losses added for each step corresponds to approximately 10 times increase of OH and SH contents in ppm. We used the same factor for the two bands. Corresponding simulated SC spectra are shown in Figure 46 (c1)-2(e1). The impact of absorption peaks on SC generation in few centimeters of fiber becomes noticeable when considering extra losses at the level of several dB/cm (see Figure 46 (d1)-2(d2)). In particular, one can note the small dip around 2.9 µm in the MIR SC as well as a clear limitation of the SC expansion near 4 µm (in the -20dB bandwidth range). Finally, we have to extend losses up to 25 dB/cm for OH-peak and 75 dB/cm for the SH-peak so as to better match with our experimental SC spectrum. Such optical losses correspond to OH and SH concentrations near to 500 and 3200 ppm, respectively. We can then notice in Figure 46 (e1) an erosion of the MIR SC upper edge, which is now limited close to 3.35 µm as well as the clear presence of the OH absorption band centered at 2.9 µm. The output energy is about 60% of the input energy in Figure 46 (e1) (without taking into account Fresnel reflections), while being ~80% in Figure 46 (d1), thus corresponding to the range of the experimental measurement from (Article 1) [9]. From these considerations, we highly suppose that an aging process occurs on the surface of the suspended MOF core, leading to an increase of OH and SH absorptions.

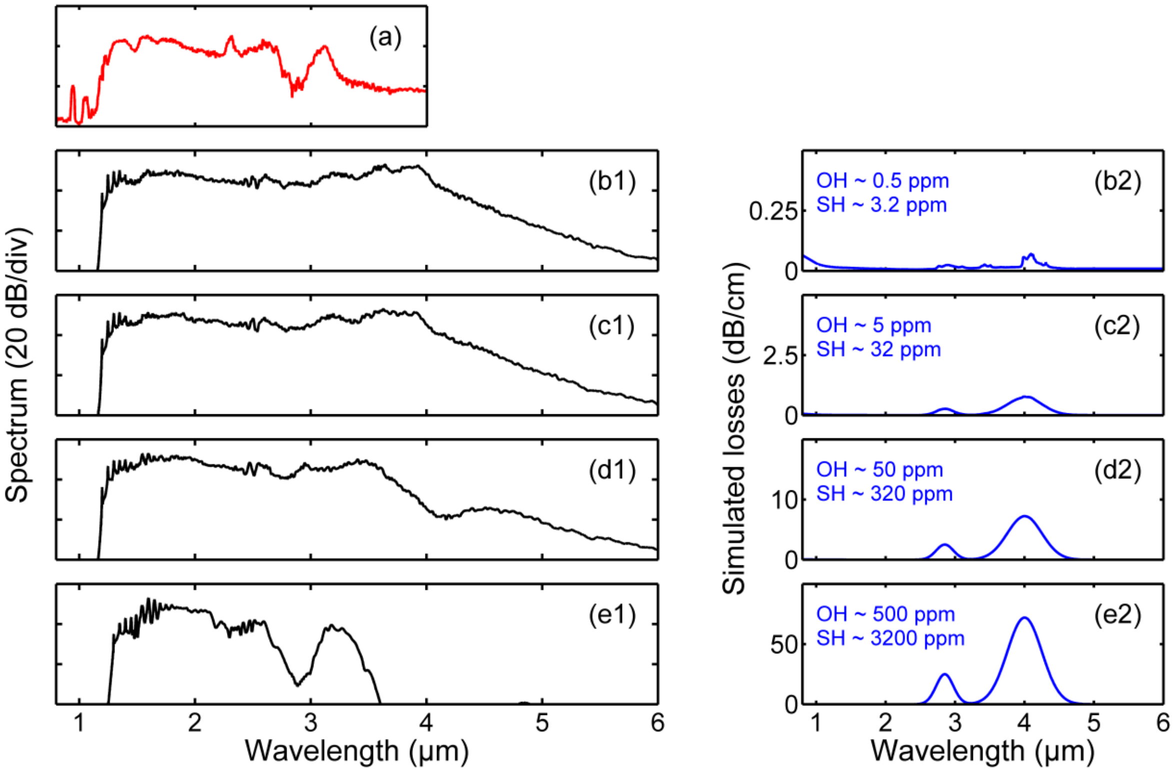

Figure 46: (a) Experimental SC generated in a 45-mm-long sample of MOF, (b1-e1) Corresponding numerical simulations taking into account different levels of OH and SH absorption bands depicted in (b2-e2), respectively.

4. Optical and structural aging

In order to confirm the preceding dynamics, we investigated the effect of atmospheric conditions on our sulfide MOF as a function of exposure time, in particular for hydroxyl species. We used a 3-m-long segment of 10-µm-large-core As_2S_3 MOF for FTIR analysis. Unlike the previous small core MOF, with such a large core MOF, spectral recording of transmission is possible with our FTIR setup and transmission spectra were systematically recorded over a 46-h period until a significant evolution of the transmission around 2.9 µm was obtained (Figure 47).

This study was performed at a temperature varying from 15 to 20°C and relative humidity between 50 and 60%. The fibre sample was mounted onto 3 axis holder in order to optimize coupling and detection of the light signal exclusively transmitted through the core of the MOF. An infrared camera was used to ensure that light was effectively coupled within the core of the MOF only. One can note that the suspended core is embedded in a robust clad which acts as a filter absorbing the unsuitable surrounding radiations potentially inducing photo-oxidation phenomena [20]. Despite that, the probed fiber was preserved in dark throughout the study period. A NICOLET 6700 *Fourier Transformed InfraRed (FTIR) spectrometer* was used to characterize the transmission spectra. The FTIR is seeded by an external halogen lamp providing higher power within the range of study (1.6-3.3µm) comparing to the standard light sources integrated within the spectrometer. In addition, signal outgoing the probed fibre was detected by means of external In-Sb detector, exhibiting high sensitivity within the range of interest. Our measurements are depicted in Figure 47 and show a naturally induced decrease in transmission and a substantial extinction of the signal around 2.9 µm upon exposure to atmospheric conditions. The deleterious impact of atmospheric moisture on As_2S_3 MOF occurs in the short time frame over the first hours (Figure 47). Few hours are sufficient to completely attenuate the light signal in this wavelength region. These results prove the critical need for a moisture-free storage immediately after the drawing process and prior to nonlinear experiments. Additionally, a degradation of the transmission occurs (Figure 47), in the short wavelength range. After 46 hours of exposure, this degradation reaches almost 20% below 2.0 µm. Such a phenomenon could be due to surface defects that emerge on the surface of the waveguide [15, 16], thus leading to light scattering.

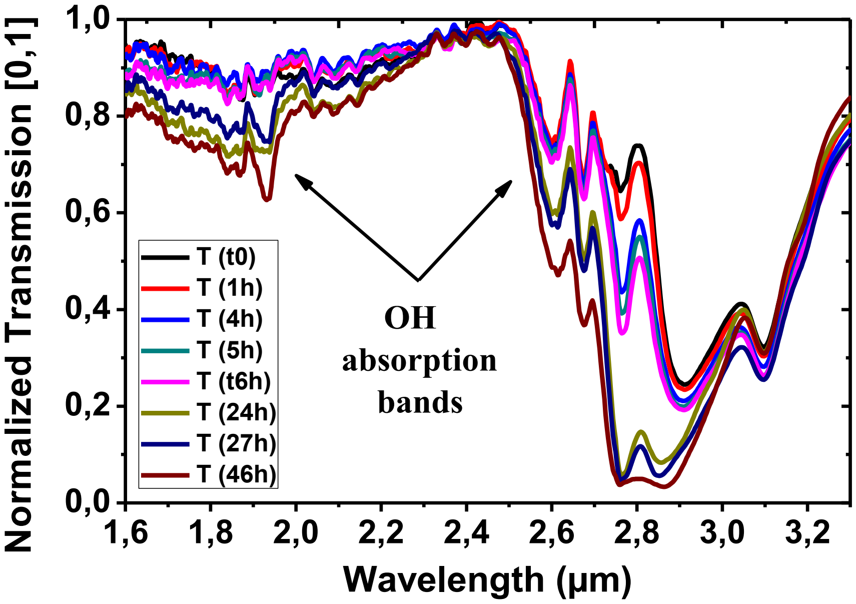

Figure 47: FTIR transmission spectra of large-core As_2S_3 MOF registered in-situ as a function of exposure time to atmospheric conditions.

To confirm this point, we therefore investigated the impact of the atmospheric moisture on surface roughness of As_2S_3 bulk glass. For that purpose, a glass sample was polished using SiC paper and diamond suspensions. One can precise that there is a difference in initial surface quality between AFM bulk samples and fiber samples, due to the polishing of bulks that might enhance aging through preliminary OH contamination or As_2O_3 formation. However, the impact of polishing does not interfere substantially in the aging process studied here. Indeed, rectangular fiber samples carefully prepared under dry atmosphere and exposed to similar conditions show, as on bulk samples, a substantial increase of their surface roughness. The specimen was stored under atmospheric conditions similar to those reported for fiber transmission study. Since all the surface of the sample is exposed to the environment, it is thus most prone to any contaminations. The evolution of glass surface at the nanometric scale was observed through AFM analysis (Bruker, Nanoscope 8) under controlled atmosphere in Peak Force mode. Throughout the exposure period, the bulk specimen was kept in a cleanroom dedicated for AFM measurements, in dark away from any surrounding light. As shown in Figure 48, the exposure to the previously defined conditions during 12 days, induces the appearance of random bumps which develop into faceted pyramids with square cross-section. However, the dimensions of these evolving defects substantially increase from

~15 nm on fresh sample to reach ~60 nm after 12 days of exposure to ambient conditions. The similarity of morphology in the present work and previous studies [21, 22] strongly suggests that surface defect are As_2O_3 crystals.

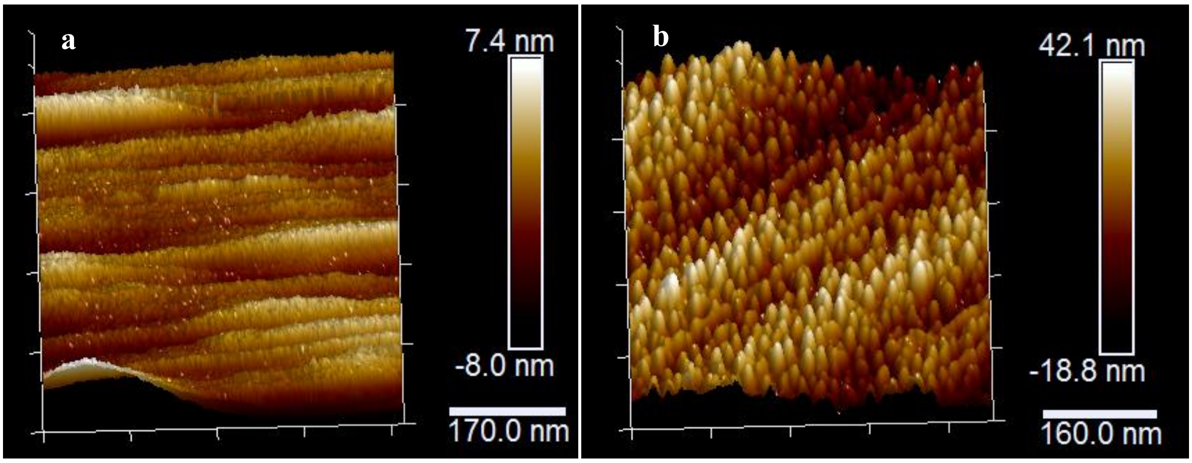

Figure 48: Top view of AFM 3D-pictures of the As_2S_3 bulk glass surface: (a) fresh sample; (b) 12 days of exposure.

We have also checked the evolution of the chemical bonds at the bulk sample surface through XPS analysis, by comparison of a fresh glass sample and a sample exposed to atmospheric conditions inside a dark compartment during 7 days. Note that fresh sample is probed immediately after polishing. XPS measurements were carried out by means of PHI Versaprobe 5000 apparatus (AlKa monochromated X-Ray source and 58 eV of pass energy for best resolved core level acquisitions). Peaks arising on XPS survey spectra are assigned to As and As-O core levels using a PHI Handbook for XPS spectra. Such measurements demonstrate a deviation from ideal As_2S_3 composition as illustrated in Figure 49, with the apparition of As-O bonds when the sample is exposed to ambient atmosphere. This observation is consistent with the AFM ones, and strengthens the hypothesis of As_2O_3 crystals growing at the glass surface. It demonstrates that the sulfide glass is susceptible to room temperature chemical reaction naturally induced in ambient atmosphere. This reaction process may diffuse in depth leading to local shift of the chemical composition inside the bulk glass [23].

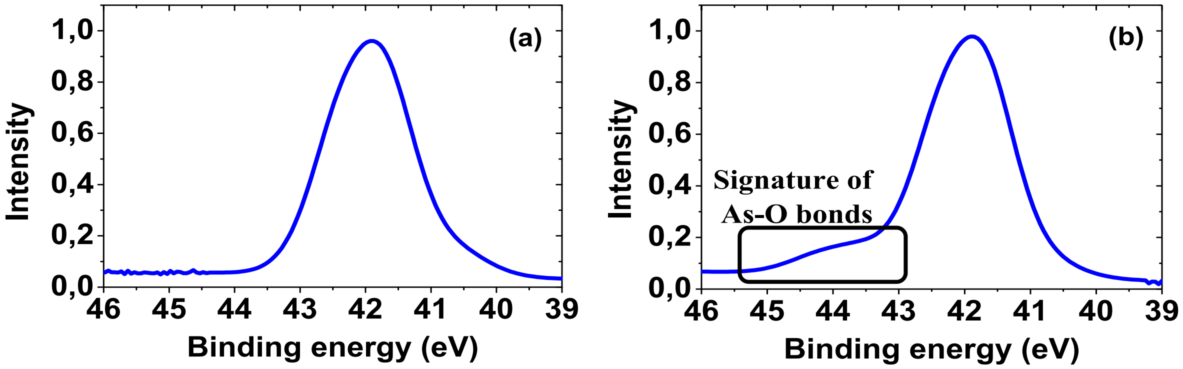

Figure 49: XPS spectra of As 3d core level of As_2S_3 glass: (a) fresh glass; (b) exposed to air during 7 days.

Finally, all of these results suggest an initial reaction of the glass with the atmospheric moisture surrounding the MOF core, which leads to the rapid apparition of absorbing -OH and -SH groups in the glass, with a subsequently evolution towards As_2O_3 species formation associated with an increase of glass surface roughness. These different phenomena contribute to increase the optical losses of As_2S_3 MOFs and degrade all their optical properties, including SC generation. However, it might be mitigated by the storage of freshly drawn MOF samples in dry atmosphere. In order to confirm the aforementioned hypothesis, the previous nonlinear experiment was recently reproduced using a sample stored in dry atmosphere [10]. Thus, an improvement of SC generation in the protected sample was indeed achieved by reaching a longer MIR edge around 4 µm without significant OH-induced dip at 2.9 µm as shown in Figure 50.

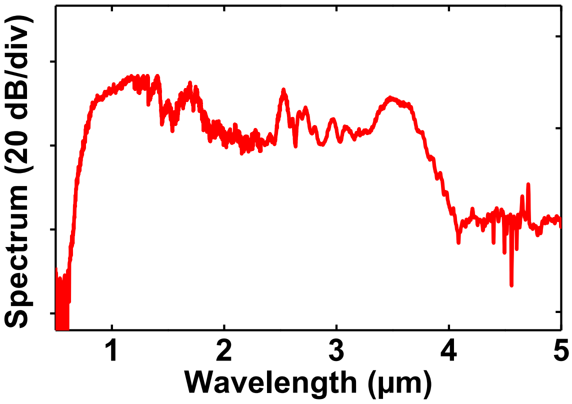

Figure 50:.Experimental supercontinuum registered on 20-mm-long segment of MOF protected from aging factors by storing in dry atmosphere [10].

Finally, all of these results suggest an initial reaction of the glass with the atmospheric moisture surrounding the MOF core, which leads to the rapid apparition of absorbing -OH and -SH groups in the glass, with a subsequently evolution towards As_2O_3 species formation associated with an increase of glass surface roughness. These different phenomena contribute to increase the optical losses of As_2S_3 MOFs and degrade all their optical properties, including SC generation. However, it might be mitigated by the storage of freshly drawn MOF samples in dry atmosphere. In order to confirm the aforementioned hypothesis, the previous nonlinear experiment was recently reproduced using a sample stored in dry atmosphere [12]. Thus, an improvement of SC generation in the protected sample was indeed achieved by reaching a longer MIR edge around 4µm without significant OH-induced dip at 2.9 µm.

5. Conclusion

Through FTIR, AFM and XPS measurements, we demonstrate the deleterious time evolution of As_2S_3 MOFs upon exposure of the MOFs core to atmospheric moisture. FTIR experiments confirm that extra losses related with OH bands at 2.9 µm occur in the MOFs. Moreover a deleterious evolution of SH absorption band is likely to occur simultaneously. The exposure of As_2S_3 glass to atmospheric conditions leads to the development and the growth of pyramidal shapes surface defects, which increase glass surface roughness observed by AFM. These surface structures arise from reaction with the atmosphere and strong suggestion for As_2O_3 crystals formation is emphasized by XPS results. Substantial amplification of OH absorption bands occurring over the first hours imposes the necessity of specific storage of As_2S_3 MOFs in dry conditions, immediately after the drawing process. The efficiency of specific storage allowed to overcome the OH limitation and to extend the supercontinuum up to 4 µm.

Acknowledgments

We acknowledge the financial support from the Conseil Régional de Bourgogne through thePhotcom PARI program, as well as the French DGA. This project has been performed incooperation with the Labex ACTION program (contract ANR-11-LABX-0001-01).

6. References

1. J. M. Dudley, and J. R. Taylor, *Supercontinuum generation in optical fibers* (Cambridge University Press, 2010).
2. T. M. Monro, S. Warren-Smith, E. P. Schartner, A. François, S. Heng, H. Ebendorff-Heidepriem, and S. Afshar V, "Sensing with suspended-core optical fibers," Optical Fiber Technology **16**, 343-356 (2010).
3. V. Ta'eed, N. J. Baker, L. Fu, K. Finsterbusch, M. R. E. Lamont, D. J. Moss, H. C. Nguyen, B. J. Eggleton, D.-Y. Choi, S. Madden, and B. Luther-Davies, "Ultrafast all-optical chalcogenide glass photonic circuits," Optics Express **15**, 9205-9221 (2007).
4. J. S. Sanghera, L. Brandon Shaw, and I. D. Aggarwal, "Chalcogenide glass-fiber-based mid-IR sources and applications," IEEE Journal of Selected Topics in Quantum Electronics, **15**, 114-119 (2009).
5. A. Cerqueira, "Recent progress and novel applications of photonic crystal fibers," Reports On Progress In Physics **73**, 024401 (2010).
6. J. H. V. Price, T. M. Monro, H. Ebendorff-Heidepriem, F. Poletti, P. Horak, V. Finazzi, J. Y. Y. Leong, P. Petropoulos, J. C. Flanagan, G. Brambilla, F. Xian, and D. J. Richardson, "Mid-IR Supercontinuum Generation From Nonsilica Microstructured Optical Fibers," IEEE Journal of Selected Topics in Quantum Electronics **13**, 738-749 (2007).
7. M. R. Lamont, B. Luther-Davies, D.-Y. Choi, S. Madden, and B. J. Eggleton, "Supercontinuum generation in dispersion engineered highly nonlinear (γ = 10/W/m) As_2S_3 chalcogenide planar waveguide," Optics Express **16**, 14938-14944 (2008).
8. S. D. Le, D. M. Nguyen, M. Thual, L. Bramerie, M. Costa e Silva, K. Lenglé, M. Gay, T. Chartier, L. Brilland, D. Méchin, P. Toupin, and J. Troles, "Efficient four-wave mixing in an ultra-highly nonlinear suspended-core chalcogenide $As_{38}Se_{62}$ fiber," Optics Express **19**, 653-660 (2011).
9. I. Savelii, O. Mouawad, J. Fatome, B. Kibler, F. Désévédavy, G. Gadret, J. C. Jules, P. Y. Bony, H. Kawashima, W. Gao, T. Kohoutek, T. Suzuki, Y. Ohishi, and F. Smektala, "Mid-infrared 2000-nm bandwidth supercontinuum generation in suspended-core microstructured Sulfide and Tellurite optical fibers," Optics Express **20**, 27083-27093 (2012).
10. O. Mouawad, J. Picot-Clémente, F. Amrani, C. Strutynski, J. Fatome, B. Kibler, F. Désévédavy, G. Gadret, J. C. Jules, D. Deng, Y. Ohishi, and F. Smektala, "Multioctave midinfrared supercontinuum generation in suspended-core chalcogenide fibers," Optics Letters **39**, 2684-2687 (2014).

11. A. E. Kurganova, G. E. Snopatin, and M. F. Churbanov, "Purification of glass melts in the As-Se system with vacuum distillation," Glass Physics and Chemistry **38**, 300-306 (2012).
12. V. Q. Nguyen, J. S. Sanghera, B. Cole, P. Pureza, F. H. Kung, and I. D. Aggarwal, "Fabrication of arsenic sulfide optical fiber with low hydrogen impurities," Journal of the American Ceramic Society **85**, 2056-2058 (2002).
13. G. E. Snopatin, V. S. Shiryaev, V. G. Plotnichenko, E. M. Dianov, and M. F. Churbanov, "High-purity chalcogenide glasses for fiber optics," Inorganic Materials **45**, 1439-1460 (2009).
14. P. Toupin, L. Brilland, D. Mechin, J. Adam, and J. Troles, "Optical aging of chalcogenide microstructured optical fibers," Journal of Lightwave Technology **32**, 2428-2432 (2014).
15. M. F. Churbanov, V. S. Shiryaev, V. V. Gerasimenko, A. A. Pushkin, I. V. Skripachev, G. E. Snopatin, and V. G. Plotnichenko, "Stability of the optical and mechanical properties of chalcogenide fibers," Inorganic Materials **38**, 1063-1068 (2002).
16. Y.-F. Niu, J.-P. Guin, A. Abdelouas, T. Rouxel, and J. Troles, "Durability of an As_2S_3 chalcogenide glass: optical properties and dissolution kinetics," Journal of Non-Crystalline Solids **357**, 932-938 (2011).
17. J. S. Sanghera, and I. D. Aggarwal, "Active and passive chalcogenide glass optical fibers for IR applications: a review," Journal of Non-Crystalline Solids **256-257**, 6-16 (1999).
18. G. Fonteneau, D. Trégoat, and J. Lucas, "Determination du coefficient d'extinction molaire de OH- dans les verres fluores a base de metaux lourds," Materials Research Bulletin **20**, 1047-1051 (1985).
19. V. G. Borisevich, V. G. Plotnichenko, I. V. Scripachev, and M.F. Churbanov, "Extinction coefficient of SH groups in vitreous arsenic sulphide," Russian High Purity Substances Journal **4**, 759-762 (1990).
20. D.-Y. Choi, S. Madden, D. Bulla, A. Rode, R. Wang, and B. Luther-Davies, "SU-8 protective layer in photo-resist patterning on As_2S_3 film," physica status solidi (c) **8**, 3183-3186 (2011).
21. J. Dikova, N. Starbov, and K. Starbova, "The mechanism of photoinduced transformations in amorphous As_2S_3 thin films," Journal of Non-Crystalline Solids **167**, 50-58 (1994).
22. J. T. Bloking, S. Krishnaswami, H. Jain, M. Vlcek, and R. P. Vinci, "Photoinduced changes in the surface morphology of $As_{50}Se_{50}$ chalcogenide glass films," Optical Materials **17**, 453-458 (2001).

23. S. H. Messaddeq, V. R. Mastelaro, M. Siu Li, M. Tabackniks, D. Lezal, A. Ramos, and Y. Messaddeq, "The influence of oxygen in the photoexpansion of GaGeS glasses," Applied Surface Science **205**, 143-150 (2003).

VII. Conclusion

In summary, we successfully demonstrated an experimental supercontinuum spanning over 2000 nm in few centimeters of sulfur-based chalcogenide suspended-core microstructured optical fiber. The later bandwith was increased up to 3500 nm when fibers were subject to preventive protection procedures. Such procedures allow to control the naturally induced drift of optical and chemical properties of the fiber device.

The global SC system consists in optical parametric oscillator pumped with Ti-sapphire laser, followed by the low loss, highly nonlinear As_2S_3 MOFs segments. The seed source generates ultrashort pulses of 200-fs FWHM at 80 MHz repetition rate. Advantageously, it is tunable between 1.7 and 3.2 µm, allowing thus a suitable fiber pumping in the anomalous dispersion regime, highly favorable for efficient SCG.

A continuous supercontinuum of 2000 nm bandwidth, extending from ~1.2 µm to ~3.2 µm, with characteristic dip around 2.9 µm, were registered in 4.5 cm segment of As_2S_3 MOF, pumped in the anomalous dispersion regime, close to its ZDW. The dip is consistent with the extrinsic OH absorption band mostly related to the glass synthesis technique and the aging phenomenon. The supercontinuum bandwidth is successfully increased on protected fibers. Protection of fiber devices is realized by continuous storing of the freshly drawn fiber's specimen under dry atmosphere prior to nonlinear optics experiments. We successfully registered a flat spectrum spreading over 3500 nm, extending from ~0.6 µm to ~4.1 µm, in 2.0 cm segment of As_2S_3 MOFs. Herein, no dip is interrupting the spectrum flatness. In both cases, As_2S_3 fibers with comparable geometric design and optical loss level have been used in the experiments.

Theoretical simulations and modeling have been carried out to study the SC generation mechanism and investigate the limits of SC long wavelength edge limits of SC in the chalcogenide fibers. The supercontinua generated within the fibers are characterized by a strong and rapid self-phase modulation process followed by soliton fission in the earlier centimeters of the fiber. In this case the soliton fission occurs randomly due to the significant role of modulation instability when $N >> 20$.

The MIR spectrum wavelength edge is primarily limited by the hydrogenated (OH and SH) extrinsic absorption losses and their time evolution, dramatically decreasing the nonlinear effects efficiency and leading to more and more narrow spectrum. Taking into account the loss level experimentally measured for the freshly drawn fiber, the simulated SC spectrum does not match with that registered on unprotected sample. In order to reach a good agreement, extra losses of 2500 dB/m for OH absorptions at 2.9µm and 7500 dB/m for SH absorptions at 4.0µm have to be taken into account. Compared to values measured on freshly drawn fiber, the absolute content of OH and SH moieties have increased 1000 times upon aging process. This imposes the necessity of special storage of MOF in suitable conditions, immediately after the drawing process. In addition, exposure of As_2S_3 glass to atmospheric conditions initiates the development and the growth of pyramidal shapes surface defects and induces structural changes within the glass network.

Part 3: Optical, Topological and Structural Aging in As_2S_3 Microstructured Optical Fibers and Impact on Mid-Infrared Supercontinuum Spanning

I. Introduction

In the previous part, we demonstrated a crucial degradation of As_2S_3 MOFs upon exposure to ambient atmosphere. The holey nature of these fibres makes them prone to contamination and to subsequent degradation of their performance, particularly at OH and SH absorptions related wavelengths. The degradation dynamics are associated with glass hydration caused by H_2O and formation of OH bonds, preventing further extension of the SC long wavelength edge in the mid-IR region. This is extensively presented in part 2-Article 3. In addition, FTIR measurements demonstrate a substantial amplification of OH absorption bands occurring over the first hours of exposure to atmospheric conditions. This coincides with the emergence of pyramidal shape bumps defects which increases the glass surface roughness as shown by AFM. These surface structures are probed by XPS technique. We attribute them to the formation of As_2O_3 crystals arising from reaction with the ambient atmosphere.

The later observations motivated detailed investigations of MOF's time-dependent deterioration related to OH and SH contamination. MOF's surface and structural features evolving over time are also examined. Results of these studies are detailed in the following part.

Article 1 reports an extensive study of transmission aging of As_2S_3 MOFs with regards to exposure-time to ambient atmosphere. A time evolution of transmission spectra are surveyed using FTIR-spectroscopy technique. The most sever deleterious effects occur over the first 24 hours. Absorption bands are detailed and attributed to corresponding vibration modes. Based on Beer-Lambert law using the appropriate extinction coefficient reported in the literature, we estimated the absolute content of hydroxyl species accumulated over time as a result of this aging process. Finally, we demonstrate a proved promising preventive and protection tool.

In the light of previous studies discussed in Part1-Article 1, Article 2 presents a study of the hydration interactions between water vapor and the glass network. The later interactions are associated with shrinkage of As-S bonds glassy backbone within the glass matrix and grow of defects on the glass surface. The evolution of the glass network chemical composition is surveyed by FTIR spectroscopy. To respond to experimental requirements, a short length

MOF fiber sample is used in this study. The temporal evolution of the transmission spectra shows a progressive growth of new absorption bands, announcing modifications of the glass structure. The corrosive impact of atmospheric moisture on As_2S_3 glass is proved. On the other hand, the evolution of the surface roughness is conducted by means of Atomic Force Microscopy (AFM) technique. A specially designed rectangular fiber is used for these experiments. The surface roughness of glass samples is monitored with regards to time exposure to different hygrometric and thermal conditions.

II. Article 1:

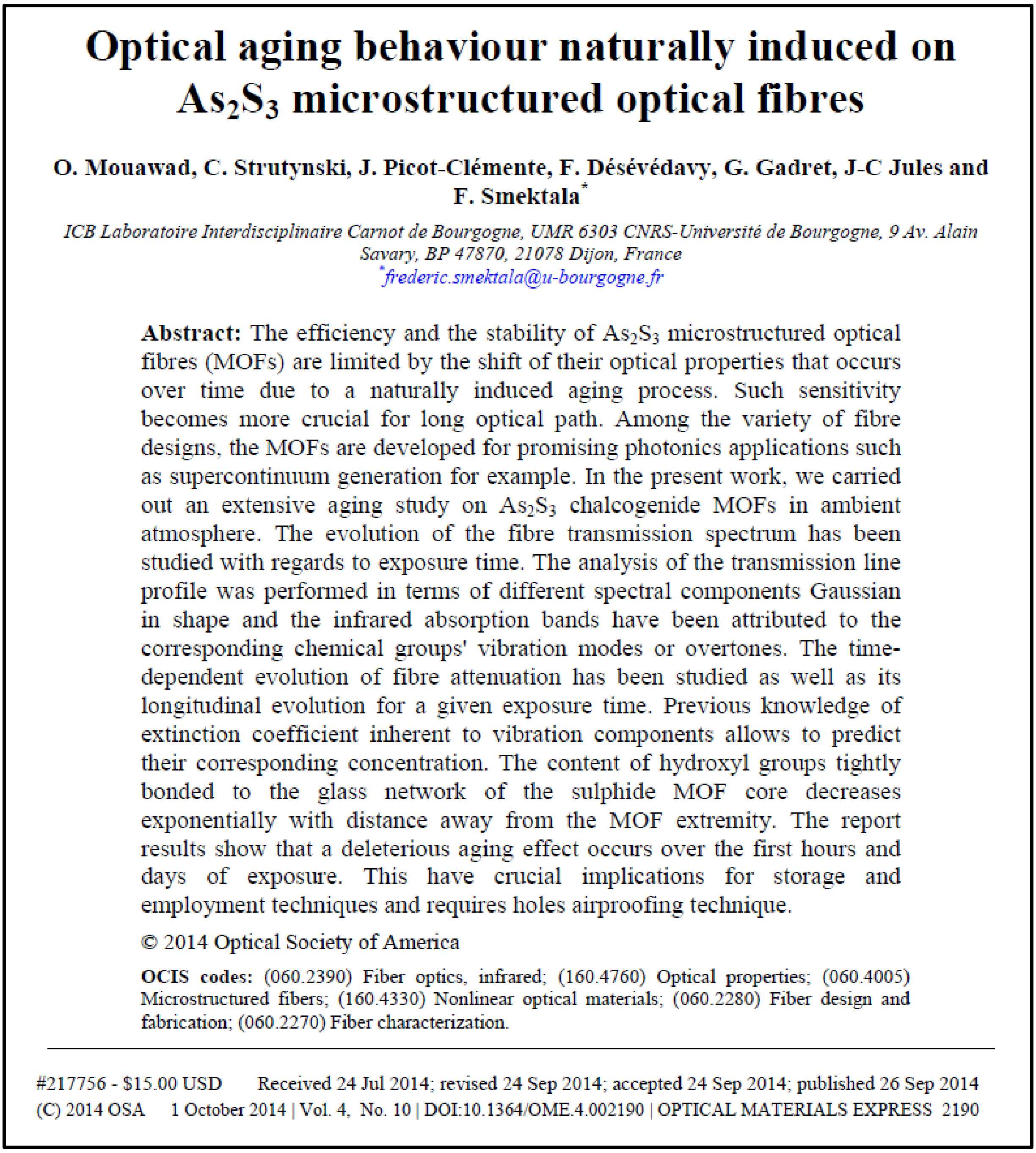

Optical aging behaviour naturally induced on As_2S_3 microstructured optical fibres

O. Mouawad, C. Strutynski, J. Picot-Clémente, F. Désévédavy, G. Gadret, J-C Jules and F. Smektala[*]

ICB Laboratoire Interdisciplinaire Carnot de Bourgogne, UMR 6303 CNRS-Université de Bourgogne, 9 Av. Alain Savary, BP 47870, 21078 Dijon, France
[*]*frederic.smektala@u-bourgogne.fr*

Abstract: The efficiency and the stability of As_2S_3 microstructured optical fibres (MOFs) are limited by the shift of their optical properties that occurs over time due to a naturally induced aging process. Such sensitivity becomes more crucial for long optical path. Among the variety of fibre designs, the MOFs are developed for promising photonics applications such as supercontinuum generation for example. In the present work, we carried out an extensive aging study on As_2S_3 chalcogenide MOFs in ambient atmosphere. The evolution of the fibre transmission spectrum has been studied with regards to exposure time. The analysis of the transmission line profile was performed in terms of different spectral components Gaussian in shape and the infrared absorption bands have been attributed to the corresponding chemical groups' vibration modes or overtones. The time-dependent evolution of fibre attenuation has been studied as well as its longitudinal evolution for a given exposure time. Previous knowledge of extinction coefficient inherent to vibration components allows to predict their corresponding concentration. The content of hydroxyl groups tightly bonded to the glass network of the sulphide MOF core decreases exponentially with distance away from the MOF extremity. The report results show that a deleterious aging effect occurs over the first hours and days of exposure. This have crucial implications for storage and employment techniques and requires holes airproofing technique.

OCIS codes: (060.2390) Fiber optics, infrared; (160.4760) Optical properties; (060.4005) Microstructured fibers; (160.4330) Nonlinear optical materials; (060.2280) Fiber design and fabrication; (060.2270) Fiber characterization.

#217756 - $15.00 USD Received 24 Jul 2014; revised 24 Sep 2014; accepted 24 Sep 2014; published 26 Sep 2014
(C) 2014 OSA 1 October 2014 | Vol. 4, No. 10 | DOI:10.1364/OME.4.002190 | OPTICAL MATERIALS EXPRESS 2190

Optical aging behaviour naturally induced on As_2S_3 microstructured optical fibres

O. Mouawad, C. Strutynski, J. Picot-Clémente, F. Désévédavy, G. Gadret, J-C Jules and F. Smektala*

ICB Laboratoire Interdisciplinaire Carnot de Bourgogne, UMR 6303 CNRS-Université de Bourgogne, 9 Av. Alain Savary, BP 47870, 21078 Dijon, France

Corresponding author: frederic.smektala@u-bourgogne.fr*

Abstract

The efficiency and the stability of As_2S_3 microstructured optical fibres (MOFs) are limited by the shift of their optical properties that occurs over time due to a naturally induced aging process. Such sensitivity becomes more crucial for long optical path. Among the variety of fibre designs, the MOFs are developed for promising photonics applications such as supercontinuum generation for example. In the present work, we carried out an extensive aging study on As_2S_3 chalcogenide MOFs in ambient atmosphere. The evolution of the fibre transmission spectrum has been studied with regards to exposure time. The analysis of the transmission line profile was performed in terms of different spectral components Gaussian in shape and the infrared absorption bands have been attributed to the corresponding chemical groups' vibration modes or overtones. The time-dependent evolution of fibre attenuation has been studied as well as its longitudinal evolution for a given exposure time. Previous knowledge of extinction coefficient inherent to vibration components allows to predict their corresponding concentration. The content of hydroxyl groups tightly bonded to the glass network of the sulphide MOF core decreases exponentially with distance away from the MOF extremity. The report results show that a deleterious aging effect occurs over the first hours and days of exposure. This has crucial implications for storage and employment techniques and requires holes airproofing technique.

OCIS codes: (060.2390) Fiber optics, infrared; (160.4760) Optical properties; (060.4005) Microstructured fibers; (160.4330) Nonlinear optical materials; (060.2280) Fiber design and fabrication; (060.2270) Fiber characterization.

1. Introduction

Chalcogenide glasses of different compositions are progressively developed for their potentials in a widespread variety of applications in the field of optic, spectroscopy [1], telecommunication [2] or biology. The reputation of these materials is attributed to their combined properties of broad transparency window, reasonably low optical losses, nonlinear properties, reasonable chemical and physical durability [3, 4]. The performance of chalcogenide based devices is strongly related to these combined fundamental characteristics. However, the scientific reliability and economic profitability impose a long-term service of the considered device, even if exposure of chalcogenide based devices to the real operation environment will eventually result in changes in the original physical and chemical properties. These changes correspond to an aging process, through chemical and physical processes.

Glass chemical aging is defined as a process of chemical interactions between glassy materials and their environment. It refers to chemical and structural modifications over time trough different mechanisms. Thermo-oxidative [5, 6], photo-induced [7, 8] and hydrolytic [9, 10] are the most known chemical degradation mechanisms. These processes become increasingly severe by extending exposure time, as by raising temperature levels, simultaneously as well as separately. Among others, this evolution is characterized by changes in glass transmission spectrum; new absorption bands appear while others are significantly amplified. Such process could eventually be of major benefits for different applications such as chemical sensing.

Glass physical aging is a process of structural relaxation [11]. The material evolves toward thermodynamic equilibrium. This is related to the preparation procedure of inorganic glasses [6, 12]. Glasses are defined as liquids which are frozen on time scale of experimental observation. They are considered thermodynamically metastable compared to crystals. Their enthalpy, free volume and entropy levels are higher than those of most stable forms. Thus, a glass matrix is continuously relaxing toward the equilibrium state of crystals over time. During real-time aging, this continual evolution of bulk properties is too slow to be measured and frequently unnoticeable. According to [6, 12] few and up to many years are needed to detect measurable changes in the mechanical properties for example. By heating glass above

Tg at sufficiently high temperature and quenching of the glass melt, initial material could be recycled. Therefore, physical aging is a thermo-reversible process.

Previous studies [6, 12-14] have shown a natural and induced physical as well as chemical aging of chalcogenide glasses. R.Ya. Golovchak and al. [6] showed that AsSe based-glasses exhibit physical aging after several months of storage. These phenomena might be accelerated by exposure to sub-band gap and above-band gap light. Herein, Se-based samples subjected to aging influences, lose their excess of configurational entropy, enthalpy or free volume (gained during melt quenching) to reach a more favourable thermodynamic state. M.F. Churbanov and al. [13] studied the stability of optical and mechanical properties of As-S-Se based chalcogenide glass fibres under different conditions. They underlined an essential preventive function of fibre coating, which allows maintaining the original properties of the fibres. Uncoated fibres have shown a tremendous decrease of mechanical and optical properties after few days of exposure to atmospheric conditions. This collapse becomes more dramatic under hostile conditions such as water [15] and acetone. The observed changes during storage are due to the nucleation and propagation of cracks on the fibre surface, impurity adsorption and other microstructural changes. Toupin and al. [14] have briefly reported an optical aging on As_2S_3 six holes-design microstructured optical fibre upon exposure to air. The optical aging was associated with a dynamic grow of OH and H_2O attributed absorption bands. Recently, our group has demonstrated the deleterious time evolution of As_2S_3 suspended core MOFs upon exposure of the MOF's core to atmospheric moisture and its impact on mid-infrared supercontinuum generation [16]. The kinetic of these changes reported in the literature has been studied on time scale from few hours to several years. It demonstrates that the optical properties are highly sensitive and severely degenerated in a few days. It was reported that 24 h are sufficient to completely quench the transmission of an As_2S_3 fibre immersed in water [15], whereas after 64 days of immersion in water, an As_2S_3 bulk sample lost almost 20% of its initial transmission [9]. In the case of fibres, optical losses level remains the most critical parameter. The control of this key criterion is a complicated process. It is based on sequential operations which are not limited to the synthesis technique. It extends to glass machining and device‘s storage. The recent significant improvements of synthesis strategies allow the fabrication of low loss chalcogenide fibres exhibiting standard or microstructured profile [3, 17-20]. Subsequent stages are necessary to preserve the amorphous material‘s optical loss at its post-synthesis level. Therefore, an aging study is needed, especially in the case of microstructured fibres, to provide an overview of exposure effects. It allows identifying the nature, the sources and the impacts of deterioration factors.

Thus, in this work, the chemical aging of sulphide based chalcogenide microstructured optical fibres in ambient atmosphere is accurately assessed. The purpose of the paper is to correlate the detrimental effect of atmospheric moisture with the aging behaviour of sulphide MOFs. We have undertaken a detailed study of components contributing to optical aging using infrared spectroscopy and we report results on real time monitoring of this optical aging in As_2S_3 MOFs. The transmission spectra were systematically registered until sixteen days of exposure under ambient thermal and hygrometric conditions. An estimation of content of absorbing species was calculated based on their attenuation measurements and their extinction coefficient. Finally, a preventive solution allows reducing aging kinetics and controlling resulting effects.

2. Samples preparation.

The highly pure As_2S_3 ingots were prepared by the conventional melt quenching method under vacuum inside silica ampoule using elemental highly pure starting products. Sulphur and arsenic were loaded into silica glassware and subjected to purification process under vacuum prior to their enclosing in the synthesis ampoule. Synthesis ampoule was loaded into a rocking furnace and heated up to the synthesis temperature for several hours. The final glass rod was obtained after quenching the melt and annealing the glass around the glass transition temperature. The mechanical drilling technique previously developed on chalcogenide glass in our lab permits to prepare the preform which is then drawn into suspended core MOF with specific parameters adapted for ease handling and technical requirements. The detailed used procedures have been already described elsewhere [19, 21, 22]. The fibre has 310 µm outer diameter and 10 µm of core diameter. No external coating is applied. Figure 51 shows a cross section picture of tested fibre captured by means of Scanning Electron Microscopy (SEM).

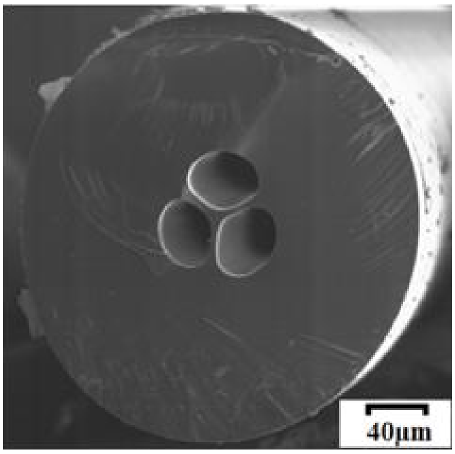

Figure 51: Profile of the tested chalcogenide As_2S_3 suspended-core fibre captured by means of SEM.

3. Experimental measurements.

The transmission spectra were recorded for wavelengths from 1.0 μm to 3.9 μm on 2.80 m of suspended core MOF sample. Measurements were carried out over 16 days at temperature ranging from 20 °C to 26 °C and relative humidity (RH) varying between 50 and 60%. A NICOLET 6700 Fourier Transformed InfraRed (FTIR) spectrometer was used to obtain the transmission spectra. Its source is an external halogen lamp emitting in the 0.1-5 μm range, providing higher output power than the optical source initially integrated in the spectrophotometer and allowing performing successfully this study on MOF sample within the range of interest. The MOF was mounted onto 3 axis holder in order to optimize light coupling exclusively in the MOF core. An infrared camera is used at the output end of the fibre to ensure that light is effectively guided in the core of the MOF only. This is important to stultify the possibility of any significant contribution of the fibre clad in the aging process since the fibre is not coated. At the input end a reflective objective is used to avoid chromatic effect. The beam transmitted along the fibre core is focused into an In-Sb detector using an optimal aspheric AMTIR lens. Note that previous in-situ experiments have proved the stability of the measurement system through the experimental period.

4. Experimental results and discussions.

4.1. Optical aging and speciation of absorbing species in As_2S_3 MOF.

Figure 52 shows the ratio of As_2S_3 MOF transmission spectra measured over time in conditions as described above. The transmission spectra (T_t) registered at different time are normalized to the initial one (T_0) plotted shortly after fibre drawing. Therewith, dramatic degradation of the optical transmission is observed in the whole transparency window over time. Furthermore, for 16 days of exposure, a significant decrease at a rate of 90% (resp. 40%) is registered at 1.0 µm (resp. 2.4 µm) transmission wavelength, whereas for the same 16 days exposure period, 15% average decrease is noted in the region above 3.3 µm. This phenomenon has been correlated to local structural modifications that occur on the surface of the fibre core such as cracks and roughness [9, 23]. In addition to the surface defects, nucleation and growth of nanometre and micrometre-sized particles at the exposed surface may induce additional scattering losses. The impact of these effects is more severe in the short wavelengths range because of the dimensions of concerning defects [10, 24, 25]. The growth and the contribution of these defects were unequivocally demonstrated in our previous study [16].

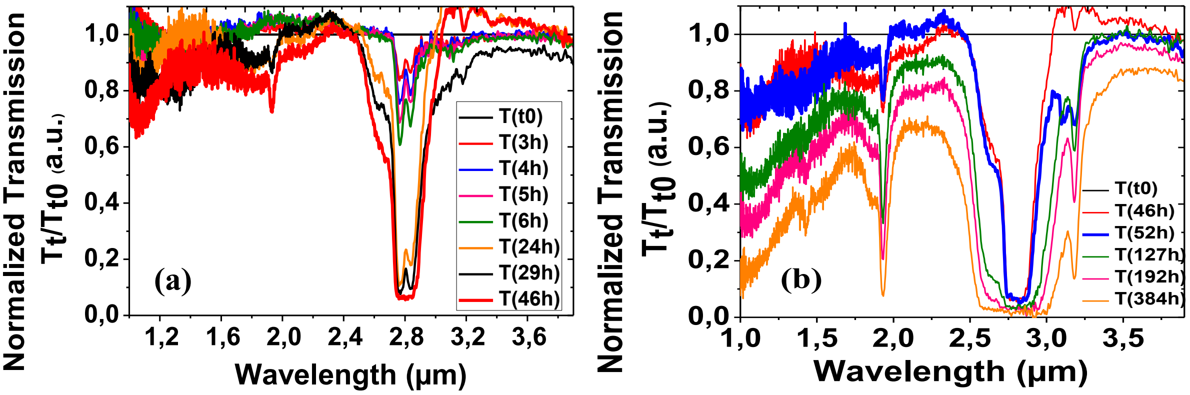

Figure 52: Transmission spectra registered on As_2S_3 MOF with amplification of absorption bands for an exposition time of (a) 0 to 46 h (b) 46 to 384 h.

The OH extrinsic absorption bands are inherent to chalcogenide glasses as for many other glasses. The combination of different vibration modes (stretching and bending) of weakly H-bonded OH groups and free OH in the glass, provide absorption bands located at well-defined wavelengths. Figure 52 shows the set of fundamental as well as combinations of OH and SH absorption peaks evolving in time. Moreover, new time-dependent absorption peaks arise over time. For sake of clarity, the results are selected according to their time evolution (Figure 52 (a) and Figure 52(b)).

Figure 52 (a) shows a highly deleterious impact of moisture on fibre over the first 24 h. The transmissions severely decreases at characteristic absorption bands centred on 2.77 µm and 2.84 µm. These characteristic bands can be assigned to the vibration modes of OH bonds in isolated adsorbed H_2O molecules [26-34]. At these wavelengths, OH absorption reaches 40% (resp. 33%) in less than 6 h and continues to rise until 90% (resp. 85%) after 24 h before reaching the detection limits after 46 h of storage in ambient conditions. These facts reflect a severe water-sorption on the surface of the guiding medium. Consequently, the first aging process corresponds to the adsorption of water molecules on the surface of the core of the MOF, where water molecules are weakly bonded to glass network. The water comes from the ambient atmosphere present in the holes surrounding the core of the MOF. Note that at this stage, no dramatic decrease is registered on transmission window despite the almost 20% of transmission loss below 1.3 µm. Following this early extinction of light signal around 2.8 µm, a gradual broadening of the absorption band occurs upon exposure time to natural atmosphere (Figure 52 (b)). This enlargement progress to the short wavelength side more than the opposite side. It reaches a maximum width of 800 nm centred at 2.8 µm after 384 h. This phenomenon is explained by the participation of the combination of different vibration modes of weakly H-bonded OH and free OH bonds, which are embedded under the overall peak. It is also reported in the literature that SH and OH absorption bands may occur above 3.0 µm [26]. Thus, the shift of the absorption signature towards 3.2 µm is the results of the implication of SH vibration modes at 3.11 µm [33] and vibration modes at 3.18 µm that we assume due to molecular water [9].

The survey of transmission spectra of tested MOF over time verifies thus a dramatic deviation of molecular water absorption band. However, additional vibration components remain embedded under the whole band. In order to discern and to attribute the set of vibration components involved in the aging process, a careful fitting of experimentally plotted spectra was conducted. The whole spectra have been fitted, assuming different peaks specific to different vibration modes previously reported for As_2S_3 glasses [9, 26-37] and summarized in Table 4.

Each spectrum was subjected for background correction by subtracting a linear background between the long and short wavelength edges of concerned peaks.

Figure 53 shows a typical ratio (T_t/T_0) of transmission spectrum after 32 h and 103 h respectively. Figure 54 shows the evolution of spectra over time between 4 h and 32 h, where spectra have been subjected to the fitting process with Gaussian components. We arranged different scales related to the spectra for better contrast. In

Figure 53 (a) corresponding to 4 h of MOF exposure to ambient atmosphere, the overall spectrum essentially consists in three peaks. The 2.77 µm and 2.84 µm absorptions are caused by the fundamental symmetric stretching vibration bands of OH bonds in molecular-adsorbed H_2O [37]. The 2.91 µm absorption band is related to OH groups tightly linked to the glass network trough arsenic (Table 4) [33]. Figure 54 (a)-(b) show resolved spectra for respectively 4 h and 6 h of exposure, where the absorption bands are unequivocally identified. In order to keep a good agreement between the experimental spectra and the fitting results for longer exposure times (24h and 32h, Figure 54 (c)-(d)), it was necessary to take into account the peak at 3.0 µm attributed to OH absorption bands in As_2S_3 glass [31]. The contribution of this absorption peak is clearly seen on Figure 54 (c)-(d).

The results of fitting allow estimating the peak height of each Gaussian component and consequently estimating the contribution of each vibration mode in the overall spectrum. With increasing exposure time, new absorption peaks arise and over 24 h of exposure, peaks at 2.54 µm, 2.63 µm, 2.70 µm and 3.0 µm are present (Figure 54 (c)). The 2.63 µm [35, 36], 2.70 µm [35, 36] and 3.0 µm [31] bands are caused by OH vibrations modes (Table 4). The 2.54 µm absorption band is assigned to the combination of vibrations modes of hydrogenous tightly linked with the sulphur atoms of the glass network [32]. The spectrum continues to evolve upon exposure. Eight hours later (Figure 54 (d)), new peaks centred at 3.11 µm and 3.18 µm have appeared. Similar behaviour is registered for 1.92 µm absorption peak simultaneously, which appears after 24 h of exposure and then continues to grow. The 3.11 µm absorption band is assigned to the stretching vibration mode of S-H bond [33], the

3.18 µm peak is related to molecular water absorption [9], whereas the 1.92 µm corresponds to the combination of the fundamental OH symmetric stretching vibration and the vibration due to hydroxyl strongly bonded to arsenic of the glass network (Table 4) [33]. It appears that an active dissociation mechanism occurs at the glass surface. It leads to produce =As-O-H and =As-S-H bonds with their absorption signature at characteristic wavelengths.

Table 4: Assignment of absorption bands in As_2S_3 chalcogenide glass in the 1 – 4.0 µm range in As_2S_3 glass. [2, 10, 27-37]

1/λ (cm^{-1})	**λ (µm)**	**Assignment**
3144	**3.18**	Vibrations of molecular water
3610	**2.84**	
3521	**2.77**	
3703	**2.7**	
3802	**2.63**	
3333	**3.0**	OH vibrations in As_2S_3
6950	**1.44**	
3436	**2.91**	Vibrations of =As-O-H
5210	**1.92**	
2480	**4.03**	SH vibrations in As_2S_3
3215	**3.11**	Vibrations of =As-S-H
3940	**2.54**	

From all these considerations, the proposed mechanism of chemical aging is the following: in the first hours of As_2S_3 MOFs exposure to ambient atmosphere, growing water adsorption occurs at the surface of the MOF core, because of the atmospheric steam present in the holes surrounding the fibre core. This adsorption leads progressively to a chemical reaction between adsorbed water and the sulphide glass in which =As-S-As= bridges are broken to form As-OH and H-S-As bonds.

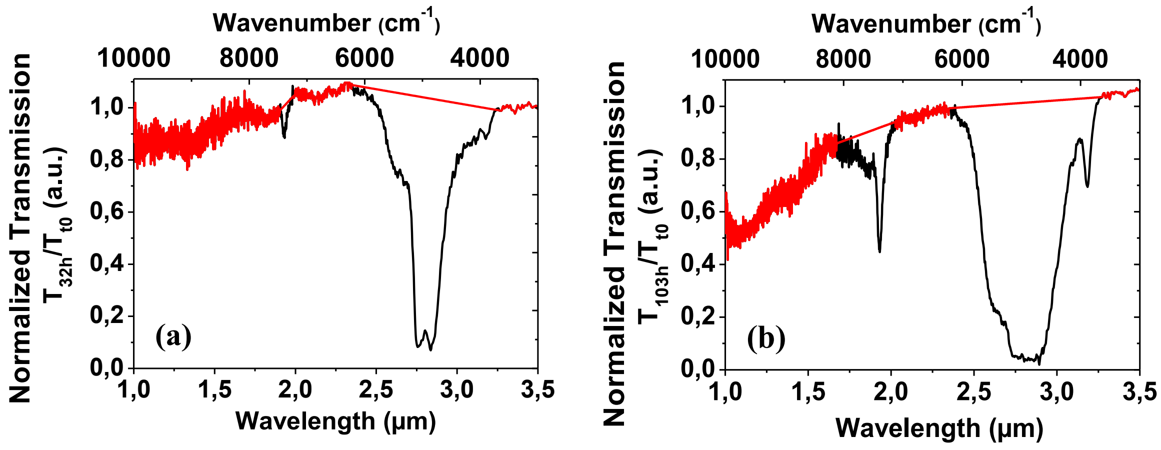

Figure 53: Ratio of Near-Infrared spectra after 32 h (a) and 103 h (b) of exposure, showing sloping background and the linear correction adopted for background subtraction.

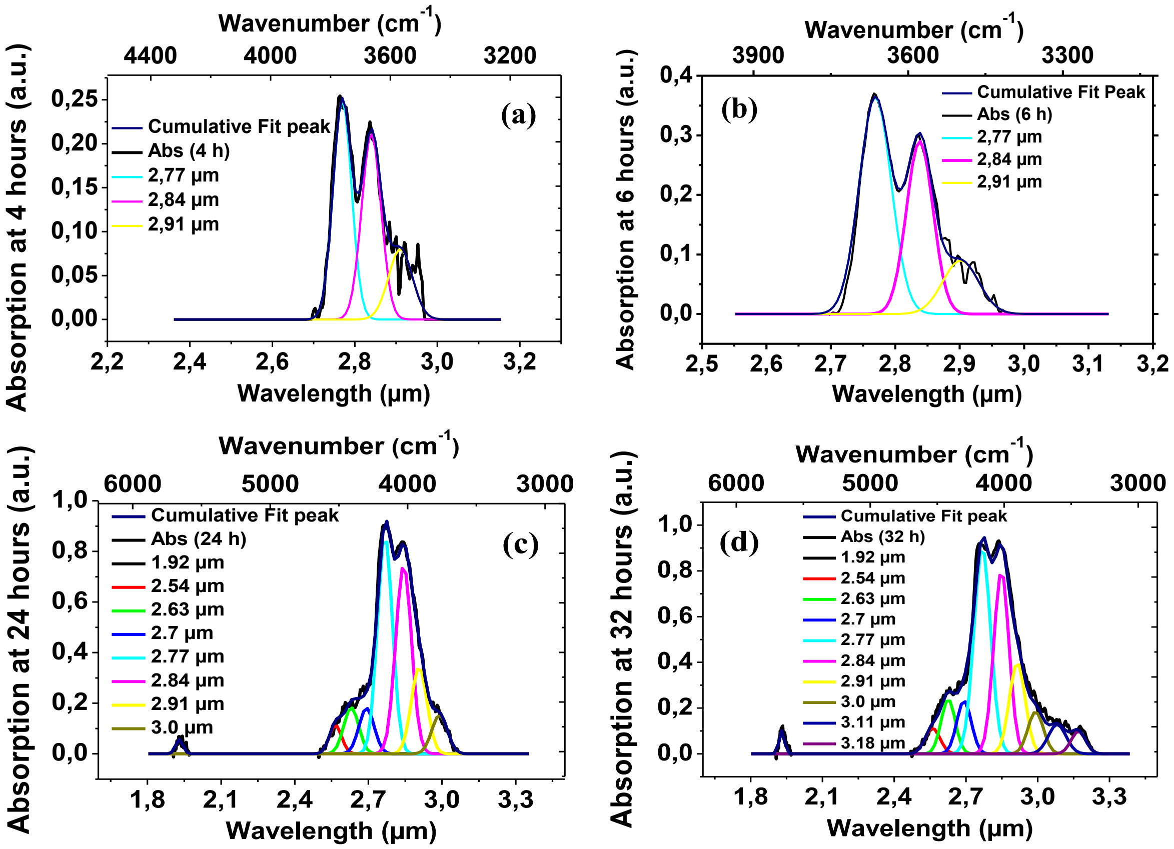

Figure 54: Deconvoluted absorption spectra over time scale (a) 4 h, (b) 6 h, (c) 24 h and (d) 32 h respectively.

4.2. Time evolution of OH attenuation.

Figure 55 illustrates the temporal evolution of additional attenuation due to aging, added to the initial optical loss spectrum of the as-drawn As_2S_3 suspended core fiber, during storage in ambient atmosphere ranging from 1 h to 384 h, for 2.8 meters of fiber. The attenuation at any time (t) is estimated using the relationship:

$$\alpha_t(dB) = 10 \times \log\left(\frac{I_t}{I_0}\right) \tag{26}$$

where I_t and I_0 are the transmitted intensity at (t) and (t_0) respectively.

In the long wavelength range, the attenuation is dominated by the absorption of extrinsic impurities. After 6 h of exposure, 2.5 dB are added to the initial attenuation at 2.77 µm. This value increases to reach 11dB, 23 h later. Finally, the first 24 h are sufficient to severally attenuate the signal.

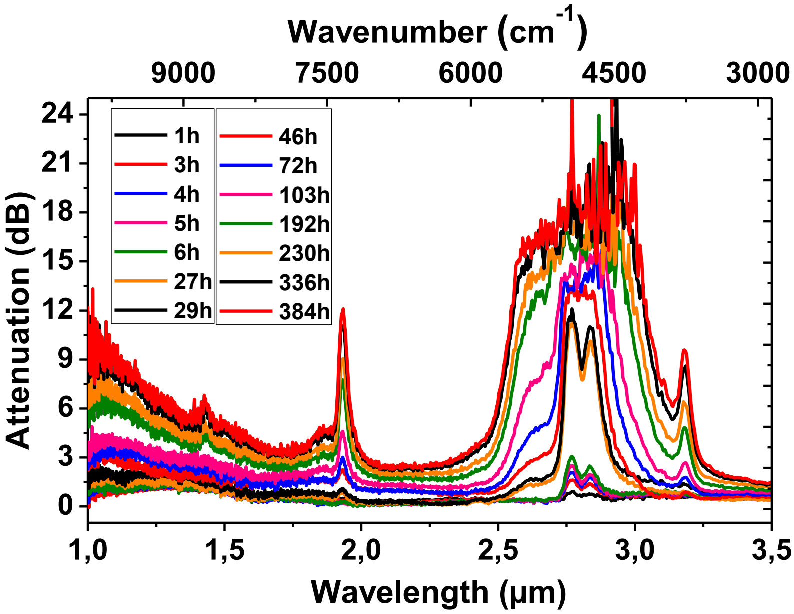

Figure 55: Additional attenuation for 2.8m of As_2S_3 MOF as a function of exposure time to ambient conditions.

These dynamics continue to develop and reach the detection limits of our detection device after 46 h, thus plotted spectra become noisy and follow evolution of peaks at 2.77 and 2.84 µm becomes impossible. However, the overall peak steadily extends over time due to the emergence of new absorption components as described above. Previous fitting procedure can be exclusively performed for resolved peaks. This explains the possible treatment of absorption peaks around 2.8 µm until 29 h, before they become noisy after 46 h of exposure to aging factors. Since 1.92 µm and 1.44 µm absorption peaks remains resolved until the end of the study, they allowed a continuous survey of their evolution. The fitting of experimentally plotted spectrum allows then to estimate the contribution of each vibration under the cumulative absorption peak. Resulting attenuations of each component are listed in Table 5.

These dynamics continue to develop and reach the detection limits of our detection device after 46 hours, thus plotted spectra become noisy and follow evolution of peaks at 2.77 and 2.84 µm becomes impossible. However, the overall peak steadily extends over time due to the emergence of new absorption components as described above. Simultaneously to this emergence, the background evolves in the short wavelength side. This is attributable to aging dynamics governed by the scattering losses (see paragraph 5.1) [10, 11, 24].

Table 5: Attenuations for each deconvoluted peak after background corrections, for 2.8 meters of As_2S_3 MOF.

	Attenuation (dB)										
T(h)	1.44 µm	1.92 µm	2.54 µm	2.63 µm	2.7 µm	2.77 µm	2.84 µm	2.91 µm	3.0 µm	3.11 µm	3.18 µm
1	--	--	--	--	--	0.9	0.74	0.1	--	--	--
3	--	--	--	--	--	1.2	0.89	0.25	--	--	--
4	--	--	--	--	--	1.74	1.28	0.32	--	--	--
5	--	--	--	--	--	2.05	1.38	0.45	--	--	--
6	--	--	--	--	--	2.58	1.85	0.6	--	--	--
27	--	0.49	0.33	0.8	0.98	10.9	9.2	2.34	0.8	0.5	0.34
29	--	0.45	0.4	1.04	1.07	11.26	9.65	2.74	1.06	0.67	0.365
46	--	0.9	--	--	--	--	--	--	--	--	--
72	--	1.8	--	--	--	--	--	--	--	--	--
103	--	3.0	--	--	--	--	--	--	--	--	--
192	0.4	4.5	--	--	--	--	--	--	--	--	--
336	1.0	7.9	--	--	--	--	--	--	--	--	--
384	1.4	8.65	--	--	--	--	--	--	--	--	--

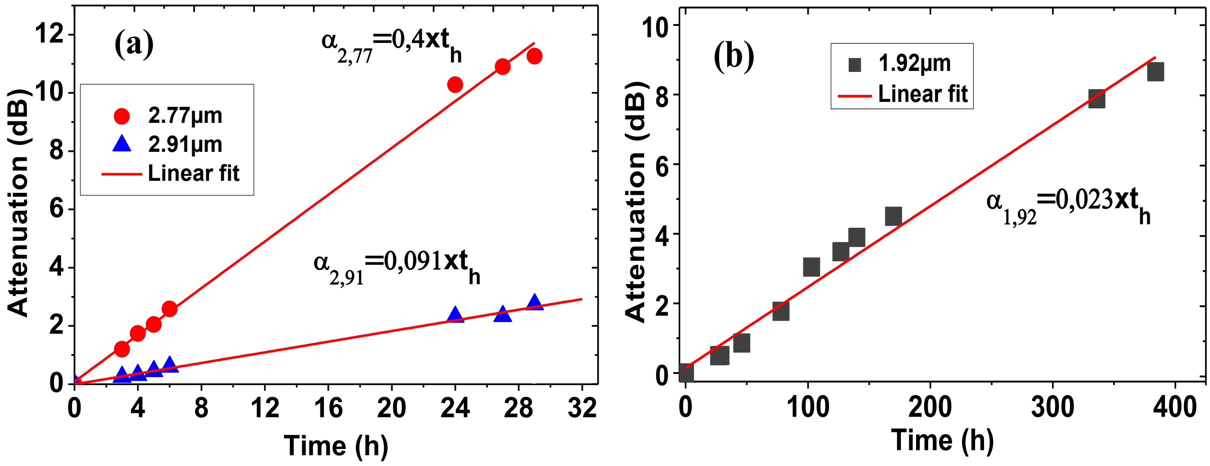

Figure 56: Kinetic of peaks height evolution of different OH groups vibration modes.

4.3. . <u>Distribution of absorbing species along the fibre.</u>

The previous analyses indicate that aged As$_2$S$_3$ MOF contains hydroxyl groups from water adsorbed on the MOF core as well as tightly bonded hydroxyl groups coming through chemical reaction between adsorbed water and the sulphide glass. The water comes from atmospheric steam which diffuses from the MOF's extremities in the holes along the core. We therefore investigate the spatial distribution of absorbing species along the fibre. To that purpose, the following experiment was carried out on the MOF exposed to ambient atmosphere during 384 h. Taking advantage of the cut back technique, a series of absorption spectra were registered along the tested fibre at different point from the output edge (Figure 57). Admitting that the diffusion dynamic is similar from both ends, our study has been limited to one half of the concerned fibre. From these spectra we obtain the attenuation α_{S_n} of different sections ($S_n = L_{n-1} - L_n$) along the MOF from the output to the middle, using the relationship:

$$\alpha_{S_n} = \frac{10}{L_{n-1}-L_n}\log\left(\frac{T_n}{T_{n-1}}\right) \qquad \text{(dB/m)} \qquad (27)$$

$\Delta L = L_0 - L_n$, $\Delta L = L_n - L_{n+1}$, L_0=2.8 m is the initial length of the fibre, L_{n-1} and L_n are the considered length where n varies between 1 and 4, T_{n-1} and T_n correspond to the transmission registered for L_{n-1} and L_n respectively. The attenuation spectra of fibre sections S_1 and S_4 are presented Figure 58. One can note that even if the different removed fibers sections are only of several centimeters long, the evolution of the recorded intensities is significant because of the large attenuation effect of OH groups, which makes the cut back technique relevant in this case.

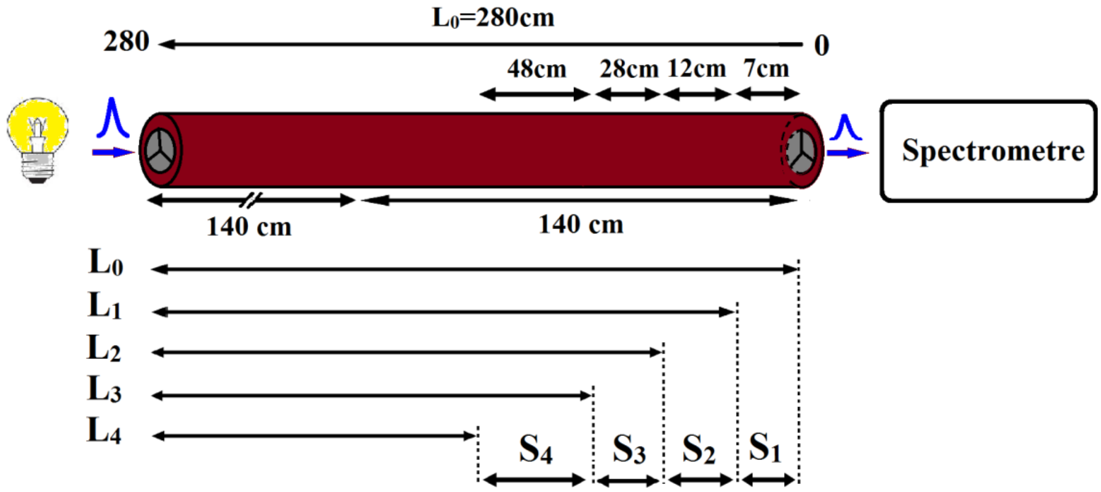

Figure 57: Schematic representation of fibre sections considered for studying the longitudinal distribution of absorbing species.

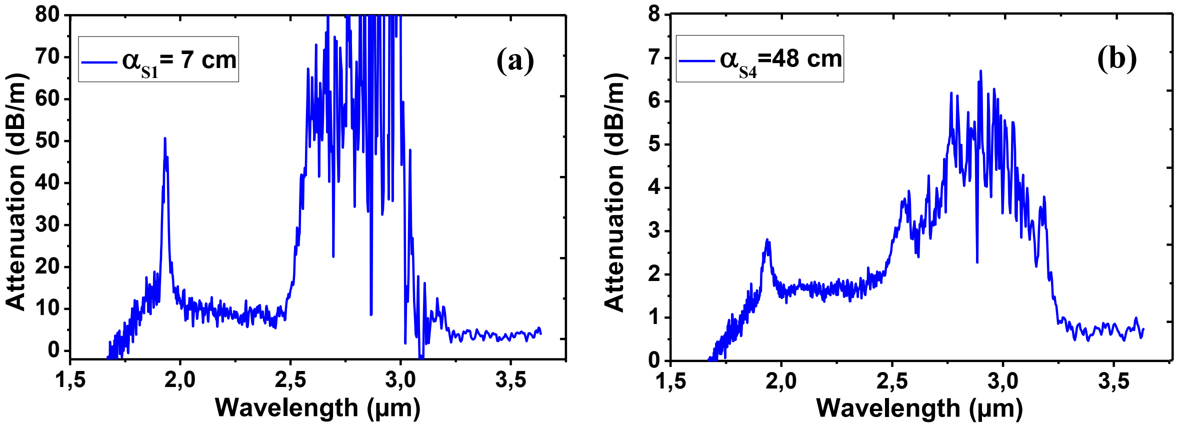

Figure 58: Attenuation spectra of sections S_1 and S_4 of the 384 h aged As_2S_3 MOF, located at different distances from the fibre's output: (a) Attenuation of section S_1, the first 7 cm of the MOF; (b) Attenuation of section S_4 located at ~100 cm from the MOF end.

The spectra illustrate a non-homogenous repartition of the hydroxyl groups along the aged MOF. By moving deeper in the fibre from an edge, the absorption in the 2.6-3.2 µm region (due to molecular water, Table 4) as well as absorption around 1.92 µm (due to OH groups tightly linked to the glass network, (Table 4) decrease. After 384h of exposure to room atmosphere, near the MOF edge in the first 7 centimetres (section S_1), the attenuation due to OH groups reaches around 50 dB/m at 1.92 µm, whereas it exceeds the 60 dB/m threshold in the 2.6-3.2 µm range. It decreases to ~3 dB/m (resp. ~6 dB/m) at 1.92 µm (resp. in the 2.6-3.2 µm region), near the middle of the MOF, in section S_4 at ~1 m from its edge. In both cases, absorptions in 2.6-3.2 µm region are strong, and the transmitted light signal is weakly detected by the detection device, explaining thus the noisy aspect of the attenuation spectra in this wavelength range. The distance-dependent nature of the hydroxyl-groups attenuation at 1.92 µm is more clearly presented on Figure 59, where the corresponding variation of OH groups' concentration with the position in the MOF is also indicated. The quantitative estimation of the hydroxyl absorbing species is given by Equation 28:

$$\left[OH\right]_{ppm} = \frac{\alpha_{dB/m}}{\beta} \tag{28}$$

Where β ($dB.m^{-1}.ppm^{-1}$) is the characteristic extinction coefficient of the corresponding absorption band. A previous knowledge of hydroxyl groups' extinction coefficient of corresponding vibration modes remains mandatory. Numerous research activities were devoted to elucidate the OH absorption and determine its absolute content in silica glasses [38, 39]. Such detailed studies on sulphide glasses were not reported. Thus, in order to estimate the OH content in As_2S_3 glasses, we use the values of β ($dB.m^{-1}.ppm^{-1}$) calculated from the molar absorptivity ε ($l.mol^{-1}cm^{-1}$) of OH groups in silica glasses. According to Stolper and al. [37], the molar absorptivity of OH groups around 1.9 µm calculated in silica glass from absorbance measurements is ε= 1.8 $l.mol^{-1}cm^{-1}$. We assume the same value for ε in As_2S_3 glass. The extinction coefficient β ($cm^{-1}.ppm^{-1}$), corresponding to an OH concentration of 1 ppm weight in As_2S_3 glassis then given by:

$$\beta\left(cm^{-1}.ppm^{-1}\right) = \varepsilon\left(l.mol^{-1}.cm^{-1}\right) \times \left[10^{-6}.\left[\rho_{As_2S_3}/M_{OH}\right]\right] \tag{29}$$

Where $\rho_{As2S3}=3.2.10^3$ g/l is the density of As_2S_3 glass and $M_{OH}=17$ $g.mol^{-1}$ is the OH molar mass. Here $\beta= 339.10^{-6}$ $cm^{-1}.ppm^{-1}$. For optical fibers, the extinction coefficient β is preferably expressed in $dB.m^{-1}.ppm^{-1}$ and directly from attenuation and absorbance definitions:

$$\beta\left(dB.m^{-1}.ppm^{-1}\right) = 1000 \times \beta\left(cm^{-1}.ppm^{-1}\right) \tag{30}$$

Here β = 339.10^{-3}(dB.m^{-1}.ppm^{-1}). This value allows to calculate the OH groups' concentration in the different section S$_n$ of the fibers according Equation.28 and reported on Figure 59.

Finally, for 384h of exposure, the most deleterious effect of atmospheric moisture occurs, from an end, over the first centimetres of the As$_2$S$_3$ MOFs which contain ~147 ppm of OH tightly bonded to the sulphide glass. The OH concentration then decreases exponentially towards the middle of the fibre to reach a minimum of ~9 ppm at the fibre mid length. Figure 59 (a) illustrates the experimentally measured fiber losses and calculated OH content cumulated over exposure time for one half of the fiber. It is worth to note that throughout the experiment, both ends of the tested fiber were exposed to the same atmospheric conditions (pressure, relative humidity, temperature). In addition, the fiber exhibits constant holes dimensions along its length. Then, we can wisely assume that the diffusion mechanism is the same from both sides and Figure 59 (b) reproduces the similar evolution of losses and OH content for the second half of the fibre. Finally, the distribution of all OH impurities along the fiber exhibits two maxima located at the input and the output ends of the fiber and a minimum in the middle.

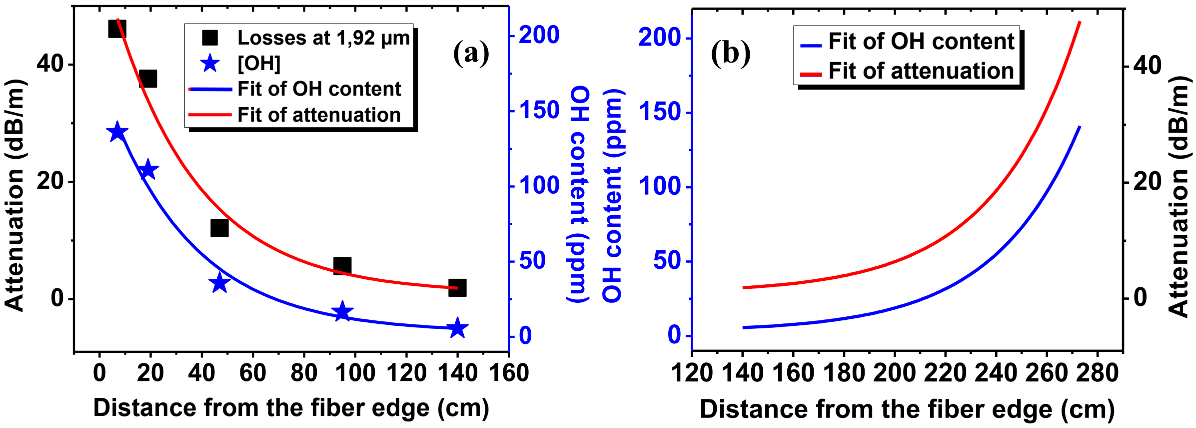

Figure 59: Attenuation (black) of 1.92 µm absorption band and absolute content (blue) of corresponding OH groups as a function of distance from the fibre edge. Results reported for an As$_2$S$_3$ MOF exposed for 384 hours to room atmosphere.

One of the main goals of As_2S_3 MOFs studied here lies in the possibility to achieve an efficient nonlinear interaction as the light signal propagates in the fibre, and especially to enable an important spectral broadening known as supercontinuum generation. These nonlinear optical processes take place within the first centimetres, even the first millimetres of the As_2S_3 MOFs [21, 40]. To achieve such efficient interactions, low optical losses are then required in this part of the fibre. However, the rapid and important contamination of the edge of these waveguides by OH absorbing groups, that we demonstrate in this work, sharply limits their efficiency and explains for IR SC extension limitation we previously observed [16, 40]. Thus, precautions and protection of the core MOFs, immediately after drawing process are necessary.

5.4. <u>Prevention of aging.</u>

Based on the foregoing, a control of the diffusion of atmospheric steam in the holes of the MOF is required in order to limit the aging process. For that purpose we have airproofed the fibre ends by means of a methacrylate-based polymer. The fibre ends were soaked in the liquid polymeric solution, and then let to polymerize in free atmosphere at room temperature. Thereafter, rigorous polishing of the fibre facets allows to get rid of the thin polymer layer formed on the cross section of the fibre and to reach the core of the fibre. Herein, the diffusion of the polymer through the holes is ensured by capillarity. In order to enhance this process, polymer viscosity was adjusted using water-free solvent. Thanks to this technique, the holes of the MOF were sealed while the core of the fibre remains free for MOF's infrared transmission measurements as a function of time to investigate the evolution of absorption peaks related with OH pollution. Figure 60 presents several absorption spectra registered on 50 cm length of an As_2S_3 MOF exposed until 216 h to room atmosphere.

These spectra maintain a remarkable stability and no evolution of OH related absorption bands is noticed. Note that exposure conditions are similar to those reported for the previous aging study. These results indicate that it is possible to protect the MOF core from OH aging. What's more, they confirm that the aging of sulphide MOF is due to atmospheric moisture diffusion in the holes of the fibre.

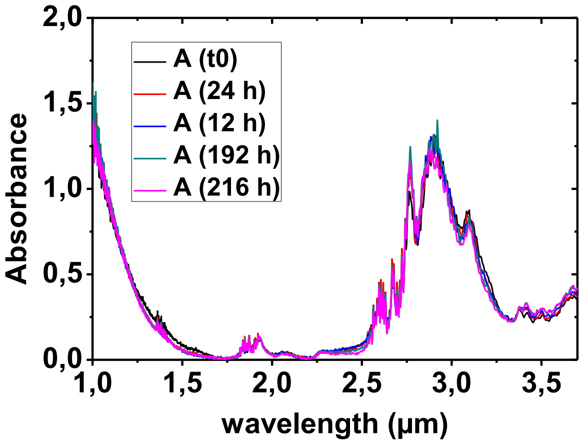

Figure 60: IR transmission spectra of airproofed As_2S_3 MOF as a function of time exposure to ambient atmosphere.

5. Conclusion

We report a detailed IR spectroscopic study of unsuitable process of atmospheric moisture adsorption and reaction onto the core surface of As_2S_3 chalcogenide microstructured optical fibres, leading to incorporation of absorbing OH groups weakly as well as tightly bonded to the MOFs core, which finally results in important additional losses. A detailed assignment of absorption bands and corresponding vibration modes is presented. The continuous evolution of the concentrations of hydroxyl groups in the MOFs as a function of exposure period is proved at least until 384h of exposure. The observed changes upon exposure period show that the deleterious effect of moisture, which corresponds to diffusion of atmospheric steam in the holes of the MOF, occurs rapidly over the first few hours and is the most important in the early centimetres of the MOF. This early part of the fibre is of major importance for implementation of non-linear optical effects such as supercontinuum generation. In order to protect the MOF core from this aging process a first successful attempt to airproof the MOF is presented herein.

Acknowledgments.

We acknowledge the financial support from the Conseil Régional de Bourgogne through the Photcom PARI program, as well as from the French DGA. This project has been performed in cooperation with the Labex ACTION program (contract ANR-11-LABX-0001-01).

6. References

1. J. Kohl-Landgraf, J.-E. Nimsch, and J. Wachtveitl, "LiF, an underestimated supercontinuum source in femtosecond transient absorption spectroscopy," Optics Express **21**, 17060-17065 (2013).
2. S. V. Smirnov, J. D. Ania-Castanon, T. J. Ellingham, S. M. Kobtsev, S. Kukarin, and S. K. Turitsyn, "Optical spectral broadening and supercontinuum generation in telecom applications," Optical Fiber Technology **12**, 122-147 (2006).
3. G. E. Snopatin, V. S. Shiryaev, V. G. Plotnichenko, E. M. Dianov, and M. F. Churbanov, "High-purity chalcogenide glasses for fiber optics," Inorganic Materials **45**, 1439-1460 (2009).
4. J. H. V. Price, T. M. Monro, H. Ebendorff-Heidepriem, F. Poletti, P. Horak, V. Finazzi, J. Y. Y. Leong, P. Petropoulos, J. C. Flanagan, G. Brambilla, F. Xian, and D. J. Richardson, "Mid-IR supercontinuum generation from nonsilica microstructured optical fibers," IEEE Journal of Selected Topics in Quantum Electronics **13**, 738-749 (2007).
5. P. J. Allen, B. R. Johnson, and B. J. Riley, "Photo-oxidation of thermally evaporated As_2S_3 thin films " Journal of Optoelectronics and Advanced Materials **7**, 1759-1764 (2005).
6. R. Y. Golovchak, A. Kozdras, and O. I. Shpotyuk, "Physical ageing in glassy As-Se induced by above-bandgap photoexposure," Solid State Communications **145**, 423-426 (2008).
7. J. S. Berkes, S. W. I. Jr., and W. J. Hillegas, "Photodecomposition of amorphous As_2Se_3 and As_2S_3," Journal of applied Physics **42**, 4908-4916 (1971).
8. F. Charpentier, M. Dussauze, M. Cathelinaud, G. Delaizir, E. I. Kamitsos, J. L. Adam, B. Bureau, and V. Nazabal, "Aging process of photosensitive chalcogenide films deposited by electron beam deposition," Journal of Alloys and Compounds **509**, 7330-7336 (2011).
9. Y.-F. Niu, J.-P. Guin, A. Abdelouas, T. Rouxel, and J. Troles, "Durability of an As_2S_3 chalcogenide glass: Optical properties and dissolution kinetics," Journal of Non-Crystalline Solids **357**, 932-938 (2011).
10. Y.-F. Niu, J.-P. Guin, T. Rouxel, A. Abdelouas, J. Troles, and F. Smektala, "Aqueous corrosion of the $GeSe_4$ chalcogenide glass: surface properties and corrosion mechanism," Journal of the American Ceramic Society **92**, 1779-1787 (2009).
11. M. M. Smedskjaer, Y. Yue, J. Deubener, H. P. Gunnlaugsson, and S. Marup, "Modifying glass surfaces via internal diffusion," Journal of Non-Crystalline Solids **356**, 290-298 (2010).

12. M. F. Churbanov, V. S. Shiryaev, V. V. Gerasimenko, A. A. Pushkin, I. V. Skripachev, G. E. Snopatin, and V. G. Plotnichenko, "Stability of the optical and mechanical properties of chalcogenide fibers," Inorganic Materials **38**, 1063-1068 (2002).
13. R. Y. Golovchak, S. A. Kozyukhin, A. Kozdras, O. I. Shpotyuk, and V. M. Novotortsev, "Physical aging of chalcogenide glasses," Inorganic Materials **46**, 911-913 (2009).
14. P. Toupin, L. Brilland, D. Mechin, J. Adam, and J. Troles, "Optical aging of chalcogenide microstructured optical fibers," Journal of Lightwave Technology, **32**, 2428-2432 (2014).
15. R. J. Curry, S. W. Birtwell, A. K. Mairaj, X. Feng, and D. W. Hewak, "A study of environmental effects on the attenuation of chalcogenide optical fibre," Journal of Non-Crystalline Solids **351**, 477-481 (2005).
16. O. Mouawad, F. Amrani, B. Kibler, J. Picot-Clémente, C. Strutynski, J. Fatome, F. Désévédavy, G. Gadret, J.-C. Jules, O. Heintz, E. Lesniewska, and F. Smektala, "Impact of optical and structural aging in As_2S_3 microstructured optical fibers on mid-infrared supercontinuum generation," Optics Express **22**, 23912-23919 (2014).
17. V. Q. Nguyen, J. S. Sanghera, B. Cole, P. Pureza, F. H. Kung, and I. D. Aggarwal, "Fabrication of arsenic sulfide optical fiber with low hydrogen impurities," Journal of the American Ceramic Society **85**, 2056-2058 (2002).
18. V. Q. Nguyen, J. S. Sanghera, P. Pureza, F. H. Kung, and I. D. Aggarwal, "Fabrication of arsenic selenide optical fiber with low hydrogen impurities," Journal of the American Ceramic Society **85**, 2849-2851 (2002).
19. M. El-Amraoui, J. Fatome, J. C. Jules, B. Kibler, G. Gadret, C. Fortier, F. Smektala, I. Skripatchev, C. F. Polacchini, Y. Messaddeq, J. Troles, L. Brilland, M. Szpulak, and G. Renversez, "Strong infrared spectral broadening in low-loss As-S chalcogenide suspended core microstructured optical fibers," Optics Express **18**, 4547-4556 (2010).
20. J. Troles, Q. Coulombier, G. Canat, M. Duhant, W. Renard, P. Toupin, L. Calvez, G. Renversez, F. Smektala, M. El Amraoui, J. L. Adam, T. Chartier, D. Mechin, and L. Brilland, "Low loss microstructured chalcogenide fibers for large non linear effects at 1995 nm," Optics Express **18**, 26647-26654 (2010).
21. O. Mouawad, J. Picot-Clémente, F. Amrani, C. Strutynski, J. Fatome, B. Kibler, F. Désévédavy, G. Gadret, J. C. Jules, D. Deng, Y. Ohishi, and F. Smektala, "Multioctave midinfrared supercontinuum generation in suspended-core chalcogenide fibers," Optics Letters **39**, 2684-2687 (2014).
22. M. El-Amraoui, G. Gadret, J. C. Jules, J. Fatome, C. Fortier, F. Désévédavy, I. Skripatchev, Y. Messaddeq, J. Troles, L. Brilland, W. Gao, T. Suzuki, Y. Ohishi, and F. Smektala, "Microstructured chalcogenide optical fibers from As_2S_3 glass: towards new IR broadband sources," Optics Express **18**, 26655-26665 (2010).

23. D. Franta, L. Zajickova, M. Karaskova, O. Jarek, D. Necas, P. Klapetek, and M. Valtr, "Optical characterization of ultrananocrystalline diamond films," Diamond and Related Materials **17**, 1278-1282 (2008).
24. D. M. Kane, R. J. Chater, D. B. Gore, and D. S. McPhail, "Corrosion at the surface of chalcogenide glass microspheres," Journal of Optics **14**, 055401 (2012).
25. S. Hendy, "Light scattering in transparent glass ceramics," Applied Physics Letters **81**, 1171-1173 (2002).
26. V. Kokorina, *Glasses for infrared optics* (The CRC Press, 1996).
27. A. P. Paiuk, A. V. Stronski, N. V. Vuichyk, A. A. Gubanova, T. A. Krys‘kov, and P. F. Oleksenko, "Mid-IR impurity absorption in As_2S_3 chalcogenide glasses doped with transition metals," Semiconductor Physics, Quantum Electronics & Optoelectronics **15**, 152-156 (2012).
28. M. S. Iovu, S. D. Shutov, A. M. Andriesh, E. I. Kamitsos, C. P. E. Varsamis, D. Furniss, A. B. Seddon, and M. Popescu, "Spectroscopic studies of bulk As_2S_3 glasses and amorphous films doped with Dy, Sm and Mn " Journal of Optoelectronics and Advanced Materials **3**, 443-454 (2001).
29. B. Frumarova, P. Nemec, M. Frumar, and J. Oswald, "Synthesis and properties of Ge-Sb-S: $NdCl_3$ glasses," Semiconductors **32**, 812-816 (1998).
30. T. Kavetskyy, R. Golovchak, O. Shpotyuk, J. Filipecki, and J. Swiatek, "On the compositional trends in IR impurity absorption of Ge–As(Sb)–S glasses," Journal of Optoelectronics and Advanced Materials **6**, 1141 - 1146 (2004).
31. T. S. Kavetskii, V. D. Pamukchieva, and O. I. Shpotyuk, "Concentration dependence of impurity absorption in chalcogenide glasses of the Ge-Sb-S system," Journal of Applied Spectroscopy **67**, 687-692 (2000).
32. C. T. Moynihan, P. B. Macedo, M. S. Maklad, R. K. Mohr, and R. E. Howard, "Intrinsic and impurity infrared absorption in As_2Se_3 glass," Journal of Non-Crystalline Solids **17**, 369-385 (1975).
33. T. Kanamori, Y. Terunuma, S. Takahashi, and T. Miyashita, "Transmission loss characteristics of $As_{40}S_{60}$ and $As_{38}Ge_5Se_{57}$ glass unclad fibers," Journal of Non-Crystalline Solids **69**, 231-242 (1985).
34. T. S. Kavetskyy, A. P. Kovalskiy, V. D. Pamukchieva, and O. I. Shpotyuk, "IR impurity absorption in Sb_2S_3-GeS_2(Ge_2S_3) chalcogenide glasses," Infrared Physics & Technology **41**, 41-45 (2000).

35. G. Navarra, I. Iliopoulos, V. Militello, S. G. Rotolo, and M. Leone, "OH-related infrared absorption bands in oxide glasses," Journal of Non-Crystalline Solids **351**, 1796-1800 (2005).

36. V. G. Plotnichenko, V. O. Sokolov, and E. M. Dianov, "Hydroxyl groups in high-purity silica glass," Journal of Non-Crystalline Solids **261**, 186-194 (2000).

37. E. Stolper, "Water in silicate glasses: An infrared spectroscopic study," Contributions to Mineralogy and Petrology **81**, 1-17 (1982).

38. J. M. Stone, and J. C. Knight, "From zero dispersion to group index matching: How tapering fibers offers the best of both worlds for visible supercontinuum generation," Optical Fiber Technology **18**, 315-321 (2012).

39. O. Humbach, H. Fabian, U. Grzesik, U. Haken, and W. Heitmann, "Analysis of OH absorption bands in synthetic silica," Journal of Non-Crystalline Solids **203**, 19-26 (1996).

40. I. Savelii, O. Mouawad, J. Fatome, B. Kibler, F. Désévédavy, G. Gadret, J. C. Jules, P. Y. Bony, H. Kawashima, W. Gao, T. Kohoutek, T. Suzuki, Y. Ohishi, and F. Smektala, "Mid-infrared 2000-nm bandwidth supercontinuum generation in suspended-core microstructured Sulfide and Tellurite optical fibers," Optics Express **20**, 27083-27093 (2012).

III. Article 2

This manuscript is submitted to "Optical Materials" journal

Further Demonstration of Atmospheric Optical Aging and Surface Degradation in As_2S_3 Optical Fibers.

O. Mouawad, P. Vitry, C. Strutynski, J. Picot-Clémente, F. Désévédavy, G. Gadret, J-C Jules, E. Lesniewska, and F. Smektala*

ICB, Laboratoire Interdisciplinaire Carnot de Bourgogne, UMR 6303 CNRS-Université de Bourgogne, 9Av. Alain Savary, BP47870, 21078 Dijon, France
**Corresponding author: frederic.smektala@u-bourgogne.fr*

Abstract

Microstructured optical fibers (MOF) can be seen as next generation fiber of significance in advancing the compact optics because of its excellent compatibility in integrated optics. However, the degradation of their physicochemical properties limits their efficiency and lifetime. Atmospheric moisture is responsible for the degradation of amorphous systems especially chalcogenide glasses. In the light of previously reported studies, in order to clarify the aging process continuously evolving in sulfide microstructured optical fiber over time, a detailed investigation of this phenomenon has been conducted. The time-dependent transmission and glass chemical deterioration have been studied for As_2S_3 MOF with regard to their exposure to different atmospheric conditions. Results show a substantial impact of atmospheric moisture through an interaction with the glass network. Significant improvement has been registered by storing the fibers under dry atmosphere.

Keywords: Microstructured optical fibers, Fiber losses, Chalcogenide glass, Durability, Corrosion behavior.

1. Introduction

Chalcogenide glass finds widespread applications as both active and passive optical elements in integrated-optics systems and devices. The chalcogenide vitreous system could be successfully doped with rare earth element, providing thus additional more efficient potential functions [1]. Apart from their bulk optic components, chalcogenide glasses have found various applications in different geometric forms, including fiber form, planar waveguides geometry and microspheres, leading to different applications including infrared laser power transmission, imaging and spectroscopy, chemical sensing [2] or supercontinuum generation (SCG) [3-6]. Indeed, for infrared supercontinuum generation, these glasses are highly suitable because they exhibit a wide transmission window extended further in the IR as well as high third-order non-linearity estimated at two to three order of magnitude greater than silica [7, 8]. Thus, thanks to these combined properties chalcogenide glass fibers have gained attentions and lead to striking achievements [3, 7]. Microstructured fiber geometry allowed to overcome and to adapt the opto-geometrical parameters of the fiber, providing a powerful technique for fabrication of special structure and fibers with tight mode confinement, allowing thus an efficient nonlinear interaction, leading for promising results. Detailed studies allowed a better understanding of the interactions between the glass system and the transmitted light beam [9]. However, extending the current spectrum broadening further in infrared (IR) requires a delicate engineering of the glass optical quality. Ultrapure glasses are needed. Over recent years, the synthesis techniques of chalcogenide glasses have been extensively developed. Well adapted purification and synthesis strategies allow to fabricate low loss fibers [7, 10-15]. Furthermore, optimized fabrication strategies to elaborate glass preforms designed to draw microstructured fibers are well developed to avoid any additional losses [16]. According to Aggrawal and al. [17], efficient supercontinuum generation in chalcogenide microstructured fibers requires optical loss low enough to spread the continuum in the mid-IR, typically less than 1 dB/m, a threshold which has been reached by several labs [7, 10-15]. Despite the success of the previous techniques, there is still a number of serious issues that limit the fiber efficiency. Chalcogenide glasses suffer from a shift of their properties in time due to the aging process. During aging process, many physicochemical changes occur. The physical aging changes correspond to structural relaxation. They are generally related to the preparation technique of the glass, namely melt quenching process. The chemical aging changes correspond to modification of the local composition of the glass system. Such modifications result from a deleterious reactions process between the glass and the surrounding medium [18-24]. Physicochemical aging studies have been carried out by many researchers over the last years. A detailed durability studies performed on bulk samples were reported by Niu and al. [18, 24]. On the other hand, similar investigations were carried out on other geometries. In this context, the photoinduced aging of chalcogenide films was extensively studied [25-27]. Chalcogenide glass fiber has been also investigated on the long and short term. In frame of these investigations, Churbanov and al. [19] has reported studies performed on the long term scale (up to many years), whereas Curry and al. [20] have reported other studies conducted on the short time scale (few hours up to several days) under extreme conditions. Concerning MOFs, Toupin and al. [21] have briefly reported on optical aging behavior of chalcogenide MOFs with six-holes structure. Among the various chalcogenide compositions covered by these studies, all glass systems were prone to OH contamination, whereas the aging rate depended on the glass composition. Recently, our group has demonstrated [23] and studied [22] the tremendous deterioration of optical quality of three-holes As_2S_3 suspended core MOFs under ambient atmosphere. Investigations of aging and degradation of MOFs have pointed out a glass hydrolysis process [22, 23]. This process denotes that adsorbed water coming from atmospheric steam undergoes chemical reaction with the glass and locally modifies its composition. This conclusion was essentially based on IR studies of OH groups absorption bands evolution and preliminary AFM and XPS studies [23]. However, the simultaneous evolution of SH groups IR absorptions as well as detailed investigations of glass surface modifications resulting from this process were not presented. The present study focuses then on exploring the aging behavior of As_2S_3 optical fibers in atmosphere by considering previous parameters, in order to further demonstrate the glass surface hydrolysis process undergone by the fibers.

2. Experimental

2.1. Samples fabrication.

As_2S_3 glass was synthesized by the conventional melt quenching technique as detailed elsewhere [16]. High purity elemental arsenic and sulfur in stoichiometric quantities were enclosed under vacuum inside a sealed silica ampoule which was then loaded into a rocking furnace and heated at 700°C for several hours. The melt batch was then water-quenched to glassy, followed by a 12 hours annealing around the glass transition temperature (T_g=210°C) for stress revealing allowing sample manufacturing. Resulting glass rod is of 16 mm of diameter and 80 mm in length. The cylindrical glass rod was sliced to two preforms using a diamond saw. The first preform was designed to draw large mode area microstructured fiber. The mechanical drilling technique previously developed on chalcogenide glasses [16] in our lab permits to prepare the preform which is then drawn under dry atmosphere into suspended core fibers with specific parameters adapted for handling and technical requirements. The MOF has 250 µm outer diameter and 8.0 µm of core diameter (Figure 61 (a)). The second preform was mechanically polished in order to conceive rectangular fiber presenting planar surfaces adapted for AFM study. The roughness profile induces by this shaping procedure shows surface defects of maximum height around 80 nm. It is about 10 times lower than that induced by the mechanical drilling technique on the surface of the core, previously measured around the µm scale and reported in [28]. The preform was drawn into rectangular geometry fiber of 300 µm (resp. 370 µm) of height (resp. width). (Figure 61 (b)).

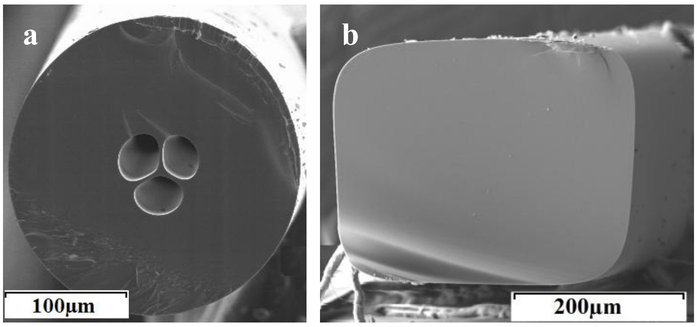

Figure 61: Cross section profiles of the probed (a) large-core microstructured fiber and (b) rectangular fiber.

2.2. Atomic Force Microscopy (AFM) measurements.

In the present studies, a NanoScope V MultiMode 8 AFM and a FastScan AFM by Bruker in combination with a home-built sample holder, which provides mechanical fixation capabilities, were used. We have employed PeakForce QNM® (Quantitative Nanomechanical Property Mapping) mode which allows quantitative nanomechanical mapping of material properties, including modulus and adhesion, while simultaneously imaging sample topography at high resolution using specific cantilever (Bruker ScanAsyst Air of spring constant k~0.4 N/m) in air. For dynamic, we have used FastScan mode associated with miniaturized Olympus AC10 cantilever (spring constant k=0.1 N/m, resonant frequency f~450-600 kHz in liquid). Imaging under gases and liquids was performed by means of Si_3N_4 cantilevers with a cantilever of spring constant of 0.06-0.36 $N.m^{-1}$. Imaging under gases in oscillating contact mode was carried out by means of silicon cantilevers of spring constant of 1-2 $N.m^{-1}$ and resonance frequencies of about 75 kHz to probe chemical modification. The scan rate was adjusted to 2-10 Hz, and a resolution of 512 x 512 $pixels^2$ per image was selected. Quantitative evaluation of the image data was performed using Nanoscope off-line analysis software. A controlled atmosphere was achieved by means of a steel tube which ends 2 mm above the sample surface without interfering with the laser beam of the detection system or other sensitive parts of the AFM. Further isolation of the optical head was not necessary in order to use this simple setup as a ―climate chamber". Defined relative humidity was achieved during measurements by mixing dry nitrogen gas with nitrogen saturated with water by means of flow meters. Measurements under nitrogen were performed at a flow rate of 10 L/h. All measurements were carried out at room temperature (22°C).

2.3. Transmission measurements.

The evolution of the optical transmission of As_2S_3 MOF was quantitatively studied as a function of exposure time to ambient temperature and relative humidity (RH). In these experiments, measurements were carried out over 48 hours, in dark, at temperature ranging from 20 °C to 25 °C and relative humidity (RH) varying between 50 and 60%. A NICOLET 6700 Fourier Transformed InfraRed (FTIR) spectrometer was used to obtain the transmission spectra. The source is an external halogen lamp emitting in the 0.1-5 µm range, providing higher power than the original source integrated in the spectrophotometer, allowing thus to perform this study on MOF samples in the range of interest. The transmission spectra were registered between 1.2 µm to 4.5 µm through a 0.5 m long As_2S_3 glass MOF presenting a large-core diameter of 8 µm linked to the robust cladding by three thin struts (Figure 61 (a)). This fiber was maintained in a fix position all along the experimental period in such a way the coupled power remains unchanged, whereas collected intensity exclusively depended on the dynamic evolution of optical characteristics of the vitreous core. For light coupling a reflective objective was used to avoid chromatic effects. At the output, the signal transmitted along the fiber core was focused into an In-Sb detector using an optimal aspheric AMTIR lens. An infrared camera was used at the output end of the fibre to ensure that light was effectively guided in the core of the MOF only. This is important to stultify the possibility of any significant contribution of the fibre clad in the aging process since the fibre is not coated. The stability of the incident beam intensity has been previously verified, to assure that it remains unchanged through the experiment. The optical aging, after a time t of exposure to room atmosphere, is given in terms of the relative transmission T_t/T_{t0} defined as the ratio between the transmission at time t and the transmission registered at t_0 immediately after drawing.

3. Results and discussions.

3.1. FTIR spectroscopy.

Figure 62 shows the FTIR survey relative transmissions registered immediately after drawing and after well defined periods of exposure to room atmosphere in dark as described above. The depicted spectra show a time deviation in shapes, intensities and positions of characteristic absorption peaks present on the initial transmission spectrum T_{t0}. In parallel, new peaks arise revealing a dynamic evolution of chemical composition upon exposure time. Figure 62 illustrates the principal features which are: (1) strong peaks evolving at 2.77 µm, 2.84 µm and 2.91 µm whose intensities are related to exposure time to ambient atmosphere; (2) a strong enlargement of absorption in the 2.5-3.2 µm which becomes measurable after 5 hours of exposure, and grow rapidly with further exposure to laboratory conditions; (3) an absorption peak around 1.92 µm assigned to OH groups strongly bonded to glass network evolving strongly over time. This set of characteristic absorption bands have previously been attributed to different vibration modes of OH groups strongly and weekly bonded to the glass network and a detailed study of OH groups absorption evolution and absolute content was reported in our previous work [22].

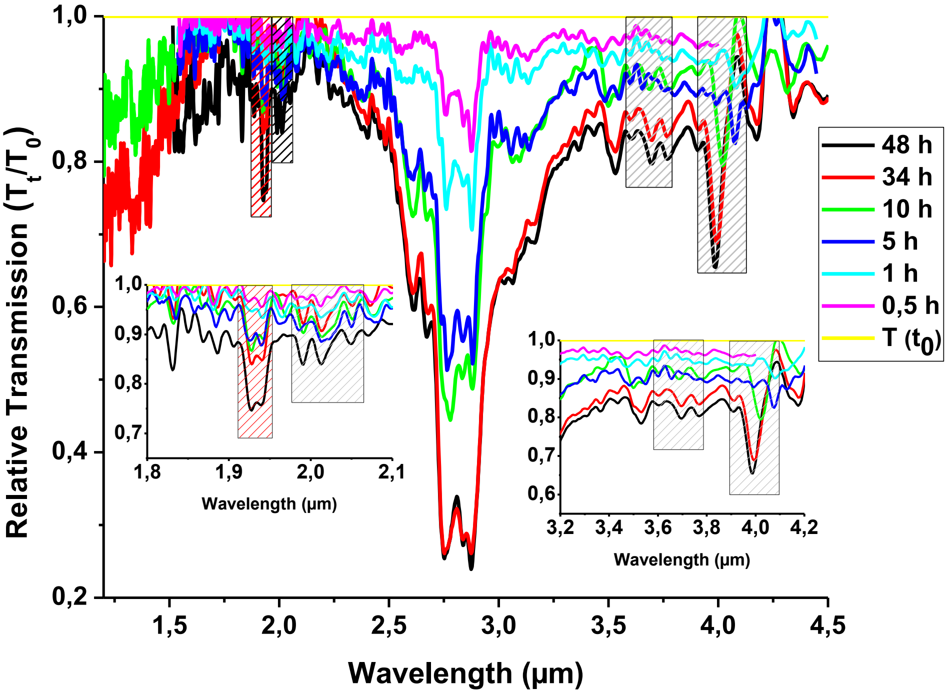

Figure 62: MIR-FTIR survey spectra registered on 0.5 m length of 8 µm core diameter of an As_2S_3 MOF upon storing in ambient conditions at 20-25°C and RH 50-60%.

Regarding SH groups IR signature, another set of absorption bands located around 2.0, 2.05, 2.54, 3.11, 3.64, 3.69 and 4.03µm appear upon exposure time (Figure 62) [29, 30]. They always maintain the same relative intensity with respect from one to another, but whose absolute intensities increase with exposure to atmospheric conditions. These bands are attributed to S-H vibrations and their combinations with other vibration modes [29, 30]. The absorption band located at 4.03 µm is attributed to the fundamental SH stretching vibration [29]. The peaks around 2.0-2.05 µm correspond to the first overtones of the fundamental SH stretching vibrations [29, 30]. The absorption at 2.54 µm is produced by the first fundamental stretching mode of SH combined to two vibrations of As-S-H, whereas the absorption peak at 3.11 µm is due to the first fundamental stretching mode of SH combined to a unique vibrations of As-S-H [29, 30]. It is also reported in the literature a set of peaks assigned to combination of fundamental stretching vibration of SH bonds combined to the fundamental stretching vibrations of the As_2S_3 glass network which manifest themselves in the 3.64-3.69 µm region [29, 30]. Thus, absorption peaks in the 3.64-3.69 µm region (Figure 62) are due to the aforementioned vibrations.

These absorptions bands which grow with exposure to ambient atmosphere come from an interaction between glass and atmospheric steam. As we previously reported [22], the proposed mechanism of chemical aging is the following: in the first hours of As_2S_3 MOFs exposure to ambient atmosphere, growing water adsorption occurs at the surface of the MOF core. This adsorption leads progressively to a chemical reaction between adsorbed water and the sulphide glass in which =As-S-As= bridges are broken to form As-O-H and H-S-As bonds:

$$=\mathrm{As\text{-}S\text{-}As}= + H_2O \Rightarrow =\mathrm{As\text{-}O\text{-}H} + \mathrm{H\text{-}S\text{-}As}$$

This mechanism is here confirmed by observation of SH groups IR absorption. On a first step, weakly-bonded OH-attributed absorption bands (at 2.77 and 2.84 µm) gradually increase. Then, after 5 hours, the relative intensity of both As-O-H (1.92 µm) and S-H (4.0 µm) absorption bands start to grow, together with IR signature of As-S-H groups.

3.2. Surface evolution of aged fiber.

3.2.1. Atomic Force Microscopy (AFM) analysis on fiber samples.

Scattering losses are present on FTIR spectra Figure 62 and are function of the incident wavelength. This impact severely occurs in the high frequency range, whereas such tendency is lowered and less significant in the low frequency range. Such phenomenon is due to surface defects arisen on the glass surface [23]. To determine the nature of this surface changes, a detailed study of the evolution of the core surface was needed. However, because of experimental constraints, such detailed study was impossible. Thus, in order to perform AFM measurements on a glass fiber surface, a rectangular fiber was conceived and drawn (Figure 61 b). The freshly drawn samples were stored in dark inside a close compartment at 50°C under well-defined relative humidity (RH) levels along the period of study**.** For sake of clarity, the samples were numbered according to their RH exposure: RH=35% (SI), RH=65%

(SII) and RH=75% (SIII). The aged specimens were regularly imaged on time scale by AFM technique on large scale (i.e. 25 µm scan range) to identify defects on glass surface. Pictures were taken before and after RH exposure by a digital camera. Figure 63 and Figure 64 show top views of samples at different periods and conditions of exposure. We arranged different scales related to the images for better contrast. Shortly after drawing, several bumps emerge randomly on the fiber surface (Figure 63 (a)). Arisen bumps then developed into faceted pyramids (Figure 63 (b)) with a square cross-section. The dimensions of these defects keep increasing with exposure time and reach a factor 20 after 23 days of exposure.

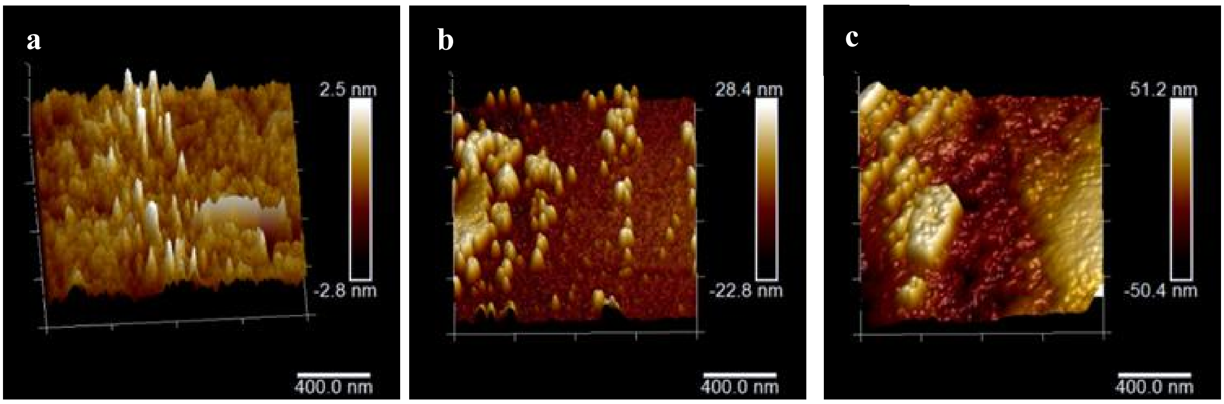

Figure 63: Top view of AFM 3D-pictures of As_2S_3 fiber surface: (a) fresh sample; SI after (b) 7 days and (c) 23 days of exposure.

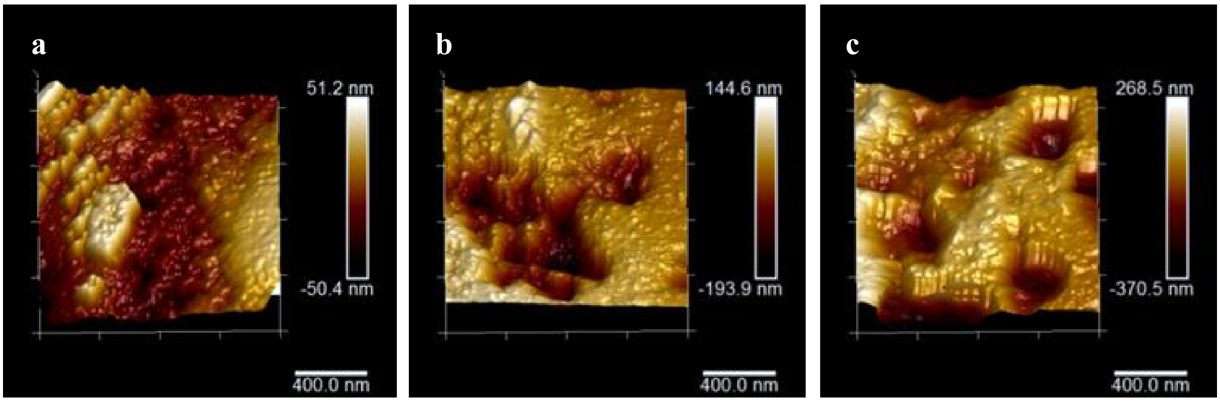

Figure 64: Top view of AFM 3D-pictures As_2S_3 fiber surfaceregistered after 23 days of exposure for SI (a), SII (b) and SIII (c) respectively.

The evolution of the surface morphology was determined following the shape, the height and the fraction of area covered by these defects upon exposure. During the first days (Figure 63 (b)), the bumps maintain a regular pyramidal shape and corresponding heights continue to increase over time. This is the first stage of surface aging. As reported by John Berkes and al. [26], these small bumps growth on the surface of As_2S_3 samples are attributed to As_2O_3 crystals evolving upon time. Here, we have unequivocally identified compositionally these As_2O_3 crystals by electron dispersive spectroscopy (EDS) method. One can note that similar photo-induced defects morphology were reported on As-selenide films exposed to air, whereas for samples treated under vacuum, oxygen and moisture-free atmosphere, no significant changes were detected [27]. Extending the exposure period results in losing the pyramidal shapes, given rise to bigger structures (Figure 63 (c)). The growth process of large particles at the expense of smaller ones because of the decreasing surface energy is known as Ostwald ripening [31] and such behavior has been previously reported by Berkes and al. [26] in the case of As_2S_3 glass surface modification. This is accompanied by an increase in the sizes of phase regions and a decrease in their number and in the total surface area of the exposed facet. The Ostwald ripening ceases when the growing particles reach a stable state at a given time and given temperature.

Figure 64 illustrates the tremendous impact of RH on the topological evolution of the exposed surface. Top views of surface changes of samples SI, SII and SIII respectively, are presented after 23 days of exposure. The number of bumps, their growth kinetic as well as their agglomeration tendency severally increase with RH. After 23 days of exposure to aging conditions, the morphological changes on the surface of SI were exclusively represented by the pyramid bumps and clusters resulting from the Ostwald ripening phenomenon (Figure 64 (a)). However, for SII sample exposed to higher RH, and after the same exposure period, the surface degradation is more pronounced than for SI (Figure 64 (b)) and we note that holes start to appear on the surface of the sample. This dynamic becomes more obvious with further increase of the RH, as shown for sample SIII (Figure 64 (c)).

Figure 65 presents the evolution of the heights of defects growing on the surface of exposed samples, as a function of exposure time. Regardless the RH at which the sample is exposed, the heights of defects increases over time. After 2 days of exposure, maximum heights of

10 nm, 89 nm and 157 nm were registered on SI, SII and SIII, respectively. 5 days later, these values increase and reach 50 nm, 147 nm and 270 nm respectively. After 18 days, the maximum heights rise to 100 nm, 339 nm and 640 nm, respectively. Herein, the impact of the RH is clearly pointed out: sample SIII stored at a RH 10% higher than that of SII, developed holes almost twice deeper than those measured on SII, for the same exposure period.

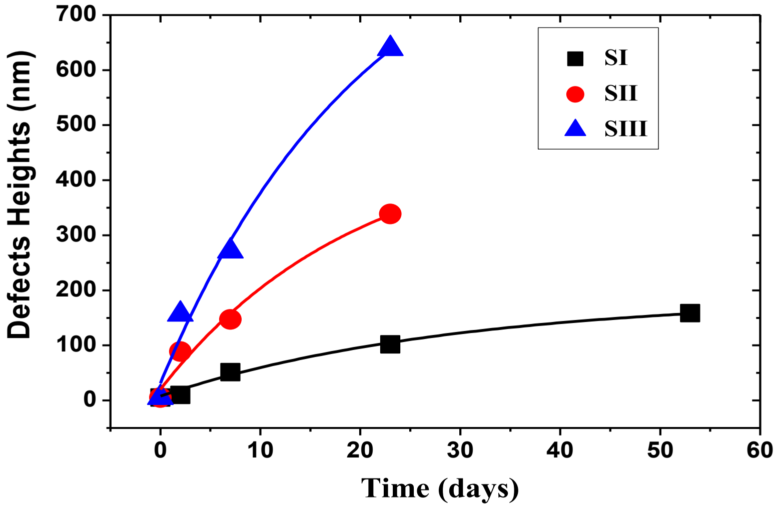

Figure 65: Heights evolution of defect growing at 50°C, on the surface of samples SI, SII and SIII, as a function of exposure time.

3.2.2. Prevention of glass fibers aging.

The previously discussed data show a deterioration of the glass surface due to the corrosive action of atmospheric moisture. In attempts to block or delay the whole process, an As_2S_3 fiber sample was stored in anhydrous atmospheric conditions during 6 months. Throughout this period, the sample was stored in dark, at temperature varying between 20-35°C, inside a glove box where moisture level was maintained less than 0.5 ppm. During the same period, another part of the same fiber was stored in ambient atmospheric conditions. Figure 66 gathers top views of AFM 3D-pictures registered on fresh sample (immediately after being drawn) and on the two previously described samples. This experiment confirms that the morphology changes occurring on the surface of glass fibers are significantly reduced under moisture-free atmosphere. The maximum defects height registered after six month of exposure did not exceed the 50 nm threshold for the samples stored in dry conditions (Figure

66 (b)), when it reaches 480 µm for the counterpart sample stored in air (Figure 66 (c)).These results provide new evidence on the necessity of water adsorption on the surface of the sulphide glass to lead to a significant chemical aging via the hydrolysis processes discussed above.

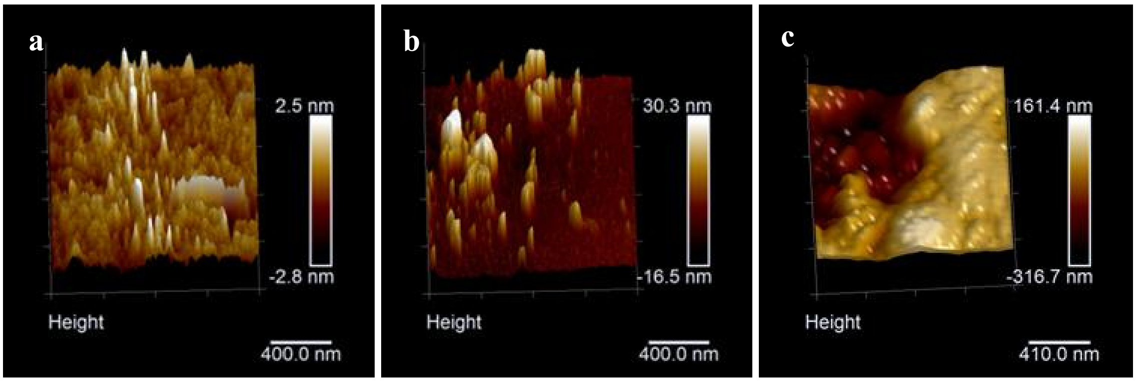

Figure 66: Top view of AFM 3D-pictures of the surface of As_2S_3 glass fibers: (a) fresh sample; (b) 6 months of storage in dry atmosphere at room temperature; (c) 6 months of storage in air at room temperature.

3.3. Depth diffusion of impurities.

Results previously discussed confirm a hydrolysis reaction taking place on the surface of the glass (Section 3.1), leading to locally deteriorate the glass network and giving rise to holes on its surface which continue to sink in depth over time (Section 3.2). Thus, a question arises about the limits in depth reached by the hydrolysis process, as well as the resulting changes in glass composition. The resulting local drift of the glass composition will induce a local shift of the glass nano-mechanical properties, especially the friction properties [32]. Thus, at the boundary between contaminated and uncontaminated zones, the friction properties change and become inhomogeneous over these two zones. Based on the aforementioned and in order to study the depth diffusion of the aging-induced structural modifications of the glass, we investigated the homogeneity of the friction properties on the cross section of glass fiber samples stored under wet and dry conditions. The qualitative evolution of the friction properties was studied by means of an advanced mode of the AFM technique, known as lateral force microscopy (LFM) with a scanning angle rotated at 90°. Figure 67 represents a schematic illustration of the investigated zones. Results of the investigations are gathered in Figure 68.

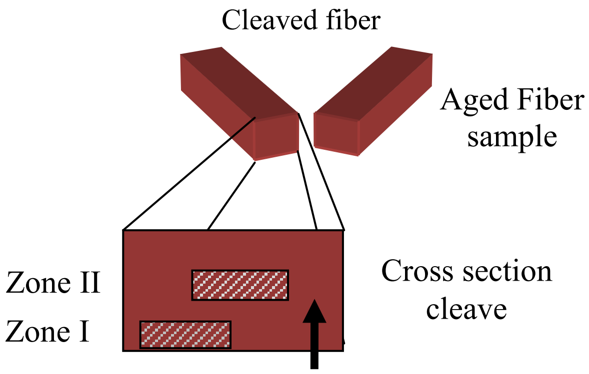

Figure 67: Illustration of investigated zones on the cross section of the glass fiber.

Figure 68 illustrates fracture profile registered on the cross sections of As_2S_3 fibers upon exposure to ambient (wet) and dry surrounding atmosphere. One rectangular fiber sample has been exposed to room atmosphere during 7 days, at a temperature ranging between 20 and 25°C and a RH around 65%. Another fiber sample has been stored in a glove box for 6 months, in the same temperature range and under dry atmosphere (around 0.5 ppm H_2O). The views of the fiber exposed to dry atmosphere shows homogeneous friction properties (Figure 68 (a-b)) throughout the investigated area, I and II (Figure 67), whereas that exposed to wet atmosphere displays different distinct surfaces of different friction characteristics (Figure 68 (c-d)). Additionally, for the sample exposed to wet atmosphere, by approaching the center of the specimen (zone II-Figure 67), the sample restores the homogenous friction properties of the original glass material (Figure 68 (d)). In addition, the signature of heterogeneous friction properties appears inside the fiber, down to 30 µm in depth from the surface of the specimen (Figure 68 (d)). In other words, the signature of glass hydrolysis by atmospheric conditions took place inside the fiber, at 30 µm from its surface, after 7 days of aging. Thus, based on the aforementioned, we can wisely conclude that the hydrolysis process, and indirectly the H_2O molecules diffusion have reached the 30µm depth threshold.

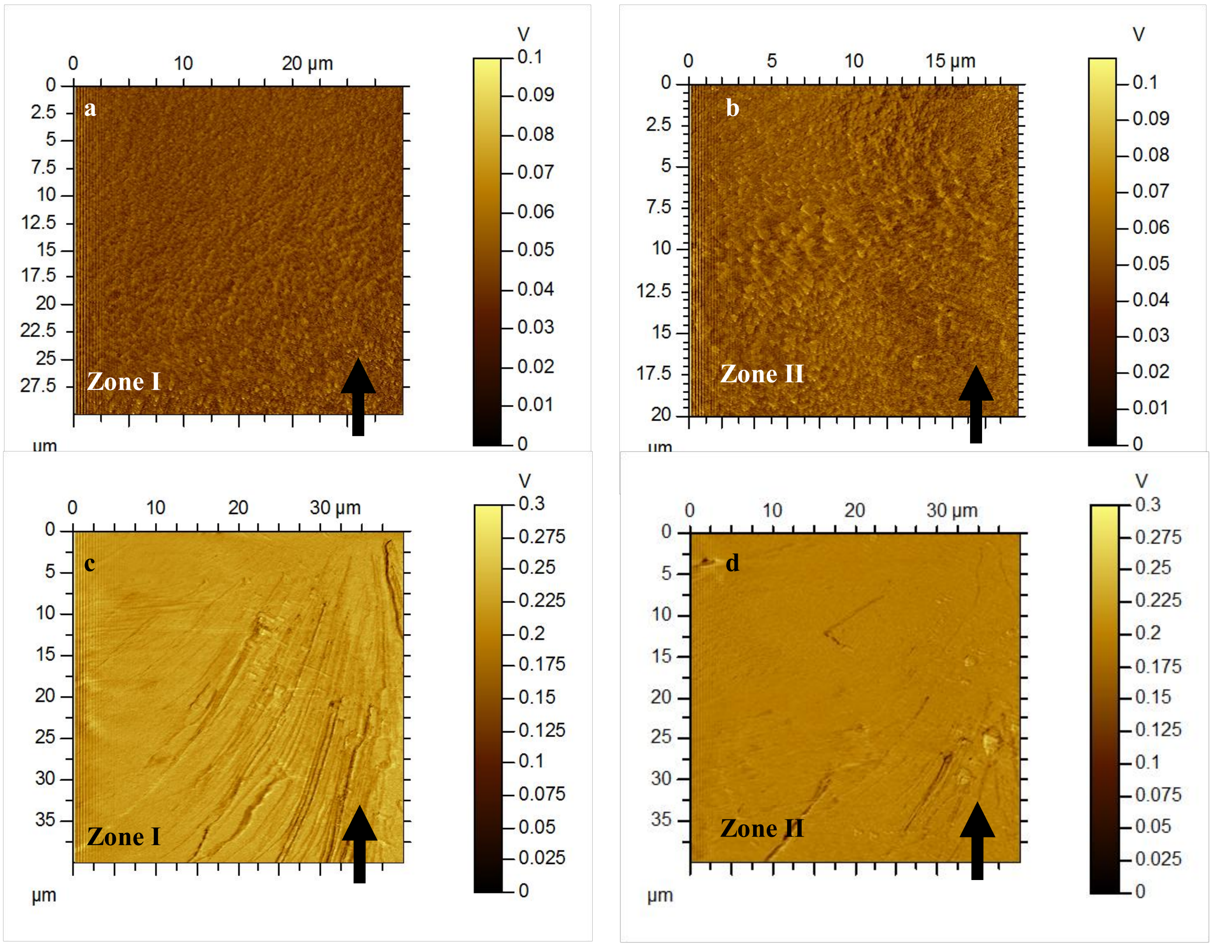

Figure 68: Friction micrographs revealing the fracture feature on the cross section of As_2S_3 fiber. (a)-(b) Fracture features on fiber exposed to dry atmosphere during 6 months on the surface and the center respectively; (c)-(d) Fracture features on fiber exposed to ambient atmospheric conditions during 7 days on the surface and the center, respectively. The black arrow shows the inward direction from the surface to the center of the fiber.

Theoretically, under the external surroundings, the glass structure undergoes a structural rearrangement to reach more stable equilibrium state consistent with the new conditions [33]. Consequently, the mechanical properties originate from the new structural rearrangement under the influence of applied stress will be different from those of the original sample [32]. In this context, water vapor and oxygen was found to be a hostile chemical environments for the chalcogenide glasses [19]. Traces of water in the glass structure may significantly weaken the glass [33]. For As_2S_3 glass fibers exposed to ambient conditions, physical and structural properties of the glass are seriously affected. Studies performed on single-index fiber previously reported by Golovchak and al. [34, 35] and Churbanov and al. [19] have shown an increase of the mechanical losses on uncoated fibers exposed to ambient atmosphere, whereas coated fibers did not show any deviation. These results are consistent with those reported herein, where non deviation of friction signature appeared within the sample stored in dry atmosphere (Figure 68 (a-b)), whereas opposite behavior was registered on sample exposed to wet atmosphere (Figure 68 (c-d)). Thus, heterogeneous friction response and mechanical damping of chalcogenide glasses are particularly due to the hydrolysis process of the glass induced by water adsorbed on its surface. These results indicate that the aforementioned phenomenon is dominated by the moisture vapor.

3.4. Cracks proliferation on the surface of aged fiber.

Results mentioned above confirm that atmospheric moisture deteriorate the glass network and diffuse from the surface deeply inside the glass. In addition, according [18, 19], water is known to initiate crack propagation on the glass surface and to decrease the mechanical strength of chalcogenide glasses. However, such phenomena depends on the glass composition, the presence of protective coat, surrounding atmosphere as well as the temperature [18, 19]. Niu and al. [18] reported the growth of cracks on the surface of As_2S_3 corroded bulk when it is soaked in water. The previously described features are attributed to a corrosive surface reaction taking place between the glass and water, which is considered as an extremely deleterious surrounding medium. Note that the kinetic of the aforementioned reaction depend on the pH of the leach and the experimental temperature. On the other hand, Churbanov and al. [19] attributed the strength collapse of the aged fiber to cracks defects growing on uncoated As-S fibers. Herein, Figure 69 displays the growth of cracks on the surface of the fiber upon exposure to different atmospheric conditions obtained by scanning electron microscopy (SEM Jeol 6500). After 6 months of storage in moisture-free atmosphere, the glass fiber exhibits a surface exempt of cracks (Figure 69 (a)), and maintain a smooth surface as it originally appears immediately after drawing process. However, after 7 days of exposure to atmospheric moisture surrounding, cracks appear on the fiber surface and dig deeply over time (Figure 69 (b)). These results are consistent with the hydrolysis process between the glass and the surrounding moisture vapour.

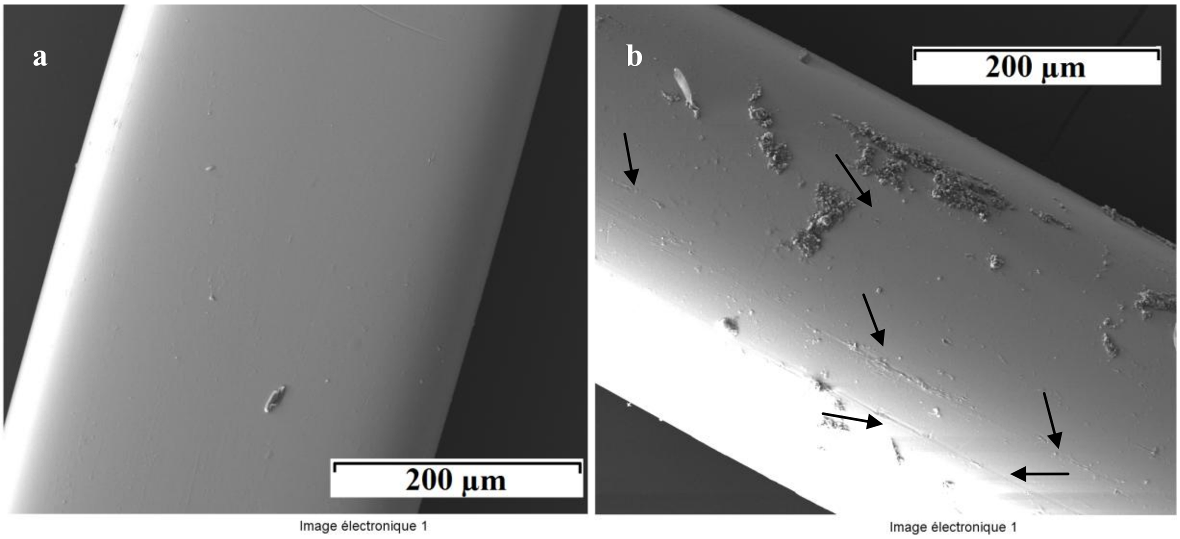

Figure 69: SEM images of the surface of As_2S_3 rectangular fibers: (a) preserved in dry atmosphere; (b) conserved 7 days in ambient laboratory atmosphere at 25°C and 65% RH. The black arrows point on the cracks and craters evolving on the fiber surface upon aging.

4. Conclusion

IR and AFM fiber studies performed upon exposure to different atmospheric conditions show that As_2S_3 fibers undergo, under room atmospheric conditions, an optical aging, a degradation of their surface and a gradual alteration of the glass network which evolves in depth. When stored under ambient conditions, the As_2S_3 glass optical fiber is severely attacked by atmospheric moisture which is the critical factor involved in this aging process. A hydrolysis process takes place associated with shrinkage of As-S glassy backbone. This aging is particularly to be taken into account when using microstructured fibers, for which a small glassy core is surrounded by ambient atmosphere and thus especially subjected to a strong impact of its reaction with atmospheric steam. This strictly implies to use that type of fibers in a dry environment.

Acknowledgements.

We acknowledge the financial support from the Conseil Régional de Bourgogne through the Photcom PARI program, as well as from the French DGA. This project has been performed in cooperation with the Labex ACTION program (contract ANR-11-LABX-0001-01).

5. References

1. D. Lezal, "Chalcogenide glasses - survey and progress," Journal of Optoelectronics and Advanced Materials **5**, 23-34 (2003).
2. J. S. Sanghera, and I. D. Aggarwal, "Active and passive chalcogenide glass optical fibers for IR applications: a review," Journal of Non-Crystalline Solids **256-257**, 6-16 (1999).
3. R. R. Gattass, L. Brandon Shaw, V. Q. Nguyen, P. C. Pureza, I. D. Aggarwal, and J. S. Sanghera, "All-fiber chalcogenide-based mid-infrared supercontinuum source," Optical Fiber Technology **18**, 345-348 (2012).
4. I. Savelii, O. Mouawad, J. Fatome, B. Kibler, F. Désévédavy, G. Gadret, J. C. Jules, P. Y. Bony, H. Kawashima, W. Gao, T. Kohoutek, T. Suzuki, Y. Ohishi, and F. Smektala, "Mid-infrared 2000-nm bandwidth supercontinuum generation in suspended-core microstructured Sulfide and Tellurite optical fibers," Optics Express **20**, 27083-27093 (2012).
5. W. Gao, M. El Amraoui, M. Liao, H. Kawashima, Z. Duan, D. Deng, T. Cheng, T. Suzuki, Y. Messaddeq, and Y. Ohishi, "Mid-infrared supercontinuum generation in a suspended-core As_2S_3 chalcogenide microstructured optical fiber," Optics Express **21**, 9573-9583 (2013).
6. J. Troles, Q. Coulombier, G. Canat, M. Duhant, W. Renard, P. Toupin, L. Calvez, G. Renversez, F. Smektala, M. El Amraoui, J. L. Adam, T. Chartier, D. Mechin, and L. Brilland, "Low loss microstructured chalcogenide fibers for large non linear effects at 1995 nm," Optics Express **18**, 26647-26654 (2010).
7. O. Mouawad, J. Picot-Clémente, F. Amrani, C. Strutynski, J. Fatome, B. Kibler, F. Désévédavy, G. Gadret, J. C. Jules, D. Deng, Y. Ohishi, and F. Smektala, "Multioctave midinfrared supercontinuum generation in suspended-core chalcogenide fibers," Optics Letters **39**, 2684-2687 (2014).
8. J. H. V. Price, T. M. Monro, H. Ebendorff-Heidepriem, F. Poletti, P. Horak, V. Finazzi, J. Y. Y. Leong, P. Petropoulos, J. C. Flanagan, G. Brambilla, F. Xian, and D. J. Richardson, "Mid-IR supercontinuum generation from nonsilica microstructured optical fibers," IEEE Journal of Selected Topics in Quantum Electronics **13**, 738-749 (2007).
9. J. M. Dudley, G. Genty, and S. Coen, "Supercontinuum generation in photonic crystal fiber," Reviews of Modern Physics **78**, 1135-1184 (2006).
10. V. Q. Nguyen, J. S. Sanghera, P. Pureza, F. H. Kung, and I. D. Aggarwal, "Fabrication of arsenic selenide optical fiber with low hydrogen impurities," Journal of the American Ceramic Society **85**, 2849-2851 (2002).

11. A. E. Kurganova, G. E. Snopatin, and M. F. Churbanov, "Purification of glass melts in the As-Se system with vacuum distillation," Glass Physics and Chemistry **38**, 300-306 (2012).
12. D. Thompson, S. Danto, J. D. Musgraves, P. Wachtel, B. Giroire, and K. Richardson, "Microwave assisted synthesis of high purity As_2Se_3 chalcogenide glasses," European Journal of Glass Science and Technology Part B **54**, 27-34 (2013).
13. N. Prasad, D. Furniss, H. L. Rowe, C. A. Miller, D. H. Gregory, and A. B. Seddon, "First time microwave synthesis of $As_{40}Se_{60}$ chalcogenide glass," Journal of Non-Crystalline Solids **356**, 2134-2145 (2010).
14. G. E. Snopatin, V. S. Shiryaev, V. G. Plotnichenko, E. M. Dianov, and M. F. Churbanov, "High-purity chalcogenide glasses for fiber optics," Inorganic Materials **45**, 1439-1460 (2009).
15. S. Danto, D. Thompson, P. Wachtel, J. D. Musgraves, K. Richardson, and B. Giroire, "A comparative study of purification routes for As_2Se_3 chalcogenide glass," International Journal of Applied Glass Science **4**, 31-41 (2013).
16. M. El-Amraoui, G. Gadret, J. C. Jules, J. Fatome, C. Fortier, F. Désévédavy, I. Skripatchev, Y. Messaddeq, J. Troles, L. Brilland, W. Gao, T. Suzuki, Y. Ohishi, and F. Smektala, "Microstructured chalcogenide optical fibers from As_2S_3 glass: towards new IR broadband sources," Optics Express **18**, 26655-26665 (2010).
17. I. D. Aggarwal, F. Kung, J. S. Sanghera, L. B. Shaw, and P. A. Thielen, "IR supercontinuum source," (Google Patents, 2006).
18. Y.-F. Niu, J.-P. Guin, A. Abdelouas, T. Rouxel, and J. Troles, "Durability of an As_2S_3 chalcogenide glass: Optical properties and dissolution kinetics," Journal of Non-Crystalline Solids **357**, 932-938 (2011).
19. M. F. Churbanov, V. S. Shiryaev, V. V. Gerasimenko, A. A. Pushkin, I. V. Skripachev, G. E. Snopatin, and V. G. Plotnichenko, "Stability of the optical and mechanical properties of chalcogenide fibers," Inorganic Materials **38**, 1063-1068 (2002).
20. R. J. Curry, S. W. Birtwell, A. K. Mairaj, X. Feng, and D. W. Hewak, "A study of environmental effects on the attenuation of chalcogenide optical fibre," Journal of Non-Crystalline Solids **351**, 477-481 (2005).
21. P. Toupin, L. Brilland, D. Mechin, J. Adam, and J. Troles, "Optical aging of chalcogenide microstructured optical fibers," Journal of Lightwave Technology, **32**, 2428-2432 (2014).
22. O. Mouawad, C. Strutynski, J. Picot-Clémente, F. Désévédavy, G. Gadret, J. C. Jules, and F. Smektala, "Optical aging behaviour naturally induced on As_2S_3 microstructured optical fibres," Optical Materials Express **4**, 2190-2203 (2014).

23. O. Mouawad, F. Amrani, B. Kibler, J. Picot-Clémente, C. Strutynski, J. Fatome, F. Désévédavy, G. Gadret, J. C. Jules, O. Heintz, E. Lesniewska, and F. Smektala, "Impact of optical and structural aging in As_2S_3 microstructured optical fibers on mid-infrared supercontinuum generation," Optics Express **22**, 23912-23919 (2014).
24. Y.-F. Niu, J.-P. Guin, T. Rouxel, A. Abdelouas, J. Troles, and F. Smektala, "Aqueous corrosion of the $GeSe_4$ chalcogenide glass: surface properties and corrosion mechanism," Journal of the American Ceramic Society **92**, 1779-1787 (2009).
25. L. Petit, N. Carlie, T. Anderson, J. Choi, M. Richardson, and K. C. Richardson, "Progress on the photoresponse of chalcogenide glasses and films to Near-Infrared femtosecond laser irradiation: a review," IEEE Journal of Selected Topics in Quantum Electronics, **14**, 1323-1334 (2008).
26. J. S. Berkes, S. W. I. Jr., and W. J. Hillegas, "Photodecomposition of amorphous As_2Se_3 and As_2S_3," Journal of applied Physics **42**, 4908-4916 (1971).
27. S. Krishnaswami, H. Jain, and A. C. Miller, "Effect of oxygen on the photoinduced changes in the electronic structure of $As_{50}Se_{50}$ glass films," Journal of Optoelectronics and Advcanced Materials **3**, 695-702 (2011).
28. M. El Amraoui, "Fibres Optiques Microstructurées Chalcogénures Fortement Non Linéaires à base de As_2S_3: vers de Nouvelles Sources Supercontinuum Infrarouges," PhD in ICB - Université de Bourgogne (Université de Borgogne, Dijon, France (2010).
29. T. Kanamori, Y. Terunuma, S. Takahashi, and T. Miyashita, "Transmission loss characteristics of $As_{40}S_{60}$ and $As_{38}Ge_5Se_{57}$ glass unclad fibers," Journal of Non-Crystalline Solids **69**, 231-242 (1985).
30. V. Kokorina, *Glasses for infrared optics* (The CRC Press, 1996).
31. E. Finot, E. Lesniewska, J. C. Mutin, and J. P. Goudonnet, "Reactivity of gypsum faces according to the relative humidity by scanning force microscopy," Surface Science **384**, 201-217 (1997).
32. A. Erdemir, S. Li, and Y. Jin, "Relation of certain quantum chemical parameters to lubrication behavior of solid oxides," International Journal of Molecular Sciences **6**, 203-218 (2005).
33. W. Zdaniewski, G. Rindone, and D. Day, "The internal friction of glasses," Journal of Materials Science **14**, 763-775 (1979).
34. R. Y. Golovchak, A. Kozdras, and O. I. Shpotyuk, "Physical ageing in glassy As-Se induced by above-bandgap photoexposure," Solid State Communications **145**, 423-426 (2008).

35. R. Y. Golovchak, S. A. Kozyukhin, A. Kozdras, O. I. Shpotyuk, and V. M. Novotortsev, "Physical aging of chalcogenide glasses," Inorganic Materials **46**, 911-913 (2010).

IV. SumUp.

The overall conclusions resulting from the previous work on As_2S_3 glasses are gathered in schematic illustration in Figure 70**.**

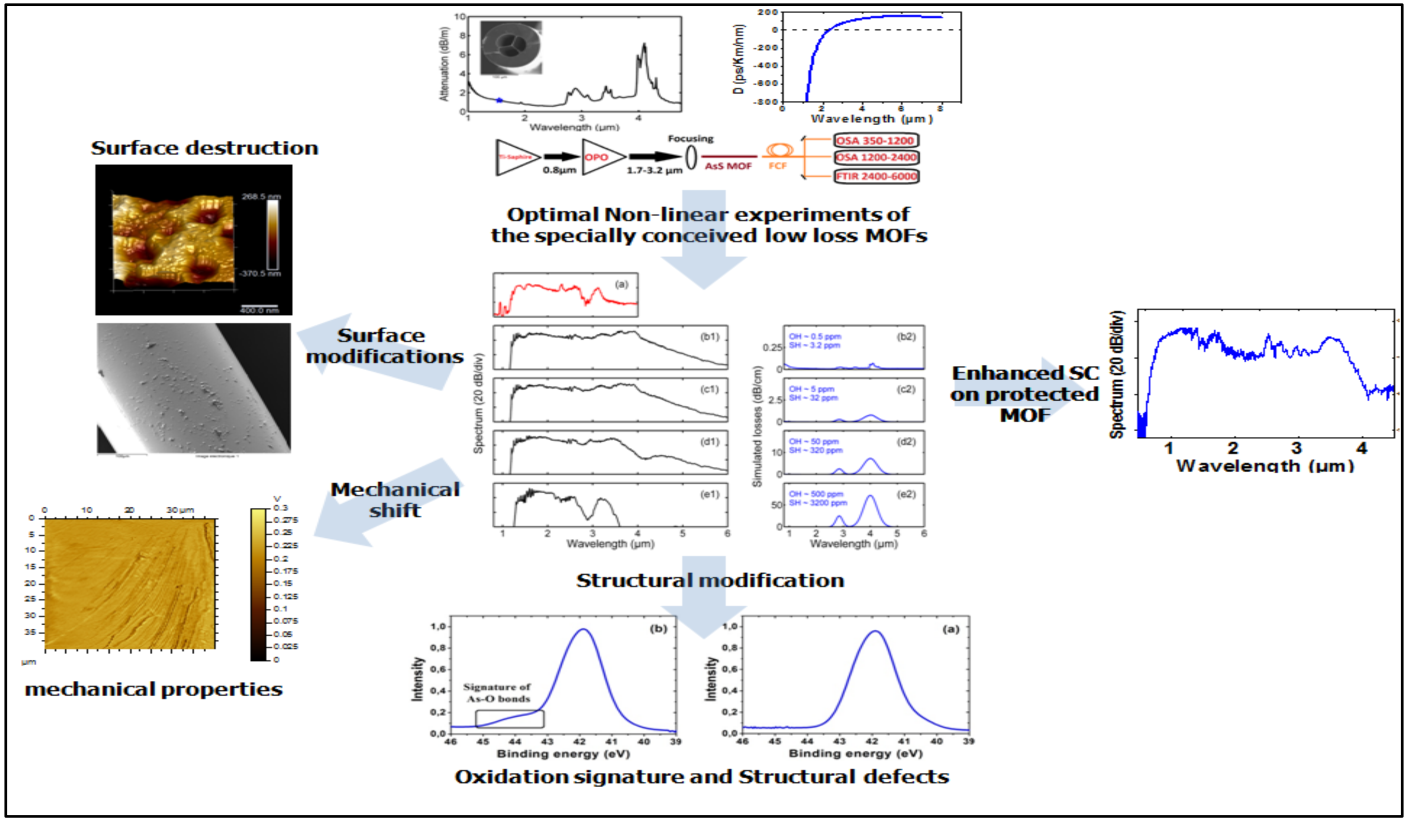

Figure 70: overall conclusions arising from this work summarized in schematic illustration.

V. Conclusion

In conclusion, great strides have been made in the understanding of the optical aging behavior of the As_2S_3 glass in fiber shape. We report on the first detailed spectroscopic study on unsuitable aging process of As_2S_3 chalcogenide microstructured optical fibers after few days of exposure to laboratory atmospheric conditions. The evolution and the impact of moisture-sorbed and hydroxyl impurities upon aging process have been studied on microstructured fibers using near-visible and infrared spectroscopy. The observed changes upon exposure period show that most of the deleterious effects of moisture occur over the first few hours.The rapid degradation recalls the dramatic increase of optical absorption in the 2.54-3.18 µm range, as well as at 1.9 µm and 1.44 µm. The growth of these bands results from a substantial reaction undergone between the glass and the adsorbed vapor moisture. This reaction is associated with breakage of As-S bonds glassy backbone within the glass matrix, associated with formation of OH and SH bonds.

The regular evolution of the absorption bands of hydroxyl components in glass fibers as a function of exposure period is pointed out. Based on experiments performed to investigate the local degradation in MOF's, it was found that the fibre degradation occurs heterogeneously along the fiber. This degradation decreases exponentially from the fibre ends towards the centre. Based on the changes of the loss levels that have been measured for different sections, depending on the position with respect to the end, the concentration of hydroxyl group is determined. The content estimates were performed on the basis of Beer-Lambert law, using the absorption coefficient of the concerned absorption band. Since there is no well defined absorption coefficient reported on chalcogenide glasses, we used as traditionally the parameters measured on silica glasses, and reported in literature. After 384 hours of exposure, the concentration of OH bonds vibrating at 1.92 µm is estimated to be ~147 ppm near the end of the aged fiber. This value decreases to ~10 ppm at 1.0 m from the end.

We also proved the naturally induced topological aging of the glass surface under ambient conditions. Great strides have been made in the understanding of origin of the scattering losses responsible for the transmission degradation at advanced stage. Advanced aging stages have showed an optical extinction of the fiber transmission attributed to surface defects evolving over time. The growth of surface defects is due to advanced chemical degradation at room temperature in presence of humidity, leading to formation of surface irregularities. These surface imperfections are essentially associated with small crystals of As_2O_3 (bumps), holes and cracks. However, these surface features grow in a sequential manner under humid atmosphere. The first step consist in formation of regular pyramidal bumps, assigned as crystals of As_2O_3, resulting from the oxidation of the glass network. Once these oxides species are formed, they will remain in a mobile state until it will amalgamate itself in a growth sites. Extending the exposure period results in losing the geometric regularity of superficial pyramidal bumps, given rise to new clusters. The process of growth of large particles at the expense of smaller ones because of the diminishing surface energy is known as Ostwald ripening. Later, deep holes dig within the glass volume. It was shown that these surface modifications dynamics might be accelerated by water and temperature. In addition, the glass contamination diffuses in depth inside the glass, and reaches several micrometers from its surface.

Part 4: Green Chalcogenide Ge-Based Glass Fibers Exempt of Toxic Arsenic and Antimony Components

I. Introduction

Among the various chalcogenide glass systems, the most important results were obtained for glasses based on chalcogenides of arsenic and germanium, including As_2S_3, As_2Se_3, GeAsSe. Except the GaLaS system [1, 2] and GeSe system [3, 4], the presence of arsenic and/or antimony seems mandatory, in order to fabricate chalcogenide glasses owing physicochemical properties suitable for fiber drawing. However, at the same time, these elements present the drawback to be highly toxic, and according to European "Registration, Evaluation and Authorisation of Chemicals (REACH)" Reglementation [5], it is suitable to remove them from glass composition. The arsenic- and antimony-free GaLaS glass system suffers from relatively poor thermal stability and consequently difficult to be drawn into crystal free fibers [1]. On the other hand, GeSe glass system exhibits low Tg, is not transparent in the visible and has high material dispersion. For these reasons, our work has focused on germanium-based sulfide glasses compatible with drawing process.

In the first section, we briefly describe the properties of the glass systems explored in this study. We first investigated the sulphur-based Ge-S and Ge-Ga-Ssystems. Because of fiber drawing difficulties, selenium was partially substituted for sulphur in GeSeS glass system. The second section is devoted to detail the optimal operation conditions for producing chalcogenide glasses by means of the melt quenching technique. The last section of the chapter presents the fiber drawing attempts of previously fabricated glasses and discusses the results.

II. Glass systems

II.1 Ge-S glass system

First study aimed to determine the phase diagram of the binary GeS_x system was performed by A. V. Novoselova and al. [6, 7]. For this purpose, the authors used the data of differential thermal analysis (DTA) an X-ray diffraction (XRD). Subsequent work studied carefully compositions neighboring to GeS and GeS_2 compounds and lead to refine the GeS phase diagram as shown in Figure 71 [7, 8]. With further research of Kawamoto and Tsuchihashi

[9], improvements were introduced on the study of forming region for bulk glass. Glass formation with water quenching of the glass melt is possible when "x" in GeS_x extends from 56.7 to 60 % atomic sulfur. Air cooling technique appears to be more optimum for glass formation when "x" lies in the 60-90 % range of atomic sulfur. Forming region for GeS_x glass fibers seems to be limited by the crystallization in the Ge-rich region (x < 50%). According to I. Kanamori and al. [10], it ranges between 75 and 85 % atomic sulfur. Shibata and al. [11] succeeded to more extend this range down to 68% since they draw fiber of $GeS_{2.2}$ composition.

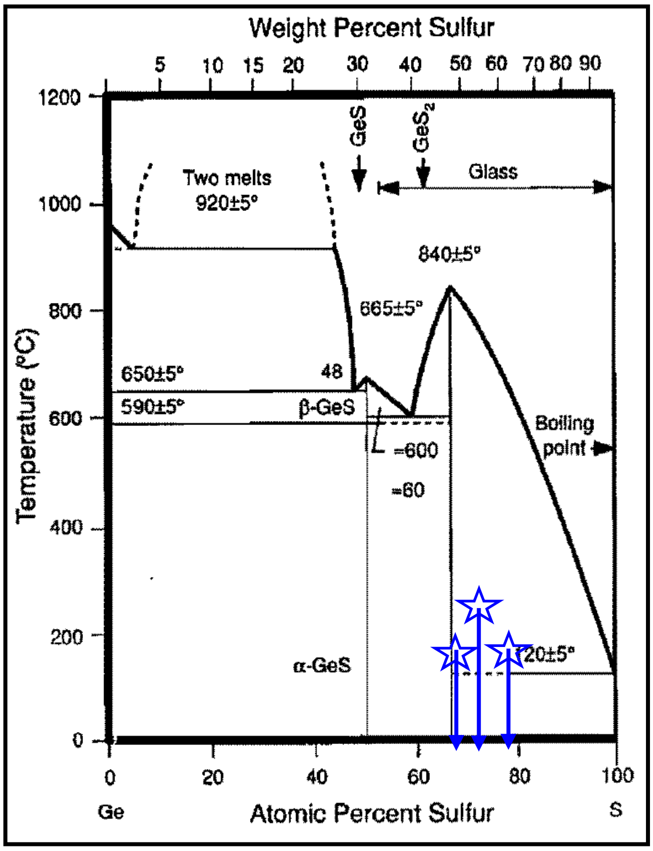

Figure 71: Phase diagram of Ge-S system [6, 7]. Glasscompositions studied in this work are gathered on the Phase diagram.

The transmission window of germanium sulfide chalcogenide glass system spreads from 0.5 to 11 µm on bulk sample [11-13]. The thermal behavior of these glasses was investigated by different studies [12, 14, 15]. They showed that the glass transition temperatures T_g exhibit arrow shape. It increases concurrently with the increase in the proportion of sulfur and reaches a maximum for $Ge_{0.65}S_{0.35}$ system. Further increase of sulfur reduces T_g of the binary compounds. Unlike the evolution of T_g, the glass stability regularly increases when the proportion of sulfur in the glass system increases [12].

II.2 Ge-Ga-S glass system

The first study of the ternary germanium gallium sulfide glass system was performed in the early 1975th by Loireau-Lozac'h and al. [16]. Auhors used results of DTA and XRD to construct the phase diagram of the GeS_2-Ga_2S_3 system. Later, glass formation, phase separation crystallization and the physical properties of GeGaS glass system have been studied [12].

Sulfide glasses suffer from phase separation upon glass synthesis. This phenomenon clearly interferes in sulfur rich compositions. Crystallization arises in germanium/gallium rich (sulfur poor) compositions. The glass-forming regions of GeGaS system is shown in Figure 72.

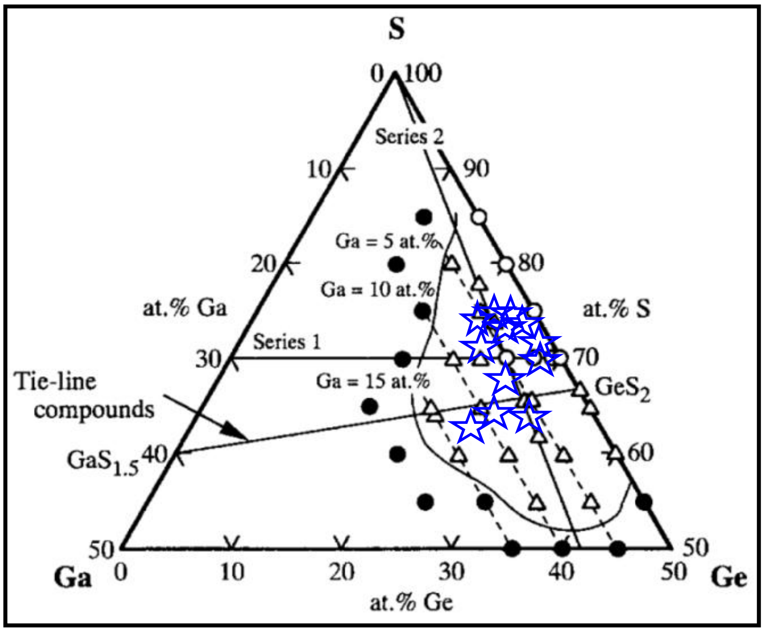

Figure 72: Glass formation in the Ge-Ga-S ternary system as determined by Abe and al. [11]. The fraction of Ge, Ga and S are expressed in %atm. Circles: glasses formed by slow air cooling; triangles: glass formed by fast iced-water quenching; dark circle: crystallized glasses. Bleu stars represent the glass compositions studied in this work.

The ternary GeGaS glass system exhibits a transmission window similar to that reported for GeS compounds, it extends from 0.5 to around 12 µm [7, 13, 17] on bulk specimen. Comparing to GeS system, GeGaS shows the same behavior concerning the transition temperature (Tg), and opposite behavior concerning the glass stability [12]. The glass transition temperatures T_g in all the series have maxima at the tie line-compounds shown in Figure 72. Above this maxima, T_g substantially decreases [12].

II.3 Ge-S-Se glass system

The glass forming regime in the ternary GeSSe system was constructed by gathering the work of several investigators [18-20]. The glass forming domain of this ternary system spreads over a wide region depending on the cooling rate of the glass melt. Alekseeva and al. [18, 19] studied the glass formation for low solidification rate, achieved by switching-off the furnace or by cooling in ambient atmosphere. The presence of two separate glass domains was confirmed upon low cooling rate applied for glass weight of 5 g. The phase diagram built by Alekseeva and al. is presented in Figure 73.

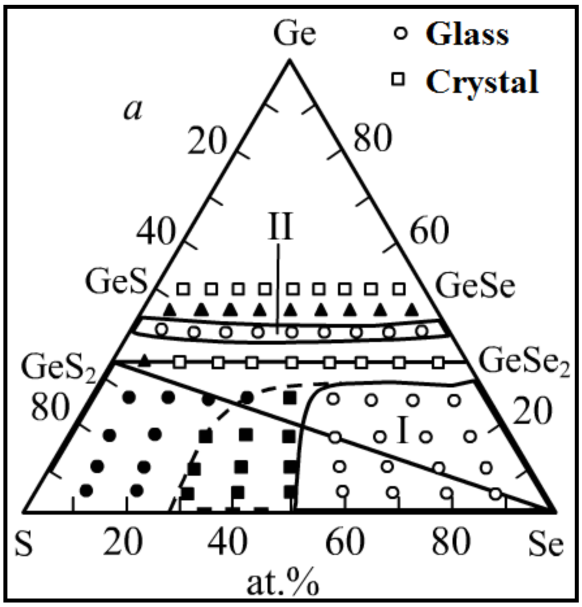

Figure 73: Glass formation in the Ge-S-Se ternary system as determined by Alekseeva and al. for low cooling rate. Regions I and II represent the forming regions of homogenous glasses. Black dots represent compositions for which glass stratifies.

Figure 74 shows the glass forming region derived from sharp quenching of GeSSe melt as established by Migolinec and al. [19, 20] for glass weight of 10-12 g. The high cooling rate quenching was achieved using ice-water or liquid nitrogen. Evidently, faster solidification of melt leads to significantly extend the region of stable glass over four domains (Figure 74).

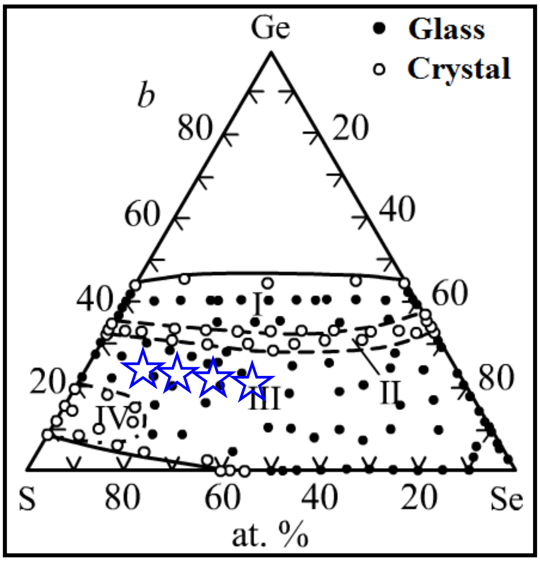

Figure 74: Glass formation in the Ge-S-Se ternary system as determined by Migolinets and al. for high cooling rate [18, 19]. Regions I and III represent the forming region of homogenous glasses. Regions II and IV represent the regions suffering from crystallization and stratification, respectively. Blue stars represent the glass compositions studied in this work.

III. Preparation of chalcogenide glasses.

III.1 Generalities about glass fabrication

The varieties of binary and ternary chalcogenide-based glasses were prepared by the conventional melt-quenching technique inside a vacuum-sealed silica ampoule. Elemental germanium (5N), sulfur (5N) and gallium (3N) reagents used in these experiments were of analytical grade purity.

In this study, the first aim was to select optimal glass composition with the maximum stability of the vitreous phases against devitrification upon fiber drawing. Thus, raw materials were not subject to purification processes prior to glass preparation. In these experiments, glass batches of 10 g to 50 g were prepared inside sealed silica ampoules.

Table 6 : Compositions of Germanium-based mono-chalcogenide (GeS and GeGaS) and di-chalcogenide (GeSSe) glasses prepared in frame of this work. D_I and T represent the inner diameter and the thickness of the various ampoules used to prepare the glass rods.

Glass composition	Batch weight (g)	Ampoule dimensions		Optimal quenching
		D_I (mm)	T (mm)	
GeS_x	10-15	9-16	2-3	Free air
$Ge_xGa_yS_z$	10-15	9-16	2-3	Compressed air
$Ge_xS_ySe_z$	50	16	3	Water

Germanium ingot was grinded into powder, since it increases the specific surface and consequently accelerates the glass forming reaction comparing to pieces of large size. Grinding was performed inside an inox mortar in ambient atmosphere. Thereafter, germanium particles were mixed with other elements in different molar ratios which are represented by blue stars and summarized in Figure 71, Figure 72 and Figure 74 (see Annex 4). The charge was then loaded into silica tube (see Table 6 for dimension) and connected to turbo vacuum pump then sealed as for As_2S_3 synthesis (see Synthesis of bulk.) This allows to prepare a glass rod by solidification of the glass melt through quenching either in air, pressurized air or water (Table 8 & Table 9) according to glass composition and batch weight. After melt quenching, the glass rods were annealed near, but below, their glass transition temperatures for 12 hours and in most cases thermally induced stresses were annealed out

III.2 Silica ampoule

During the first attempts of GeS_x glasses synthesis we encountered numerous ampoule explosions because of the high internal pressure in the ampoule at synthesis temperature due to sulfur vaporization; hence it is necessary to consider its vapor pressure evolution with temperature. Indeed vapor pressure of germanium is negligible compared to sulfur one [21]. In [21] a sulfur vapor pressure of 6.4 bars at 590°C is emphasized. For higher temperature no data are available in the literature. However, the small volume of the ampoule (10^{-5} m^3)

compared to the amount of sulfur (≥10g) allows to assume that the liquid-vapor equilibrium is reached in the silica ampoule at the synthesis temperature. In that case an estimation of the pressure inside the ampoule is possible by using the Clapeyron relationship (Equation 31),

$$\frac{dP}{dT} = \frac{L}{T\Delta V} \tag{31}$$

where P is the pressure, T the temperature, ΔV is the specific volume and L is the specific latent heat of the considered transition. In the case of vaporization and/or sublimation, the condensed phase volume (liquid and/or solid) is negligible. Thus ΔV is approximated by the gas volume V_{gas} which is estimated from perfect gases law. Finally after integration the following relationship between pressure and temperature is obtained:

$$P_{eq} = P_{ref}\frac{L}{R}\left(\frac{1}{T_{ref}} - \frac{1}{T_{eq}}\right) \tag{32}$$

where P_{ref} (bar) and T_{ref} (Kelvin) are the parameters for known conditions, L is the specific heat of vaporization of sulfur (considered fixed at 45 $kJ.mol^{-1}$) and R is ideal gas constant (8.314 $J.K^{-1}.mol^{-1}$). T_{eq} (Kelvin) is the synthesis temperature at which we consider equilibrium is reached and P_{eq} (bar) is the corresponding pressure we want to estimate. When taking as reference the standard (P_{ref} = 1 bar) boiling point of sulfur (T_{ref} = 717K) and the synthesis temperature of 950°C (Teq = 1223K) we obtained P_{eq} = 23 bars.

In order to overcome the difficulty coming from this high ampoule internal pressure we worked on two aspects: the mechanical properties of the silica ampoule and the thermal synthesis profile.

III.2.1 Ampoule dimensions

Despite the approximations in previous internal pressure estimation, the numerical result is consistent with experimental observations about ampoule explosions and mechanical resistance of silica tubes. Indeed, according to silica based glasses data sheet [22] the allowable pressure for a glass tube with the dimensions we currently used (16 mm inner diameter and 2 mm thickness) is around 17 bars, explaining thus the occasional ampoule explosions.

In accordance with Barlow formula (see Equation 33), increasing the thickness and/or decreasing the diameter improves internal pressure resistance of the ampoule.

$$P = \frac{2St}{D} \quad (33)$$

where P is allowable pressure, S allowable stress, D outer diameter and t the wall thickness. A 1 mm thicker ampoule with 15 mm inner diameter increases the allowable pressure to 24 bars [22] decreasing the ampoule explosion risk.

III.2.2 Time-temperature regime of glass synthesis process

Dernbovskii and al. [23, 24] have studied and reported the temperature of the reaction between germanium and sulfur or selenium. The interaction of germanium with sulfur occurs in the 407-655 °C temperature range, and with selenium in the 547-590 °C interval. Based on these data, the thermal profile of melting process of mono and di-chalcogenide compounds is established. Temperature profile consists of two-stages: the first one corresponds to the temperature of the reaction between germanium and chalcogen to form the melt and the second one corresponds the melt homogenization. However, we experimentally confirmed that the reaction at Dernbovskii temperature (first stage) was too slow. Thus, following a successful series of experiments, the first stage was raised to a higher temperature of 750 °C. If we increased further the temperature to higher levels, silica ampoule did not withstand the pressure and exploded.

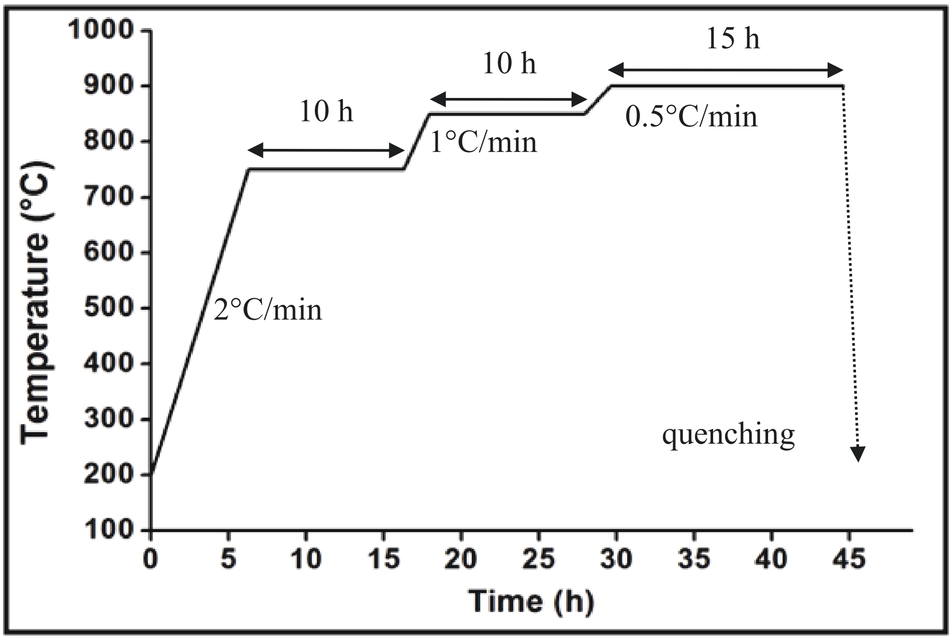

Figure 75: Typical temperature profile for glass melting of 50 g of glass.

In practice, despite the improvement allowed by the lifting of the first stage to a higher level of temperature, the process of the two-stage time-temperature profile remained time-consuming. Thus, with a view to speed up the process, efficient intermediate stage at 850°C has been added. The intermediate stage allowed to reduce the period at 750 °C and 900 °C to below 10 h and 15 h, respectively. A typical heating schedule for glass melting is showed in Figure 75.

Batches of mono- and di-chalcogenide glasses of weight up to 50g were successfully and repeatedly prepared inside a silica ampoule, typically of 20 cm length, 22 mm outer diameter and 3 mm wall thickness.

III.3 Glass-melt quenching.

Glass is obtained by cooling the melt in water, air or pressurized air. The quenching technique depends on the glass composition, the batch weight and the wall thickness of the synthesis ampoule. In general, higher cooling rates are needed when the weight of the batch or/and the wall thickness increases.

In the experiments, homogenous and solid glass rods of GeS mono-chalcogenide binary system were systematically quenched in free air (Table 6). Prior the quenching, the melt was kept in vertical position and gradually cooled down 50°C below synthesis temperature. This allowed to evacuate bubbles from the melt and leaded to a glass rod exempt of defects. When compressed air replaced the free air cooling strategy, the glass rods were weakened and showed deep cracks which persisted after annealing. These defects became more crucial when the batch was quenched in water. In the last case, it was not possible to obtain a glass rod.

Ternary mono-chalcogenide GeGaS system showed greater sensitivity to crystallization upon quenching. Free air quenching seemed to be unconvincing strategy since crystals appeared in the glass rods, whereas water chocked the glass upon quenching resulted in cracked glass as we have previously seen on GeS glass system. Compressed air was the best compromise between the slow and the rapid quenching. For the same purpose as above, quenching was conducted from 50°C below the synthesis temperature (Table 6).

Di-chalcogenide ternary Ge-S-Se glasses of 50 g were systematically prepared in ampoules of 16 mm of inner diameter and 3 mm of wall thickness. Prior quenching in water, furnace was kept in vertical position and glass melt was cooled down at 0.5 °C/min to a temperature 100°C below the synthesis temperature.

IV. Materials' optical properties - Transmission window

Transmission spectra, for wavelengths from the ultraviolet to the near infrared (350-2500 nm range), were measured with a Perkin Elmer Lambda 900 UV/VIS/NIR spectrophotometer. A Bruker IFS 28 Spectrophotometer was used to scan from 1.7µm to 25 µm. GeS_3, $Ge_{25}Ga_5S_{70}$, $GeSe_4$ and $Ge_{23.8}S_{57.1}Se_{19.1}$ glasses samples and their optical transmissions are presented in Figure 76 and Figure 77 respectively.

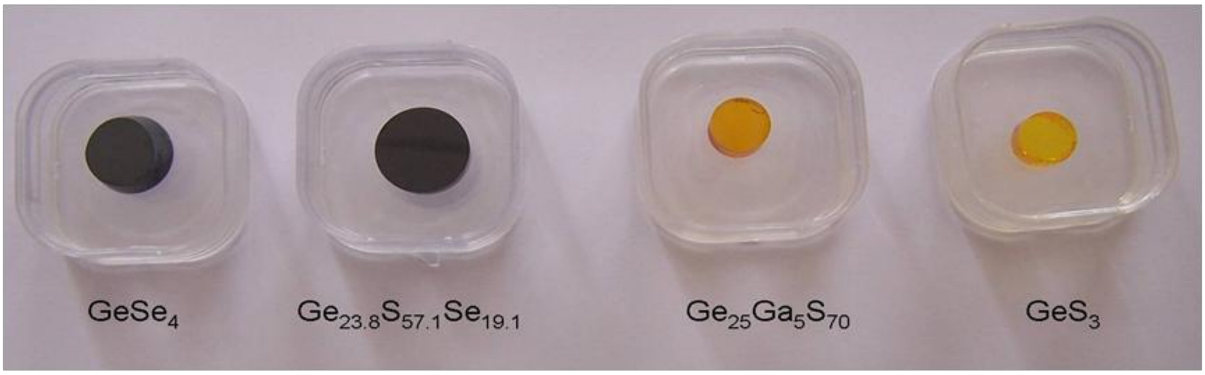

Figure 76: Glass samples used for transmission measurements

Figure 77 shows that GeS_3 and $Ge_{25}Ga_5S_{70}$ glasses exhibit a long wavelength cut-off located around 11.5 µm due to strong 2-phonon absorption process centered around 13.2 µm, and attributed to Ge-S and Ga-S bonds [25-27].

Substitution of all the sulfur by the heavier selenium element leads to shift the glass long multiphonon edge further in the IR. This is for the case of $GeSe_4$ glass. As shown in Figure 77, its cut-off wavelength is located around 17 µm. The hybrid mixture of S and Se within $Ge_{23.8}S_{57.1}Se_{19.1}$ glass maintains the same multiphonon edge around 11.5 µm as Se-free compositions.

Apart from intrinsic absorptions (band gap and multiphonon), principal sources contributing to the absorption peaks were found to be impurities such as oxides and hydrogenate entities.

The set of the main absorption peaks interrupting the glass transmission is presented on Figure 77. Peak assignments were based on the published literature on various systems [7, 10, 27-29]. Due to the oxygen-pollution of the glass, strong absorptions attributed to Ge-O and Ga-O bonds arise around 8.0 µm. The later absorptions become more crucial on long path samples such as optical fibers and narrow the operational transmission window around these characteristic vibrations frequencies.

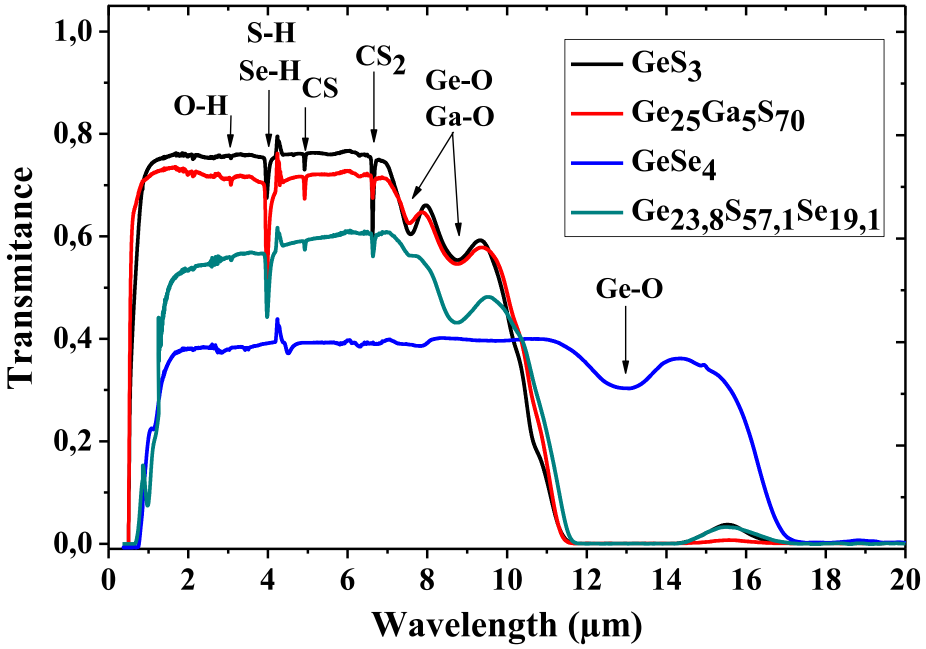

Figure 77: Optical transmission of the GeS_3 (6.72 mm), $Ge_{25}Ga_5S_{70}$ (5.9 mm), $GeSe_4$ (5.73 mm) and $Ge_{25}S_{55}Se_{20}$ (7.15 mm) glass systems.

V. Thermal properties - Transition and crystallization temperatures

The difference between the glass transition (T_g) and crystallization (T_x) temperatures defines empirically the glass stability (ΔT). This parameter determines the extent of resistance of the glass to crystallization. In this section, we overview the glass transition and crystallization temperatures of chalcogenide glasses previously presented.

Glass transition temperature (T_g) and crystallization temperature (T_x) are determined by differential calorimetric analysis (DSC) [7, 29].

These measurements were performed using DSC 2920 Modulated DSC-TA Instruments. Both reference and probed samples were heated simultaneously in aluminum crucible at a rate of 10 °C/min from ambient temperature to 400 °C, while the difference in energy inputs (heat flow) between the sample and reference is measured. The thermographs are depicted in Figure 78.

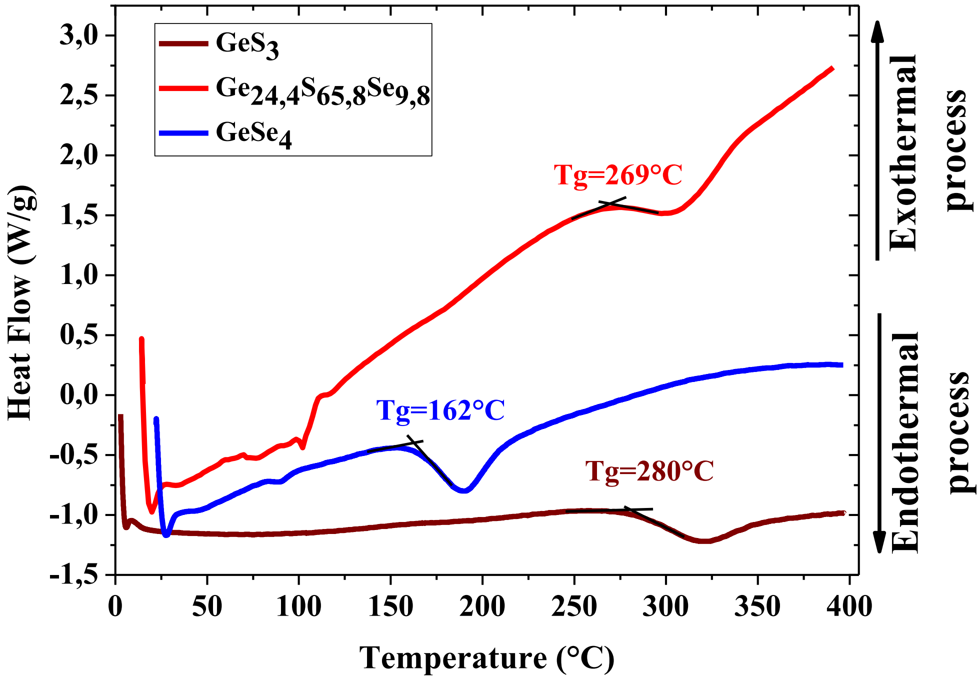

Figure 78: Differential scanning calorimetry curves for several glasses study.

No indication of crystallization (as evidenced by a crystallization peak) can be seen for these measurements. This indicates a good thermal stability of the investigated glasses against crystallization which is consistent with data reported in the literature [7, 12-15, 29]. Consequently, the thermal stability (ΔT) of GeS_3, $Ge_{24.4}S_{65.8}Se_{9.8}$ and $GeSe_4$ glasses are expected to exceed 127°C, 120°C and 238°C, respectively.

VI. Fiber drawing essays.

Drawing essays carried out in the frame of this work were applied on different glass compositions (Table 7). Preforms used herein exhibit an outer diameter varying between 9 and 16 mm, and a length of 50 mm.

Table 7: Fiber drawing ability, crystallization tendency and guidance potentials of different chalcogenide glass compositions.

Glass composition	Preform diameter (mm)	Crystallization upon drawing	Fiber drawing	Fiber guidance capability
Ge-S glasses	9-12	High rate	Failure	--
Ge-Ga-S glasses	9-12	High rate	Failure	--
$Ge_{24.4}S_{65.8}Se_{9.8}$	16	Low rate	Successful	Medium
$Ge_{23.8}S_{57.1}Se_{19.1}$	16	Absent	Successful	Good
$Ge_{23.2}S_{48.8}Se_{27.9}$	16	Absent	Successful	Good
$Ge_{22.7}S_{40.9}Se_{36.4}$	16	Absent	Successful	Good

GeS and GeGaS glasses were prone to crystallization upon drawing process, regardless the glass composition or the drawing operation conditions. During drawing attempts, the viscosity of the soften glass rods did never decrease enough for the glass to start flowing under the influence of gravity, thus finally leading to the crystallization (Figure 79).

Figure 79: GeS_3 sample crystallised during fiber drawing attempt.

The stability of GeS_3 glass materials to crystallization was reported by Churbanov and al. [30]. It was characterized by the rate of nucleation of the crystal phase, and the linear rate of crystal growth, as a function of temperature. Nucleation and growth of GeS_3 crystals are both in a narrow temperature range. These phenomena become more farther apart on GeS_2 based glass explaining their higher stability [7]. Nucleation and crystallization rates of GeS_3 compounds occur at 425°C and 485°C, respectively [7, 30]. The nucleation process within GeS_2 glass takes place in the same temperature range as in GeS_3 system (425°C), growth of crystals appears at higher temperature (510-620°C). Despite the higher thermal stability of GeS_2-based glasses, corresponding viscosity within the drawing operation temperature (Tx-Tg) remains significantly high [14], thereby preventing the possibility of successful fiber drawing.

Ga-containing GeS_3- and GeS_2-based glasses with different compositions have also been tested for drawing (see appendix 4). Despite the interesting results reported by Schimmel and al. [17], our work indicate that addition of gallium does not improve enough the ability of GeS-based glasses for fiber drawing.

The crystallization behavior and network structure of Ge- and Ga containing chalcogenide glasses have been reported in several studies [31-34]. Structural investigations revealed that gallium acts as a network co-former and introduces changes within the Ge-S network, modifying thus corresponding physicochemical properties [35-37]. Upon adding gallium to GeS_x glasses, the weaker Ga–S bonds forming at the expense of stronger Ge–S ones determine the lowering of Tg which is mainly related to the energy required to break and re-form covalent bonds in a random network lattice [31]. High content of Ga induced the growth of Ga-Ga bonds, reducing thus the network connectivity and shifting again Tg to lower temperature levels. Loireau-Lozac'h and al. [16] have studied the crystallization behavior of the $(GeS_2)_x(Ga_2S_3)_y$ glass system. This study confirmed that the kinetics of crystallization depends on the Ga_2S_3 content in the glass. It significantly increases in high Ga-content compounds. When Ga_2S_3 does not exceed the 15% threshold within the stoichiometric $(GeS_2)_x(Ga_2S_3)_y$ system, a single crystallization peak arise around 520°C. By increasing the absolute content of Ga_2S_3, new crystallization peaks arise between 450 and 480°C. Simons [7] reported that excess-sulfur content within $(GeS_3)_x(Ga_2S_3)_y$ weakened the glass resistance against devitrification.

In light of the unfitness of addition of single Gallium element to improve enough the physicochemical characteristics of the GeS_x glass to commensurate with the requirements of fiber drawing, sulfur has been replaced progressively by selenium. Se addition allowed us to successfully draw glass fibers from different compositions as reported in Table 7. This progress can be explained by the average bond strengths present in the glass ($E_{Ge\text{-}Se}$=230 kJ/mol, $E_{Ge\text{-}S}$=279 kJ/mol [38]), which are higher in the sulfide glasses than in the selenide glass, and the modification of the viscosity-temperature behavior.

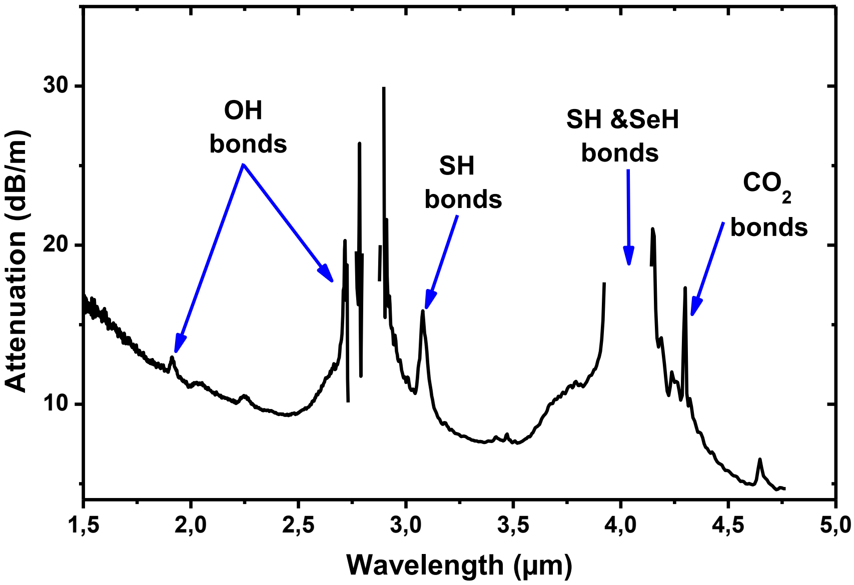

Figure 80: Early attenuation spectrum for un-purified $Ge_{23.8}S_{57.1}Se_{19.1}$ fiber.

Figure 80 displays an early attenuation spectrum registered on un-purified $Ge_{23.8}S_{57.1}Se_{19.1}$ glass fiber. The experimental data are depicted in the range of 1.5 to 5 µm. Despite that strong absorptions bands appear in the zone at which the OH, SH and SeH manifest themselves, this fiber shows a good guiding potential. These unsuitable absorptions persist since no purifications were carried out for raw materials. At the moment, after the selection of the suitable glass composition in view of fiber drawing, efforts are devoted to fabricate a highly pure GeSSe MOFs for SCG. For this purpose, on the first hand, we are working on optimization of a purification process in order to fabricate highly pure glass fibers. In parallel, the optimization of drilling technique used to prepare the glass preform, as well as the MOFs drawing process are in progress.

VII. Conclusion

Germanium based binary and ternary chalcogenide glasses have been successfully prepared. The synthesis time-temperature regime and the synthesis ampoule dimensions are optimized to allow the preparation of 50 g of glass batch. Both GeS and GeGaS binary systems have a strong tendency for crystallization upon fiber drawing conditions, preventing thus a successful drawing of corresponding glass rods into fibers. The GeSSe ternary glass system exhibits higher thermal stability and better viscosity-temperature behaviour at high temperature, allowing thus to fabricate fibers without crystallization. Experiments are going on with the purpose to reach suitable microstructured fibers from these "green" glasses.

VIII. References

1. Y. D. West, T. Schweizer, D. J. Brady, and D. W. Hewak, "Gallium lanthanum sulphide fibers for infrared transmission," Fiber and integrated optics **19**, 229-250 (2000).
2. H. Takebe, B. J., H. W., and M. K., "Thermal properties of Ga_2S_3-based glass and their consideration during fiber drawing," Journal of non-crystalline solids **258**, 239-243 (1999).
3. J. Troles, V. Shiryaev, M. Churbanov, P. Houizot, L. Brilland, F. Desevedavy, F. Charpentier, T. Pain, G. Snopatin, and J. L. Adam, "$GeSe_4$ glass fibres with low optical losses in the mid-IR," Optical Materials **32**, 212-215 (2009).
4. H. Patrick, S. Frédéric, C. Vincent, T. Johann, and G. Ludovic, "Selenide glass single mode optical fiber for nonlinear optics," Optical Materials **29**, 651-656 (2007).
5. http://www.hse.gov.uk/reach/whatisreach.htm
6. L. C. Hua, A. S. Pashinkin, and A. V. Novoselova, "Research on the system Ge-S," Dokl. Akad. Nauk SSSR **151**, 1335 (1963). (in Russian)
7. D. R. Simons, "Germanium Gallium Sulfide Glasses for Pr-doped Fiber Amplifiers at 1.3 µm," PhD in *Eindhoven University of Technology* (Eindhoven University of Technology, Netherlands, 1995).
8. P. N. Kumta, and S. H. Risbud, "Novel glasses in rare-earth sulphide systems," Ceramic Bulletin **69**, 1977-1984 (1990).
9. Y. Kawamoto, and S. Tsuchihashi, "Glass-forming regions and structure of glasses in the system ge-s," Journal of the American Ceramic Society **52**, 626-627 (1969).
10. T. Kanamori, Y. Terunuma, S. Takahashi, and T. Miyashita, "Chalcogenide glass fibers for mid-infrared transmission," Journal of Lightwave Technology **2**, 607-613 (1984).
11. S. Shibata, Y. Terunuma, and T. Manabe, "Sulfide glass fibers for infrared transmission," Materials Research Bulletin **16**, 703-714 (1981).
12. K. Abe, H. Takebe, and K. Morinaga, "Preparation and properties of Ge—Ga—S glasses for laser hosts," Journal of Non-Crystalline Solids **212**, 143-150 (1997).
13. X. F. Wang, X. J. Zhao, Z. W. Wang, H. T. Guo, S. X. Gu, J. G. Yu, C. L. Liu, and Q. H. Gong, "Thermal and optical properties of GeS_2-based chalcogenide glasses," Materials Science and Engineering: B **110**, 38-41 (2004).
14. J. Malek, and J. Shanelova, "Viscosity of germanium sulfide melts," Journal of Non-Crystalline Solids **243**, 116-122 (1999).

15. G. Saffarini, "On topological transitions and chemical ordering in network glasses of the Ge-Ga-S system," Solid State Communications **91**, 577-580 (1994).

16. A. M. Loireau-Lozac'h, and M. Guittard, "Système GeS_2-Ga_2S_3 diagramme de phases, obtention et propriétés des verres," Annale de chimie **10**, 101 (1975).

17. R. C. Schimmel, A. J. Faber, H. d. Waardt, R. G. C. Beerkens, and G. D. Khoe, "Development of germanium gallium sulphide glass fibers for 1.3 µm praseodymium-doped fiber amplifier," Journal of Non-Crystalline Solids **284**, 188-192 (2001).

18. I. V. Alekseeva, A. A. Obraztsov, Z. U. Borisova, and M. D. Balmakov, "Stekloobrazovanie v sistemah Ge-S-Se," Fiz. i Him. Stekla. **4**, 411-415 (1978). (in Russian)

19. D. I. Bletskan, "Glass formation in binary and ternary chalcogenide systems," Chalcogenide Letters **3**, 81-119 (2006).

20. I. M. Migolinec, and M. Y. Sichka, "Stekloobrazovanie v sistemah Ge-S-Se," Fiz. Him. Stekla **5**, 287-290 (1979). (in Russian)

21. Y. Mehrotra, "Preparation and Properties of Chalcogenide Glasses In As-Ge-S and As-Ge-Se systems," PhD in *Georgia Institute of Technology* (Georgia Institute of Technology, Georgia, 1976).

22. http://www.ilpi.com/glassblowing/techdata.html

23. S. A. Dernbovskii, E. N. Loitsker, and I. Akacl., "Preparation and study of some properties of germanium dichalcogenide single crystals," Izv. Akacl. Nauk SSSR, Neorg. Mater. **1**, 2092-2094 (1967). (in Russian)

24. D. I. Bletskan, "Material synthesis and growth of the crystals of the type $A^{IV}B^{VI}$ and $A^{IV}B_2{}^{VI}$ " Chalcogenide Letters **4**, 1-16 (2007).

25. D. S. Ma, P. S. Danielson, and C. T. Moynihan, "Multiphonon absorption in xAs_2S_3-(1-x)GeS_2 glasses," Journal of Non-Crystalline Solids **81**, 61-70 (1986).

26. B. Frumarova, J. Oswald, P. Krecmer, M. Frumar, V. Cerny, and V. Smrcka, "Synthesis and physical properties of the system $(GeS_2)_{80}$-$x(Ga_2S_3)_{20}$:xPr glasses," Optical Materials **6**, 217-223 (1996).

27. T. Kanamori, Y. Terunuma, S. Takahashi, and T. Miyashita, "Transmission loss characteristics of $As_{40}S_{60}$ and $As_{38}Ge_5Se_{57}$ glass unclad fibers," Journal of Non-Crystalline Solids **69**, 231-242 (1985).

28. V. Kokorina, *Glasses for infrared optics* (The CRC Press, 1996).

29. R. Schimmel, "Toward more effecient praseodymium doped fiber amplifiers for the O-band," PhD in *Technische Universiteit Eindhoven* (Technische Universiteit Eindhoven, Netherland, 2006).

30. M. F. Churbanov, "High-purity chalcogenide glasses as materials for fiber optics," Journal of Non-Crystalline Solids **184**, 25-29 (1995).

31. C. Lin, L. Calvez, H. Tao, M. Allix, A. Moréac, X. Zhang, and X. Zhao, "Evidence of network demixing in GeS_2-Ga_2S_3 chalcogenide glasses: A phase transformation study," Journal of Solid State Chemistry **184**, 584-588 (2011).

32. C. Lin, L. Calvez, M. Rozé, H. Tao, X. Zhang, and X. Zhao, "Crystallization behavior of $80GeS_2$-$20Ga_2S_3$ chalcogenide glass," Applied Physics A **97**, 713-720 (2009).

33. Y. Ledemi, B. Bureau, L. Calvez, M. L. Floch, M. Rozé, C. Lin, X. H. Zhang, M. Allix, G. Matzen, and Y. Messaddeq, "Structural investigations of glass ceramics in the Ga_2S_3-GeS_2-CsCl system," The Journal of Physical Chemistry B **113**, 14574-14580 (2009).

34. M. Rozé, L. Calvez, Y. Ledemi, M. Allix, G. Matzen, and X.-H. Zhang, "Optical and mechanical properties of glasses and glass–ceramics based on the Ge–Ga–Se system," Journal of the American Ceramic Society **91**, 3566-3570 (2008).

35. C. Julien, S. Barnier, M. Massot, N. Chbani, X. Cai, A. M. Loireau-Lozac'h, and M. Guittard, "Raman and infrared spectroscopic studies of Ge-Ga-Ag sulphide glasses," Materials Science and Engineering: B **22**, 191-200 (1994).

36. S. Barnier, M. Guittard, M. Palazzi, M. Massot, and C. Julien, "Raman and infrared studies of the structure of gallium sulphide based glasses," Materials Science and Engineering: B **14**, 413-417 (1992).

37. Z. G. Ivanova, "Local ordering studies of semiconducting ((GeS_2)100-xGax glasses," Journal of Molecular Structure **245**, 335-340 (1991).

38. G. Guery, J. D. Musgraves, C. Labrugere, E. Fargin, T. Cardinal, and K. Richardson, "Evolution of glass properties during a substitution of S by Se in $Ge_{28}Sb_{12}S_{60-x}Se_x$ glass network," Journal of Non-Crystalline Solids **358**, 1740-1745 (2012).

GENERAL CONCLUSIONS and FUTURE WORK

The works presented in this thesis have mainly been concerned with developing sulfur-based chalcogenide microstructured optical fibers with the purpose of reaching a sustainable infrared supercontinuum fibered source.

The manuscript begins with theoretical background review, in which we focused on the linear and nonlinear optical phenomena, as well as on the properties of nonlinear materials, allowing to understand results of supercontinuum generation presented in later Parts.

Part 2 focused on experimental investigations and enhancement of supercontinuum generation in As_2S_3 suspended-core MOFs. We successfully demonstrated an experimental supercontinuum spanning over 2000 nm in As_2S_3 suspended-core MOF. During our investigations, we have encountered detrimental physical and optical phenomena, namely aging phenomena. The MOF core undergoes a significant shift of its optical and chemical properties under atmospheric conditions. This process should be taken into account when new As_2S_3 broadband sources are to be developed. In the light of the aforementioned, the protection of fiber devices is required. Thanks to a preventive protection procedure, we controlled the deleterious naturally induced drift of optical and chemical properties of the fiber device. Consequently, we successfully increased the continuum bandwidth up to 3500 nm on protected fibers. It is worth to note that in both cases, As_2S_3 MOFs used in these experiments are of the same length scale. They also exhibit the same geometric design and comparable optical loss levels. In addition, these fibers were pumped using the same pump source in similar pumping conditions (pumped in their anomalous dispersion regime, close to their ZWD). Thus, the spectral improvement described on protected sample is mainly attributed to the management of the aging process.

In the framework of these experiments, we elucidated the nonlinear mechanisms responsible for the spectral broadening and limitations that prevent the MIR extension of the SC towards long wavelength edge. We showed that the supercontinuum generated within the fibers is characterized by a strong and rapid self-phase modulation process, followed by soliton fission in the earlier centimeters of the fiber. In addition, the spectrum MIR wavelength edge is primarily limited by the hydrogenated (OH and SH) extrinsic absorption losses, and their time evolution, leading to a discrepancy between simulation results and experimental ones. We adjusted this scatter by considering additional losses of hydrogenated absorptions (OH at 2.9 µm and SH at 4.0 µm). Compared to values measured on freshly drawn fiber, the absolute content of OH and SH moieties in the MOF core have increased 1000 times upon 12 days of exposure to atmospheric conditions.

Part 3 focused on studying in details the detrimental aging process occurring within As_2S_3 microstructured fibers upon exposure to atmospheric conditions, which is responsible of the collapse of the spectrum spanning. We extensively studied the optical, morphological and chemical aging behavior of As_2S_3 glass fibers. We studied the optical degradation of large core As_2S_3-MOF exposed to the atmospheric water vapor using FTIR technique. We showed that the deleterious effects of moisture rapidly occur over the first few hours of exposure and continue to progress over time. This optical aging manifests itself as a strong increase of OH and SH absorption bands. We confirmed that the aging process begins by adsorption of water molecules on the glass surface, especially on the MOF core, and progresses by a substantial decomposition reaction of the glass structure, leading to breakage of glassy backbone of As-S bonds within the glass matrix and formation of As-OH and S-H bonds. Besides that, we showed that the distribution of these bonds along the fiber core is not homogeneous, it decreases exponentially from the fibre ends towards the centre. This confirmed that atmospheric steam diffuses through the MOF holey structure from the fibre ends. This behavior has highly detrimental repercussions on the spectral broadening, since the nonlinear effects from which originates a spectral spanning take place within the first millimeters of the MOF as previously confirmed in part 2. This has implications for the special storage of MOF in suitable conditions, immediately after the drawing process. We succeed to achieve this purpose by airproofing the holes of the MOF. This technique allows a continuous protection of the guiding-core of the MOF during optical experiments.

In the framework of these experiments, the naturally induced deterioration of the glass surface under ambient conditions is confirmed. The surface aging is observed as an increase of surface imperfections which are essentially associated with bumps, holes and cracks. However, these surface features evolve sequentially under wet atmosphere. The first step consists of formation of regular pyramidal crystals of As_2O_3 randomly dispersed on the surface, resulting from the reaction between the glass network and the surrounding ambient steam containing atmosphere. On second step, these crystals amalgamate themselves in growth sites and give rise to new clusters. In a last stage, holes dig within the glass volume.

We experimentally showed that the contamination of the glass diffuses in depth inside the glass from its exposed surface. The set of these phenomena exclusively appears under wet atmosphere. The dynamics of these modifications might be accelerated by increasing the humidity and the temperature of the storage compartment.

Part 4 confirms by experimental achievements the ability of optimization of the composition and synthesis of germanium-based Ge-S-Se chalcogenide glasses for successful fiber drawing, unlike Ge-S and Ge-Ga-S compounds. The purpose of these experiments is to develop green non toxic germanium-based chalcogenide glass fibers, free from highly toxic arsenic and antimony elements. We optimized the glass synthesis process, including the time-temperature synthesis profile, the synthesis glassware dimensions, and the melt quenching technique.

Finally, as major results, a very broad infrared supercontinuum generation with a very flat spectrum, almost three octave spanning, between around 0.5 µm and 4 µm, has been obtained in an As_2S_3 MOF. The actual limitations of these MOFs, preventing further extension of the supercontinuum in the infrared, have been understood and explained. Despite that the As-S MOF is highly sensitive to atmospheric conditions, benefit of its potential remains possible, but this imposes the need to protect continuously the MOF‘s core along the fiber lifetime. By maintaining the advantageous MOF geometry, such purpose is achieved by sealing the holes as proposed in this work. Therefore additional work is still needed to optimize the seeling materials and the seeling technique. Another possible strategy is to develop devices allowing the fiber to operate continuously in a controlled dry atmosphere.

In the context of the progressive implementation of REACH reglementation, early green germanium-based arsenic and antimony-free glass fibers have been promissingly developed. Of course, future work should emphasize on the optimization of the glass optical quality, but purification processes already exist for that purpose, and there is no doubt that this target will be reached. Efficient green MOFs will require to engineer and optimized chromatic dispersive properties through adequate transverse profile with regards to their refractive index behavior (pattern, pitch, holes diameter, core size….) The room temperature drilling for preform preparation and the fiber drawing parameters will need to be adjust for these fibers and it will be necessary to characterize the behavior of these green fibers cores under room atmospheric conditions.

APPENDIX

Appendix 1 : Fourrier Transform Infrared Spectroscopy (FTIR).

1. Theory

Infrared spectroscopy (IR) is one of the most important tools to investigate the glass optical quality by probing molecular absorption of species formed within the glass systems in the course of synthesis process. In addition, IR is highly suitable method to study relevant adsorption systems on surfaces in course of adsorption reaction. The principle of infrared spectroscopy is based on the vibrational excitation of molecules by absorption of infrared light[4]. The information of these vibrational spectra is related to the chemical nature of the absorbing species within the glass volume, as well as the chemical nature of adsorbed molecules and also to the substrate and adsorbate-adsorbate interactions.

In an infrared absorption experiment, infrared radiation with an intensity I_0 and frequency $\nu_0 = c/\lambda_0$ is passed through a sample and the intensity of the transmitted light I is measured as a function of its frequency. Absorption of light at $\Delta E = h\nu_0 = h\, c/\lambda_0$[5]occurs at frequencies corresponding to the energies of vibrational transitions. The function is described as Beer-Lambert law[5, 6]:

$$I = I_0 . \exp(-\varepsilon l c)$$

Here, I_0 and I denote the intensities of the incident and transmitted beams, respectively, ε is the molecular absorption coefficient, c and l are the concentration of the sample and the cell length, respectively. In IR spectroscopy, both the percentage transmission (T(%)), and absorbance (A) are usually plotted versus the wave number. The definitions of T and A are

$$T(\%) = 100 \times \frac{I}{I_0} \text{and } A = \log(I_0/I) = \varepsilon l c$$

Atoms of a molecule vibrate with a definite frequencies that depends on the mass of the atoms, the force of the binding and the structure of the molecule[5, 7]. The molecules will absorb incident electromagnetic radiations at characteristic frequencies corresponding to the energy of vibration of molecules, providing that a change in dipole moment occurs with the vibrations. [5, 7, 8] For better understanding of absorption dynamics, the basic principles of infrared spectroscopy shall be explained.

2. Harmonic and Anharmonic oscillators

Vibrational transitions in a molecule occur between distinct vibrational energy levels[5, 7]. Intramolecular vibrations and intermolecular vibrations are contributing to the spectrum. The simplest possible situation is a vibration between two atoms of a diatomic molecule.

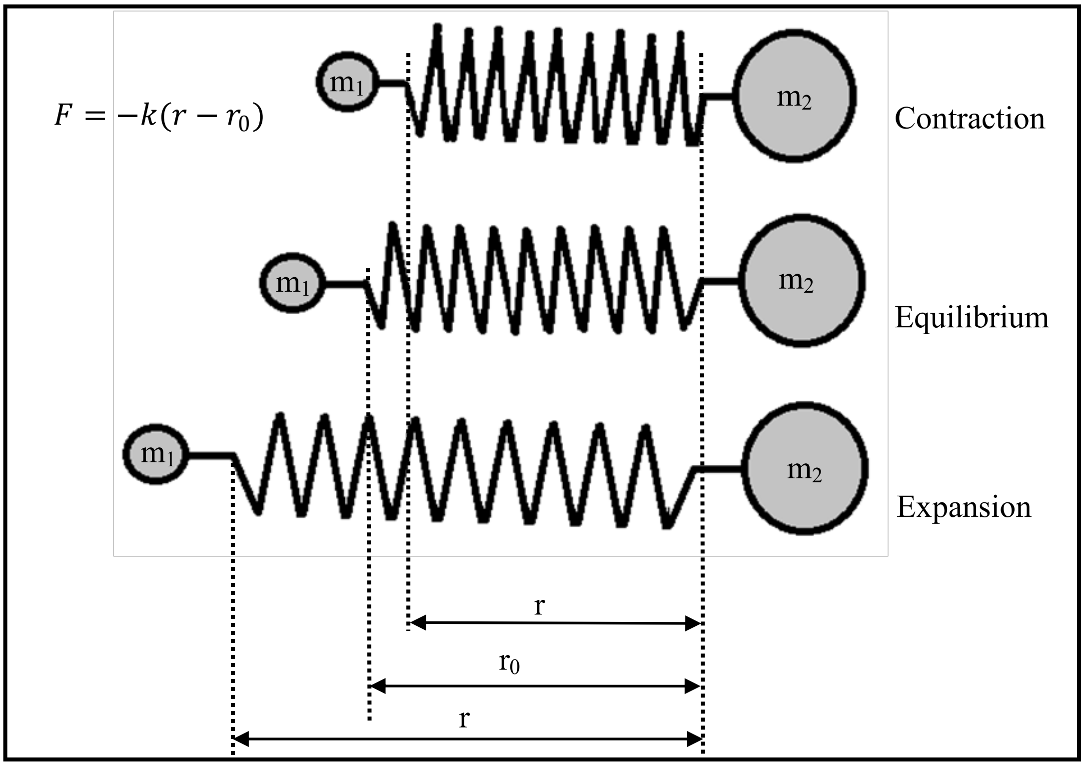

Figure 81: Model of oscillating diatomic molecules vibrating around an equilibrium distance "r_0"

The atoms are separated by r inter-nuclear distance which represents the bond length. An attempt to squeeze the atoms more closely together will lead to a rapid increase of the repulsive force between the two atoms. An attempt to pull them apart is resisted by the attractive force. Both displacements require an input of energy which can be described as a function of the distance between the two atoms. Considering two spheres of the masses $m_1$and m_2 connected through a spring [7].

The force of compression or expansion is then given by Hook‘s law[7]:

$$F = -k(r - r_0)$$

k is a constant, $r - r_0$ the distance difference to the equilibrium distance generated by the force (F). The force is directed against the displacement of the atoms and thus has a negative sign. The potential energy of the oscillating system:

$$E = -\frac{1}{2}K(r - r_0)$$

increases symmetrically when the distance between both atoms is decreased or increased compared to the equilibrium distance. The vibration of such a diatomic molecule is characterized by an oscillation frequency that is given by classical mechanics [4]:

$$\nu_{vib} = \frac{1}{2}\sqrt{\frac{k}{\mu}}$$

Here, μ represents the reduced mass of the considered system, it is given by [4]:

$$\mu = \frac{m_1 \times m_2}{m_1 + m_2}$$

It clearly seen that the oscillation frequency exclusively depends on the masses of oscillating atoms and on the force constant. Consequently, as the mass of an oscillating atom increases, the frequency of the vibration decreases.

In contrast to classical mechanics, vibrational energies of molecules are quantized like all other molecular energies. The allowed vibrational energies are expressed as follow [4]:

$$E_\nu = \left(\nu + \frac{1}{2}\right)h\nu_{vib}$$

where v is called the vibrational quantum number. The equation implies that the lowest vibrational energy (i.e. for$\nu = 0$) is $E = 1/2\, h\nu$. The implication is that a molecule can never have zero vibrational energy; the atoms can never be without a vibrational motion. The quantity $E = 1/2\, h\nu$ is known as the zero-point energy, that depends on the classical oscillation frequency and hence on the strength of the chemical bond and on the masses of atoms that participate in this bond.

Further use of the quantum mechanics leads to a simple selection rule for the harmonic oscillator undergoing vibrational changes:

$$\Delta\nu = \pm 1$$

In addition to this selection rule the condition must be fulfilled that vibrational energy changes will only be observed in a spectrum if the vibration energy can interact with adiation,i.e. if the dipole moment of the molecule is changing with the vibration. Thus infrared spectracan be observed only in heteronuclear diatomic molecules, since homonuclear diatomic molecules have no dipole moment. The energy of a transition between two vibrational states is then given by:

$$E_{\nu-1} - E_{\nu} = \left(\nu + 1 + \frac{1}{2}\right) h\nu - \left(\nu + \frac{1}{2}\right) h\nu = h\nu$$

To have resonance between the vibrating molecule and the exciting radiation, the frequency of the radiation must be identical to the frequency of the vibration.

The above resolution presumed that the vibration behavior of the interconnected masses could be described by the harmonic motion. In fact, the bonds connecting the atoms are elastic, but do not exhibit a harmonic vibrations, thus, they do not obey the Hook's law [4]. The oscillations are characterized by maximum stretching amplitude. Above this characteristic stretching amplitude, the bonds can break and the molecule will dissociate. A purely empiric description of such a behavior of diatomic anharmonic oscillators is proposed by P.M. Morse and given as follow [4]:

$$E = D \times [1 - exp\{-a(r - r_0)\}]^2$$

where D is the dissociation energy and a represents a characteristic constant of particular bond in a specific electronic state.

An expression of vibrational energy in terms of harmonic frequency ν and the anharmonicity constant χ is given as follow [4]:

$$E_{\nu} = \left(\nu + \frac{1}{2}\right) h\nu - \left(\nu + \frac{1}{2}\right)^2 h\nu\chi$$

The energy of the anharmonic oscillators is adjusted to that of harmonic one through this equation. Anharmonic behavior induces tow main features comparing to harmonic vibrations. Firstly, the energy between two successive vibrational levels changes as a function of the bond length. For anharmonic oscillators, this energy decreases as the bond length increases (Figure 82 (b)), whereas it maintains a constant value for harmonic oscillators under the same conditions Figure 82 (a)). Secondly, for harmonic oscillators, permitted vibrational changes are strictly governed by the selective rule ($\Delta\nu = \pm 1$) as discussed above. The later selective rule becomes not rigorous for the anharmonic vibrations, herein transitions with $\Delta\nu = \pm 2$ and $\Delta\nu = \pm 3$ are allowed [4].

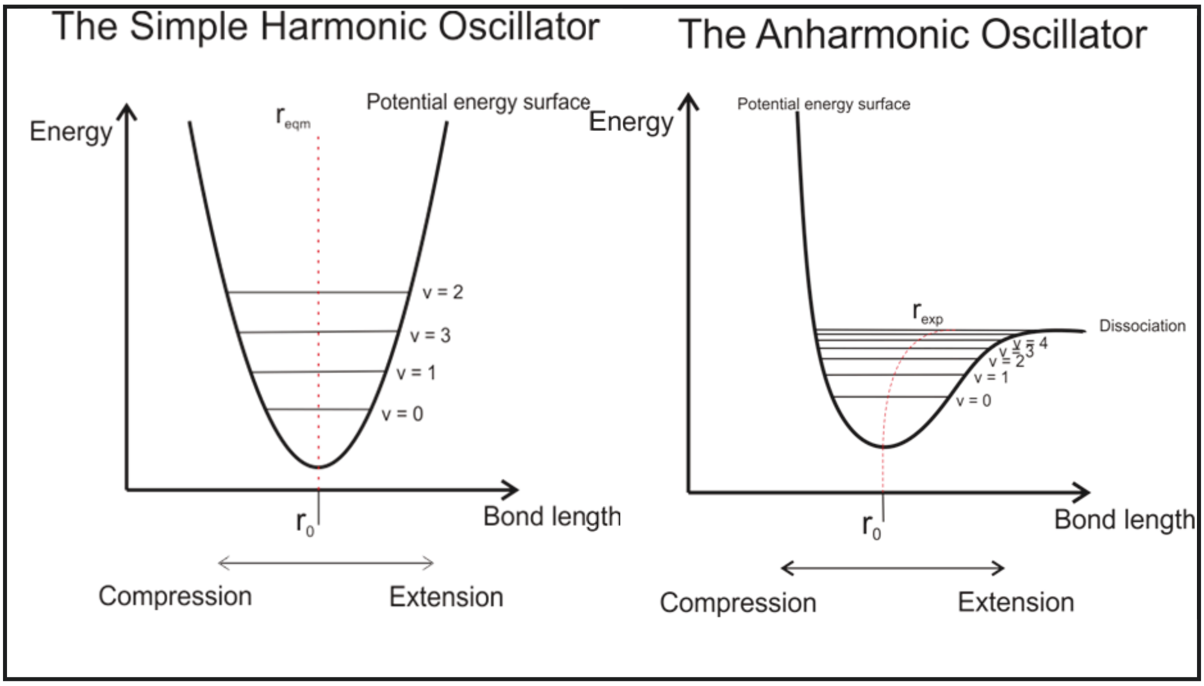

Figure 82 : Vibrational transitions in harmonic and anharmonic oscillators

The transition corresponding to change in quantum number of $\Delta\nu = \pm 1$ are known as fundamental transitions. Corresponding frequency is known as fundamental frequency. If the change in quantum number increases to $\Delta\nu = \pm 2$ or $\Delta\nu = \pm 3$, corresponding transitions are called the first and the second overtone respectively.

Polyatomic molecules exhibits additional vibrations derived from the simultaneous changes in different quantum number of different atoms. Resulting vibrations are called as combination bands.

3. Vibrational modes of polyatomics molecules

The location of each atom within a molecule composed of N atoms, can be described by the locations in space by three coordinates, x, y, z. The total number of such coordinates is therefore $3\,N$. Consequently, the molecule exhibits $3\,N$ degrees of freedom. In such a description, the position of the molecule and the bond-angles are fixed. The translation of the molecule in space is described by three degrees of translational freedom (x, y, z). For the rotational motion of a nonlinear molecule we need additional three degrees of freedom (x, y, z), for a linear molecule just two since the rotation around the bond axis of a linear molecule does not result in a change of the coordinates of the atoms. Therefore, a non-linear molecule must have $3N - 3 - 3 = 3N - 6$ (for non-linear molecules) and $3N - 3 - 2 = 3N - 5$ (for linear molecules) degrees of freedom of internal vibration [5].

Depending on the maintenance of the symmetry in the molecule, vibrations are classified as symmetric and asymmetric vibrations.

4. Fourrier Transform Infrared Spectrometer

Modern spectrometers especially those used in infrared spectroscopy, today almost always make use of Fourier transform techniques to record the spectrum. The heart of the Fourier transform infrared spectrometer is a Michelson interferometer, a device for analyzing the frequencies present in a composite signal.

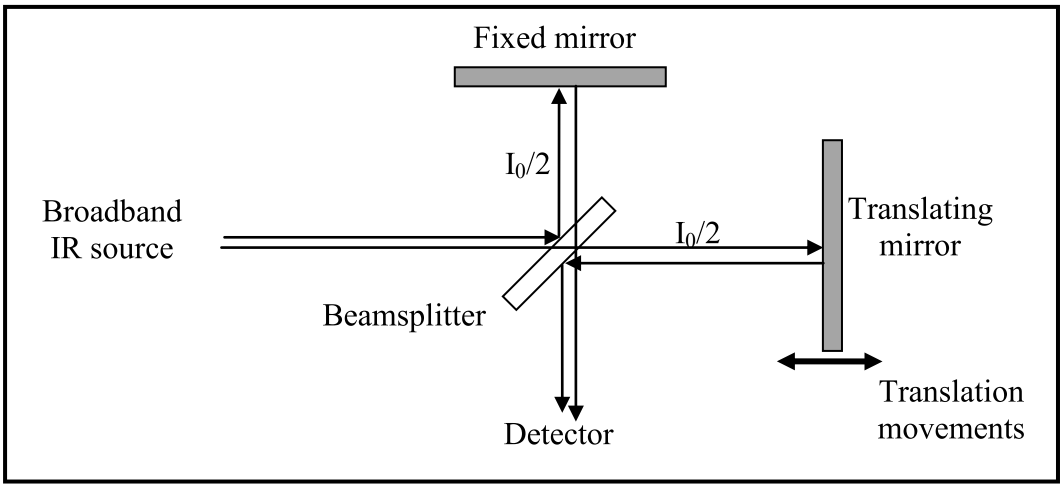

Figure 83 : Schematic diagram of the Michelson Interferometer.

Figure 83 displays a schematic diagram of the Michelson interferometer[6, 9].

The interferometer consists of a broadband IR source, beamsplitter, fixed mirror, moving mirror and a detector. The collimated incident IR beam I is partially transmitted to the moving mirror and partially reflected to the fixed mirror by the beam splitter. These two IR beams are then reflected back to the beam splitter by the mirrors. The moving mirror modulates each frequency of light with a different modulation frequency. In general, the paths of light returning from the fix mirror and the moving mirror are not in phase. The reflected beams interfere constructively or destructively depending on the wavelength of the light and the optical path difference between the mirrors. The latter is usually referred to as retardation, δ. The resulting beam intensity *I(*δ*)*, called interferogram. If the path difference δ is zero, constructive interference occurs, leading to a maximum in the interferogram. For all the other δ values a partial or totally destructive interference occurs, resulting in a fast oscillation decrease on both sides of the interferogram maximum [9].

As mentionned above, detected signal oscillates as the two components alternately come into and out of phase as the path difference is changed. If the radiation has the wavenumber $\bar{v} = v/c = 1/\lambda = E/hc$, the intensity of the detected signal due to radiation in the range of wavenumbers varies with the difference in path length δ as follow:

$$I(\delta) = \int_{0}^{\infty} I(\bar{v})\,(1 + \cos 2\pi\bar{v}\delta)d\bar{v}$$

Performing a mathematical Fourier transform on this signal results in a spectrum identical to that from conventional infrared spectroscopy. The variation in intensity as a function of wavenumber $I(\bar{v})$ is given by:

$$I(\bar{v}) = 4\int_{0}^{\infty} \left[I(\delta) - \frac{1}{2}I(0)\right]\cos(2\pi\bar{v}\delta)\,d\delta$$

This integration is usually performed by a computer that is interfaced to the spectrometer.

FTIR spectrometers are strongly advantageous comparing to classical spectrometers. They are cheaper than conventional spectrometers because building of interferometers is easier than the fabrication of a monochromator. In addition, measurement of a single spectrum is faster for the FTIR technique because the information at all frequencies is collected simultaneously. This allows multiple samples to be collected and averaged together resulting in an improvement in sensitivity. Virtually all modern infrared spectrometers are FTIR instruments.

Appendix 2 : Atomic Force Microscopy (AFM) and Lateral Force Microscopy (LFM)

1. Atomic force microscopy (AFM)

Atomic force microscopy is a unique method of characterizing many of the properties of a sample, as among the others, the surface morphology and topography [10, 11]. The term "microscopy" can be misleading, as an atomic force microscope (AFM) does not use light to capture an image. Instead, it senses the surface in a similar way as a blind man might read braille text by running his finger across the surface features. An AFM is a non-destructive technique, it uses a nanometer-scale version of the blind finger, it is called "cantilever". The cantilever moves across the surface and collect data.

In atomic force microscope (AFM) experiments performed in this work, a cantilever is placed parallel to the surface. The cantilever has a sharp, force-sensing tip at its end, which interacts with the surface. As the interaction force between the cantilever tip and the surface varies, vertical deflections are produced in the cantilever. The deflections are measured and used to compile a topographic image of the surface [11, 12].

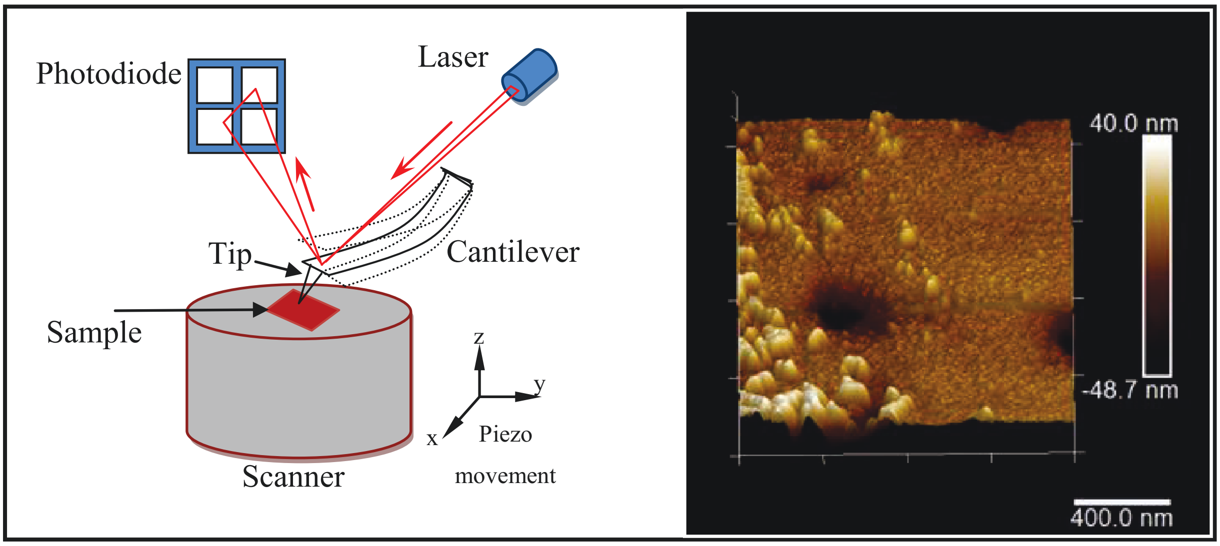

Figure 84 : Scheme of the AFM in which the main components are indicated: the cantilever with the tip at its end, the sample mounted on top of the piezo scanner and the optical system for the cantilever deflection detection (a), and AFM image to show the vertical deviation of the aged glass sample surface (b).

The vertical deflection of the cantilever also generates a depth profile (or height profile) to show the vertical deviations along the surface in the nanometer range (as shown in Figure 84).

The amplitude of the vertical deviations is normally used to calculate the roughness of the surface. In this case, AFM is usually operated in the contact mode for topography imaging and height analysis.

R_a and R_{rms} are the two most commonly used amplitude parameters to describe the surface roughness. Ra is the arithmetic average of absolute amplitude values and R_{rms} corresponds to the root mean squared amplitude values. They are defined as follow:

$$R_a = \frac{1}{n}\sum_{i=1}^{n}|A_i|$$

$$R_{rms} = \sqrt{\frac{1}{n}\sum_{i=1}^{n}A_i^2}$$

where A is the amplitude value of the vertical deviations.

AFM topography imaging and roughness measurements on rectangular chalcogenide fibers surfaces studied in this work were performed in collaboration with Pr. Eric Lesniewska at the Université de Bourgogne.

2. Lateral force microscopy measurements (LFM).

The AFM apart from generating the information about the topography of the sample features can be used to obtain various other informations about the properties of samples. Among the numerous variety of the advanced modes of the AFM, Lateral Force Microscopy (LFM) is of major interest for our study [13, 14].

LFM provides surface sensitive local information about nano-mechanical properties, such as friction coefficient [13]. This technique allows to distinguish areas with different friction and also to obtain edge-enhanced images of any surface. Since the friction coefficient is directly correlated to the chemical composition [15] of probed specimen, a slight chemical deviation within the sample induces a local deviation of friction parameters. Thus, LFM is very useful for studying a sample whose surface consists of inhomogeneous compounds [16]. We used this capability in conjunction with topographical images during one scan for complete characterization of the evolution of mechanical properties of our aged samples.

During a typical LFM scan, torsional bending of the cantilever occurs in the scan direction and the lateral deflection is measured in addition to its vertical deflection due to surface topography. The lateral deflection is measured by applying a force on the cantilever while it horizontally moves across the sample and strength of the lateral deflection signal is related to the friction force between the sample surface and the tip, the topography of the sample surface and the cantilever lateral spring constant. Also, the angle of torsion is proportional to the magnitude of the lateral force. On scanning a flat surface with different friction factor regions, the angle of torsion changes in every region and this allows measurement of the local friction force, and consequently localized the chemical drift appeared as punctual inhomogeneities [16], which evolved within the homogeneous system upon exposure to hostile surrounding.

The LFM uses the quadrilateral photodiode, also known as position sensitive photo detector (PSPD) to indicate the friction between the probe tip and the sample surface. As shown in Figure 85, the PSPD is composed of four photosensitive domains. The top and bottom halves of the detector monitor deflection for AFM imaging whereas the right and left halves report twisting of the cantilever for lateral force imaging. The quadrilateral photodiode detectors are engineered to be extremely sensitive to minute deflections in order to maintain a high degree of precision.

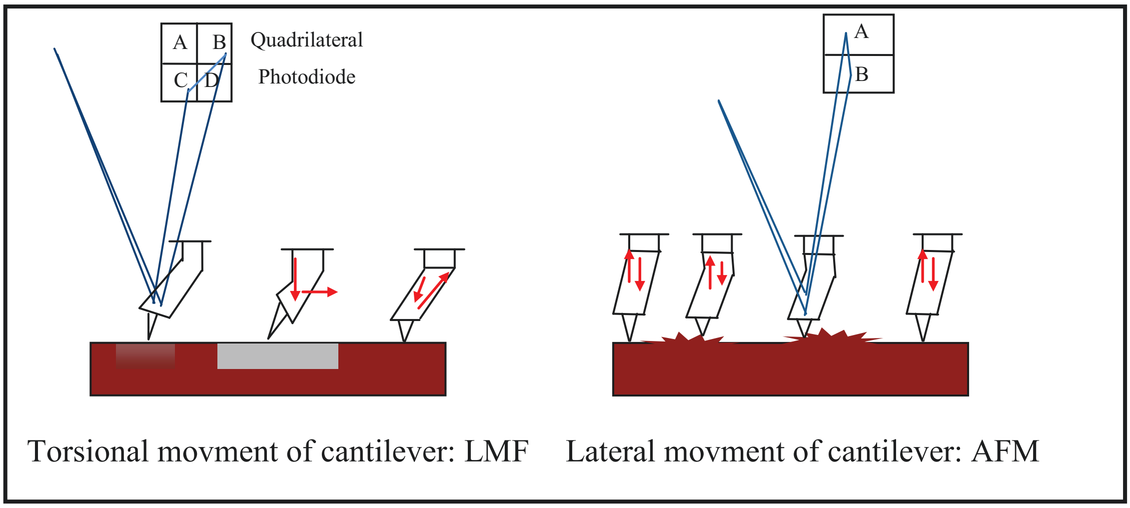

Figure 85 : Torsional and lateral movement of cantilever: AFM and LFM

Appendix 3 : X-ray photoelectron spectroscopy (XPS)

1. Theory

X-ray photoelectron spectroscopy (XPS) is currently the most widely used for used surface analytical non-destructive technique. In this work, XPS measurements were performed and the spectra were applied for qualitative and quantitative surface analysis.

The principle of the XPS technique is the emission of electrons from atoms by absorption of photons. The sample is often irradiated with monoenergetic X-rays, and Mg Ka (1253.6 eV) or Al Ka (1486.6 eV) is used. Photoelectron emission occurs when a photon transfers its energy to an electron, and a photoelectron can be emitted only when the photon energy is larger than the binding energy of the electron. The emitted photoelectrons have kinetic energies, E_{kin}, described by the Einstein equation[12, 17, 18]:

$$E_{kin} = h\nu - E_b - \psi$$

where $h\nu$ is the energy of the incident photon (h and ν are the Plank constant and the incident ray frequency respectively), E_b is the binding energy of the atomic orbital from which the electron originates and ψ is the work function of the spectrometer. As the energy of the photons and the spectrometer work function are known quantities, the measurement the electron binding energies can be obtained by measuring the kinetic energies of the photoelectrons.

XPS is a very surface sensitive analysing method. Since the kinetic energies emitted X-ray photons is low in the energy range used in XPS, photoionisation normally leads to two emitted electrons: a photoelectron and an Auger electron. This is due to the relatively short inelastic mean free path for the photoelectrons, the transportation of emitted electrons, generated in the solid, to the surface can only occur from a certain depth (60-80 Angströms order of magnitude). However, using XPS it is possible to detect all elements except for H and He.

2. XPS survey spectra and chemical shift

Figure 86 shows a survey scan XPS spectrum of As_2S_3 glass fibers. Obviously, the sharp photoelectron peaks are the most prominent in the spectrum. The photoelectrons from As3d and S2p orbitals generate two characteristic peaks arising at about 42.5 eV and 161.5 eV, respectively. In addition we find a peak attributed to O1s orbital at around 532 eV. These peaks indicate the presence of As_2S_3 and corresponding oxide on the specimen surface.

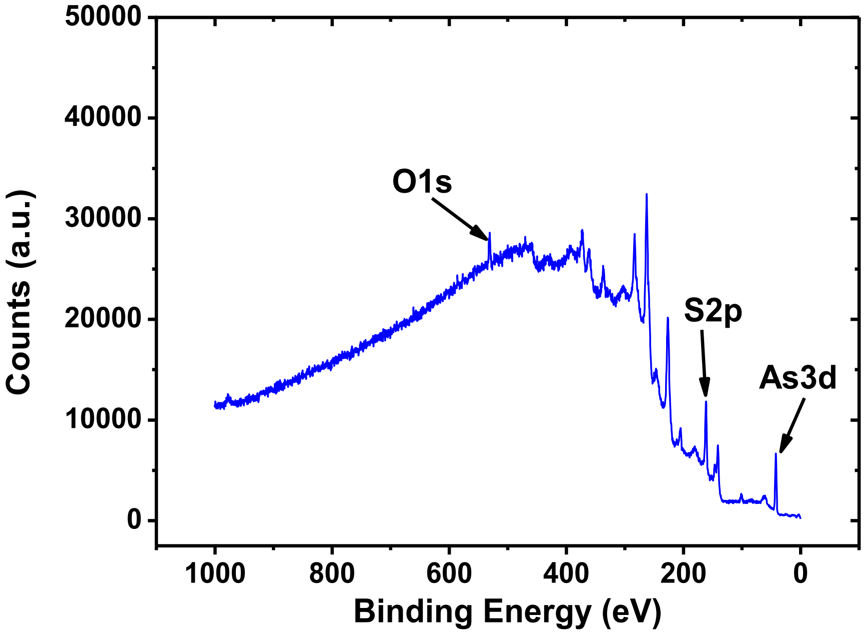

Figure 86 : XPS survey spectrum of As_2S_3 exposed to atmospheric conditions

An XPS spectrum shows the number of photoelectrons as a function of binding energy. The spectrum will be a superposition of photoelectron and Auger lines with accompanying satellites and loss peaks and a background due to inelastic scattering in the substrate. However, the main advantage of using the XPS-technique lies in the fact that the binding energy of a photoelectron is sensitive to the chemical surrounding of the atom, i.e. there is a chemical shift in the binding energy. These shifts are very important since they provide a tool to identify individual chemical states of an element. Unfortunately, it is not always straightforward to interpret these chemical shifts because they depend both on initial and final state effects. In general, the chemical shift increases with increasing positive charge of the element of interest. More precisely, when a sulfur or arsenic atom is bound to oxygen atom, the electron density around the electron density around them will decreases, and the effective nuclear charge increases. Therefore, the core level electrons are more strongly attracted to the nucleus, resulting in a higher binding energy.

An XPS machine is usually equipped with an ion gun, thus enabling ion etching of the surface to produce elemental depth profiles. It is possible to perform sputter depth profiling of a sample to obtain elemental distribution as a function of depth. Another way to obtain compositional information as a function of depth is by tilting the sample relative to the analyzer, which decreases the effective sampling depth, and makes the analysis more surface sensitive. Such feature makes possible to draw conclusions about compositional properties of adsorbed species at the sample surface.

3. Multiplet splitting of As and S elements.

The total angular momentum (j) of an electron correspond to the sum of the individual electron angular (l) and spin (s) momenta, $j = l + s$ [18]. All orbital levels except the "s" levels ($l = 0$) give rise to a doublet with the two possible states having different binding energies. This is known as spin-orbit splitting (or *j-j* coupling). For the As 3d orbital, the quantum number n equals 3, corresponding angular momentum quantum number l equals 2. The electron spin momentum quantum number varies between +1/2 and -1/2, depending on whether the tow electrons are parallel or anti-parallel. Therefore, j can be $j_+ = 5/2$ or $j_- = 3/2$. In this way, the As 3d orbital splits to two different energy states, As $3d_{5/2}$ and As $3d_{3/2}$. Additionally, For the S 2p orbital, the quantum number n equals 2, corresponding angular momentum quantum number l equals 1. Admitting the same values of the electron spin momentum quantum number according to the spin orientation, j can be $j_+ = 3/2$ or $j_- = 1/2$. Consequently, the S 2p orbital also splits as tow energy states, S $2p_{3/2}$ and S $2p_{1/2}$.

The intensity of the doublets is is determined by the occupation probability of the tow different energy states, which also be expressed as the multiplicity, $M = 2j + 1$. Therefore, the intensity ratio of As $3d_{5/2}$ to As $3d_{3/2}$ as well as S $2p_{3/2}$ to S $2p_{1/2}$ can be calculated as 6/4 and 4/2 respectively.

Appendix 4 : Germanium-based glass system

Table 8 : Compositions of Germanium-based mono-chalcogenide (GeS and GeGaS) and di-chalcogenide (GeSSe) glasses prepared in frame of this work. D_I and T represent the inner diameter and the thickness of the various ampoules used to prepare the glass rods.

Glass composition	Batch weight (g)	Ampoule dimensions		Optimal quenching
		D_I (mm)	T (mm)	
$GeS_{2.2}$ ($Ge_{31.25}S_{68.75}$)	10-15	9-16	2-3	Free air
$GeS_{2.5}$ ($Ge_{28.57}S_{71.43}$)	10-15	9-16	2-3	Free air
GeS_3 ($Ge_{25.0}S_{75.0}$)	10-15	9-16	2-3	Free air
$Ge_{23.75}Ga_{1.25}S_{75}$	10-15	9-16	2-3	Compressed air
$Ge_{24.0}Ga_{2.45}S_{73.5}$	10-15	9-16	2-3	Compressed air
$Ge_{18.0}Ga_{7.0}S_{75.0}$	10-15	9-16	2-3	Compressed air
$Ge_{20.0}Ga_{5.0}S_{75.0}$	10-15	9-16	2-3	Compressed air
$Ge_{23.0}Ga_{2.0}S_{75.0}$	10-15	9-16	2-3	Compressed air
$Ge_{30.0}Ga_{5.0}S_{65.0}$	10-15	9-16	2-3	Compressed air
$Ge_{31.0}Ga_{0.06}S_{69.3}$	10-15	9-16	2-3	Compressed air
$Ge_{28.0}Ga_{0.06}S_{71.5}$	10-15	9-16	2-3	Compressed air
$Ge_{24.5}Ga_{0.055}S_{70.0}$	10-15	9-16	2-3	Compressed air
$Ge_{24.3}Ga_{1.1}S_{74.6}$	10-15	9-16	2-3	Compressed air
$Ge_{26.0}Ga_{9.0}S_{65.0}$	10-15	9-16	2-3	Compressed air
$Ge_{23.5}Ga_{11.7}S_{64.7}$	10-15	9-16	2-3	Compressed air
$Ge_{28.0}Ga_{0.56}S_{71.8}$	10-15	9-16	2-3	Compressed air
$Ge_{24.4}S_{65.8}Se_{9.8}$	50	16	3	Water
$Ge_{23.8}S_{57.1}Se_{19.1}$	50	16	3	Water
$Ge_{23.2}S_{48.8}Se_{27.9}$	50	16	3	Water
$Ge_{22.7}S_{40.9}Se_{36.4}$	50	16	3	Water

Table 9 : Fiber drawing ability, crystallization tendency and guidance potentials of different chalcogenide glass compositions.

Glass composition	Preform diameter (mm)	Crystallization upon drawing	Fiber drawing	Fiber guidance capability
$Ge_{31.25}S_{68.75}$	9-12	High rate	Failure	--
$Ge_{31.25}S_{68.75}$	9-12	High rate	Failure	--
$Ge_{25.0}S_{75.0}$	9-12	High rate	Failure	--
$Ge_{23.75}Ga_{1.25}S_{75}$	9-12	High rate	Failure	--
$Ge_{24.0}Ga_{2.45}S_{73.5}$	9-12	High rate	Failure	--
$Ge_{18.0}Ga_{7.0}S_{75.0}$	9-12	High rate	Failure	--
$Ge_{20.0}Ga_{5.0}S_{75.0}$	9-12	High rate	Failure	--
$Ge_{23.0}Ga_{2.0}S_{75.0}$	9-12	High rate	Failure	--
$Ge_{30.0}Ga_{5.0}S_{65.0}$	9-12	High rate	Failure	--
$Ge_{31.0}Ga_{0.06}S_{69.3}$	9-12	High rate	Failure	--
$Ge_{28.0}Ga_{0.06}S_{71.5}$	9-12	High rate	Failure	--
$Ge_{24.5}Ga_{0.055}S_{70.0}$	9-12	High rate	Failure	--
$Ge_{24.3}Ga_{1.1}S_{74.6}$	9-12	High rate	Failure	--
$Ge_{26.0}Ga_{9.0}S_{65.0}$	9-12	High rate	Failure	--
$Ge_{23.5}Ga_{11.7}S_{64.7}$	9-12	High rate	Failure	--
$Ge_{28.0}Ga_{0.56}S_{71.8}$	9-12	High rate	Failure	--
$Ge_{24.4}S_{65.8}Se_{9.8}$	16	Low rate	Successful	Medium
$Ge_{23.8}S_{57.1}Se_{19.1}$	16	Absent	Successful	Good
$Ge_{23.2}S_{48.8}Se_{27.9}$	16	Absent	Successful	Good
$Ge_{22.7}S_{40.9}Se_{36.4}$	16	Absent	Successful	Good

References

1. D. N. Sathyanarayana, *Vibrational Spectroscopy: Theory And Applications* (New Age International (P) Limited, 2007).
2. P. Atkins, and J. de Paula, *Atkin's physical chemistry* (Oxford University Press, 2006).
3. D. Campbell, R. A. Pethrick, and J. R. White, *Polymer characterization: physical techniques* (CRC press, 2000).
4. D. C. Harris, and M. D. Bertolucci, *Symmetry and spectroscopy: an introduction to vibrational and electronic spectroscopy* (Courier Dover Publications, 1978).
5. B. Stuart, "Infrared Spectroscopy," in *Kirk-Othmer Encyclopedia of Chemical Technology* (John Wiley & Sons, Inc., 2000).
6. B. C. Smith, *Fundamentals of Fourier transform infrared spectroscopy* (CRC press, 2011).
7. G. Zavala, "Atomic force microscopy, a tool for characterization, synthesis and chemical processes," Colloid and Polymer Science **286**, 85-95 (2008).
8. S. N. Magonov, and M.-H. Whangbo, *Surface analysis with STM and AFM: experimental and theoretical aspects of image analysis* (John Wiley & Sons, 2008).
9. J. C. Vickerman, and I. Gilmore, *Surface Analysis: The Principal Techniques, 2nd Edition* (John Wiley & Sons, 2009).
10. M. Falvo, and R. Superfine, "Mechanics and friction at the nanometer scale," Journal of Nanoparticle Research **2**, 237-248 (2000).
11. B. Lorenz, *Contact mechanics and friction of elastic solids on hard and rough substrates* (Forschungszentrum Julich, 2012).
12. A. Erdemir, S. Li, and Y. Jin, "Relation of certain quantum chemical parameters to lubrication behavior of solid oxides," International Journal of Molecular Sciences **6**, 203-218 (2005).
13. J.-A. Ruan, and B. Bhushan, "Atomic-scale friction measurements using friction force microscopy: part I-general principles and new measurement techniques," Journal of Tribology **116**, 378-388 (1994).
14. P. M. A. Sherwood, *Auger and X-ray photoelectron spectroscopy* (Chichester, England, 1990).
15. B. K. Agarwal, *X-ray spectroscopy: an introduction* (Springer-Verlag, 1991).